SAPIENZA
UNIVERSITÀ DI ROMA

Sapienza Università di Roma
Facoltà di Ingegneria
Dipartimento di Scienza e Tecnica dell'Informazione e Comunicazione

Dottorato di Ricerca in Telerilevamento
XXII ciclo

Multichannel Passive Radar: signal processing and experimental prototype development

Candidato: Carlo Bongioanni

Tutor: Prof. Pierfrancesco Lombardo

INDEX

I INTRODUCTION

In the framework of research activity on passive radar systems for target detection and localization in this thesis three main topics are presented: (i) the joint exploitation of the signals of opportunity received at multiple carrier frequencies, which can provide the best performance in term of detection capability, since it exploits all available information and makes the detection scheme robust with respect to both the content of the broadcast radio program and the propagation channel conditions; (ii) the set-up of a new acquisition device with up to four input channels; (iii) the exploitation of new promising waveforms of opportunity (DVB-T signals), which represent an interesting choice for PBR systems development.

In Section II the principles of passive bistatic radar systems are introduced and described, together with a short focus on some geometrical considerations related to the bistatic geometry. The passive, non-cooperative operation implies that the transmitted waveform is not known at the receiver, which needs an additional receiving channel (reference channel) to collect the directly transmitted signal. This is used to perform both the clutter/multipath cancellation and the long integration required to provide an acceptable detection capability. A major point in this process is that – while the detection and localization performance depend on the transmitted waveform – this is not within the control of the radar designer, who cannot select it appropriately to guarantee desired properties (e.g. narrow peak in both range and Doppler and low side-lobes). It is therefore likely that target echoes are masked by both the small fraction of the direct signal received by the side/backlobe of the receiver antenna (which might be larger than the clutter echo), by strong clutter/multipath echoes, and even by other targets with higher returns. Thus specialized signal processing techniques have been developed to remove these undesired contributions on the received signal, [6]-[9]. Despite the effectiveness of the cancellation techniques, the PBR performance still depends on the characteristics of the received waveform; moreover, these characteristics can be variable in time in an unpredictable manner. This is clearly the case with the transmitted FM radio waveforms which result in a PBR ambiguity function with characteristics that usually have a time-varying structure, involving both range resolution and sidelobe level which exist at a level not largely lower than the peak, [10]-[11]. In turn, the target detection performance depends on range resolution, sidelobe level, and their interaction with the detection threshold, typically selected adaptively to guarantee a constant rate of false alarms. Therefore, also detection performance is time

varying and largely depends on:

(i) the instantaneous transmitted waveform on the channel under consideration;

(ii) the instantaneous characteristics of the propagation for the considered channel.

This time varying behaviour is illustrated in Section III , as the main motivation for the presented multi-frequency integration approach, together with the standard increase of equivalent Signal-to-Noise Ratio (SNR) clearly achievable trough the integration. The joint exploitation of the signals of opportunity received at multiple carrier frequencies, corresponding to different FM radio channels, can provide the best performance in term of detection capability, since it exploits all available information and makes the detection scheme robust with respect to both the content of the broadcast radio program and the propagation channel conditions. The considered multi-frequency integration approaches are introduced and discussed, together with the corresponding adaptive thresholds, in Section IV , where also some implementation details are reported. To allow the practical application, as well as a fair performance comparison, in the same Section we find analytical relationships between probability of false alarm and adaptive threshold. These allow us to set for each integration scheme the appropriate detection threshold to guarantee the same desired probability of false alarm. A specifical sub-section (IV.3) shows the results of a comparative analysis of the detection probability obtained by simulation for the introduced integration and detection schemes, with reference to a set of specific study cases, that give some insights into the properties of the different ways to perform the multi-frequency integration.

However, a full validation of the effectiveness and of the relative performance of the different multi-frequency techniques is provided though the application against live multi-channel PBR data. To this purpose, we have developed two experimental PBR prototypes that are able to properly receive the signals broadcasted in the whole FM bandwidth 88÷108 MHz. Section V describes the developed systems, together with the experimental acquisition campaigns that have been carried out in an area with a reasonable density of air traffic. A selection procedure has been developed for the identification of the FM radio channels that are able to provide the best detection performance. In order to validate the performance of the developed prototypes and verify the improvement available through the multi-frequency approach, the data collected at the selected channels have been processed according to the signal processing techniques developed in [8]-[9]. The results obtained operating with the selected single FM radio channels are reported in Section VI , as a reference for the performance evaluation, while Section VII is devoted to a thorough comparative analysis of the performance achieved with the presented multi-frequency integration techniques.

Section VIII is fully dedicated to a new acquisition device (named ICS-554B), acquired in order to extend the developed dual channel PBR prototypes to a new prototype with up to four receiving channels. This new device allows the acquisition of data with up to four different antennas, thus offering the possibility to exploit several new receiver configurations: for example, it is possible to set up a receiving configuration with two reference and two surveillance antennas, with different polarizations, thus having a simultaneous acquisition with a couple of antennas (reference and surveillance) in vertical polarization and another couple in horizontal polarization. Moreover, it is possible to have one reference antenna and two (or three) surveillance antennas, aiming at performing not only target detection but also localization (Direction of Arrival – DOA – estimation), and so on. The main features of this new acquisition device are described in the first part of this section, together with the analysis and tests performed to validate its performance both with data from a signal generator and acquired with the antennas. Finally, the first results of a new acquisition campaign carried on 29th and 30th April 2009 with this new device are reported.

As it is apparent, this thesis is mainly focused on the description of a multichannel passive radar based on FM radio signals as waveform of opportunity. Moreover, among broadcast transmitters, digital transmissions such as Digital Audio Broadcasting (DAB) and Digital Video Broadcasting-Terrestrial (DVB-T) represent an interesting choice as waveform of opportunity for such a system [12]-[15]. Currently, digital broadcasting is proliferating and rapidly replacing the analogue counterparts. Specifically, with reference to television broadcast, a number of countries have already switched or planned to switch to the DVB-T standard. These signals show both excellent coverage and wider frequency bandwidth, which results in increased range resolution achievable. Following these considerations, the research activity of the group is also focused on digital broadcasting signals, aiming at the realization of a multichannel passive radar prototype based on these signals. This is the reason why in Section IX of this thesis the attention is focused on DVB-T signals and on the problems arising from their use as opportunity waveform in PBR systems.

II PASSIVE BISTATIC RADAR WORKING PRINCIPLE

II.1 *Introduction*

In recent years there has been a renewed interest in Passive Bistatic Radar (PBR), using existing transmitters as illuminators of opportunity to perform target detection and localization with many advantages such as low cost, covert operation, low vulnerability to electronic countermeasure, reduced Electro-Magnetic pollution, etc., e.g. [1]. PBR is based on the exploitation of an existing transmitter as an illuminator of opportunity and on a receiving system that is appropriately designed and sited to provide coverage of a specific area. Broadcast transmitters represent some of the most attractive choices for long range surveillance application due to their excellent coverage: different transmitters are available and have been used in the past as sources of opportunity [2]-[3]. The most common signals for PBR in use today are FM radio and UHF television broadcasts, [4]-[5], as well as digital transmissions such as Digital Audio Broadcasting (DAB) and Digital Video Broadcasting-Terrestrial (DVB-T), [2]-[3]. In particular, the broadcast transmitters of the commercial radio stations in the FM band 88-108 MHz are especially attractive for the generally high level of transmitted power, for the wide coverage, and for the limited cost of the required receivers, [4]-[5]. Due to the variable and unpredictable characteristics of the transmitted waveform (out of control of the radar designer), the side-lobes of the ambiguity function have often a time-varying structure and a level not much lower than the peak, [1], [10]-[11]. It is therefore likely that target echoes are masked by: (i) the fraction of the direct signal received by the side/back-lobe of the surveillance antenna, (ii) strong clutter/multipath echoes, and (iii) echoes from other strong targets, even in the presence of large range-Doppler separations. Thus the cancellation of these undesired contributions becomes a crucial issue for target detection, [1], [7]-[9]. Additional limitations are due to the need of a dedicated receiving channel to collect a copy of the transmitted signal for matched filtering (usually named reference signal), which might be affected by multipath. Moreover, practical limitations are related to the system implementation, as channel mismatch, dynamic range, impact of the e.m. “environment”, and co-/adjacent-channel interference.

The typical PBR processing scheme is depicted in Figure 1. The low level signal reflected from the target is collected by the PBR receiver (surveillance channel), using a directive antenna steered toward

the area where surveillance is desired. The surveillance channel should ideally collect only the signals reflected by desired targets; in reality, it is affected also by a fraction of the direct signal coming from the transmitter and received by the side/backlobe of the surveillance antenna, and by strong clutter/multipath echoes. These undesired contributions can mask the low signals reflected from targets and/or introduce false alarms. The directive antennas used in the prototype described in this work are characterized by a front to back ratio greater than 20 dB in order to partially reject the direct signal at the surveillance channel (by properly pointing the antenna whit its pattern null in the direction of the selected transmitter of opportunity). However, this approach can not yield a complete disturbance removal, so the signal collected at the reference channel is first used to remove undesired contributions on the surveillance channel. Different approaches have been proposed to cope with this problem, potentially yielding remarkable cancellation performance and acceptable computational load ([4], [6]-[9]). After the cancellation stage, the detection process is based on the evaluation of the Bistatic Range-Velocity Cross-Correlation Function (2D-CCF) between the surveillance and the reference signal. A Constant False Alarm Rate (CFAR) threshold can be then applied on the obtained map to automatically detect the potential targets according to a specific CFAR detection scheme.

II.2 *Geometry and Doppler relationships*

A bistatic radar is defined as a radar system with transmitting and receiving antennas not co-located. In Figure 2 the coordinate system and parameters defining bistatic radar operation in the plane containing transmitter (T_x), receiver (R_x) and Target are sketched. This plane is called the bistatic plane. The distance L between the transmitter and receiver is called the baseline range, or simply baseline. The angles Θ_T and Θ_R are, respectively, the transmitter and receiver look angles, which are taken as positive when measured clockwise from North. The bistatic angle β is the angle between the transmitter and receiver with the vertex at the target, and is defined as:

$$\beta = \Theta_T - \Theta_R \tag{II.1}$$

A bistatic radar usually measures target range as the range sum as:

$$R_B = R_T + R_R \tag{II.2}$$

A contour of constant range sum, or isorange contour, is described by an ellipse (see Figure 3, where a 3D ellipsoidal isorange surface is sketched), which is defined as the locus of points in which the sum of the distance from two fixed points is constant. When the two fixed points are the T_x and R_x sites, we have:

$$R_B = R_T + R_R = 2a \tag{II.3}$$

where a is the semimajor axis of the ellipse. In a monostatic radar, $R_T = R_R$ and its isorange contour is a circle of radius a, the limiting case for a bistatic isorange contour.

A canonical definition of bistatic Doppler, or Doppler shift, f_B, ignoring relativistic effects, is the rate of change of the total path length of the scattered signal, normalized by the wavelength λ. Because the total path length is the bistatic range R_B (see II.2), we can write f_B as:

$$f_B = \frac{1}{\lambda}\left[\frac{d}{dt}(R_T + R_R)\right] = \frac{1}{\lambda}\left[\frac{dR_T}{dt} + \frac{dR_R}{dt}\right] \tag{II.4}$$

When the transmitter and receiver are stationary, and the target is moving (with a velocity vector **V** projected onto the bistatic plane), the target's bistatic Doppler at the receiver site is developed as

follows. The term dR_T/dt in II.4 is the projection of the target velocity vector onto the transmitter-to-target Line Of Sight (LOS):

$$\frac{dR_T}{dt} = V\cos(\delta - \frac{\beta}{2}) \tag{II.5}$$

where β/2 is the angle of the bistatic bisector and δ is the angle between the velocity vector V and the bistatic bisector. Similarly, dR_R/dt is the projection of the target velocity vector onto the receiver-to-target LOS:

$$\frac{dR_R}{dt} = V\cos(\delta + \frac{\beta}{2}) \tag{II.6}$$

Combining II.4, II.5 and II.6 yields

$$f_B = \frac{V}{\lambda}\left[\cos(\delta - \frac{\beta}{2}) + \cos(\delta + \frac{\beta}{2})\right] = \frac{2V}{\lambda}\left[\cos\delta\cos\left(\frac{\beta}{2}\right)\right] \tag{II.7}$$

Further information about bistatic geometry and Doppler relationships can be found in [16].

II.3 *Bistatic radar equation*

With reference to the geometry sketched in Figure 2, received power can be expressed as:

$$P_R = \frac{P_T G_T}{4\pi R_T^2} \frac{\sigma_b}{4\pi R_R^2} \frac{G_R \lambda^2}{4\pi} \tag{II.8}$$

where:

- P_R is the received power
- P_T is the transmitted power
- G_T is the transmitter antenna gain
- G_R is the receiver antenna gain
- λ is the signal wavelength [m]
- σ_b is the Bistatic Radar Cross-Section (BRCS) [m^2]
- R_T is the transmitter-target distance
- R_R is the receiver-target distance

The first factor in the right-hand side of eq. II.8 represents the power density per surface unit emitted by the transmitter, the second factor is the portion of power scattered from the target in the receiver direction, the third factor represents the antenna effective area, expressed as a function of the receiver gain.

In order to evaluate the BRCS, we can use some relations with the monostatic RCS that can yield to good approximations. Specifically, we can consider three different regions as a function of the bistatic angle β: *quasi-monostatic*, *bistatic* and *forward-scatter* region. Inside the first region (*quasi-monostatic*), the BRCS value can be approximated with the monostatic RCS multiplied by $cos(\beta/2)$, and this relation stands for low bistatic angles ($\beta<5°$) and for low frequencies. For bistatic angles higher than 5° (bistatic region), BRCS is quite different from the monostatic one, and the following relation is valid:

$$-20dB < \frac{\sigma_{bistatic}}{\sigma_{monostatic}} < -12dB \tag{II.9}$$

Finally, if the target is on the baseline ($\beta=180°$), we are in the *forward-scatter* region.

Received power P_R in II.8 can be replaced with the smallest received power that can be detected by the radar, S_{MIN}, expressed by

$$P_R = S_{MIN} = KT_0 B_n F_n \left(\frac{S}{N}\right)_{MIN} \tag{II.10}$$

and also the loss factors L_{PT} and L_{PR} (both lower or equal than one), which represent the losses from transmitter to target and from receiver to target, respectively, can be included, thus obtaining the following relation:

$$\left(\frac{S}{N}\right) = \frac{P_R}{P_N} = \frac{P_T G_T G_R \lambda^2 L_{P_T} L_{P_R} \sigma_b}{(4\pi)^3 R_T^2 R_R^2 KT_0 B_n F_n} \tag{II.11}$$

In the bistatic triangle of Figure 2, formed by target, transmitter and receiver, if the product between R_T and R_R is constant, the locus of points defined by target positions is known as Oval of Cassini. These ovals are composed by points characterized by constant power levels (SNR) at the receiver; in order to obtain the Cassini Ovals we need to consider all the parameter of the bistatic radar equation as constant except for R_T and R_R, so that II.11 can be written as

$$\left(\frac{S}{N}\right) = \frac{k}{R_T^2 R_R^2} \tag{II.12}$$

with

$$k = \frac{P_T G_T G_R \lambda^2 L_{P_T} L_{P_R} \sigma_b}{(4\pi)^3 KT_0 B_n F_n} \tag{II.13}$$

This simplified version of bistatic radar equation highlights that, for each point of the space, SNR measured at the receiver depends on the target position with respect to both the transmitter and the receiver.

II.4 *Figures*

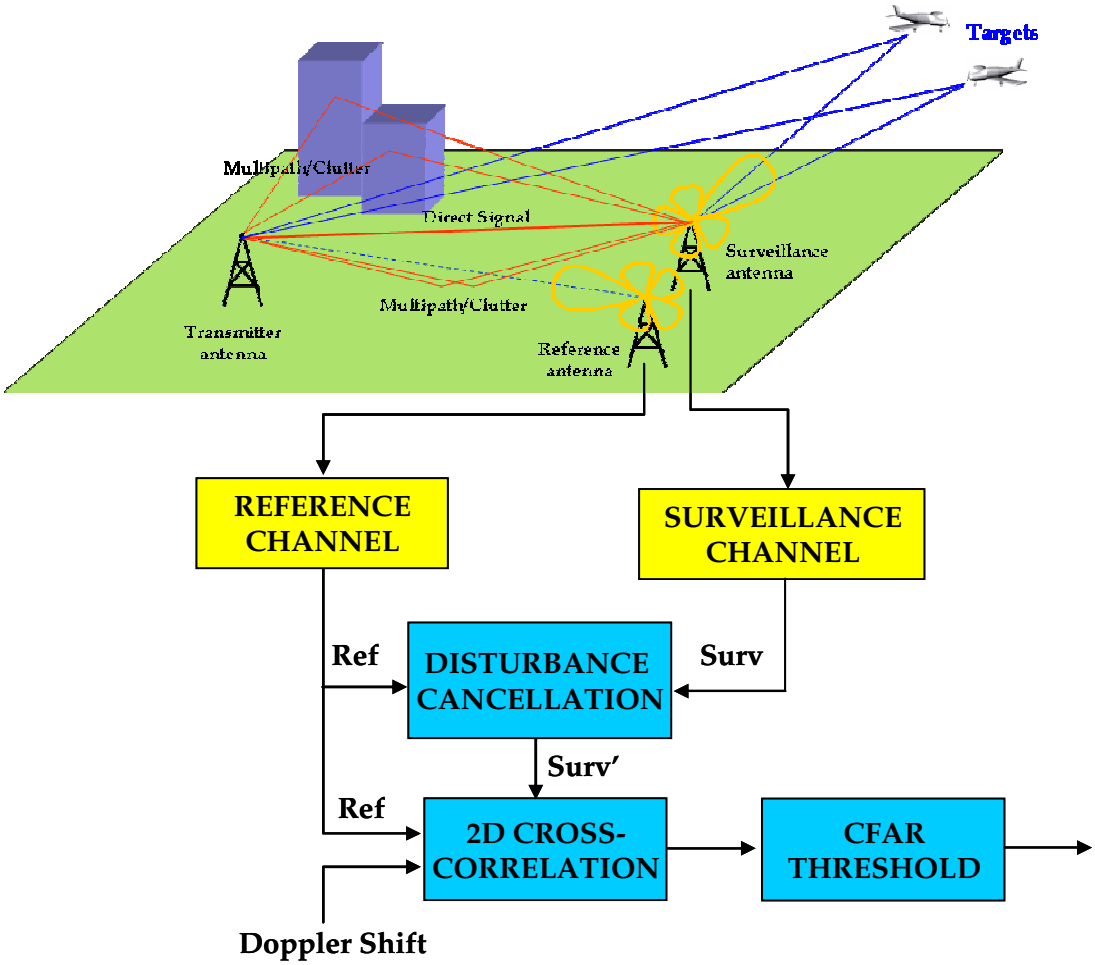

Figure 1 – PBR Processing scheme

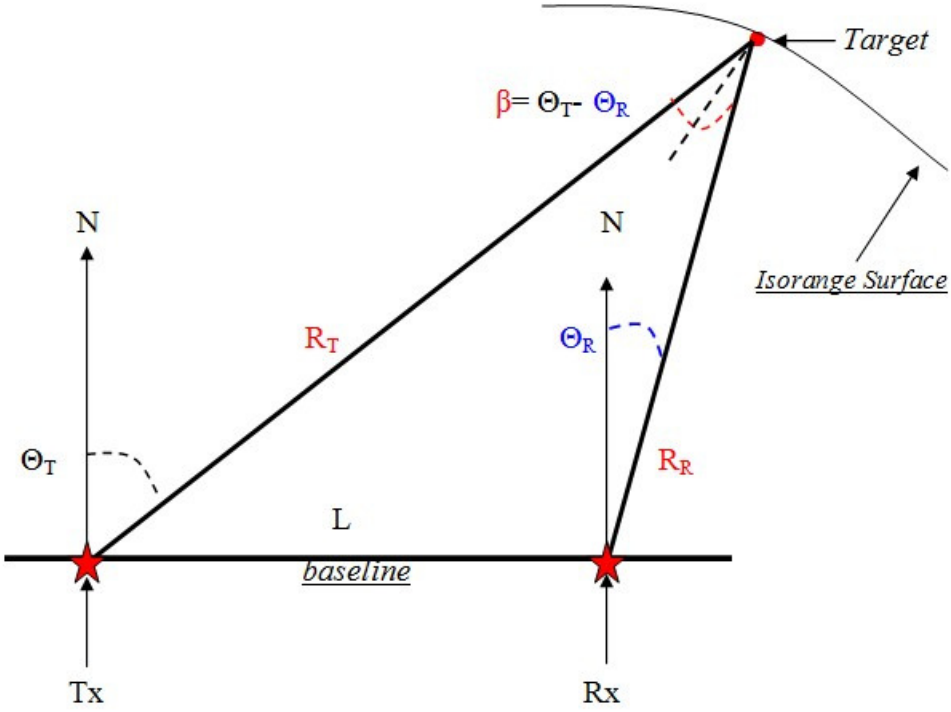

Figure 2 – Bistatic geometry.

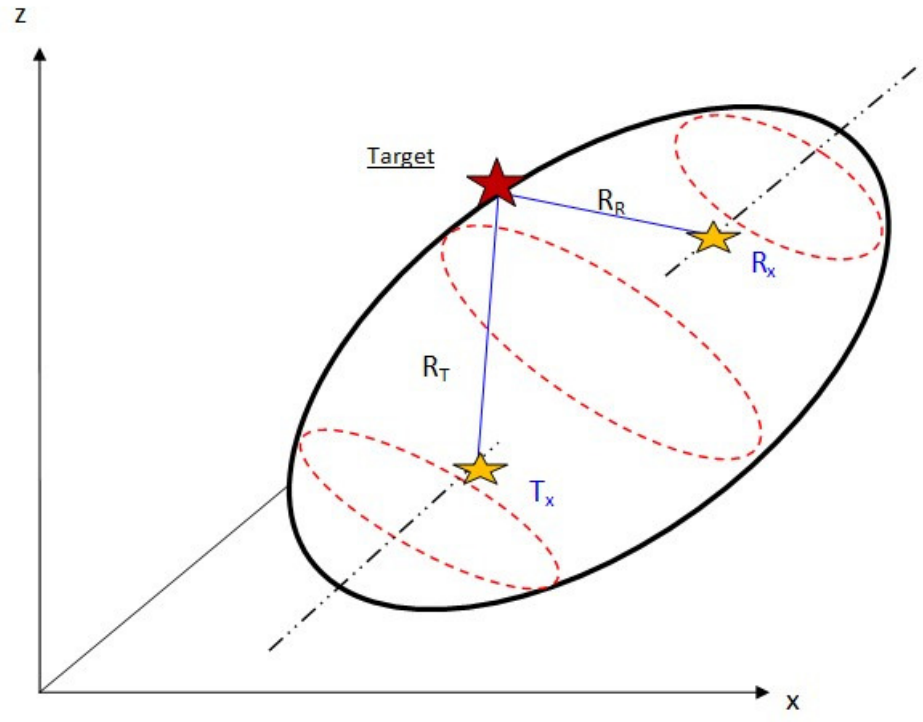

Figure 3 – 3D ellipsoidal isorange surface.

III INSTANTANEOUS CHARACTERISTICS OF THE RECEIVED FM RADIO SIGNALS

III.1 *Introduction*

As apparent from the description in the previous section, the target detection performance of the PBR is highly dependent on the characteristics of the received waveform, which is not under the control of the radar designer. Therefore, in contrast to the standard (active) radar case, where the transmitted waveform is carefully selected and designed in relation to the radar operational modes and requirements, the PBR needs to cope with waveforms that are not tailored for the radar application and that often show characteristics that change with time. The time-varying characteristic of the received waveforms of opportunity generally depends on two reasons:

A. the instantaneous characteristics of the transmitted waveform;

B. the instantaneous characteristics of the e.m. environment (namely the radio propagation channel).

In the following we consider both points (in sub-sections III.2 and III.3 , respectively), and the corresponding variability of the detection characteristics with reference to the PBR in the FM radio band.

III.2 *The instantaneous characteristics of the transmitted waveform*

For the FM radio broadcast in the 88-108 MHz frequency range, a nominal frequency bandwidth of 200 kHz is assigned by the standard to each FM radio channel. A typical FM radio transmission occupies generally only a frequency bandwidth of about 100 kHz inside it, with a significant power level, thus yielding a radar range resolution of about 1.5 km. Specifically, the power spectral density of the FM signal has the same shape of the probability density function (PDF) of the modulating signal's amplitude. Therefore, the actual range resolution is the first highly varying parameter, which changes with the instantaneous transmitted waveform and thus with the considered FM radio channel. In theory, the PDF is not strictly dependent on the program content and both music and voice can reach optimum conditions (namely wide bandwidths and therefore high range resolutions), which only depend on the amplitude level of the modulating signal. However, usually the average level of the music is higher than for the voice, leading to a slightly better range resolution, [10]-[11]. In contrast, the presence of long periods of silence or speech pauses in the program content can dramatically degrade the achievable range resolution. As an example, Figure 4 reports the spectrograms of different data files of about 1.1 sec length collected at different times for different FM radio channels. The figures clearly show the fast temporal variability of the FM radio signal instantaneous frequency bandwidth and the highly different behaviour of the waveforms contemporaneously transmitted at different carriers.

A second highly varying characteristic of the self-ambiguity function concerns the level of its sidelobes. As an example the Peak-to-Side Lobe Ratio (PSLR) was evaluated for 32 different real data tracks with different program contents and is represented in Figure 5 ordered on a content basis. With the exception of the silence, which leads to a periodic ambiguity function, due to the stereo pilot tone (totally ambiguous) thus yielding a PSLR of 0 dB, an average value of about 20 dB is obtained for music tracks and lower for voice tracks. The obtained values confirm that the PSLR can have a significant impact on target detection since it can yield a significant masking effect for the weakest targets present in the considered scenario. Even though there is not always a different PSLR for voice and music, the latter is usually slightly better since it is likely that a voice track can contains short silence pauses. However, the three categories of content (music, voice, silence) are typically all present in turn on each specific FM radio channel, with different durations and timing. Typically, the mixing largely depends on the type of radio channel and there is a large variability inside the 88÷108 MHz band.

Finally, we cannot omit to recall that the global power transmission level of the considered FM radio channels plays a key role, which strongly affects the PBR detection performance. However, a given transmitting station broadcasts many radio programs on the different available FM channels, with different power levels due to different coverage requirements. The power level of the single transmitter is usually only slowly varying with time; however a given FM radio channel can experience an abrupt power loss due to a temporary failure, to a coverage planning modification, or just simply a change of coverage between different hours of the day time. These effects should be taken into account when a continuous reliability is to be guaranteed for the resulting PBR.

III.3 *The instantaneous characteristics of the e.m. environment*

Among the characteristics of the environment, which significantly affect the PBR performance, the multipath reflections should be considered. The effect of multipath on both reference channel and surveillance channel is also time varying and can depend both on the specific transmission carrier frequency and on the instantaneous characteristics of the transmitted waveform. As an example, Figure 6 shows the PDF of both the modulus and the in-phase component for two registrations of the signals received from the same transmitter at Monte Mario (Rome, Italy) at frequencies (a) 90.9 MHz and (b) 92.7 MHz.

Following the theoretical analysis presented in [11] for a simple channel model, it is evident that the distributions in Figure 6(a) are mainly related to thermal noise since they show the typical shape obtained for a constant modulus FM signal in additive Gaussian distributed disturbance. In contrast, the distributions in Figure 6(b) are dominated by the presence of a strong multipath echo since they appear to be similar to those obtained for the superposition of two delayed replicas of a FM signal and thermal noise. It is then apparent that, even when receiving from the same transmitter, it might be possible to experience different propagation channel conditions at different FM radio channels. The multiple reflection phase and extra path can also vary with time due to the meteorological conditions and the soil moisture at the reflection point.

Another typical effect related to the PBR e.m. environment is the presence of co- and inter- channel interferences. In fact, due to the high density of FM radio transmissions over the 88÷108 MHz bandwidth (and despite the attempts of the regulations present in each country that aim at avoiding these), it is likely that (i) the same frequency is used by different transmitters covering different but neighbouring geographical areas; (ii) a high power transmission is present on a channel adjacent to the selected channel. This undesired signals act as interferences in the selected channel bandwidth thus increasing the system noise floor and consequently reducing the achievable detection performance.

This is quite evident in rural areas which are covered by many high power transmitters. Obviously the power ratio between co-/adjacent-channel transmissions is regulated by the ITU regulations (usually it is set at about 20/30 dB). However it is to be noticed that the surveillance antenna is pointed toward an opposite direction with respect to the exploited transmitter of opportunity thus enhancing the power of the signals transmitted by other transmitters at the same/adjacent FM radio channels. As an example of this effect, Figure 7 reports the power spectral density of the data collected at the reference and the

surveillance antennas over the 89.7÷92.3 MHz frequency band. The green arrows indicate the carrier frequencies of the FM radio channels broadcasted by the transmitter of opportunity located in Monte Argentario (Italy). As expected, for many of those FM radio channels, the power level measured at the reference antenna is significantly higher than the level measured at the surveillance antenna. Specifically, since the two receiving antennas are identical, almost co-located, steered 180° apart and assuming the direct signal coming from the transmitter to be the main contribution to the received power, the ratio of the power levels measured over a single channel at the two antennas should be comparable to the Front-to-Back ratio of the used antennas. However, for the channel at 90.6 MHz, the power lever measured at the two receiving antennas are quite comparable; in this case it is likely that a co-channel interference affects the surveillance antenna at the considered carrier frequency. In fact, demodulating the corresponding FM signal, different radio programs can be listened at the two antennas. Moreover notice that the FM radio channels received at the surveillance antenna at 90.1 MHz, 91.0 MHz, and 91.3 MHz, are highly affected by inter-channel interferences coming from adjacent channels in the considered band.

As apparent, for a selected FM radio channel, the time-varying characteristics of both transmitted waveform and e.m. environment yield a PBR detection performance that changes with time. This behaviour might strongly affect the instantaneous reliability of a PBR system. In fact, even choosing a "good channel" (namely a RF channel that shows in the average: high power level, high range resolution and high PSLR, together with a nice propagation channel), there might be various times where the instantaneous performance has largely degraded characteristics for PBR purposes. As an extreme example, the very low PSLR characteristic of a long silence in the modulating signal, yields a very spread 2D-CCF even for a strong target return; in this case the CFAR scheme tends to raise the threshold and the target is not detected. Similarly, other undesired effects due to the time-varying characteristics will be demonstrated in Section VI with reference to a real data set.

These considerations suggest that the use of a single frequency channel does not guarantee always high quality of PBR detection performance.

III.4 *Figures*

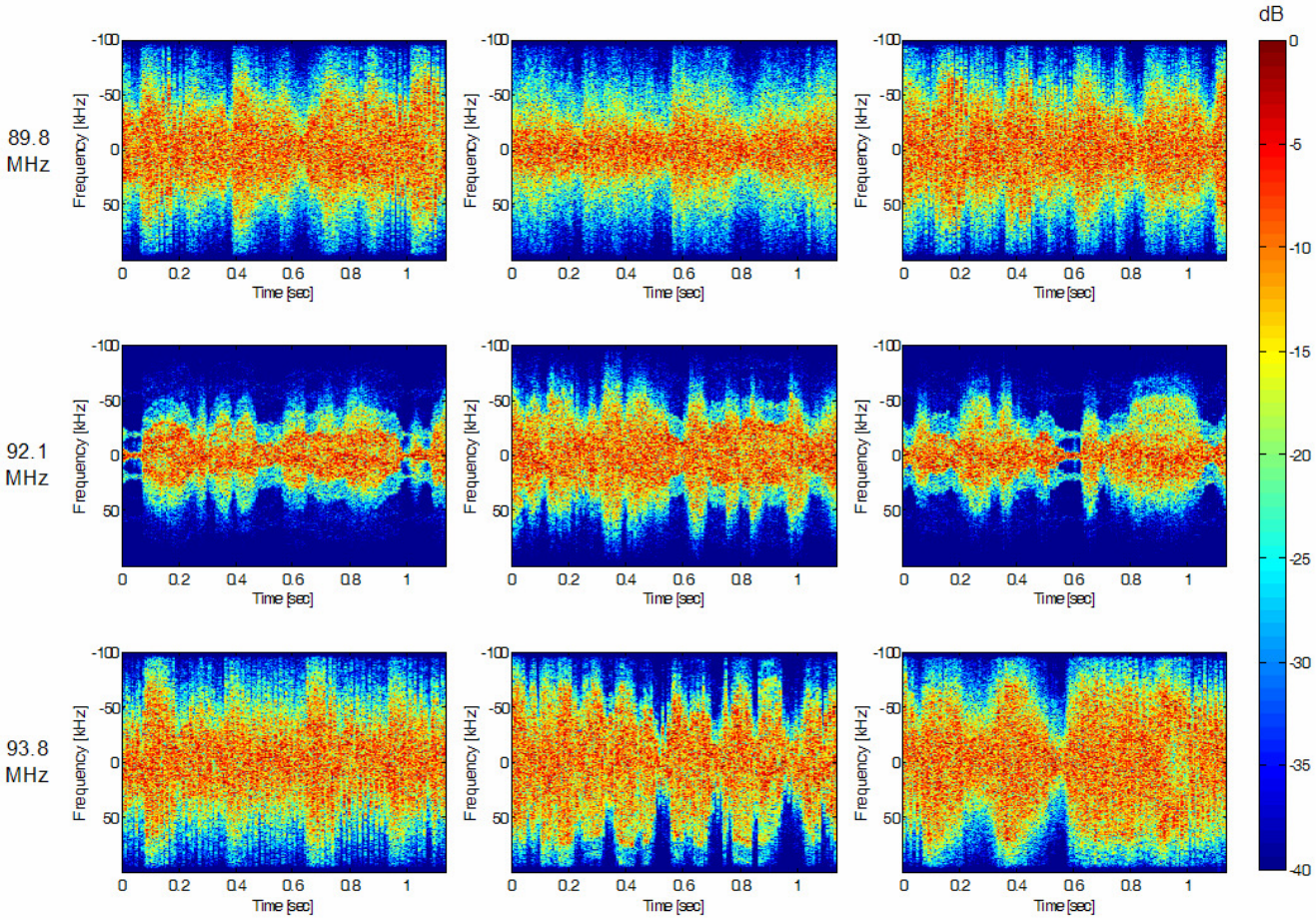

Figure 4 – Spectrograms of the signals collected at different times for different FM radio channels.

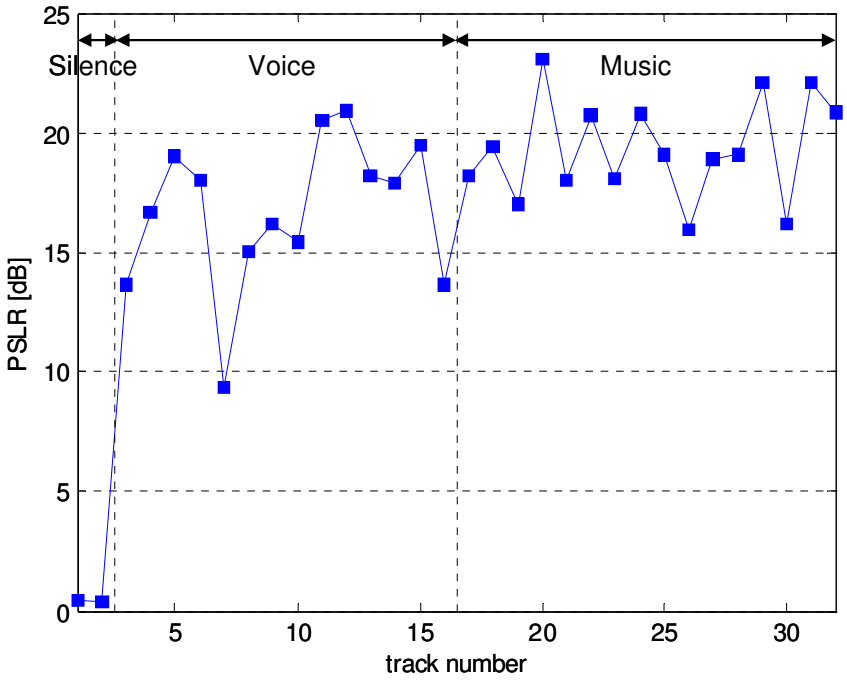

Figure 5 – PSLR of the waveform ambiguity function evaluated over different real data tracks.

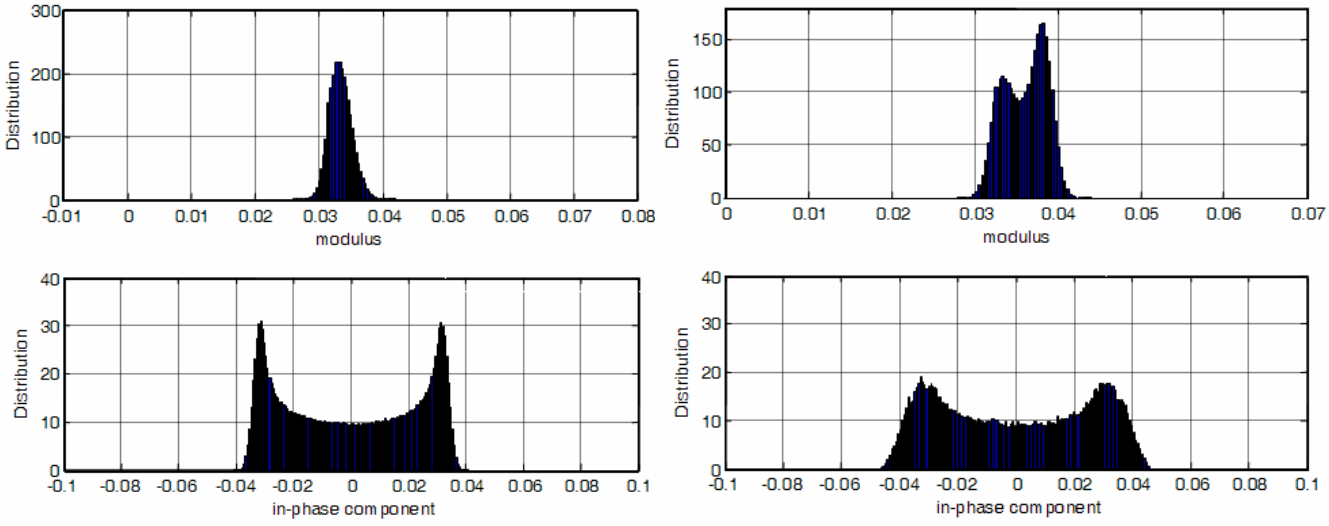

(a) (b)

Figure 6 – Modulus and in-phase component distributions for two records transmitted by Monte Mario at frequencies (a) 90.9 MHz and (b) 92.7 MHz.

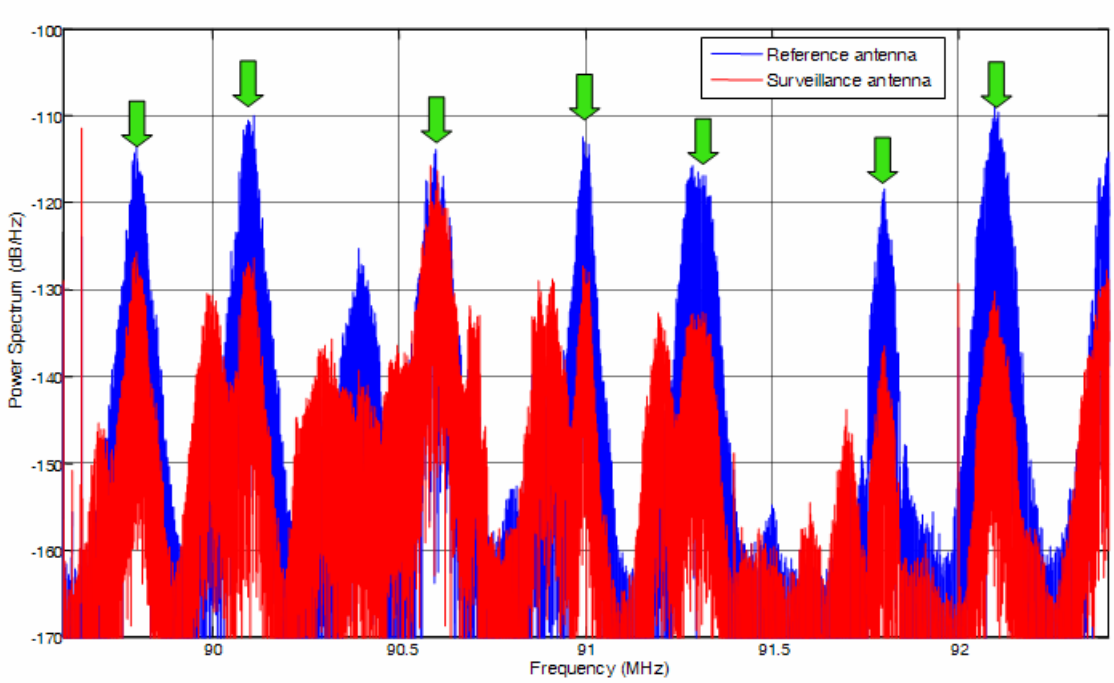

Figure 7 – Power Spectral Density of the data for the reference and the surveillance antenna over the 89.7÷92.3 MHz frequency range.

IV THE MULTI-FREQUENCY APPROACHES

IV.1 *Introduction*

Following the analysis and the considerations presented in Section III, it is quite reasonable to assume that – while the instantaneous characteristics of a specific FM radio channel are highly varying in time – for any assigned time instant, it is possible to identify one or more FM radio channels (very often transmitted by the same geographical location) yielding signals with desirable characteristics for PBR purposes. The availability of N different FM radio channels provides a large diversity and it is likely that the joint exploitation of the signals of opportunity received on multiple carrier frequencies yields the best performance in term of detection capability. In fact, the joint exploitation of the different channels makes the performance robust with respect to both the content of the broadcasted radio program and also with respect to the e.m. environment conditions. To take advantage of this situation, the PBR system should be able to collect at the same time the signals at different carrier frequencies. Moreover, appropriate processing strategies must be designed to exploit the large diversity of information conveyed by different FM radio channels.

To jointly exploit the detection capabilities available at the multiple FM radio channels, we assume that the N radio channels are transmitted by the same transmitting radio station and received by the same PBR receiver, so that a specific target is observed at all channels with the same bistatic range and bistatic velocity. However, since the different radio channels also have a different carrier frequency, the echo from the same target is received at the different channels with different Doppler frequencies. This implies that, if the same integration time T_{INT} is used at the different carrier frequency f_i, the same Doppler resolution Δf is achieved which in turn corresponds to slightly different Velocity resolution Δv_i. In order to obtain Range-Velocity maps at the different FM radio channels that can be directly compared or integrated, slightly different integration times T_{INTi} are used on the N channels according to the following criterion:

$$\Delta v_i = \frac{c}{f_i}\frac{1}{\Delta T_{INTi}} = \text{cost} = \Delta v \;\Rightarrow\; \Delta T_{INTi} = \frac{c}{\Delta v f_i} \quad i = 1,..,N \tag{IV.1}$$

where c is the light speed.

Having appropriately defined the Range-Velocity maps obtained for the different FM radio channels so that they can be integrated pixel-by-pixel, the coincidences of the detections at the different channels can be exploited both for increasing the detection capability (by reducing the undesired degradation effects of the single channel waveform/environment characteristics) and for reducing the false alarms.

The potentialities of the non-coherent integration are well known in the radar literature ([17]-[19]), where typically this is used to:

(i) increase the detection performance by exploiting multiple target echoes received with the same SNR on multiple channels;

(ii) average over the fluctuation of the target radar cross section (especially when using frequency agility);

However, for the multi-frequency PBR, we aim at exploiting the non-coherent integration to make detection scheme robust with respect to the time-varying characteristic of the received waveform. Therefore, together with the standard integration approaches, we look for specific integration strategies aiming at mitigating the drawbacks caused by the random waveform used. Specifically, the following approaches are considered:

A. Centralized Linear integration (SUM). Among the standard integration approaches, which operate with the full dynamic range, the linear integration (after square root detector) is largely the most common solution. Assuming that most of the exploited FM radio channels yield a reasonable SNR at the Range-Velocity location of a given target, the corresponding 2D-CCFs are incoherently summed aiming at enhancing the resulting SNR on the integrated map, [20]. Obviously, with this approach, the instantaneous characteristics of the worse channels are likely to be averaged with the good ones thus yielding a limited impact on the final detection performance. However, the effect of a "bad" waveform with high sidelobes on a single channel is not totally removed, but only averaged out with the others.

B. Decentralized integration (L/N). The alternative approach, which is usually considered for the non-coherent integration with standard radar systems, is to use a binary integration after applying a first detection threshold separately on each channel. According to this strategy, a detection is declared at a given pixel when L detections out of N channels are obtained for the considered pixel over the single-channel maps. Obviously this approach is expected to yield reasonable detection performance improvement when at least L of the N exploited FM radio channels yield a reasonable SNR at the

Range-Velocity location of a given target. The advantage of the non-linear integration rule in the presence of one or few (<*N-L*) FM radio channel with a "bad waveform" with high sidelobes is related to its capability to remove the corresponding effect on the final detection.

In addition to the standard integration approaches above, it is interesting to attempt the exploitation of non-linear detection rules able to remove the impact of the "bad waveforms" with high sidelobes, together with an integration approach operating with the full dynamic range of power values (also known as centralized strategy). In particular, the maximum and the minimum modulus can respectively be considered. The former guarantees that the highest value is always retained to avoid degrading good target echoes, whereas the latter aims at considering only very reliable targets, whose echoes are received with a reasonably high value at all FM radio channels. Therefore, we refer also to the:

C. Centralized Non-Linear integration (MAX). Assuming that only one or few of the exploited FM radio channels yield a significant SNR at the Range-Velocity location of a given target, a maximum approach should be used by selecting, for each location, the maximum value among the corresponding single channel maps locations. This approach has the drawback of preserving the sidelobes structures due to the instantaneous characteristics of a single FM channel.

D. Centralized Non-Linear integration (MIN). Aiming at significantly reducing the high peaks in the 2D-CCF due to the instantaneous characteristics of the single FM radio channel, a minimum approach should be implemented by selecting, for each map location, the minimum value among the corresponding single channel maps locations. This approach is expected to yield reasonable detection performance improvement only when all the exploited FM radio channels yield a reasonable SNR at the Range-Velocity location of a given target.

Both centralized and decentralized non-coherent integration strategies can be considered to jointly exploit the available Range-Velocity maps at the multiple FM radio channels. Moreover, each multi-channel detection scheme must include the control of the false alarms, so that only complete Constant False Alarm Rate (CFAR) detection schemes are considered. For a decentralized integration strategy, a CFAR threshold is separately applied at the single channel map and the detection results are subsequently combined.

Using a centralized strategy, the three different approaches are considered to build up the final integrated map (see Figure 8). In this case, before the different Rage-Velocity maps are integrated, a

proper normalization should be applied. To this purpose, the actual noise floor can be estimated over a map portion located at high range values, where the target contributions and the effects of the waveforms (lobes main structures) can be assumed to be negligible. Then this value is used to scale each map in order to yield the same final noise floor. The three different types of non-coherent integration of the Range-Velocity maps are obtained by taking respectively the sum, the maximum, and the minimum of the corresponding N pixels' intensity, $z_{n,\overline{m}}$ (n=0,..,N-1), in the single channel map.

To obtain the desired CFAR characteristic, three standard schemes are considered, [21]-[23]:

- the Cell Average (CA) CFAR;
- the Greatest Of (GO) CFAR;
- the Smallest Of (SO) CFAR;

The three schemes have well known behaviours for the standard radar systems both against homogeneous and non-homogeneous background. In fact, as well known, the CA scheme shows the best performance against an homogeneous disturbance background; the GO is the most effective to control the false alarm rate in the presence of disturbance showing step changes in its power level (edges); whereas the SO avoids strong detection losses in the presence of multiple targets. In the application to the multi-frequency PBR case, the different schemes must be considered either on the single channel Range-Velocity map (for decentralized integration) or on the integrated Range-Velocity map (for centralized integration). In the presence of high residual sidelobes inside the reference cells - caused by a "bad waveform" on one or multiple FM channels - the CA scheme averages it out with the other unaffected reference cells. The GO scheme tends to raise the threshold, thus keeping a strong control of the false alarms at the expense of the detection performance. In contrast, the SO scheme tends to leave the threshold almost unaffected, thus experiencing an increase of false alarms but without detection losses.

To achieve a full comparison of the resulting performance achieved by the combination of the four integration approaches (decentralized L/N; centralized SUM; centralized MIN; centralized MAX) with the three CFAR schemes (CA; GO; SO), it is required to set the thresholds in all the schemes so to achieve the desired probability of false alarm (P_{fa}). This evaluation is performed in the following section, where explicit expressions are reported for all schemes. The results will allow a fair comparison among the twelve detection chains both against simulated data and against experimental PBR data.

IV.2 *False Alarm rate of the Multi-Frequency Approaches*

To evaluate the P_{fa} achieved with the different techniques we assume that - under hypothesis H_0 (absence of target) - the pixels of the original Range-Velocity map are independent identically distributed (i.i.d.) zero-mean complex Gaussian variables with variance σ^2. Thus the Probability Density Function (PDF) under hypothesis H_0, for the single channel (square-law detector) is:

$$p_z(z \mid H_0) = \frac{1}{\sigma^2} e^{-\frac{z}{\sigma^2}} \qquad z \geq 0 \tag{IV.2}$$

and the corresponding Distribution Function is:

$$D_z(t \mid H_0) = \Pr ob\{z < t \mid H_0\} = \int_0^t \frac{1}{\sigma^2} e^{-\frac{z}{\sigma^2}} dz = 1 - e^{-\frac{t}{\sigma^2}} \tag{IV.3}$$

The transformation $f(z_{0,\overline{m}}, z_{1,\overline{m}}, ..., z_{N-1,\overline{m}})$ applied to the N Range-Velocity maps determines the statistical properties of the pixels intensity $x_{\overline{m}}$ in the resulting map which is to be used to derive the corresponding threshold according to a given CFAR detection scheme. In the following the different multi-frequency approaches are investigated. Specifically the PDFs of the pixels intensity after integration are evaluated according to different integration strategies and the corresponding CFAR thresholds are derived with reference to Cell-Averaging (CA), Greatest Of (GO) and Smallest Of (SO) detection schemes. The results for the standard case of the centralized linear integration (SUM) are well known and are briefly recalled here only for the sake of completeness. The same applies to the decentralized integration (L/N). In contrast, the derivation is reported in more details for the two specific cases explicitly introduced to cope with the specific characteristics of the PBR systems, namely the non-liner centralized integration schemes MAX and MIN.

IV.2.1 Centralized Linear integration (SUM)

In this case, the pixel value after integration can be written as:

$$x_m = \sum_{n=0}^{N-1} z_{n,m} \qquad m = 0,..,M-1 \tag{IV.4}$$

Thus the PDF of the pixels' intensity under hypothesis H_0, is given by (see Appendix A):

$$p_x(x \mid H_0) = \frac{1}{(N-1)!}\frac{1}{\sigma^2}\left(\frac{x}{\sigma^2}\right)^{N-1} e^{-\frac{x}{\sigma^2}} \qquad x \geq 0 \tag{IV.5}$$

For a CA-CFAR detection scheme (see Appendix A), the cell under test (CUT) x_0 is compared with the average pixels' intensity estimated over M secondary data x_1, ..., x_M :

$$x_0 \underset{H_0}{\overset{H_1}{\gtrless}} G_{SUM-CA} \cdot x_{CA} \tag{IV.6}$$

where

$$x_{CA} = \frac{1}{M}\sum_{m=1}^{M} x_m = \frac{1}{M}\sum_{n=0}^{N-1}\sum_{m=1}^{M} z_{n,m} \tag{IV.7}$$

and $G_{SUM\text{-}CA}$ can be evaluated using the following:

$$P_{fa} = \sum_{n=0}^{N-1}\binom{NM+n-1}{n}\left(\frac{M}{G_{SUM-CA}+M}\right)^{NM+n}\left(\frac{G_{SUM-CA}}{M}\right)^{n} \tag{IV.8}$$

where P_{fa} is the desired Probability of False Alarm.

For a GO-CFAR detection scheme (see Appendix A), the cell under test (CUT) x_0 is compared with the maximum pixels' intensity evaluated over the M secondary data:

$$x_0 \underset{H_0}{\overset{H_1}{\gtrless}} G_{SUM-GO} \cdot x_{GO} \tag{IV.9}$$

where

$$x_{GO} = \max\{x_0, x_1, \cdots, x_{M-1}\} \tag{IV.10}$$

and $G_{SUM\text{-}GO}$ can be evaluated using the following:

$$P_{fa} = \sum_{m=0}^{M}\binom{M}{m}(-1)^m \sum_{k_0=0}^{N-1}\sum_{k_1=0}^{N-1}\cdots\sum_{k_{m-1}=0}^{N-1}\frac{(N-1+k_0+k_1+\cdots+k_{m-1})!}{(N-1)!k_0!k_1!\cdots k_{m-1}!}\frac{G_{SUM-GO}^{N}}{(G_{SUM-GO}+m)^{N+k_0+k_1+\cdots+k_{m-1}}} \tag{IV.11}$$

Finally, for a SO-CFAR detection scheme (see Appendix A), the cell under test (CUT) x_0 is compared with the minimum value of the pixels' intensity out of the M secondary data:

$$x_0 \underset{H_0}{\overset{H_1}{\gtrless}} G_{SUM-SO} \cdot x_{SO} \tag{IV.12}$$

where

$$x_{SO} = \min\{x_0, x_1, \cdots, x_{M-1}\} \tag{IV.13}$$

and $G_{SUM\text{-}SO}$ can be evaluated using the following:

$$P_{fa} = 1 - \sum_{k_0=0}^{N-1} \sum_{k_1=0}^{N-1} \cdots \sum_{k_{M-1}=0}^{N-1} \frac{(N-1+k_0+k_1+\cdots+k_{M-1})!}{(N-1)!k_0!k_1!\cdots k_{M-1}!} \frac{G_{SUM-SO}^N}{(G_{SUM-GO}+M)^{N-1+k_0+k_1+\cdots+k_{M-1}}} \tag{IV.14}$$

IV.2.2 Decentralized integration (L/N)

In this case the resulting P_{fa} depends on the flase alarm rate P_{fa}^{SC} obtained over the single channel:

$$P_{fa} = \sum_{i=L}^{N} \binom{N}{i} P_{fa}^{SC\,i} (1 - P_{fa}^{SC})^{N-i} \tag{IV.15}$$

Thus, the value of P_{fa}^{SC} sets the CFAR detection threshold to be applied on each channel according to the considered detection schemes (see Appendices A, B or C for N=1):

- CA-CFAR:

$$P_{fa}^{SC} = \left(\frac{M}{G_{SC-CA} + M} \right)^M \tag{IV.16}$$

- GO-CFAR:

$$P_{fa}^{SC} = \sum_{m=1}^{M} \binom{M}{m} (-1)^{m+1} \frac{m}{G_{SC-GO} + m} \tag{IV.17}$$

- SO-CFAR:

$$P_{fa}^{SC} = \frac{M}{G_{SC-SO} + M} \tag{IV.18}$$

IV.2.3 Centralized Non-Linear integration (MAX)

In this case, the pixel value after integration can be written as:

$$x_m = \max\{z_{n,m}\}_{n=0,..,N-1} \quad m = 0,..,M-1 \tag{IV.19}$$

Thus the PDF of the pixels' intensity under hypothesis H_0, is given by (see Appendix B):

$$p_x(x \mid H_0) = \sum_{n=1}^{N} \binom{N}{n} (-1)^{n+1} \frac{n}{\sigma^2} e^{-n\frac{x}{\sigma^2}} \tag{IV.20}$$

For a CA-CFAR detection scheme (see Appendix B), the average pixels' intensity x_{CA} is estimated over M secondary data x_1,..., x_M which follow the PDF given in IV.20. Consequently, the relation between the P_{fa} and the CFAR threshold $G_{MAX\text{-}CA}$ changes as follows:

$$P_{fa} = \sum_{n=1}^{N} \binom{N}{n} (-1)^{n+1} \left[\sum_{i=1}^{N} \binom{N}{i} (-1)^{i+1} \frac{iM}{nG_{MAX-CA} + iM} \right]^M \tag{IV.21}$$

For a GO-CFAR detection scheme (see Appendix B), the detection test is given by IV.9 where x_{GO}, in this case, is

$$x_{GO} = \max\{x_0, x_1, \cdots, x_{M-1}\} = \max\{z_{n,m}\}_{n=0,..,N-1\ m=0,..,M-1} \tag{IV.22}$$

and $G_{MAX\text{-}GO}$ can be evaluated as a function of the P_{fa} as follows:

$$P_{fa} = \sum_{n=1}^{N} \binom{N}{n} (-1)^{n+1} \sum_{i=1}^{NM} \binom{NM}{i} (-1)^{i+1} \frac{i}{nG_{MAX-GO} + i} \tag{IV.23}$$

Finally, for a SO-CFAR detection scheme (see Appendix B), the cell under test (CUT) x_0 is compared with the minimum value of the pixels' intensity out of the M secondary data distributed as in IV.20; the CFAR threshold to be used can be evaluated by inverting the following equation:

$$P_{fa} = MN \sum_{k=1}^{N} \sum_{i=0}^{M-1} \sum_{l=0}^{N(i+1)-1} \binom{N}{k} \binom{M-1}{i} \binom{N(i+1)-1}{l} (-1)^{k+i+l+1} \frac{1}{kG_{MAX-SO} + l} \tag{IV.24}$$

IV.2.4 Centralized Non-Linear integration (MIN)

In this case, the pixel value after integration can be written as:

$$x_m = \min\{z_{n,m}\}_{n=0,..,N-1} \quad m = 0,..,M-1 \tag{IV.25}$$

Correspondingly, the PDF of the pixels' intensity under hypothesis H_0, is still exponential with expected value σ^2 / N (see Appendix C):

$$p_x(x \mid H_0) = \frac{N}{\sigma^2} e^{-\frac{Nx}{\sigma^2}} \qquad x \geq 0 \tag{IV.26}$$

For a CA-CFAR detection scheme (see Appendix C), the average pixels' intensity is estimated by averaging over M exponential r.v.s x_1, ..., x_M . Thus the resulting r.v. x_{CA} has a Gamma PDF and the CFAR threshold is given by:

$$P_{fa} = \left[\frac{M}{G_{MIN-CA} + M} \right]^M \tag{IV.27}$$

For a GO-CFAR detection scheme (see Appendix C), the CFAR threshold $G_{MIN\text{-}GO}$ to be used can be evaluated using the following:

$$P_{fa} = \sum_{m=1}^{M} \binom{M}{m} (-1)^{m+1} \frac{m}{G_{MIN-GO} + m} \tag{IV.28}$$

Finally, for a SO-CFAR detection scheme (see Appendix C), the minimum value of the pixels' intensity x_{SO} out of the M secondary data is still exponentially distributed and $G_{MIN\text{-}SO}$ is given by:

$$P_{fa} = \frac{M}{G_{MIN-SO} + M} \tag{IV.29}$$

IV.3 *Theoretical detection performance of Multi-Frequency Approaches*

A preliminary analysis of the proposed integration strategies is reported in this section in terms of theoretical detection performance. Specifically the benefits of the considered approaches are evaluated with reference to different simulated scenarios.

Firstly, we consider the case of the joint exploitation of N=4 FM radio channels for the detection of a target showing the same SNR over the 4 channels. Figure 9(a) shows the Detection Probability as a function of the SNR obtained by means of Monte Carlo simulation for the proposed integration approaches and a CA-CFAR detection scheme (with M=30 and $P_{fa}=10^{-4}$). Specifically all the centralized integration strategies (SUM, MAX, MIN) are considered while the decentralized strategy is applied with L=2 and L=3. Moreover the performance obtained when using a single FM radio channel is reported for comparison. As expected, a significant performance improvement is achieved with all the integration strategies due to the integrated SNR increase. The centralized linear integration (SUM) yields the best performance while both the decentralized strategies with L=2 and L=3 suffer only of a slight loss due to the limited increase in the resulting equivalent SNR. Among the non-linear centralized approaches, the MIN is to be preferred since, in this case, it allows the reduction of the noise power without any loss in terms of target power.

In practical situations, the same target can be seen with different SNR over different FM radio channels due to: (i) different transmitted power levels; (ii) different e.m. behaviour of the target at (even slightly) different carrier frequencies; (iii) different noise floor levels due to additional interferences sharing the frequency band. As an example, Figure 9(b) reports the results obtained for a target with SNR regularly decreasing of 2 dB over the 4 FM radio channels. The detection probability curves are evaluated as a function of the highest SNR and the results obtained for the best and the worst channel are reported for comparison. Only the SUM yields a remarkable improvement in the detection capability with respect to the best performing channel. However, it is to be noticed that all the considered integration approaches are able to recover the significant performance degradation given by the worst performing channel. In this case, the MAX approach should be preferred to the MIN since the target power loss (due to the selection of the pixel with the minimum intensity over the different channel) has a higher impact than the noise power attenuation. However, notice that, when a high peak is present at a given bin of a given map, due to a waveform's side-lobe structure, the MIN approach can potentially yield the benefit of controlling the P_{fa}; thus the previously analysed drawback of this approach in terms of detection capability can result in a significant advantage in terms of false alarms control.

The impact of the instantaneous waveform's characteristics is further analyzed in the following assuming that, in 2 out of the 4 channels, a strong sidelobe appears in the secondary data used by the CFAR detection scheme. Specifically, Figure 10 shows a sketch of the considered situation; we assume that the strong sidelobe structure contaminates 10 out of the 30 available secondary data and appears at different pixels at the 2 affected channels with a power ratio SIR=3 dB between the target peak and the interfering structure (Signal-to-Interference Ratio). Figure 11(a-b) reports the results obtained with the different integration strategies for CA-CFAR and GO-CFAR, respectively. Obviously in this case the actual P_{fa} obtained with the different approaches is significantly lower than its nominal value which results in a corresponding reduction of the detection probability. As apparent, the performance obtained with the worst channel largely degrades with respect to Figure 9(a). As a consequence, the DEC strategy with L=3 yields worse performance with respect to the DEC with L=2 for SNR high enough since, in this case, 2 out of the 4 available channels are affected by the interfering structure. The approaches which are the most robust to this effect are the SUM, the MIN and the DEC with L=2 which are still able to yield a significant performance improvement with respect to the best performing channel. In fact with the SUM the interference is averaged with the non-contaminated secondary data available in the other channels while, with the MIN it is discarded by the selection of the minimum pixel intensity over the 4 channels; finally with the DEC with L=2, only the non-affected channels are actually used to detect targets. According to this consideration the MIN is potentially able to yield better performance with respect to the SUM (notice that the performance loss of the MIN with respect to the SUM in Figure 11(a) is slighter than in Figure 9(a)). However this strongly depends on the interference power, the number of contaminated channels and the CFAR detection scheme adopted. As an example, when using the GO-CFAR (Figure 11(b)), the residual interference in the secondary data of the integrated map is retained by the detection scheme thus it should be used in conjunction with a highly robust integration approach; in this case the MIN yields better performance than the SUM since it is able to remove the interference contribution in the integrated map.

When a high density traffic area is considered, it is likely that the secondary data is affected by the presence of an interfering target. In this situation, the interfering target appears at all the available channels in the same position inside the training set, thus it cannot be removed by any of the integration techniques and the adopted CFAR detection scheme plays a key-role. Figure 12(a-b) reports the results obtained for an interfering target with the same power level of the target in the cell under test for a CA-CFAR and a SO-CFAR, respectively. Depending on the Doppler and Range resolution achievable with a given waveform, the strong peak response of the interfering target can smear over a different number of secondary data. However, for the purpose of our analysis we consider the unfavourable case that it

occupies 5 out of the 30 secondary data at all the available FM radio channels. As in the previous considered case study, the actual P_{fa} obtained with the different approaches is expected to be significantly lower than its nominal value and all the considered configurations experience a dramatic detection performance loss. The DEC with L=3 still yields appreciable performance for a CA-CFAR detection scheme since the interfering target returns are averaged with non-contaminated secondary data so that the reduced threshold of a '3 out of 4' approach still allows reasonable detection performance over the single channel. The MAX is still able to achieve reasonable detection capability only when a SO-CFAR detection scheme is implemented. However, when using few channels and 30 secondary data, the best performing integration strategy is the SUM which appears to be more robust in all the considered simulated scenarios.

IV.4 *Appendix A – P_{FA} of the Centralized Linear Integration (SUM)*

For a centralized linear integration approach, the generic pixel x in the integrated map, under hypothesis H_0, is the sum of N i.i.d. exponential r.v.s z_n (n=0,..,N-1) with expected value σ^2 and it has the following PDF:

$$\begin{aligned} p_x(x \mid H_0) &= p_z(x \mid H_0) * p_z(x \mid H_0) ... * p_z(x \mid H_0) = \\ &= \Im^{-1}\left\{\left[C_z(u \mid H_0)\right]^N\right\} = \Im^{-1}\left\{\left[\frac{1/\sigma^2}{1/\sigma^2 - ju}\right]^N\right\} = \\ &= \frac{1}{(N-1)!}\frac{1}{\sigma^2}\left(\frac{x}{\sigma^2}\right)^{N-1} e^{-\frac{x}{\sigma^2}} \qquad x \geq 0 \end{aligned} \tag{IV.30}$$

where $C_z(u \mid H_0)$ is the Characteristic Function of the r.v. z in the hypothesis H_0 and $\Im^{-1}\{t\}$ is the Inverse Fourier Transform of t. Correspondingly, the Probability Distribution Function is:

$$\begin{aligned} D_x(x \mid H_0) &= \int_0^x p_x(t \mid H_0)\, dt = \\ &= 1 - \int_x^\infty \frac{1}{(N-1)!}\frac{1}{\sigma^2}\left(\frac{t}{\sigma^2}\right)^{N-1} e^{-\frac{t}{\sigma^2}}\, dt = \\ &= 1 - \left\{\frac{1}{(N-1)!}\left(\frac{1}{\sigma^2}\right)^{N-1} x^{N-1} e^{-\frac{x}{\sigma^2}} + \int_x^\infty \frac{1}{(N-2)!}\frac{1}{\sigma^2}\left(\frac{t}{\sigma^2}\right)^{N-2} e^{-\frac{t}{\sigma^2}}\, dt\right\} = \\ &= 1 - \left\{\frac{1}{(N-1)!}\left(\frac{1}{\sigma^2}\right)^{N-1} x^{N-1} e^{-\frac{x}{\sigma^2}} + \frac{1}{(N-2)!}\left(\frac{1}{\sigma^2}\right)^{N-2} x^{N-2} e^{-\frac{x}{\sigma^2}} + ... + \int_x^\infty \frac{1}{\sigma^2} e^{-\frac{t}{\sigma^2}}\, dt\right\} \\ &= 1 - \sum_{n=0}^{N-1} \frac{1}{(N-n-1)!}\left(\frac{1}{\sigma^2}\right)^{N-n-1} x^{N-n-1}\, e^{-\frac{x}{\sigma^2}} \end{aligned} \tag{IV.31}$$

For a CA-CFAR detection scheme (see (IV.6)), the cell under test (CUT) x_0 is compared with the average pixels' intensity x_{CA} estimated over M secondary data x_1, ..., x_M (see (IV.7)). Thus the r.v. x_{CA} has PDF:

$$p_{x_{CA}}(x) = M p_{x'_{CA}}(Mx) \tag{IV.32}$$

where $x'_{CA} = M x_{CA} = \sum_{n=0}^{N-1}\sum_{m=0}^{M-1} z_{n,m}$ is the sum of NM i.i.d. exponential r.v.s. Thus eq. (IV.30) becomes:

$$p_{x_{CA}}(x) = \frac{1}{(NM-1)!}\frac{M}{\sigma^2}\left(\frac{Mx}{\sigma^2}\right)^{NM-1} e^{-\frac{Mx}{\sigma^2}} \qquad x \geq 0 \tag{IV.33}$$

and the P_{fa} can be evaluated as follows:

$$\begin{aligned}
P_{fa} &= \int_0^\infty \int_{G_{SUM-CA}\cdot x}^\infty p_x(t \mid H_0)\,dt\; p_{x_{CA}}(x)\,dx = \int_0^\infty \left[1 - D_x(G_{SUM-CA}\cdot x \mid H_0)\right] p_{x_{CA}}(x)\,dx = \\
&= \sum_{n=0}^{N-1} \frac{1}{(N-n-1)!}\frac{M^{NM}}{(NM-1)!}\left(\frac{1}{\sigma^2}\right)^{NM+N-n-1} G_{SUM-CA}^{N-n-1} \int_0^\infty x^{NM+N-n-2}\, e^{-\frac{(G_{SUM-CA}+M)x}{\sigma^2}}\,dx = \\
&= \sum_{n=0}^{N-1} \frac{(NM+N-n-2)!}{(N-n-1)!(NM-1)!} M^{NM} G_{SUM-CA}^{N-n-1} \left(\frac{1}{G_{SUM-CA}+M}\right)^{NM+N-n-1} = \\
&= \sum_{n=0}^{N-1} \frac{(NM+n-1)!}{n!(NM-1)!}\frac{M^{NM} G_{SUM-CA}^{n}}{(G_{SUM-CA}+M)^{NM+n}} = \\
&= \sum_{n=0}^{N-1} \binom{NM+n-1}{n}\left(\frac{M}{G_{SUM-CA}+M}\right)^{NM+n}\left(\frac{G_{SUM-CA}}{M}\right)^{n}
\end{aligned} \tag{IV.34}$$

For a GO-CFAR detection scheme, the cell under test (CUT) x_0 is compared with the maximum pixels' intensity x_{GO} evaluated over the M secondary data $\{x_0, x_1, \cdots, x_{M-1}\}$ (see (IV.9)). The maximum of M r.v.s distributed as IV.30-IV.31 has the following statistical distribution:

$$\begin{aligned}
D_{x_{GO}}(x) &= \left[D_x(x \mid H_0)\right]^M = \left[1 - e^{-\frac{x}{\sigma^2}} \sum_{k=0}^{N-1} \frac{1}{k!}\left(\frac{x}{\sigma^2}\right)^k\right]^M = \\
&= \sum_{m=0}^{M} \binom{M}{m}(-1)^m e^{-m\frac{x}{\sigma^2}} \left[\sum_{k=0}^{N-1} \frac{1}{k!}\left(\frac{x}{\sigma^2}\right)^k\right]^m = \\
&= \sum_{m=0}^{M} \binom{M}{m}(-1)^m e^{-m\frac{x}{\sigma^2}} \left[\sum_{k_0=0}^{N-1} \frac{1}{k_0!}\sum_{k_1=0}^{N-1} \frac{1}{k_1!} \cdots \sum_{k_{m-1}=0}^{N-1} \frac{1}{k_{m-1}!}\left(\frac{x}{\sigma^2}\right)^{k_0+k_1+\cdots+k_{m-1}}\right]
\end{aligned} \tag{IV.35}$$

Thus, in this case, the P_{fa} results:

$$\begin{aligned}
P_{fa} &= \int_0^\infty \left[1 - D_x(G_{SUM-GO}\,x \mid H_0)\right] p_{x_{GO}}(x)\,dx = \int_0^\infty G_{SUM-GO}\, p_x(Gx \mid H_0) D_{x_{GO}}(x)dx = \\
&= \frac{G_{SUM-GO}^N}{(N-1)!} \sum_{m=0}^{M} \binom{M}{m}(-1)^m \sum_{k_0=0}^{N-1} \frac{1}{k_0!}\sum_{k_1=0}^{N-1} \frac{1}{k_1!} \cdots \sum_{k_{m-1}=0}^{N-1} \frac{1}{k_{m-1}!} \int_0^\infty \frac{1}{\sigma^2}\left(\frac{x}{\sigma^2}\right)^{N-1+k_0+k_1+\cdots+k_{m-1}} e^{-(G_{SUM-GO}+m)\frac{x}{\sigma^2}}\,dx = \\
&= \frac{G_{SUM-GO}^N}{(N-1)!} \sum_{m=0}^{M} \binom{M}{m}(-1)^m \sum_{k_0=0}^{N-1} \frac{1}{k_0!}\sum_{k_1=0}^{N-1} \frac{1}{k_1!} \cdots \sum_{k_{m-1}=0}^{N-1} \frac{1}{k_{m-1}!} \cdot \frac{(N-1+k_0+k_1+\cdots+k_{m-1})!}{(G_{SUM-GO}+m)^{N+k_0+k_1+\cdots+k_{m-1}}} \\
&= \sum_{m=0}^{M} \binom{M}{m}(-1)^m \sum_{k_0=0}^{N-1}\sum_{k_1=0}^{N-1} \cdots \sum_{k_{m-1}=0}^{N-1} \frac{(N-1+k_0+k_1+\cdots+k_{m-1})!}{(N-1)!k_0!k_1!\cdots k_{m-1}!} \frac{G_{SUM-GO}^N}{(G_{SUM-GO}+m)^{N+k_0+k_1+\cdots+k_{m-1}}}
\end{aligned} \tag{IV.36}$$

Finally, for a SO-CFAR detection scheme, the cell under test (CUT) x_0 is compared with the minimum value x_{SO} of the pixels' intensity out of the M secondary data (see (IV.12)). The r.v. x_{SO} has the following statistical distribution:

$$\begin{aligned} D_{x_{SO}}(x) &= 1-\left[1-D_x(x\,|\,H_0)\right]^M = 1-e^{-\frac{Mx}{\sigma^2}}\left[\sum_{k=0}^{N-1}\frac{1}{k!}\left(\frac{x}{\sigma^2}\right)^k\right]^M = \\ &= 1-e^{-\frac{Mx}{\sigma^2}}\left[\sum_{k_0=0}^{N-1}\frac{1}{k_0!}\sum_{k_1=0}^{N-1}\frac{1}{k_1!}\cdots\sum_{k_{M-1}=0}^{N-1}\frac{1}{k_{M-1}!}\left(\frac{x}{\sigma^2}\right)^{k_0+k_1+\cdots+k_{M-1}}\right] \end{aligned} \tag{IV.37}$$

thus the P_{fa} is given by:

$$\begin{aligned} P_{fa} &= \int_0^\infty\left[1-D_x(G_{SUM-SO}x\,|\,H_0)\right]p_{x_{SO}}(x)\,dx = \int_0^\infty G_{SUM-SO}\,p_x(G_{SUM-SO}x\,|\,H_0)D_{x_{SO}}(x)dx = \\ &= 1-\sum_{k_0=0}^{N-1}\frac{1}{k_0!}\sum_{k_1=0}^{N-1}\frac{1}{k_1!}\cdots\sum_{k_{M-1}=0}^{N-1}\frac{1}{k_{M-1}!}\frac{G_{SUM-SO}^N}{(N-1)!}\int_0^\infty\frac{1}{\sigma^2}e^{-\frac{(G_{SUM-SO}+M)x}{\sigma^2}}\left(\frac{x}{\sigma^2}\right)^{N-1+k_0+k_1+\cdots+k_{M-1}}dx = \\ &= 1-\sum_{k_0=0}^{N-1}\frac{1}{k_0!}\sum_{k_1=0}^{N-1}\frac{1}{k_1!}\cdots\sum_{k_{M-1}=0}^{N-1}\frac{1}{k_{M-1}!}\frac{G_{SUM-SO}^N}{(N-1)!}\cdot\frac{(N-1+k_0+k_1+\cdots+k_{M-1})!}{(G_{SUM-SO}+M)^{N-1+k_0+k_1+\cdots+k_{M-1}}} \\ &= 1-\sum_{k_0=0}^{N-1}\sum_{k_1=0}^{N-1}\cdots\sum_{k_{M-1}=0}^{N-1}\frac{(N-1+k_0+k_1+\cdots+k_{M-1})!}{(N-1)!k_0!k_1!\cdots k_{M-1}!}\frac{G_{SUM-SO}^N}{(G_{SUM-SO}+M)^{N-1+k_0+k_1+\cdots+k_{M-1}}} \end{aligned} \tag{IV.38}$$

IV.5 *Appendix B – P_{FA} of the Centralized Non-Linear Integration (MAX)*

For a centralized integration strategy with a maximum approach, the generic pixel x in the integrated map, under hypothesis H_0, is the maximum of N i.i.d. exponential r.v.s z_n (n=0,..,N-1) with expected value σ^2 and it has the following statistical distribution:

$$\begin{aligned} D_x(x \mid H_0) &= \Pr ob\{z_0 < x \ \& \ z_1 < x \ \& \cdots \& \ z_{N-1} < x \mid H_0\} = \\ &= \Pr ob\{z_0 < x \mid H_0\} \cdot \Pr ob\{z_1 < x \mid H_0\} \cdots \Pr ob\{z_{N-1} < x \mid H_0\} = \left[D_z(x \mid H_0)\right]^N = \\ &= \left[1 - e^{-\frac{x}{\sigma^2}}\right]^N = \sum_{n=0}^{N} \binom{N}{n} (-1)^n e^{-n\frac{x}{\sigma^2}} \end{aligned} \tag{IV.39}$$

Correspondingly, the PDF results:

$$p_x(x \mid H_0) = \sum_{n=0}^{N} \binom{N}{n} (-1)^n \left(-\frac{n}{\sigma^2}\right) e^{-n\frac{x}{\sigma^2}} = \sum_{n=1}^{N} \binom{N}{n} (-1)^{n+1} \frac{n}{\sigma^2} e^{-n\frac{x}{\sigma^2}} \tag{IV.40}$$

For a CA-CFAR detection scheme the average pixels' intensity x_{CA} is estimated over M secondary data x_1, ..., x_M and the P_{fa} can be evaluated as follows:

$$\begin{aligned} P_{fa} &= \int_0^\infty \left[1 - D_x(G_{MAX-CA} \cdot x \mid H_0)\right] p_{x_{CA}}(x)\, dx = \\ &= \int_0^\infty \left[\sum_{n=1}^{N} \binom{N}{n} (-1)^{n+1} e^{-n\frac{G_{MAX-CA}x}{\sigma^2}}\right] p_{x_{CA}}(x)\, dx = \\ &= \sum_{n=1}^{N} \binom{N}{n} (-1)^{n+1} \int_0^\infty \int_0^\infty \cdots \int_0^\infty e^{-n\frac{G_{MAX-CA}}{\sigma^2 M}\sum_{m=0}^{M-1} x_m} p_x(x_0) p_x(x_1) \cdots p_x(x_{M-1})\, dx_0 dx_1 \cdots dx_{M-1} = \\ &= \sum_{n=1}^{N} \binom{N}{n} (-1)^{n+1} \left[\int_0^\infty e^{-n\frac{G_{MAX-CA}x}{M\sigma^2}} p_x(x)\, dx\right]^M = \\ &= \sum_{n=1}^{N} \binom{N}{n} (-1)^{n+1} \left[\sum_{i=1}^{N} \binom{N}{i} (-1)^{i+1} \frac{i}{\sigma^2} \int_0^\infty e^{-\frac{x}{\sigma^2}\left(\frac{nG_{MAX-CA}}{M}+i\right)} dx\right]^M = \\ &= \sum_{n=1}^{N} \binom{N}{n} (-1)^{n+1} \left[\sum_{i=1}^{N} \binom{N}{i} (-1)^{i+1} \frac{iM}{nG_{MAX-CA} + iM}\right]^M \end{aligned} \tag{IV.41}$$

For a GO-CFAR detection scheme, the cell under test (CUT) x_0 is compared with the maximum pixels' intensity x_{GO} evaluated over the M secondary data $\{x_0, x_1, \cdots, x_{M-1}\}$. Thus, in this case, the r.v. x_{GO} is the maximum of NM exponentially distributed r.v.s and has the following PDF:

$$p_{xGO}(x) = \sum_{n=1}^{NM} \binom{NM}{n} (-1)^{n+1} \frac{n}{\sigma^2} e^{-n\frac{x}{\sigma^2}} \tag{IV.42}$$

Thus, in this case, the P_{fa} results:

$$\begin{aligned} P_{fa} &= \int_0^{\infty} \left[1 - D_x(G_{MAX-GO} \cdot x \mid H_0)\right] p_{xGO}(x)\, dx = \\ &= \sum_{n=1}^{N} \binom{N}{n} (-1)^{n+1} \sum_{i=1}^{NM} \binom{NM}{i} (-1)^{i+1} \frac{i}{\sigma^2} \int_0^{\infty} e^{-\frac{x}{\sigma^2}(nG_{MAX-GO}+i)}\, dx = \\ &= \sum_{n=1}^{N} \binom{N}{n} (-1)^{n+1} \sum_{i=1}^{NM} \binom{NM}{i} (-1)^{i+1} \frac{i}{nG_{MAX-GO}+i} \end{aligned} \tag{IV.43}$$

Finally, for a SO-CFAR detection scheme, the cell under test (CUT) x_0 is compared with the minimum value x_{SO} of the pixels' intensity out of the M secondary data. In this case the r.v. x_{SO} has the following statistical distribution:

$$D_{xSO}(x) = 1 - \left[1 - D_x(x \mid H_0)\right]^M = 1 - \left[1 - \left[D_z(x \mid H_0)\right]^N\right]^M = 1 - \left[1 - \left[1 - e^{-\frac{x}{\sigma^2}}\right]^N\right]^M \tag{IV.44}$$

which yields the following PDF:

$$\begin{aligned} p_{xSO}(x \mid H_0) &= \frac{MN}{\sigma^2} \left[1 - \left[1 - e^{-\frac{x}{\sigma^2}}\right]^N\right]^{M-1} \left[1 - e^{-\frac{x}{\sigma^2}}\right]^{N-1} = \\ &= \frac{MN}{\sigma^2} \left[\sum_{i=0}^{M-1} \binom{M-1}{i} (-1)^i \left[1 - e^{-\frac{x}{\sigma^2}}\right]^{Ni}\right] \left[1 - e^{-\frac{x}{\sigma^2}}\right]^{N-1} = \\ &= \frac{MN}{\sigma^2} \sum_{i=0}^{M-1} \binom{M-1}{i} (-1)^i \left[1 - e^{-\frac{x}{\sigma^2}}\right]^{N(i+1)-1} = \\ &= \frac{MN}{\sigma^2} \sum_{i=0}^{M-1} \binom{M-1}{i} (-1)^i \sum_{l=0}^{N(i+1)-1} \binom{N(i+1)-1}{l} (-1)^l e^{-l\frac{x}{\sigma^2}} \end{aligned} \tag{IV.45}$$

Thus the P_{fa} is given by:

$$P_{fa} = \int_0^{\infty} \left[1 - D_x(G_{MAX-SO} \cdot x \mid H_0)\right] p_{x_{SO}}(x)\, dx =$$

$$= \frac{MN}{\sigma^2} \sum_{k=1}^{N} \sum_{i=0}^{M-1} \sum_{l=0}^{N(i+1)-1} \binom{N}{k} \binom{M-1}{i} \binom{N(i+1)-1}{l} (-1)^{k+i+l+1} \int_0^{\infty} e^{-k \frac{G_{MAX-SO} x}{\sigma^2}} e^{-l \frac{x}{\sigma^2}}\, dx = \tag{IV.46}$$

$$= MN \sum_{k=1}^{N} \sum_{i=0}^{M-1} \sum_{l=0}^{N(i+1)-1} \binom{N}{k} \binom{M-1}{i} \binom{N(i+1)-1}{l} (-1)^{k+i+l+1} \frac{1}{kG_{MAX-SO} + l}$$

IV.6 *Appendix C – P_{FA} of the Centralized Non-Linear Integration (MIN)*

For a centralized integration strategy with a minimum approach, the generic pixel x in the integrated map, under hypothesis H_0, is the minimum of N i.i.d. exponential r.v.s z_n (n=0,..,N-1) with expected value σ^2 and it has the following Probability Distribution Function:

$$\begin{aligned} D_x(x \mid H_0) &= \Pr ob\{z_0 < x \; OR \; z_1 < x \; OR \cdots OR \; z_{N-1} < x \mid H_0\} = \\ &= 1 - \Pr ob\{z_0 > x \,\&\, z_1 > x \,\&\cdots\&\, z_{N-1} > x \mid H_0\} = \\ &= 1 - \Pr ob\{z_0 > x \mid H_0\} \cdot \Pr ob\{z_1 > x \mid H_0\} \cdot \cdots \Pr ob\{z_{N-1} > x \mid H_0\} = 1 - \left[1 - D_z(x \mid H_0)\right]^N = \\ &= 1 - e^{-\frac{Nx}{\sigma^2}} \end{aligned} \tag{IV.47}$$

Correspondingly, the PDF results:

$$p_x(x \mid H_0) = \frac{N}{\sigma^2} e^{-\frac{Nx}{\sigma^2}} \qquad x \geq 0 \tag{IV.48}$$

Thus the PDF of the r.v. x after integration is still exponential with expected value σ^2 / N. For a CA-CFAR detection scheme the average pixels' intensity x_{CA} is estimated over M secondary data x_1, ..., x_M and the P_{fa} can be evaluated as follows:

$$\begin{aligned} P_{fa} &= \int_0^\infty \left[1 - D_x(G_{MIN-CA} \cdot x \mid H_0)\right] p_{x_{CA}}(x)\, dx = \int_0^\infty \left[e^{-N \frac{G_{MIN-CA} x}{\sigma^2}} \right] p_{x_{CA}}(x)\, dx = \\ &= \int_0^\infty \int_0^\infty \cdots \int_0^\infty e^{-N \frac{G_{MIN-CA}}{\sigma^2 M} \sum_{m=0}^{M-1} x_m} p_x(x_0) p_x(x_1) \cdots p_x(x_{M-1})\, dx_0 dx_1 \cdots dx_{M-1} = \\ &= \left[\int_0^\infty e^{-N \frac{G_{MIN-CA} x}{\sigma^2 M}} p_x(x)\, dx \right]^M = \left[\int_0^\infty \frac{N}{\sigma^2} e^{-\frac{xN}{\sigma^2}\left(\frac{G_{MIN-CA}}{M}+1\right)} dx \right]^M = \\ &= \left[\frac{M}{G_{MIN-CA} + M} \right]^M \end{aligned} \tag{IV.49}$$

For a GO-CFAR detection scheme, the cell under test (CUT) x_0 is compared with the maximum pixels' intensity x_{GO} evaluated over the M secondary data $\{x_0, x_1, \cdots, x_{M-1}\}$. Thus, in this case, the r.v. x_{GO} has the following PDF:

$$p_{x_{GO}}(x) = \sum_{m=1}^{M} \binom{M}{m} (-1)^{m+1} \frac{Nm}{\sigma^2} e^{-mN\frac{x}{\sigma^2}} \tag{IV.50}$$

and the P_{fa} results:

$$\begin{aligned} P_{fa} &= \int_0^{\infty} \left[1 - D_x(G_{MIN-GO} \cdot x \,|\, H_0)\right] p_{x_{GO}}(x)\, dx = \\ &= \sum_{m=1}^{M} \binom{M}{m} (-1)^{m+1} \frac{Nm}{\sigma^2} \int_0^{\infty} e^{-\frac{x}{\sigma^2} N(G_{MIN-GO}+m)}\, dx = \\ &= \sum_{m=1}^{M} \binom{M}{m} (-1)^{m+1} \frac{m}{G_{MIN-GO}+m} \end{aligned} \tag{IV.51}$$

Finally, for a SO-CFAR detection scheme, the cell under test (CUT) x_0 is compared with the minimum value x_{SO} of the pixels' intensity out of the M secondary data. Thus, in this case, the r.v. x_{SO} is the minimum of NM exponentially distributed r.v.s and it has the following PDF:

$$p_{x_{SO}}(x) = \frac{NM}{\sigma^2} e^{-\frac{NMx}{\sigma^2}} \qquad x \geq 0 \tag{IV.52}$$

Thus the P_{fa} is given by:

$$\begin{aligned} P_{fa} &= \int_0^{\infty} \left[1 - D_x(G \cdot x \,|\, H_0)\right] p_{x_{SO}}(x)\, dx = \\ &= \frac{NM}{\sigma^2} \int_0^{\infty} e^{-\frac{x}{\sigma^2} N(G+M)}\, dx = \\ &= \frac{M}{G+M} \end{aligned} \tag{IV.53}$$

IV.7 *Figures*

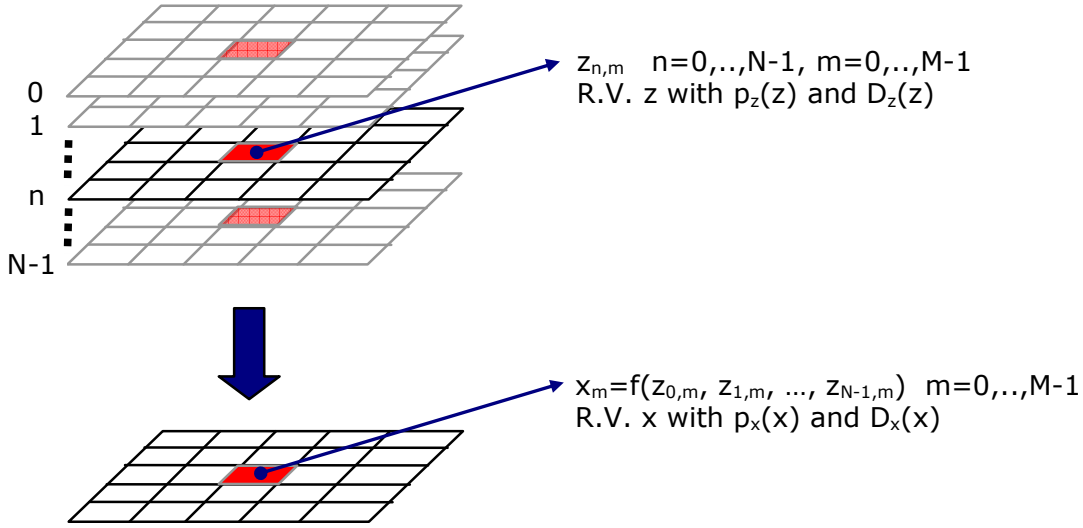

Figure 8 – Sketch of the multi-frequency approach.

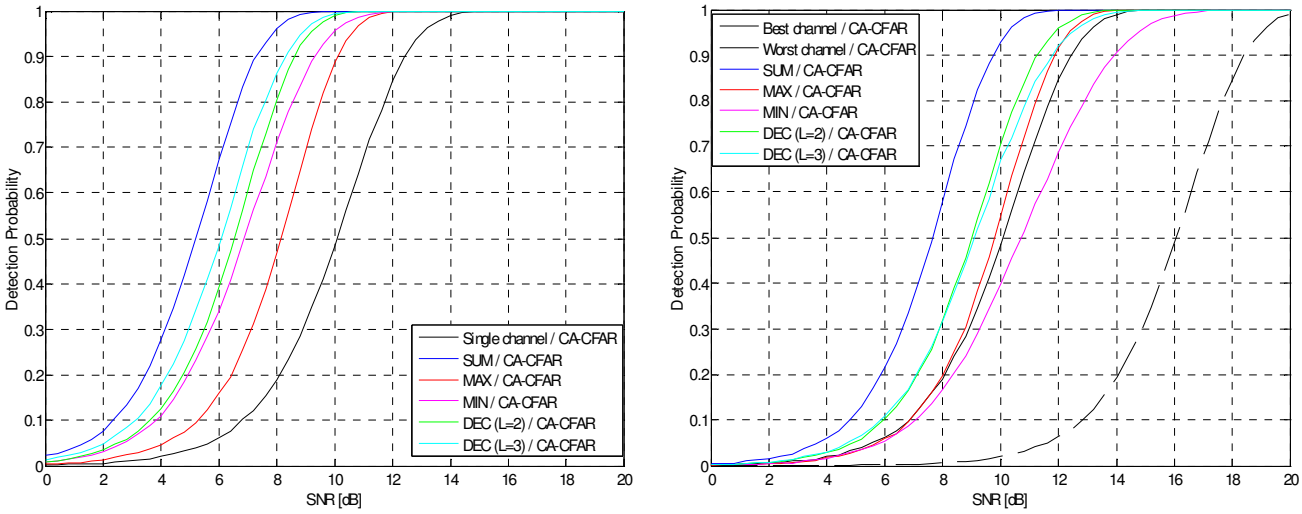

(a) (b)

Figure 9 – Detection Probability vs SNR for the different integration schemes over N=4 FM radio channels and a CA-CFAR (with M=30 and $P_{fa}=10^{-4}$): (a) same SNR over the N channels, (b) SNR decreasing of 2 dB at each channel (results as a function of the highest SNR).

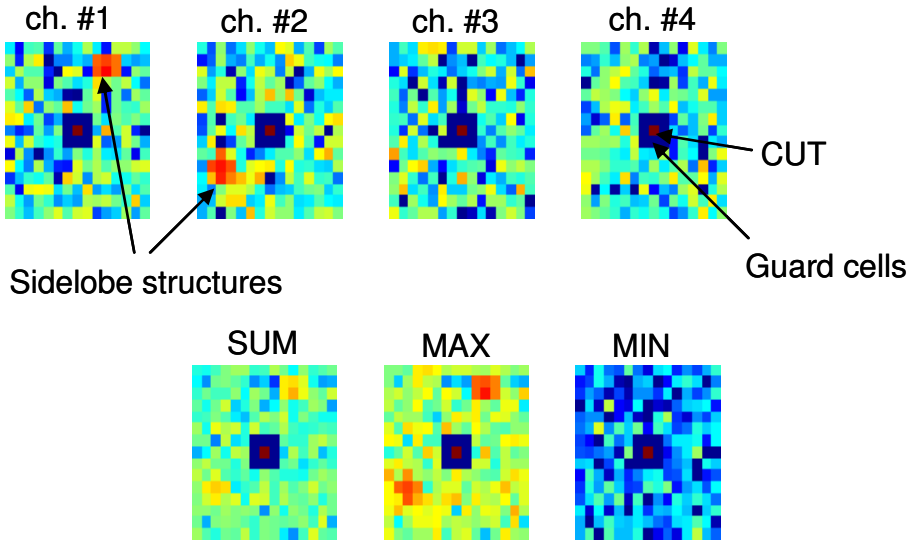

Figure 10 – Sketch of the simulated scenario for the case of interfering sidelobe structures affecting the secondary data in 2 out of the 4 available FM radio channels.

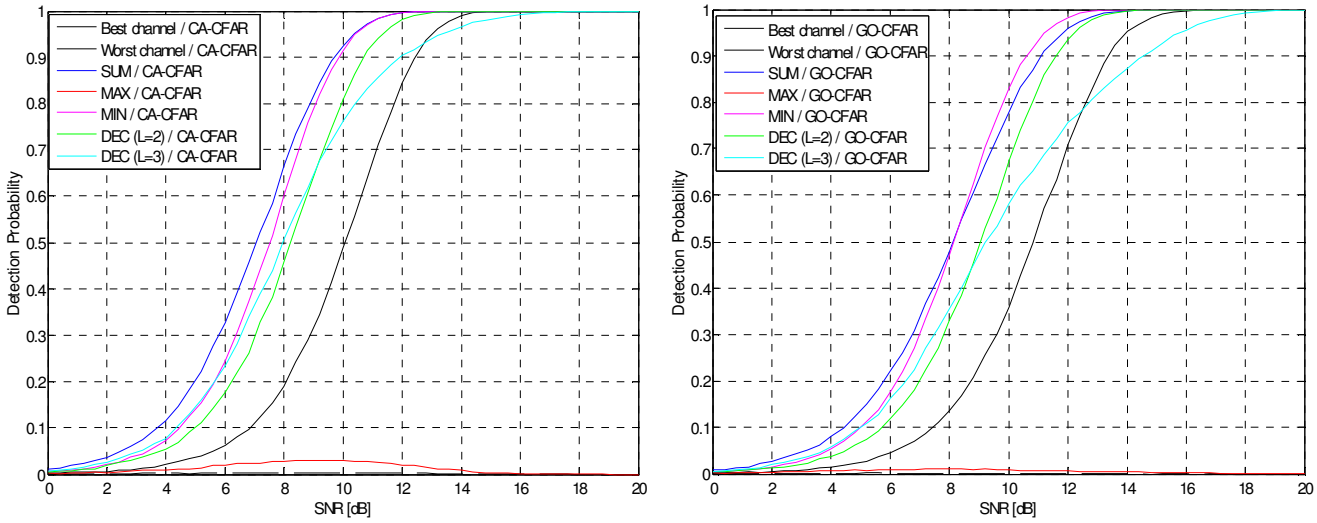

(a) (b)

Figure 11 – Detection Probability vs SNR ($P_{fa}=10^{-4}$) for the different integration schemes in the presence of sidelobe structures affecting the secondary data in 2 out of the 4 FM radio channels (SIR=3 dB, 10 cells affected out of the M=30): (a) CA-CFAR; (b) GO-CFAR

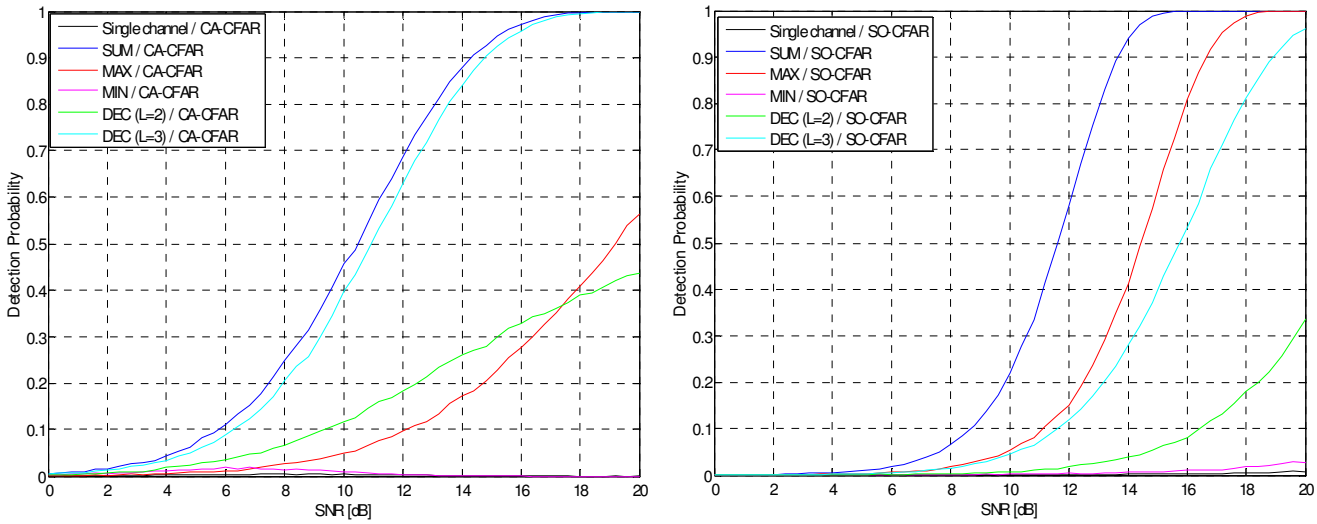

(a) (b)

Figure 12 – Detection Probability vs SNR ($P_{fa}=10^{-4}$) for the different integration schemes in the presence of an interfering target affecting the secondary data in all the 4 FM radio channels (SIR=0 dB, 5 cells affected out of the M=30): (a) CA-CFAR; (b) SO-CFAR.

V PBR PROTOTYPES DESCRIPTION AND ACQUISITION CAMPAIGNS

Aiming at exploiting the whole 88÷108 MHz frequency band of the FM radio broadcast, two wide-band PBR prototypes have been developed and fielded at the INFOCOM Dept. of the University of Rome "La Sapienza", [24]-[25], based on two different approaches: (i) direct RF sampling; (ii) signal down-conversion & baseband sampling.

The first approach (sketched in Figure 13) is based on the use of a high quality dual channel A/D converter with a wide dynamic range (software selectable), that has a -3dB input bandwidth of about 100 MHz. By properly selecting the sampling frequency of the A/D converter by means of an external stable and tunable oscillator, the ADC replicates the input signal in all Nyquist zones. Sampling must be greater than twice the bandwidth of the signal. With this approach the baseband replica of the whole 88÷108 MHz frequency bandwidth is achieved (with only a small SNR degradation for the high frequency channels in the bandwidth [100 MHz÷108 MHz]).

The second approach (sketched in Figure 14) uses a fully coherent down-conversion stage for the two channels, so as to move the central frequency of the broadcast bandwidth (namely 98MHz) to an intermediate frequency of 10.7MHz. After adequate filtering and amplification, the whole bandwidth can be sampled at a rate slightly larger than 40MHz, thus making available all radio channels for potential PBR processing. Further details about the devices used in both the developed prototypes can be found in Appendix D.

In both the described approaches two logarithmic type directional antennas operating in the 88÷108MHz FM band were used. The antennas are characterized by a beamwidth of about 90° and a front to back ratio greater than 20 dB so that the direct signal impinging on the antenna used for detection (Surveillance Antenna) is partially rejected.

Key elements in the prototypes design are:

(i) achievement of a wide linear dynamic range which can be limited by the distortion effects generated by the devices in the receiving chain (inter-modulation products, quantization noise, etc.)

(ii) high coherence maintenance between the two receiving channels, which can be limited by phase and gain imbalances due to filters design, clock jitter, local oscillator phase noise, etc.

(iii) control of the global signal level, which might have strong variations with the distance from the transmitters.

These elements are more critical than in narrow-band PBR receivers, which however do not allow the multi-frequency operation proposed in this paper. An alternative to the wideband PBR is the use of a multi-channel narrowband PBR receiver (see Section VIII).

Due to the selected values of the sampling frequency, a data flow greater than 220MB/s can be reached. In this regard the main system bottleneck is represented by the PCI bus data transfer rate, 132MByte/s, that does not allow a real-time transfer of the acquired data from the internal A/D memory to the on-board memory of the Controller. To avoid overflow, only short consecutive acquisitions are possible. Specifically the single acquisition duration is still upper limited by the internal A/D memory size and there is a trade-off between size of the single acquisition and temporal separation between consecutive acquisitions, which is limited by the time required by the data transfer. The acquired and stored data are then processed off-line with digital filters properly designed to extract the FM radio channels of interest.

In order to verify the disturbance cancellation capability achievable with the PBR prototypes, several tests were performed in controlled situations. In particular the signal of a single antenna was split with a power divider and sent to the two receiving channels (single antenna acquisition). The acquired data sets were processed using the cancellation algorithms described in [8]-[9] and the obtained cancellation was evaluated as the ratio between the power levels measured, over a 200 kHz bandwidth, at the input and at the output of the cancellation filter. In the considered situation, this parameter only depends on the correlation properties between the signals at the two receiving channels. Since the two receiving channels are fed with exactly the same input signal, this test allowed us to characterize the channel decorrelation effects due to the devices non-idealities and thermal noise thus leading to the evaluation of the theoretical maximum cancellation level that can be obtained. The performed analysis showed that the developed prototype is able to achieve a cancellation value up to about 65-70 dB, which guarantees the correct operation of the PBR, since it is well above the actual cancellation levels achievable in practical situations (dual antennas acquisition). Further details about the tests and controlled experiments performed to verify system compliance to thermal noise specifications and the achievable cancellation capability of the developed prototypes can be found in Appendix E.

Many acquisition campaigns were carried on using the wide-band PBR prototypes at different sites. In the following sections we show the results out of the acquisition campaigns that were carried on May 17th and May 18th 2007 by Riva di Traiano (Civitavecchia) about 70 km north-east of Rome (Italy). The reference antenna was steered toward a transmitter located on Monte Argentario (approximately pointing to north-west), while the surveillance antenna was pointed at about 180° (approximately toward south-east), as illustrated in Figure 18. The transmitter-receiver baseline is of approximately 70 km. Due to the large antenna beam, many of the standard departure routes of the Leonardo da Vinci Airport in Fiumicino are contained into the 3 dB surveillance antenna pattern (basically most of the routes for the north-west of Europe), as well as a number of the standard arrival routes, that mainly lead the aircrafts to join the descend path of the ILS for runway 34.

A detailed analysis of the data in both temporal and spectral domain suggested the selection of a limited number of FM radio channels inside the available frequency bandwidth. Specifically, according to the considerations in Section III, the following main criteria were used for the selection of the best suited channels for PBR purposes:

(1) Direct signal-to-Noise Ratio (DNR): the channels characterized by higher values of the DNR were firstly selected since this parameter allows to identify the high power transmissions and strongly affects the theoretical cancellation and the detection performance of the system.

(2) Reference to Surveillance Power Ratio: as previously mentioned, in the selected geometry, the ratio of the power levels measured over a single channel on the two antennas should be comparable to the Front-to-Back ratio of the used antennas. This criterion allowed us to identify the FM radio channels transmitted by transmitters contained into the 3 dB reference antenna pattern, as required by the PBR geometry. Moreover it allows to roughly discard all the FM radio channels which are highly affected by multipath and co-/inter-channel interferences.

(3) Program content: due to the deep impact of the waveform's characteristics on the PBR performance, it is reasonable to prefer FM radio channels usually broadcasting music and to discard the ones that usually or currently transmit speech radio programs.

As apparent from Figure 7, the described criteria can be roughly applied operating over the RF raw data thus allowing to reduce the number of FM radio channels extracted for the following processing stage. According to these criteria, five radio broadcast signals were selected transmitted at the following frequencies: 89.8MHz, 91.3MHz, 92.1MHz, 93.8MHz and 94.3MHz. All these channels were later

discovered to be high power transmissions coming from the same transmitter in Monte Argentario (see Table 1).

ID	Frequency (MHz)	FM radio broadcast	DNR ref antenna (dB)	DNR surv antenna (dB)
SFC1	89.8	M20	50.5	38.6
SFC2	93.8	Radio Dim. Suono Roma	52.8	34.7
SFC3	92.1	RAI R.2	56.0	35.6
SFC4	91.3	Lattemiele	51.3	35.6
SFC5	94.3	RAI R.3	57.1	41.8

Table 1 – Selected FM radio channels info.

During the considered acquisition campaigns, several sequential data acquisitions were performed; each acquisition is of about 1.1 sec duration, with a temporal spacing of about 23 sec between two consecutive acquisitions. Each acquisition was stored in a different file whose name reports the date and time of acquisition (e.g. “pcl_170507_10.50.58” is the first file collected during the first day). Due to limitations given by the PCI bus data transfer rate and by the internal A/D memory size, a time duration of about one sec represented the best trade-off between the integration time requirement and the temporal spacing between consecutive acquisitions. Data sets acquired with this approach cover a total time duration of about one hour (approximately 150 data files) for each day of the acquisition campaigns and for each developed prototype. Correspondingly, live ATC (Air Traffic Control) registrations have been collected during the described acquisition campaigns. These registrations refer to the area where the acquisition campaigns were performed, so that a complete comparison is possible between real air traffic and the detection results obtained with the developed prototype. Moreover, the availability of live ATC registrations allowed a complete and effective comparison of the results obtained with the single FM radio channels and with the multi-frequency approaches, both in terms of detection probability and false alarm rate (as described in the following sections).

V.1 *Appendix D – Devices in the developed prototypes*

V.1.1 A/D converter (NI PXI-5122)

The A/D converter used in both the previously described approaches has the following main features:

- two 100MS/s simultaneously sampled input channels
- input impedance software selectable (two possible values, 50 Ω or 1 M Ω)
- sampling rate: 100 MS/s (there is also the possibility to use an external clock source for applications that require very specific sampling frequencies, as in the case described in this work, see sub-section V.1.2)
- resolution: 14-bit per sample
- three different frequency responses selectable, with -3 dB cut frequencies equal to 20 (noise filter on), 35 (antialias filter on) and 100 MHz (filters off), respectively (see Figure 15)
- software selectable vertical range: 0.2, 0.4, 1, 2, 4, 10 e 20 V (20 V only with 1 MΩ impedance)
- programmable vertical offset, see Table 2.

50 Ω		1 MΩ	
Range (V_{pk-pk})	Vertical Offset Range (V)	Range (V_{pk-pk})	Vertical Offset Range (V)
0.2	±0.1	0.2	±0.1
0.4	±0.2	0.4	±0.2
1	±0.5	1	±0.5
2	±1	2	±1
4	±2	4	±2
10	—	10	±5
		20	—

Table 2 – Vertical offset values.

- internal memory:
    - Total size: 1 GB
    - Total size (per input channel): 512 MB

V.1.2 Clock Generator (NI PXI-5404)

This device as been used to select a specific sampling frequency for the A/D conversion of experimental data acquired with the developed prototypes. It has the following main features:

- two outputs, 1 sine and 1 cosine (both generate same frequency simultaneously)
- frequency range: 9 kHz to 105 MHz
- frequency resolution: 1.07 µHz

V.1.3 RF Amplifier (ZHL-2010)

The RF amplifier used in the wide-band down-conversion approach has the following main features:

- wide bandwidth: 50 – 1000 MHz
- low noise figure: 3.7dB (typical), see Figure 16(a)
- high IP3: +46 dBm (typical)
- impedance: 50 Ω
- gain: 20dB minimum, see Figure 16(b)

V.1.4 IF Amplifier (ZHL-32A-S)

The IF amplifier used in the wide-band down-conversion approach has the following main features:

- bandwidth: 0.05 – 130 MHz
- noise figure: 6dB (typical), see Figure 17(a)
- high IP3: +38 dBm (typical)
- impedance: 50 Ω
- gain: 25 dB minimum, see Figure 17(b)

V.1.5 Low Pass Filter (BLP-21.4)

The Low-pass filter used in the wide-band down-conversion approach has the following main features:

- passband: DC – 22 MHz
- cut-off frequency (3 dB loss): 24.5 MHz
- stopband:
    - (loss > 20dB): 32 – 41 MHz
    - (loss > 40dB): 41 – 200 MHz
- impedance: 50 Ω

V.2 *Appendix E – Tests and controlled experiments*

As partially described in this section, in order to verify the disturbance cancellation capability achievable with the PBR prototypes, several tests were performed in controlled situations. Two different kinds of tests were performed:

- analysis without useful signals, aiming at verifying the system compliance to thermal noise specifications, on both the receiving channels;
- "single antenna acquisitions": the signal of a single antenna was split with a power divider and sent to the two receiving channels. The acquired data sets were processed using the cancellation algorithms described in [8]-[9] and the obtained cancellation was evaluated as the ratio between the power levels measured, over a 200 kHz bandwidth, at the input and at the output of the cancellation filter. In the considered situation, this parameter only depends on the correlation properties between the signals at the two receiving channels. Since the two receiving channels are fed with exactly the same input signal, this test allowed us to characterize the channel decorrelation effects due to the devices non-idealities and thermal noise thus leading to the evaluation of the theoretical maximum cancellation level that can be obtained.

V.2.1 Noise power evaluation

System compliance to thermal noise specifications was verified for both the receiving channels of the used A/D converter (NI PXI-5122, see Appendix D), as a function of the (software selectable) vertical range. Obtained results are summarized in Table 3.

V.R. [V]	Vrms [μV]	NI PXI-5122 Noise Figure [dB]	Specified Noise Power [dBm]	Measured Noise Power Ch.0 [dBm]	Measured Noise Power Ch.1 [dBm]
0.2	66	27.11	-94.07	-94.83	-94.48
0.4	100	29.75	-91.43	-91.23	-91.25
1.0	250	37.71	-83.47	-82.63	-83.49
2.0	500	43.73	-77.45	-76.99	-76.99
4.0	1000	49.75	-71.43	-70.37	-71.15
10.0	2500	57.71	-63.47	-62.47	-63.10

Table 3 – Noise power levels measured on both the A/D channels

Each table rows reports the vertical range and the following values:

- V_{rms}, measured in μV, peak tension as reported in the device specifications
- NI PXI-5122 Noise Figure, evaluated as

$$10Log_{10}\left(\frac{V^2}{50}\right)-10Log_{10}\left(\frac{KT}{2}\right)-10Log_{10}\left(B_{5122}\right) \quad \text{(V.1)}$$

where V is the V_{rms} value measured in Volts, K is the Boltzmann constant ($1.38\cdot10^{-23}$ [(Watt/Hz)/°K] = -198.6 (dBm/Hz)/°K), T is the system temperature, measured in Kelvin (typically 307K, about 34°C), and B_{5122} is half the -3dB A/D working bandwidth (50 MHz for all the vertical ranges except for V.R. = 0.2V where it is equal to 40 MHz)

- specified noise power is the A/D noise power measured in the bandwidth of interest (B = 180 KHz for the values reported in Table 3), obtained as

$$P_N\,|_{dBW} = P_{NInBand}\,|_{dBW} + 10Log_{10}\left(\frac{B}{B_{5122}}\right) \quad \text{(V.2)}$$

where $P_{NInBand}$ is given by

$$P_{NInBand}\,|_{dBW} = 10Log_{10}\frac{V^2}{50} \quad \text{(V.3)}$$

(50 is impedance value, in Ω). Obtained values are then converted in dBm, as for measured noise power levels.

As it is apparent from the table, measured power levels on both A/D channels are largely comparable with theoretical ones.

V.2.2 Single antenna acquisitions

When the two receiving channels are fed with exactly the same input signal, achievable cancellation should be ideally limited only by thermal noise (theoretical cancellation), which represents the only element of difference (decorrelation source) between the two channels. However, the presence of other decorrelation effects is expected, due to devices non-idealities (power divider, mixers and/or amplifiers if present, A/D converter), different cables length, etc. Correlation coefficient ρ is the parameter that allows the evaluation of these non-idealities between the two receiving channels, thus leading to the evaluation of the theoretical maximum cancellation level that can be obtained.

In the following will be demonstrated that, in conditions of ideality, SNR is the parameters making correlation coefficient ρ non-zero. Indicating with *ref* and *rx* the baseband complex envelope of the reference channel signal and of the surveillance channel signal, respectively, correlation coefficient can be written as:

$$\rho = \frac{E\{ref \cdot rx^*\}}{\sqrt{E\{|ref|^2\} \cdot E\{|rx|^2\}}} = \frac{E\{(s_{R1} + n_1) \cdot (s_{R2} + n_2)^*\}}{\sqrt{E\{|s_{R1} + n_1|^2\} \cdot E\{|s_{R2} + n_2|^2\}}} =$$

$$\frac{E\{s_{R1} \cdot s_{R2}^*\} + \overbrace{E\{s_{R1} \cdot n_2^*\}}^{=0} + \overbrace{E\{s_{R2} \cdot n_1^*\}}^{=0} + \overbrace{E\{n_1 \cdot n_2^*\}}^{=0}}{\sqrt{E\{|s_{R1}|^2\} + E\{|n_1|^2\} + \underbrace{E\{2\,\mathrm{Re}(s_{R1} \cdot n_1^*)\}}_{=0}} \cdot \sqrt{E\{|s_{R2}|^2\} + E\{|n_2|^2\} + \underbrace{E\{2\,\mathrm{Re}(s_{R2} \cdot n_2^*)\}}_{=0}}} = \tag{V.4}$$

$$= \frac{E\{s_{R1} \cdot s_{R2}^*\}}{\sqrt{P_{S_{R1}} + P_{n_1}} \cdot \sqrt{P_{S_{R2}} + P_{n_2}}}$$

where

- S_{R1} and S_{R2} indicate the useful signal on reference and surveillance channels, respectively
- n_1 and n_2 indicate the noise on the two channels
- P_{SR1} and P_{SR2} indicate the power of the useful signals on the two channels
- P_{n1} and P_{n2} indicate the noise power on the two channels

It is easy to verify that some terms of V.4 are equal to zero:

$$E\{s_{R1} \cdot n_2^*\} \overset{\text{segnale e rumore statisticamente indipendenti}}{=} E\{s_{R1}\} \cdot E\{n_2^*\} =$$

$$= E\{s_{R1}\} \cdot \left\{ \overbrace{E\{n_{2_i}\}}^{\substack{\text{variabile aleatoria gaussiana a valor medio nullo} \\ =0}} - j \overbrace{E\{n_{2_{Qi}}\}}^{\substack{\text{variabile aleatoria gaussiana a valor medio nullo} \\ =0}} \right\} = 0 \tag{V.5}$$

$$E\{2\,\mathrm{Re}(s_{R1} \cdot n_1^*)\} = E\{2\,\mathrm{Re}(|s_{R1}| \cdot e^{j\phi_{S_{r1}}} \cdot n_1^*)\} = 2|s_{R1}|E\{\mathrm{Re}(e^{j\phi_{S_{r1}}} \cdot n_1^*)\} = 2|s_{R1}|E\{n_{1_I}'\} = 0 \tag{V.6}$$

Due to the fact that noise on the two channels has the same statistic, we have:

$$E\{|n_1|^2\} = E\{|n_2|^2\} = P_{n_1} = P_{n_2} = P_n \tag{V.7}$$

Moreover, if the two receiving channels are perfectly identical so that we can assume that reference channel useful signal is equal to surveillance channel useful signal ($s_{R1} = s_{R2} \Rightarrow E\{s_{R1} \cdot s_{R2}^{*}\} = P_{S_{R1}} = P_{S_{R2}} = P_{S_R}$), the expression of the correlation coefficient becomes:

$$\rho = \frac{E\{s_{R1} \cdot s_{R2}^{*}\}}{\sqrt{P_{S_{R1}} + P_{n_1}} \cdot \sqrt{P_{S_{R2}} + P_{n_2}}} = \frac{P_{S_R}}{\sqrt{P_{S_R} + P_n} \cdot \sqrt{P_{S_R} + P_n}} = \frac{1}{1 + \frac{1}{SNR}} \qquad \text{(V.8)}$$

with $SNR = \frac{P_{S_R}}{P_n}$

If useful signal is the same on both the channels, correlation coefficient ρ will be one only if SNR $\rightarrow \infty$, see equation V.8: so, thermal noise is a source of decorrelation.

If we assume that useful signal on reference and surveillance channels is perfectly identical, and we consider that thermal noise power (estimated from data as the mean of squared noise samples) on the first channel (reference channel) is different from thermal noise power on the second channel (surveillance channel) only because it is a different realization of the same random variable, the expression of the correlation coefficient becomes:

$$\rho = \frac{E\{s_{R1} \cdot s_{R2}^{*}\}}{\sqrt{P_{S_{R1}} + P_{n_1}} \cdot \sqrt{P_{S_{R2}} + P_{n_2}}} = \frac{P_{S_R}}{\sqrt{P_{S_R} + P_{n_1}} \cdot \sqrt{P_{S_R} + P_{n_2}}} = \frac{1}{\sqrt{1 + \frac{1}{SNR_1}} \cdot \sqrt{1 + \frac{1}{SNR_2}}} \qquad \text{(V.9)}$$

with $SNR_1 = \frac{P_{S_R}}{P_{n_1}}$ and $SNR_2 = \frac{P_{S_R}}{P_{n_2}}$.

The expression above has been used to evaluate the theoretical correlation coefficient in the following tables. As previously mentioned, the idea is to demonstrate that the correlation coefficient evaluated from signals sampled on the two channels is not one only as a consequence of the summation of different noise realizations to the useful signals.

SNR values on the two channels (SNR_1 and SNR_2) are evaluated by dividing the average signal power for each channel (obtained as temporal average) for the thermal noise power obtained in the previous analysis (see sub-section V.2.1). Specifically, signal power is obtained as:

$$P_{ref} = P_{SR} + P_{n1} \cong \frac{\sum_{n=1}^{N} ref[n] \cdot ref^{*}[n]}{R} \qquad \text{(V.10)}$$

$$P_{rx} = P_{SR} + P_{n2} \cong \frac{\sum_{n=1}^{N} rx[n] \cdot rx^{*}[n]}{R} \tag{V.11}$$

where R is the receiver impedance (50Ω) and N is the number of samples in the considered integration time.

Table 4 reports the cancellation values obtained for single antenna acquisitions performed with the reference antenna in the scenario sketched in Figure 19, where the antenna pointing is highlighted. Selected transmitter of opportunity for these tests is located in Vatican City (Rome).

V.R. [V]	SNR Ch.0 [dB]	SNR Ch.1 [dB]	CANC TEO [dB]	CANC MEAS [dB]
0.2	80.86	81.80	78.29	71.31
0.4	80.14	81.05	77.56	74.88
1.0	72.59	73.46	69.99	69.22
2.0	66.62	67.57	64.06	63.71
4.0	60.65	61.47	58.03	57.25
10.0	53.10	53.86	50.45	49.88

Table 4 – single (reference) antenna cancellation values

Each table rows reports the vertical range and the following values:

- SNR values on the two channels, obtained as previously described
- theoretical cancellation value, obtained as

$$CA = \frac{P_{Rx}}{P_{Rx} \cdot (1 - |\rho|^2)} = \frac{1}{1 - |\rho|^2} \tag{V.12}$$

  where P_{Rx} indicates the signal power on the surveillance channel, and ρ is evaluated according to equation V.9

- measured cancellation value, evaluated as the ratio between the power levels measured, over a 200 kHz bandwidth, at the input and at the output of the cancellation filter.

By replacing in V.12 the expression of correlation coefficient ρ given by equation V.8 (but the same result is achieved by using equation V.9, due to the high and almost identical SNR values on the two channels), we obtain

$$CA = \frac{1}{1-\left(\frac{1}{1+\frac{1}{SNR}}\right)^2} = \frac{1}{1-\left(\frac{1}{\frac{SNR+1}{SNR}}\right)^2} = \frac{1}{1-\frac{SNR^2}{(SNR+1)^2}} = \frac{(SNR+1)^2}{(SNR+1)^2 - SNR^2} = \tag{V.13}$$

$$= \frac{SNR^2}{2SNR+1} + 1 \underset{se\ SNR>>}{\cong} \frac{SNR}{2}$$

This results shows that, as expected, the achievable cancellation (theoretical cancellation) is only limited by thermal noise, and in particular it is equal to half the SNR value. The same results can be achieved following the consideration that, during the cancellation operation, the noise power of the reference channel is added to the noise power of the surveillance channel, thus resulting in the most general case in a doubling of noise power. By indicating with P_{Out} the power at the output of the cancellation filter (ideally equal to twice the noise power, P_N) and with P_{In} the power before cancellation, we have:

$$CA = \frac{P_{In}}{P_{Out}} = \frac{P_{In}}{2 \cdot P_N} = \frac{SNR}{2} \tag{V.14}$$

As expected, SNR decreases as V.R. increases, because thermal noise power increases (see Table 3). Moreover, obtained cancellation values are very similar to corresponding expected values for V.R. equal or higher than 1, when theoretical cancellation is lower than 70 dB, while there is a difference of at least 3 dB for lower V.R. values. A possible explanation of this behaviour is that theoretical cancellation values have been evaluated taking into account only thermal noise as source of decorrelation; if we consider the typical Spurious Free Dynamic Range (SFDR) from A/D (NI PXI-5122) specifications (-75 dBc – dB relative to the carrier – for V.R. from 0.2 to 2, -65 dBc for V.R. 4 and 10), it is easy to understand that these levels introduce a new physical limit to the achievable cancellation: a comparison between the value of the ratio between signal power and spurious (-75 dBc) and the theoretical cancellation allows to consider the spurious level as a physical limit to the achievable cancellation for lower V.R. values (0.2 and 0.4 V), thus justifying the difference with respect to evaluated theoretical cancellation.

Table 4 reports the cancellation values obtained for single antenna acquisitions performed with the surveillance antenna in the scenario sketched in Figure 20, where the antenna pointing is highlighted.

V.R. [V]	SNR Ch.0 [dB]	SNR Ch.1 [dB]	CANC TEO [dB]	CANC MEAS [dB]
0.2	65.84	67.06	63.40	62.91
0.4	65.18	66.42	62.75	61.74
1.0	57.62	58.80	55.15	54.60
2.0	51.56	52.85	49.15	48.81
4.0	45.66	46.84	43.20	42.57
10.0	38.09	39.21	35.61	34.94

Table 5 – single (surveillance) antenna cancellation values

As it is apparent, also in this case obtained cancellation values are very similar to corresponding expected values, for all the considered V.R. values. In fact, due to surveillance antenna pointing with respect to the selected transmitter of opportunity (located in Vatican City), lower SNR values yield to corresponding lower theoretical cancellation values, so that the SFDR does not represent a problem.

V.3 *Figures*

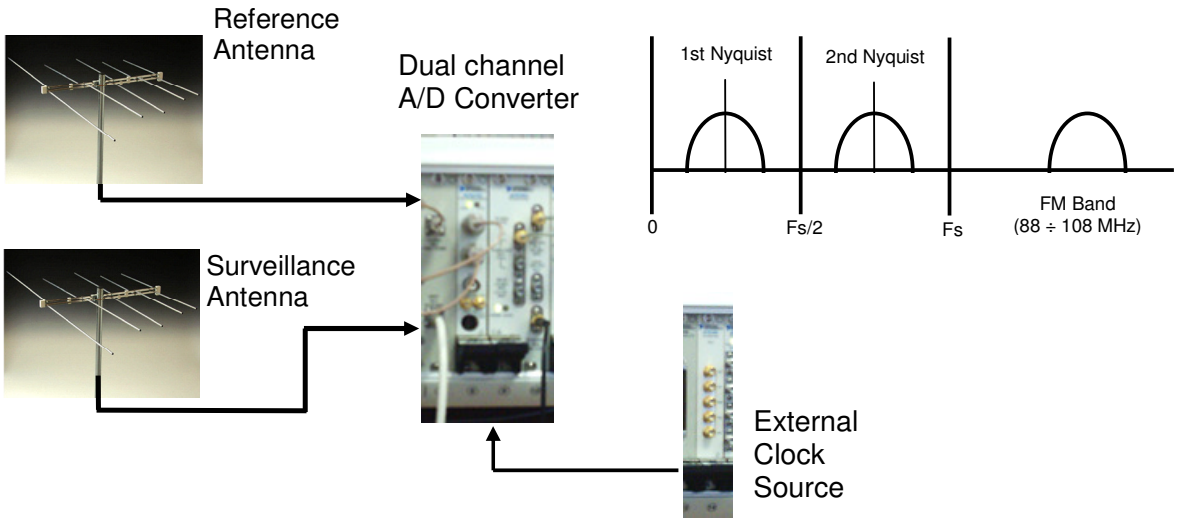

Figure 13 – Sketch of the direct RF sampling prototype.

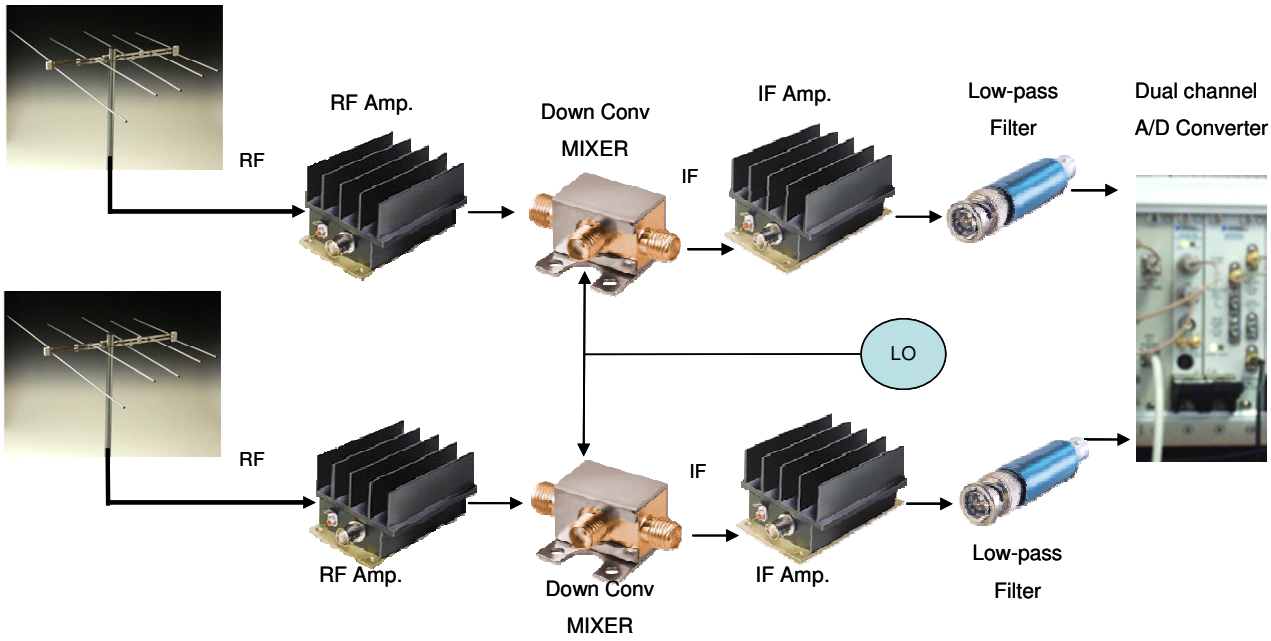

Figure 14 – Sketch of the wide-band down-conversion prototype.

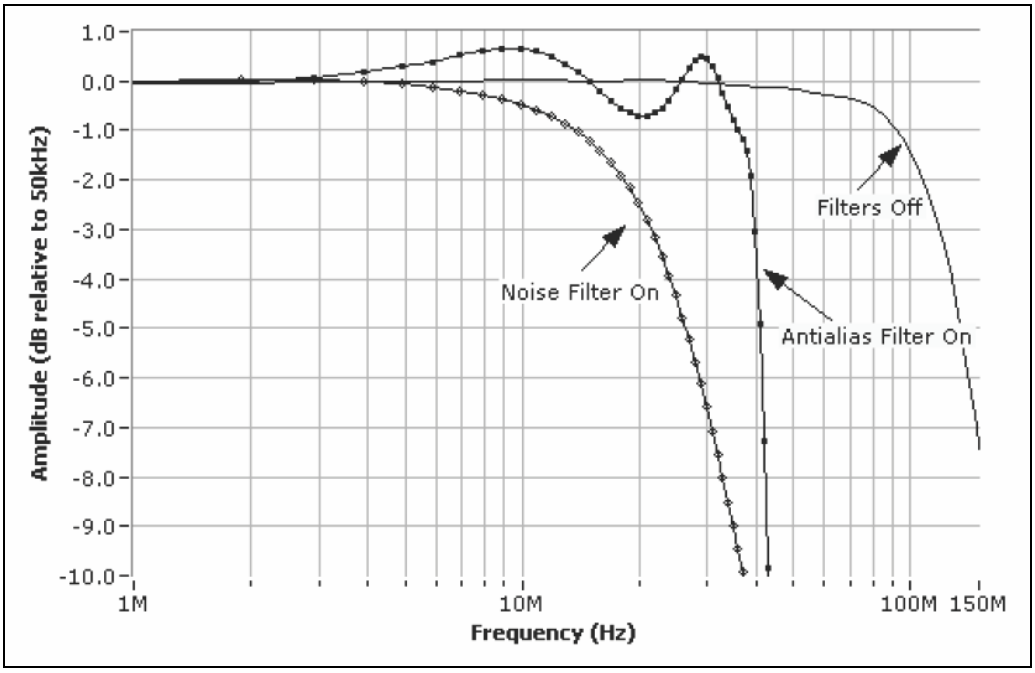

Figure 15 – NI PXI-5122 frequency responses (typical).

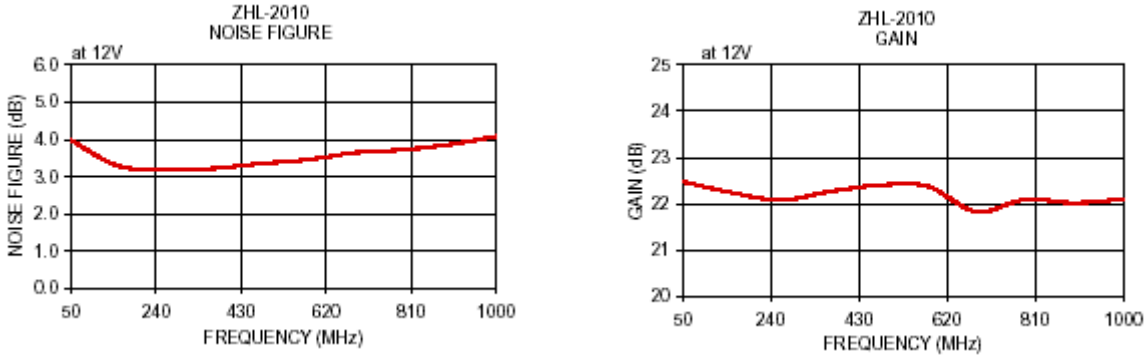

(a) (b)

Figure 16 – ZHL-2010 Noise Figure (a) and Gain (b).

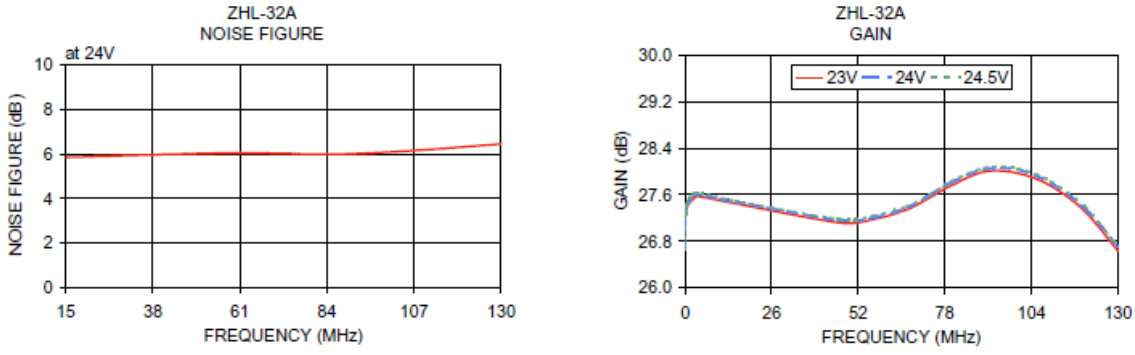

(a) (b)

Figure 17 – ZHL-32A-S Noise Figure (a) and Gain (b).

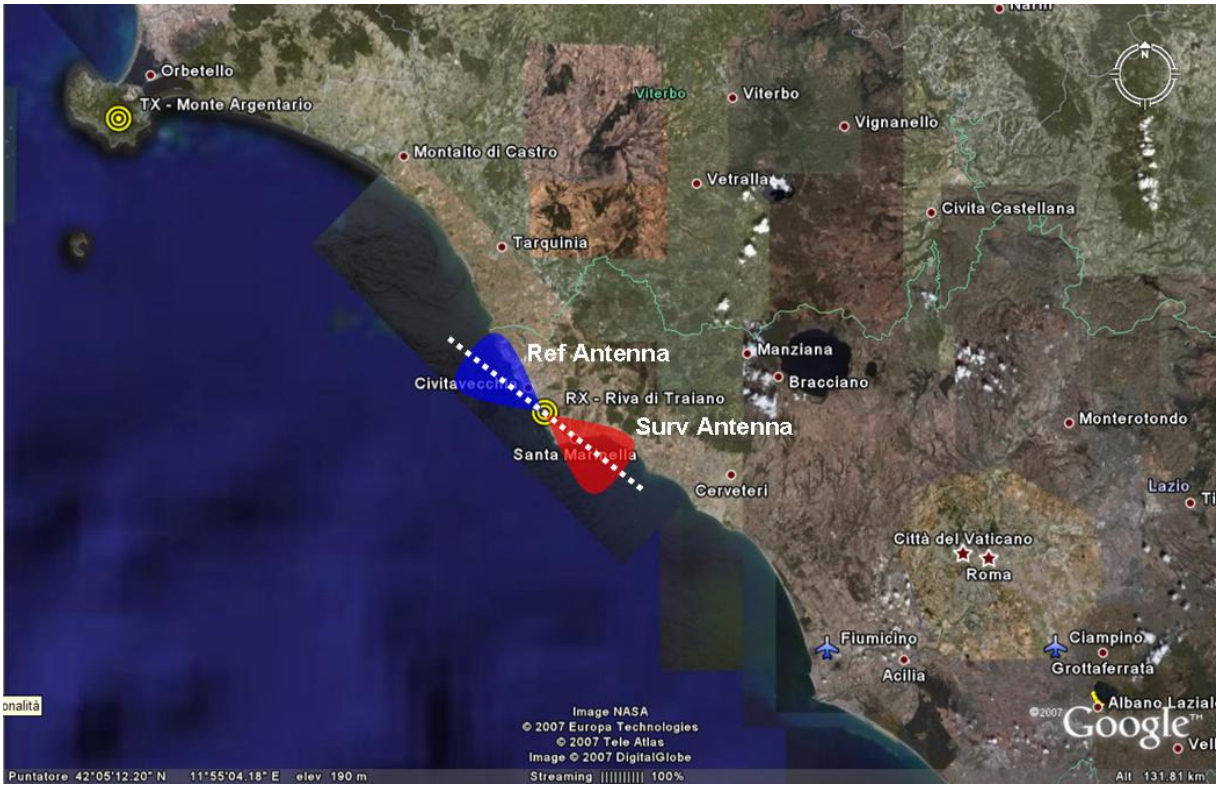

Figure 18 – Sketch of the acquisition geometry.

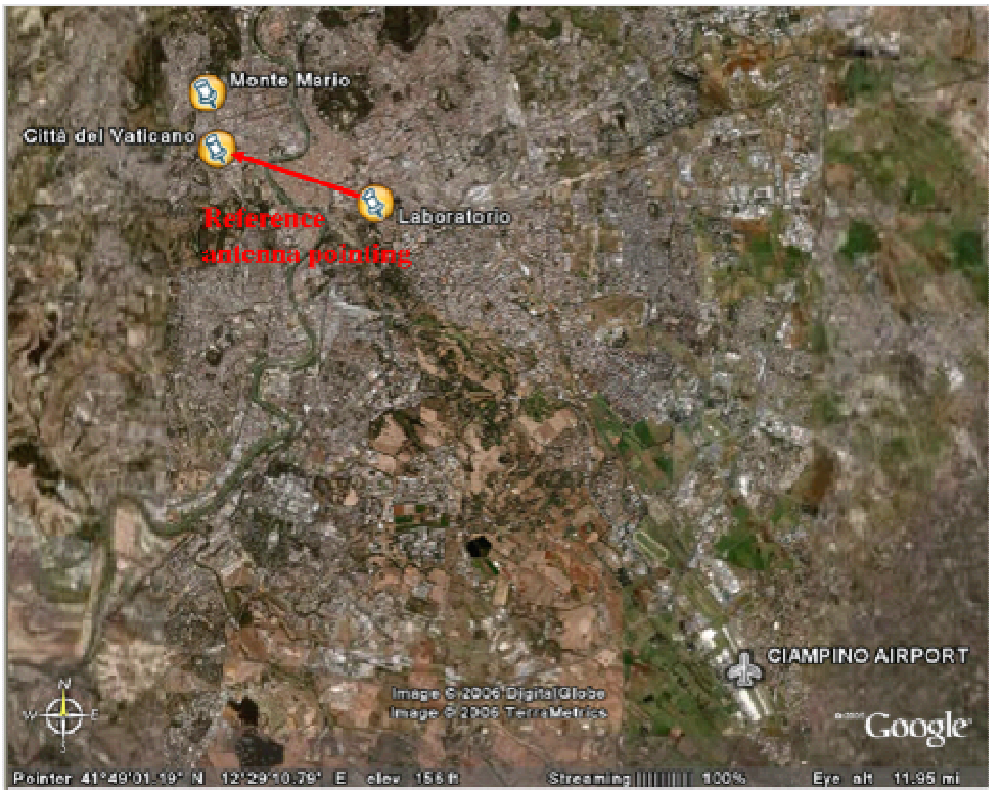

Figure 19 – Sketch of reference antenna pointing for single antenna acquisitions.

Figure 20 – Sketch of surveillance antenna pointing for single antenna acquisitions.

VI EXPERIMENTAL RESULTS AT THE SINGLE FM RADIO CHANNELS

To firstly validate the performance of the single FM radio channel operation, all the available data files have been processed, for each of the five selected FM radio channels, according to the processing scheme in Figure 1. The algorithms described in [8]-[9] have been used for the direct signal and multipath/clutter cancellation, and a standard bank of matched filters for the cross-correlation. The results have been reported on bistatic Range-Velocity maps: the use of velocity instead of Doppler frequency allows a simple and effective comparison of the results achieved on different carrier frequencies.

Obviously, these analysis were performed with reference to both the developed prototypes (direct RF sampling and signal down-conversion & baseband sampling), in order to compare the obtained performance both in terms of detection capability and false alarm rate. Moreover, these analysis was performed for each of the five selected FM radio channels, and for different Multi-Frequency Channels configurations (see also section VII). The results of this extensive analysis are not reported here for sake of brevity. However, we observed that the direct RF sampling prototype yields slightly better performance with respect to the down-conversion prototype; since their theoretical performance is largely comparable, this difference is mainly due to a slightly better exploitation of the vertical dynamic range of the ADC in the particular considered situation. For these reasons, without loss of generality, in the following only the results obtained with the direct RF sampling prototype are shown.

As an example, Figure 21(a) shows the Range-Velocity map obtained for the channel at 89.8 MHz (SFC1) of file pcl_18052007_10.05.42. As apparent a deep null appears at Range-Velocity bins where the cancellation filter has been applied. The resulting 2D Cross Correlation Function clearly shows a number of potential targets at bistatic ranges up to 180 km. This is confirmed in Figure 21(b) where the result of the application of a CFAR threshold to the data is shown using a CA-CFAR detection scheme with a nominal Probability of False Alarm $P_{fa}=10^{-4}$ when operating against thermal noise. As apparent some residual disturbance power is present, which has not been removed by the cancellation algorithm since it is spectrally distributed over non zero Doppler frequencies. This yields strong peaks at very low values of the bistatic range which clearly correspond to false alarms that can be easily removed at a

post-processing stage. Aiming at understanding the behaviour of the different FM radio channels, in the following we analyze short sequences of few consecutive acquisitions.

Specifically Figure 22(a-c) show the superposition of the detection results obtained at the five selected FM radio channels for 3 consecutive data files (pcl_18052007_10.05.42, pcl_18052007_10.06.05, pcl_18052007_10.06.29) respectively. Notice that all the plots within a relative bistatic range of 5 km have been discarded assuming that they are due to disturbance residuals. As apparent from the figures, at the different times the five channels have different detection characteristics. The comparative analysis reported in Figure 22 shows the presence of a large number of plot coincidences at the different FM radio channels considered. However, in many cases only one or two of the selected FM radio channels are able to detect a given target.

Correspondingly, Figure 23 shows the sequences of the results obtained for the 3 consecutive data files on the same Range-Velocity map, separately for each of the selected FM radio channels. A plot sequence can be easily recognized to belong to a possible target by observing that an approaching target has a positive bistatic velocity and the range rate of change is directly related to the magnitude of the bistatic velocity. However, to simplify the analysis, the available ATC registrations (corresponding to the considered time period) have been reported in each figure (small points sequences). Moreover, the identified plot sequences are indicated with circles using different line styles according with the following criterion: the continuous green line is for complete sequences containing 3 plots while the discontinuous green is for sequences containing only 2 plots. As it is apparent, reasonably complete target plot sequences are observed only at some of the considered FM radio channels, while on other ones only few plots are detected. Moreover, not the same target sequences are clearly visible at different channels. As already anticipated in Section III , missed detections can be attributed to the general degradation of the instantaneous characteristics of either the transmitted waveform or the e.m. environment. This effect is further investigated in the following with reference to the available real data set.

The FM radio channels at 89.8 MHz (SFC1) and 93.8 MHz (SFC2) are generally recognized to yield better detection performance than the others. This is mainly due to their better characteristics in terms of co- and inter-channel interferences, which set the average performance level. This is quite apparent from Figure 24 which shows the estimated actual noise level for the considered channels over the 150 consecutive acquisitions of May 18th. The estimated noise levels in this area are significantly higher than the nominal system noise floor (reported on the same figure for comparison) and their mean values account for persistent interferences at the considered channel frequency bandwidth. As it is apparent, the best performing channels (SFC1=89.8 MHz and SFC2=93.8 MHz) show lower mean values with

respect to the channels at 92.1, 91.3 and 94.3 MHz (SFC3, SFC4 and SFC5 respectively) thus yielding a higher capability to detect weaker target echoes.

Notice that high peaks appear in the estimated noise level at specific times, which account for the presence of strong sidelobe structures in the waveform ambiguity function. The FM channel transmitted at 94.3 MHz (SFC5) is generally the most affected by this effect since it usually broadcasts speech programs. As an example, Figure 25 shows the spectrum of the modulating signal extracted for this channel from the 23rd file of the sequence of 150 consecutive acquisitions and the corresponding Range-Velocity map. The transmission is clearly a monophonic transmission with a very limited actual bandwidth thus yielding seriously degraded waveform characteristics for radar purposes (no targets can be detected among the strong periodic structures that appear in the map).

Beside this extreme condition generally related to silence periods, a typical radio transmission can yield a poor side-lobe level due to the associated waveform's ambiguity function which can seriously limit the detection of weak targets. As an example, Figure 26(a-b) show the Range-Velocity and the detection maps obtained for the channel at 89.8 MHz (SFC1) at the second file (pcl_18052007_10.06.05) of the same sequence considered in Figure 22 and Figure 23. As it is apparent, higher sidelobe structures appear in this map with respect to the corresponding map obtained for the same FM radio channel at the first file in the sequence (see Figure 21(a)). As a consequence, even if this is recognized to be a good performing channel, at the considered time instant the system exploiting this FM channel fails to detect many of the targets that are instead detected with different FM radio channels (see Figure 22(b) and Figure 26(b) where discontinuous circles indicate potential detections achievable with other FM channels).

In order to provide an extensive performance evaluation for the single FM channel operation, the detection results obtained using the considered FM channels for all the data set were compared to the available air traffic control registrations for the considered area. An extensive analysis was performed over the 300 recorded data files aiming at estimating the achieved detection probability and the actual false alarm rate. Specifically, the performance has been evaluated over proper regions obtained by dividing the considered surveillance volume, contained into the 3 dB surveillance antenna pattern, over the bistatic range and elevation dimensions as depicted in Figure 27. Table 6, Table 7, and Table 8 report the results obtained for $P_{fa}=10^{-3}$ at the different single FM radio channels (SFC1-5) with CA-CFAR, GO-CFAR, and SO-CFAR detection schemes, respectively. Each table reports the number of true targets observed and the detection rate achieved for each region in the grid defined by $\Delta Rx/\Delta Ey$

(see Figure 27 for the definition of the ΔRx and ΔEy regions), together with the false alarm rate measured at each range region.

	ΔR1						ΔR2						ΔR3						ΔR4					
	num of targets	SFC1	SFC2	SFC3	SFC4	SFC5	num of targets	SFC1	SFC2	SFC3	SFC4	SFC5	num of targets	SFC1	SFC2	SFC3	SFC4	SFC5	num of targets	SFC1	SFC2	SFC3	SFC4	SFC5
ΔE1	4	0.00	0.25	0.00	0.00	0.00	73	0.03	0.04	0.11	0.03	0.07	565	0.10	0.11	0.08	0.07	0.07	317	0.05	0.05	0.05	0.06	0.04
ΔE2	3	0.67	1.00	1.00	0.67	0.33	152	0.28	0.39	0.23	0.08	0.20	173	0.23	0.35	0.24	0.11	0.13	316	0.12	0.19	0.18	0.06	0.09
ΔE3	15	0.87	0.87	0.87	0.60	0.53	139	0.45	0.65	0.47	0.14	0.35	42	0.29	0.40	0.21	0.07	0.21	47	0.15	0.26	0.19	0.02	0.13
ΔE4	52	0.75	0.77	0.75	0.37	0.69	31	0.68	0.71	0.48	0.23	0.42	39	0.26	0.44	0.38	0.15	0.10	21	0.05	0.14	0.05	0.05	0.10
ΔE5	31	0.58	0.68	0.48	0.32	0.45	3	0.33	0.33	0.67	0.00	0.33	0	-	-	-	-	-	0	-	-	-	-	-
False Alarm Rate		9.6E-4	1.1E-3	9.6E-4	9.0E-4	1.0E-3		1.1E-3	1.1E-3	1.1E-3	1.1E-3	9.6E-4		1.1E-3	1.1E-3	1.0E-3	9.4E-4	8.6E-4		1.1E-3	1.1E-3	1.1E-3	1.1E-3	8.8E-4

Table 6 – Detection performance for the different single frequency channels (SFC1-5) with a CA-CFAR detection scheme ($P_{fa}=10^{-3}$).

	ΔR1						ΔR2						ΔR3						ΔR4					
	num of targets	SFC1	SFC2	SFC3	SFC4	SFC5	num of targets	SFC1	SFC2	SFC3	SFC4	SFC5	num of targets	SFC1	SFC2	SFC3	SFC4	SFC5	num of targets	SFC1	SFC2	SFC3	SFC4	SFC5
ΔE1	4	0.00	0.00	0.00	0.00	0.25	73	0.03	0.07	0.08	0.05	0.14	565	0.10	0.11	0.12	0.13	0.12	317	0.06	0.08	0.06	0.07	0.09
ΔE2	3	1.00	1.00	1.00	1.00	1.00	152	0.35	0.41	0.41	0.46	0.44	173	0.29	0.35	0.35	0.36	0.38	316	0.13	0.21	0.19	0.22	0.21
ΔE3	15	0.80	0.93	0.87	0.93	0.93	139	0.52	0.64	0.61	0.65	0.65	42	0.36	0.36	0.36	0.36	0.38	47	0.15	0.21	0.26	0.26	0.28
ΔE4	52	0.75	0.88	0.87	0.87	0.88	31	0.77	0.81	0.77	0.77	0.81	39	0.41	0.56	0.56	0.51	0.54	21	0.24	0.14	0.14	0.19	0.24
ΔE5	31	0.55	0.68	0.68	0.68	0.68	3	0.33	0.33	0.33	0.67	0.67	0	-	-	-	-	-	0	-	-	-	-	-
False Alarm Rate		9.1E-4	9.3E-4	9.4E-4	1.0E-3	1.1E-3		1.1E-3	1.2E-3	1.2E-3	1.2E-3	1.3E-3		1.0E-3	1.1E-3	1.2E-3	1.2E-3	1.3E-3		1.1E-3	1.1E-3	1.2E-3	1.2E-3	1.3E-3

Table 7 – Detection performance for the different single frequency channels (SFC1-5) with a GO-CFAR detection scheme ($P_{fa}=10^{-3}$).

	ΔR1						ΔR2						ΔR3						ΔR4					
	num of targets	SFC1	SFC2	SFC3	SFC4	SFC5	num of targets	SFC1	SFC2	SFC3	SFC4	SFC5	num of targets	SFC1	SFC2	SFC3	SFC4	SFC5	num of targets	SFC1	SFC2	SFC3	SFC4	SFC5
ΔE1	4	0.00	0.00	0.00	0.00	0.00	73	0.03	0.05	0.01	0.01	0.01	565	0.02	0.02	0.01	0.01	0.01	317	0.03	0.01	0.02	0.03	0.01
ΔE2	3	0.00	0.33	0.00	0.00	0.00	152	0.04	0.02	0.03	0.01	0.02	173	0.03	0.04	0.01	0.02	0.02	316	0.01	0.02	0.01	0.01	0.01
ΔE3	15	0.07	0.20	0.07	0.00	0.00	139	0.02	0.06	0.01	0.03	0.04	42	0.00	0.02	0.02	0.00	0.02	47	0.04	0.02	0.04	0.00	0.00
ΔE4	52	0.04	0.12	0.13	0.06	0.02	31	0.10	0.19	0.13	0.03	0.00	39	0.03	0.00	0.00	0.00	0.00	21	0.05	0.05	0.00	0.05	0.00
ΔE5	31	0.13	0.19	0.03	0.06	0.00	3	0.00	0.00	0.33	0.00	0.00	0	-	-	-	-	-	0	-	-	-	-	-
False Alarm Rate		4.1E-4	4.1E-4	3.9E-4	4.1E-4	3.2E-4		4.1E-4	4.6E-4	3.9E-4	4.2E-4	3.2E-4		3.9E-4	4.3E-4	3.3E-4	4.0E-4	2.5E-4		4.0E-4	3.9E-4	3.7E-4	3.8E-4	2.6E-4

Table 8 – Detection performance for the different single frequency channels (SFC1-5) with a SO-CFAR detection scheme ($P_{fa}=10^{-3}$).

The following general considerations are in order:

(i) As expected, the detection capability rapidly degrades as the relative bistatic range increases, due to the higher propagation loss.

(ii) Few detections are obtained among the high number of true targets at low elevation angles, corresponding to the landing aircrafts at Fiumicino airport (see for example the region ΔR3/ΔE1); this is mainly due to the limited height of the building where the surveillance antenna is mounted, which is surrounded by other structures of similar or higher height.

The obtained False Alarm Rate is largely comparable with the nominal value used to set the threshold when operating with a CA-CFAR and a GO-CFAR detection scheme. In contrast, the SO-CFAR detection scheme does not allow a proper control of the actual false alarm rate which appears to be smaller than its nominal value; it is then possible to state that the SO-CFAR is less robust than the CA-CFAR and the GO-CFAR in the real case for which the data statistical distribution deviates from the

assumed exponential hypothesis. Correspondingly, the detection rate achieved with the SO-CFAR scheme experiences a dramatic decrease with respect to both the CA-CFAR and the GO-CFAR for all the considered FM radio channels.

The CA-CFAR and the GO-CFAR detection schemes yield comparable detection performance with a limited advantage of the GO-CFAR, especially for the FM radio channels that have been recognized to be the worse performing channels (SFC3-4-5). In fact, in those cases, the noise floor can be dominated by sidelobes and it is apparent that operating on the real data the CA-CFAR slightly over-estimates the detection threshold while the GO-CFAR yields a slightly higher P_{fa} and, consequently, a slightly improved detection capability.

Beyond these considerations, it is to be noted that, operating with both the CA-CFAR and the GO-CFAR, the detection performance highly varies with the considered FM channels at the different detection regions; it is then quite difficult to identify the best performing channel for the whole surveillance volume while we can only observe that, in many cases, different FM radio channels yield complementary or comparable performance.

VI.1 *Figures*

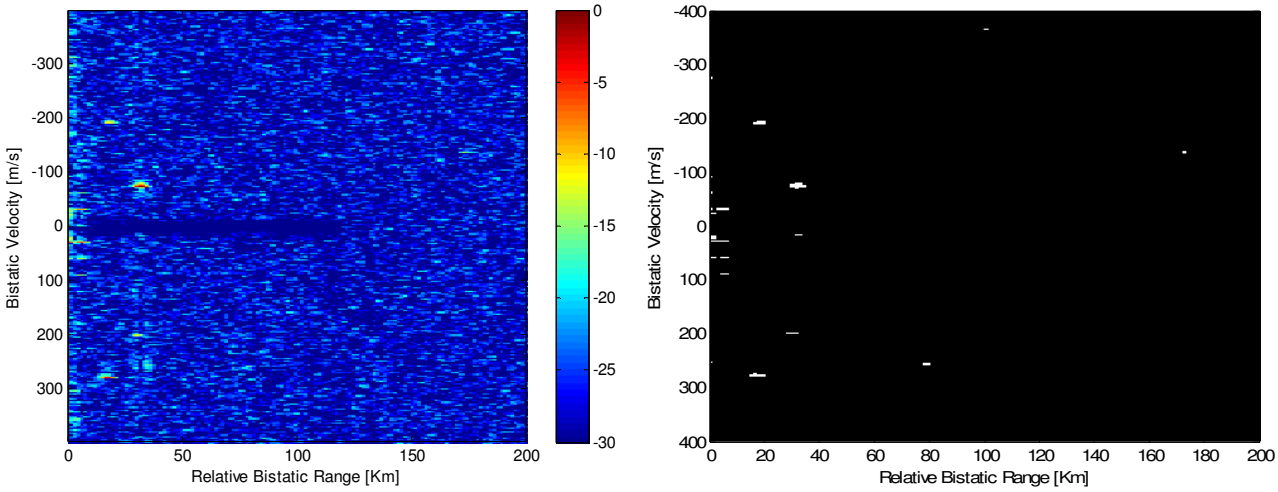

(a) (b)

Figure 21 – Range-Velocity map for the channel at 89.8 MHz (SFC1) of file pcl_18052007_10.05.42: (a) raw map; (b) result of the application of a CA-CFAR detection scheme to the data ($P_{fa}=10^{-4}$).

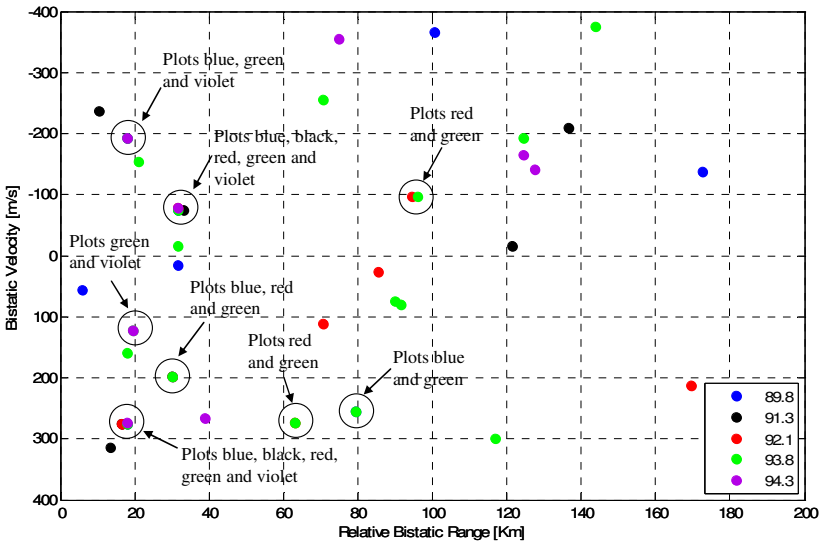

(a)

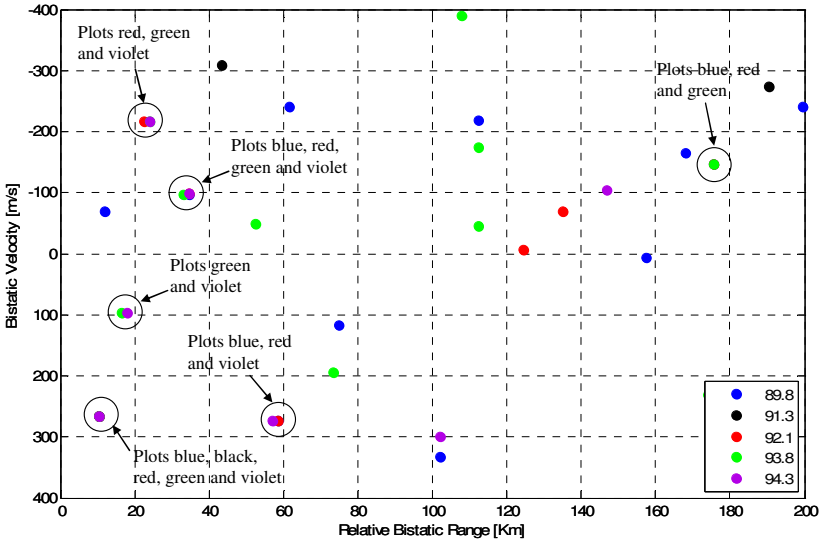

(b)

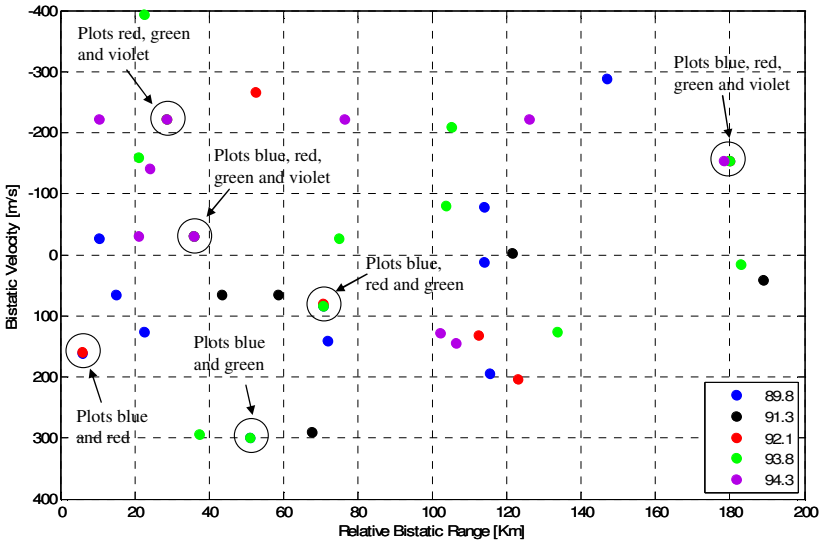

(c)

Figure 22 – Plot coincidences on the Range-Velocity map for the five FM radio channels in the three subsequent acquisitions: (a) pcl_18052007_10.05.42; (b) pcl_18052007_10.06.05; (c) pcl_18052007_10.06.29.

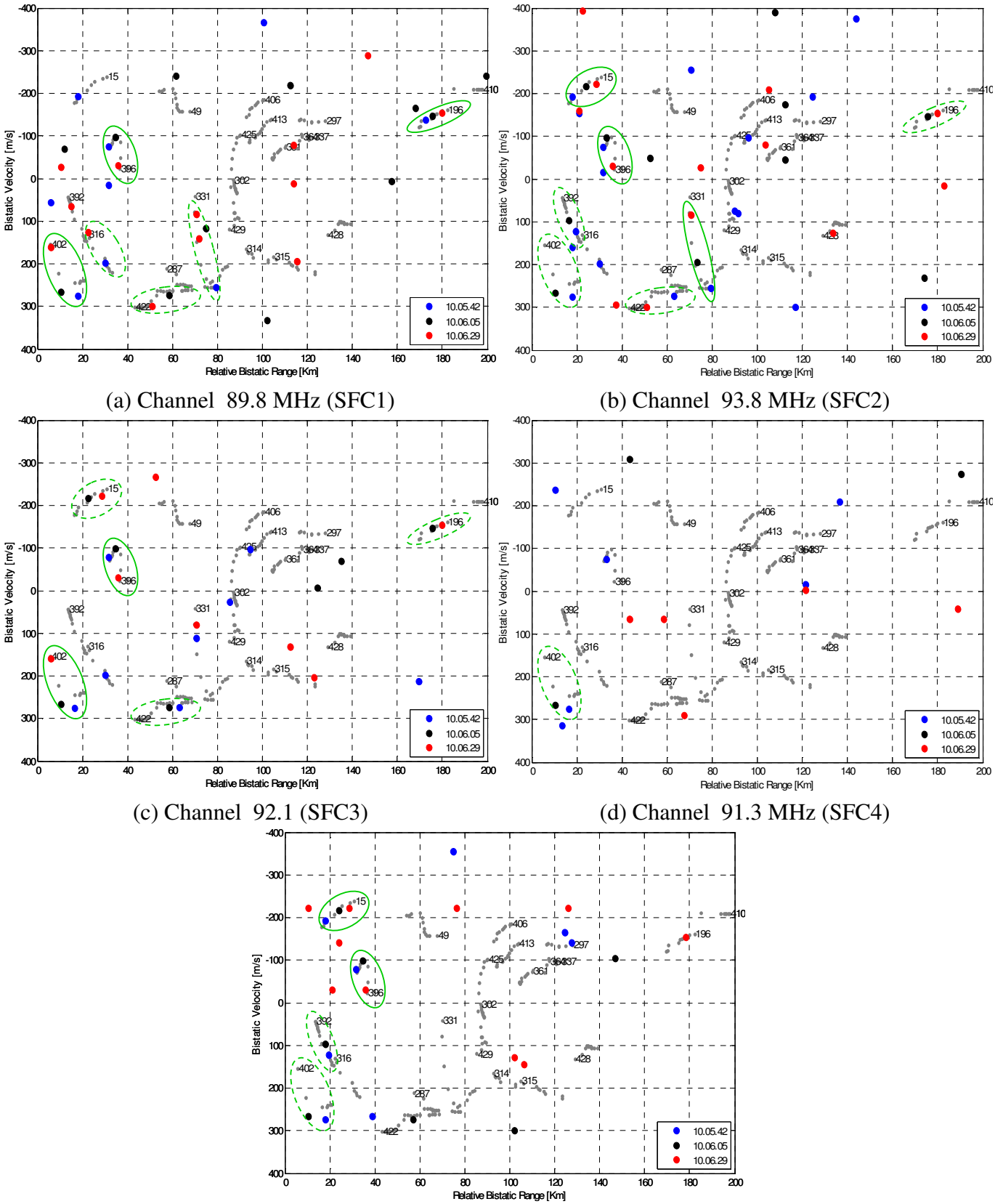

(a) Channel 89.8 MHz (SFC1)

(b) Channel 93.8 MHz (SFC2)

(c) Channel 92.1 (SFC3)

(d) Channel 91.3 MHz (SFC4)

(e) Channel 94.3 MHz (SFC5)

Figure 23 – Plot sequences in the Range-Velocity maps for different FM radio channels in the 3 consecutive acquisitions.

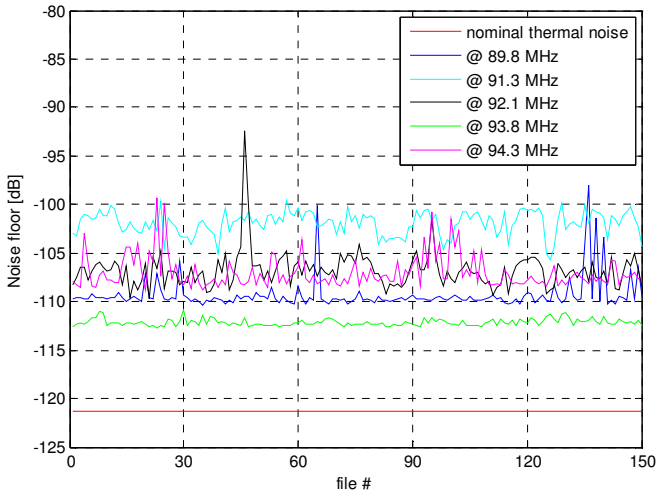

Figure 24 – Estimated noise floor levels for the FM radio channels over 150 consecutive acquisitions.

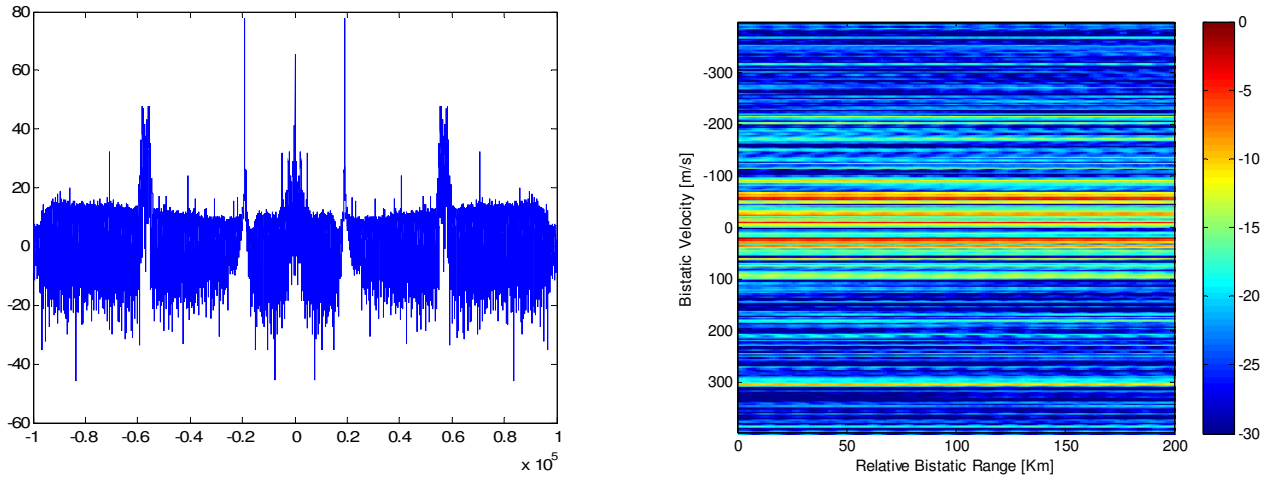

(a) (b)

Figure 25 – Waveform characteristics analysis for channel 94.3 MHz (SFC5) over the 23rd data file of May 18th (pcl_18052007_10.07.17: (a) modulating signal spectrum; (b) Range-Velocity map.

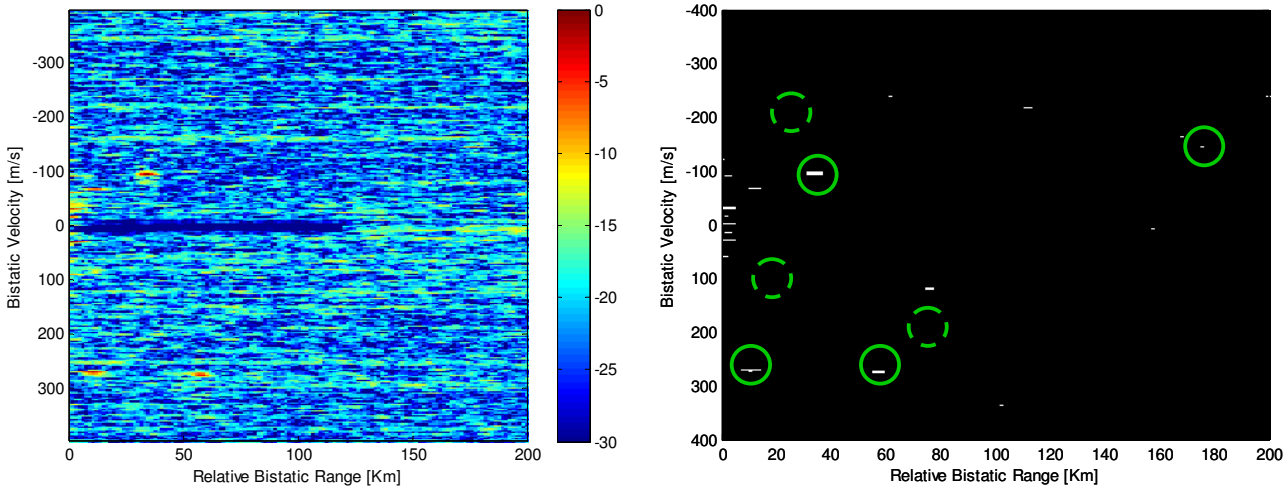

(a) (b)

Figure 26 – Range-Velocity map for the channel at 89.8 MHz (SFC1) of file pcl_18052007_10.06.05: (a) raw map; (b) result of the application of a CA-CFAR detection scheme to the data ($P_{fa}=10^{-4}$).

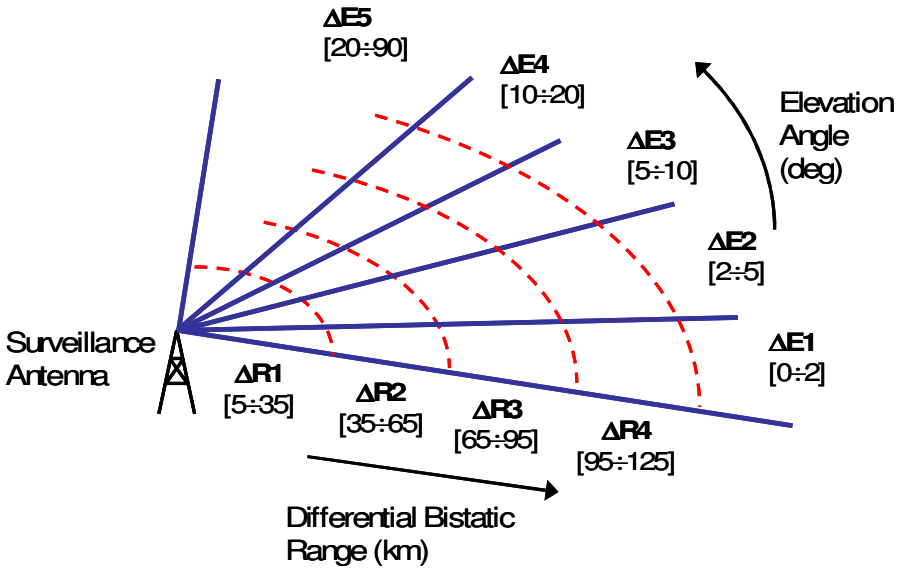

Figure 27 – Sketch of the considered regions for the detection performance evaluation.

VII EXPERIMENTAL RESULTS WITH THE MULTI-FREQUENCY APPROACH

The analysis presented in the previous section demonstrated that the availability of N different FM radio channels can collect a huge amount of information, which includes a large degree of diversity. It is than likely that the joint use of multiple frequencies can give really improved detection performance. To this purpose, the multi-frequency approaches described in Section IV have been applied to the available data set and the results are reported in the following.

According to those approaches, a constant Velocity resolution (Δv=3m/s) has been used for the different carrier frequencies, thus obtaining the values reported in Table 9 for the integration times. Then, the Range-Velocity maps obtained for the single FM channels have been normalized to the actual noise floor level (see Figure 24) estimated over a map portion located at high range values, where the target contributions and the effects of the waveforms (lobes main structures) can be assumed to be negligible. Finally, the different maps have been integrated according to the different proposed integration strategies.

Carrier Frequency (MHz)	89.8	91.3	92.1	93.8	94.3
Integration time (sec)	1.1136	1.0953	1.0858	1.0661	1.0604

Table 9– Integration times over the selected FM radio channels.

An example of the resulting Range-Velocity maps obtained with the centralized integration strategies (SUM, MAX and MIN) are shown in Figure 28(a-c) using the N=3 channels at 89.8 MHz, 92.1 MHz, 93.8 MHz for the same data file of Figure 21. As it is apparent, the SUM and the MAX yield similar results with a slightly higher background level for the MAX approach. In contrast, the MIN approach allows a strong reduction of the background level there including the strong disturbance residuals at short ranges. This can lead to a significant improvement for short range targets while it is likely that a significant SNR loss is experienced for long range targets.

To show the corresponding detection performance, Figure 29 reports the plot sequences obtained with the different integration strategies after the application of all the considered CFAR detection schemes over the same sequence of 3 acquisitions used in Figure 23 (the decentralized approach operates with L=2). As expected, the SO-CFAR detection scheme does not yield appreciable detection performance with any of the integration strategies. In fact, as long as it has been conceived, this particular scheme can

be of great potential interest only in the presence of strong interfering targets affecting the secondary data (as in the case of closely spaced target formations). The CA-CFAR and GO-CFAR detection schemes yield similar performance when operating in conjunction with the same integration strategy; only a limited loss is apparent for the GO-CFAR especially for short range targets whose detection is likely to be limited by the disturbance residuals (still above the background level). As well known, the GO-CFAR detection scheme is mainly applied to avoid false alarms rising from strong clutter edges: notice that many false alarms surrounding the cancellation area (deep notch) disappear when operating with a GO-CFAR. As a consequence a resulting detection loss should be accepted for targets falling at those unfavourable locations.

For this particular data set of 3 consecutive acquisitions, the best performing integration strategies are the SUM, the MAX and the DEC approaches which are able to detect many complete plot sequences thus significantly enhancing the performance obtained with the single channel operation. Specifically, when operating with these approaches, the completeness of the detected plot sequences is improved with respect to the best single channels (see 89.8 MHz, 93.8 MHz and 92.1 MHz in Figure 23(a,b,c)) since additional plots are detected for almost all the considered target tracks. This gives a significant advantage especially for targets that only provide isolated plots or 2-plot sequences when operating with a single channel, since their tracks are otherwise likely to be lost. Moreover, notice that the performance of the single channels are highly variable with the data file while the multi-frequency approaches are able to exploit the large diversity of information coming from the single integrated channels, thus yielding reliable performance at all the coherent processing intervals.

The performance of multi-frequency approaches has been extensively evaluated over the available data set using the same methodology described in section VI for the single frequency operation. Specifically, 5 different Multi-Frequency configurations have been considered for all the considered integration strategies:

- MFC2: 2 integrated channels (89.8-93.8 MHz);
- MFC3: 3 integrated channels (89.8-93.8-92.1 MHz);
- MFC4a: 4 integrated channels (89.8-93.8-92.1-91.3 MHz);
- MFC4b: 4 integrated channels (89.8-93.8-92.1-94.3 MHz);
- MFC5: 5 integrated channels (89.8-93.8-92.1-91.3-94.3 MHz).

First of all, aiming at exploiting the detection coincidences achievable using the single frequency channels, the decentralized integration strategy is considered and compared with the single frequency

operation in Figure 30(a-c) for different CFAR detection schemes, respectively. Specifically each figure reports the detection rates achievable with the different single/multi-channel approaches for 3 different bistatic range regions ΔR_1, ΔR_2, and ΔR_3 (see Figure 27). For clarity of presentation, these values have been obtained by merging the results obtained for elevation angles in the range 5°-90° (ΔE_3, ΔE_4, and ΔE_5) and discarding the very low elevation angles where the detection performance is limited by the building height (as noticed in the single channel case). The decentralized strategy operates with a "2 out of *N*" logic for *N*<5 (MFC2,3,4a,4b) and with a "3 out of 5" logic in the MFC5 case. Correspondingly, Table 10 reports the resulting False Alarm Rate distinguishing among the different range regions. As apparent, both the CA-CFAR and the GO-CFAR are able to maintain the desired P_{fa} value ($P_{fa}=10^{-3}$). As in the case of the single channel operation, the SO-CFAR detection scheme suffers of a limited robustness when applied against real data even if, when using a decentralized integration strategy, it allows a better control of the P_{fa} with respect to the single channel configurations. This is quite reasonable since the decentralized integration allows to increase the P_{fa} on the single integrated channel, thus increasing the robustness of the detection threshold to mismatches of the data statistical distribution.

As apparent from Figure 30(a-c), the decentralized integration strategy yields a detection performance improvement with respect to the single frequency operation since, for any given range region, it is possible to find a Multi-Frequency configuration which is able to increase the detection rate with respect to the best performing single channel. Moreover this improvement becomes higher at further bistatic ranges. Notice that it is quite difficult to identify the best performing multi-frequency configuration since the resulting detection capability strongly depends on the single integrated channels behaviour, especially in a decentralized integration strategy. This is clearly apparent from a comparison of the two MFC based on 4 integrated channels (MFC4a and MFC4b). As a consequence, the increase of the number of integrated channels does not always yield a performance improvement if the additional channels show poor performance. Thus in the following, the centralized integration strategies are analysed and compared aiming at exploiting the SNR improvement due to the direct (linear or non-linear) integration of the target power at the different channels.

		ΔR1					ΔR2					ΔR3				
		MFC2	MFC3	MFC4a	MFC4b	MFC5	MFC2	MFC3	MFC4a	MFC4b	MFC5	MFC2	MFC3	MFC4a	MFC4b	MFC5
DEC	CA-CFAR	9.7E-4	9.8E-4	1.0E-3	1.3E-3	1.1E-3	1.1E-3	1.2E-3	1.2E-3	1.3E-3	1.3E-3	1.0E-3	1.1E-3	1.2E-3	1.2E-3	1.2E-3
	GO-CFAR	9.1E-4	9.3E-4	9.4E-4	1.0E-3	1.1E-3	1.1E-3	1.2E-3	1.2E-3	1.2E-3	1.3E-3	1.0E-3	1.1E-3	1.2E-3	1.2E-3	1.3E-3
	SO-CFAR	7.6E-4	7.3E-4	7.9E-4	7.8E-4	8.9E-4	8.3E-4	7.9E-4	7.8E-4	7.5E-4	8.6E-4	8.1E-4	7.6E-4	7.4E-4	7.3E-4	8.4E-4

Table 10 – False Alarm Rate for the decentralized integration strategies with different multi-frequency configurations (MFC2-5) and different detection schemes ($P_{fa}=10^{-3}$).

Table 11 reports the false alarm rates obtained with the different centralized integration strategies in conjunction with the different CFAR detection schemes. As apparent, the CA-CFAR and the GO-CFAR detection schemes allow a proper control of the P_{fa} with all the considered integration strategies. Once again, the SO-CFAR detection scheme yields a false alarm rate comparable with the nominal one only in few cases. Thus in the following analysis only the CA-CFAR and the GO-CFAR detection schemes will be considered. Figure 31(a-b) show the comparison of the detection performance obtained with the centralized integration strategies for a CA-CFAR and a GO-CFAR integration scheme, respectively. As apparent, the MIN approach always yields the worst performance since, for any MF configuration, the achievable detection rate generally degrades with respect to both the SUM and MAX approaches operating with the same number of integrated channels. Moreover, the best performing MF configuration with the MIN approach always yields worse performance than the worst MF configuration with the SUM approach. We interpret this behaviour as follows: the MIN strategy is able to discard the disturbance residuals and sidelobe structures which appear at a single frequency channel map; however, it retains the minimum SNR for any given target which implies a significant penalty when operating with FM radio channels with largely different SNR.

		ΔR1					ΔR2					ΔR3				
		MFC2	MFC3	MFC4a	MFC4b	MFC5	MFC2	MFC3	MFC4a	MFC4b	MFC5	MFC2	MFC3	MFC4a	MFC4b	MFC5
SUM	CA-CFAR	1.0E-3	1.2E-3	1.3E-3	1.9E-3	1.9E-3	1.2E-3	1.1E-3	1.2E-3	1.4E-3	1.5E-3	1.0E-3	1.1E-3	1.1E-3	1.2E-3	1.2E-3
	GO-CFAR	9.0E-4	9.3E-4	9.6E-4	1.1E-3	1.0E-3	1.1E-3	1.1E-3	1.1E-3	1.1E-3	1.2E-3	1.0E-3	1.0E-3	1.0E-3	1.0E-3	1.0E-3
	SO-CFAR	5.6E-4	7.5E-4	9.4E-4	1.2E-3	1.5E-3	5.4E-4	6.6E-4	7.4E-4	9.1E-4	1.0E-3	5.5E-4	6.6E-4	7.2E-4	7.1E-4	8.7E-4
MAX	CA-CFAR	1.1E-3	1.3E-3	1.7E-3	2.3E-3	2.4E-3	1.2E-3	1.2E-3	1.3E-3	1.5E-3	1.6E-3	1.0E-3	1.1E-3	1.1E-3	1.1E-3	1.2E-3
	GO-CFAR	9.3E-4	9.8E-4	1.1E-3	1.3E-3	1.2E-3	1.1E-3	1.1E-3	1.1E-3	1.2E-3	1.2E-3	1.0E-3	1.0E-3	1.0E-3	1.0E-3	1.0E-3
	SO-CFAR	5.7E-4	9.1E-4	1.2E-3	1.8E-3	2.3E-3	5.7E-4	7.3E-4	8.3E-4	1.1E-3	1.2E-3	5.5E-4	7.0E-4	7.3E-4	8.5E-4	9.0E-4
MIN	CA-CFAR	1.1E-3	1.0E-3	9.4E-4	1.1E-3	1.1E-3	1.2E-3	1.2E-3	1.1E-3	1.2E-3	1.1E-3	1.1E-3	1.1E-3	1.1E-3	1.2E-3	1.1E-3
	GO-CFAR	9.7E-4	9.5E-4	8.5E-4	9.9E-4	9.9E-4	1.1E-3	1.1E-3	1.0E-3	1.1E-3	1.1E-3	1.0E-3	1.0E-3	9.9E-4	1.1E-3	1.0E-3
	SO-CFAR	4.3E-4	4.5E-4	4.6E-4	4.4E-4	4.5E-4	4.5E-4	4.3E-4	4.5E-4	4.1E-4	4.3E-4	4.4E-4	4.5E-4	4.5E-4	4.0E-4	4.2E-4

Table 11 – False Alarm Rate for the centralized integration strategies with different multi-frequency configurations (MFC2-5) and different detection schemes ($P_{fa}=10^{-3}$).

For the same reason, the SUM and the MAX integration strategies show similar performance with both the CFAR detection schemes in the short range, while the SUM has a slight advantage at far range. However, notice that the MAX approach operating with both the CA-CFAR and the GO-CFAR yields slightly higher false alarm rates at shorter ranges (see Table 11) probably due to the disturbance residuals which appear in that area of the Range-Velocity map. In fact the MAX strategy retains those residuals and sidelobe structures thus increasing the P_{fa} with respect to its nominal value which refers to the case of independent exponentially distributed noise. In terms of detection probability, the results show that the MAX is slightly better than the SUM when using a small number of integrated channels (2-3); whereas the SUM is better than the MAX for a higher number of channels (4-5). Among the

CFAR detection schemes (see Figure 30(a-b) and Figure 31(a-b)), the CA-CFAR seems preferable since it yields a slight performance improvement with respect to the GO-CFAR operating in conjunction with the same single/multi-frequency approach.

A global comparison of the proposed integration strategies is shown in Figure 32 for the three considered range regions, respectively. Specifically a CA-CFAR detection scheme is considered and the results are reported for the best performing integration approaches (DEC, SUM and MAX). Moreover, in each figure the detection rates obtained with the 2 best performing channels at each range region have been added for comparison. Notice that the detection capability of the considered PBR system is limited due to the long baseline between the TX and the RX site. However, the proposed multi-frequency approaches are shown to yield a remarkable performance improvement with respect to the best single-channels case for all the considered surveillance range regions. Unfortunately data collected with more favourable bistatic geometry (especially a shorter baseline) are not available; such data set would provide both better single channel and multi-channel performance but would not change the comparative results and the message of this work. Specifically the following configurations seem to be preferable: (i) the SUM approach with any number of channels; (ii) the MAX among the two or three best channels; (iii) the DEC of type 2/3 (and possibly 2/4). In fact, they are able to enhance the detection performance with respect to the best performing single channels with all the considered multi-frequency configurations.

Obviously this performance improvement is paid in terms of computational load since the data from N FM radio channels should be contemporaneously processed. However notice that, in our specific case, a significant increase in the number of integrated channels does not yield a further performance improvement since the additional channels have been recognized to yield poorer characteristics. In contrast, in some cases, the addition of those channels can degrade the detection capability. Specifically for the case of the SUM by integrating the 2 best performing channels (MFC2) with a SUM approach, the detection performance is enhanced since the waveforms with the best characteristics is exploited at each acquisition. By considering 3 integrated channels (MFC3) an additional performance improvement is experienced. In contrast, the use of the 4/5-channels configuration (MFC4a, MFC4b, MFC5) yields a significant advantage only in some cases since the considered additional channels (91.3 MHz and 94.3 MHz) have been recognized to yield poorer waveform's characteristics with respect to the other considered radio channels. Nevertheless, further improvement is expected by adding good-performing channels, when available. Similar behaviour is expected for the MAX, when "good channels" are available and for DEC rules not too strict (namely not of the N/N type). In this regard, the capability of automatically selecting the radio frequency channels to be integrated can be of great potential interest

since it allows to achieve the desired detection capability without significantly increasing the number of integrated channels and hence the computational load.

VII.1 *Conclusions*

After demonstrating the problems related with the variability of the characteristics of the waveforms received by PBR, especially when operating in the FM radio band, the concept of the multi-frequency integration has been introduced, aiming at the same time at (i) increasing the global SNR, and (ii) making the detection performance robust with respect to the program content broadcast by the individual radio stations.

Different approaches have been considered for the multi-frequency integration, including decentralized L/N detection, centralized linear detection (SUM), and centralized non-linear detection (MIN, MAX), which have also been provided with adequate CFAR schemes. Appropriate analytical relationships have been derived that allow us to set the adaptive detection threshold so that a predetermined false alarm rate is obtained and the corresponding theoretical detection performance has been compared.

The development of two wide-band PBR prototypes has allowed to validate and compare the multi-frequency approaches that enhance the surveillance capabilities of the PBR. Among the integration schemes the best performance is achieved by the decentralized detection 2/3, the centralized non-linear MAX with the best two or three channels, and the centralized linear approach operating with the three or four best channels, together with either a CA-CFAR scheme or a GO-CFAR scheme. These multi-frequency approaches are shown to yield significantly improved detection performance with respect to the single FM radio channels. In fact they always provide better performance than the best single channel (which might change with time). An increase is apparent in the number of target plots sequences that can be detected over temporally spaced data files, with respect to the single channel case. Moreover, the detected plot sequences have been recognized to give a good fitting with standard routes for the Rome Fiumicino airport, thus corresponding to a validated set of real target positions.

VII.2 *Figures*

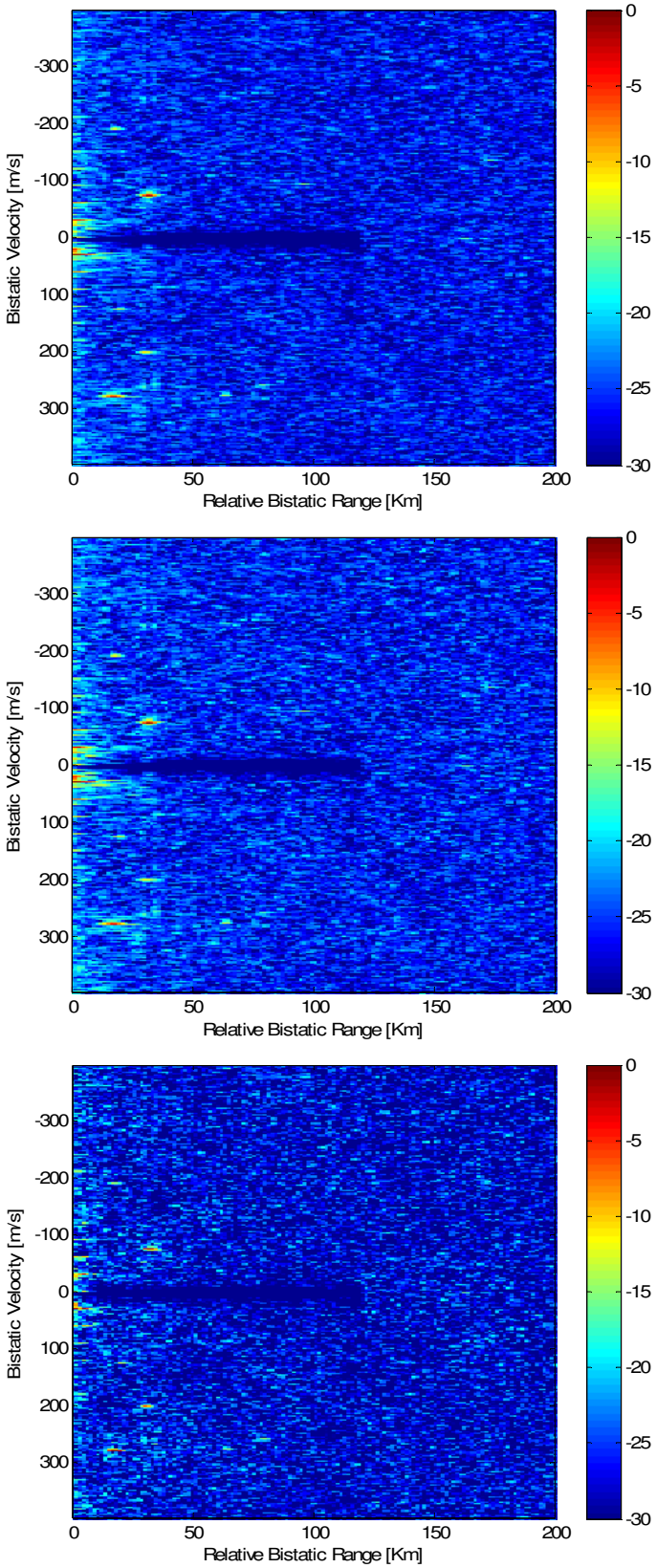

Figure 28 – Range-Velocity maps for the centralized integration strategies obtained using the channels at 89.8 MHz, 92.1 MHz and 93.8 MHz of file pcl_18052007_10.05.42: (a) SUM; (b) MAX; (c) MIN.

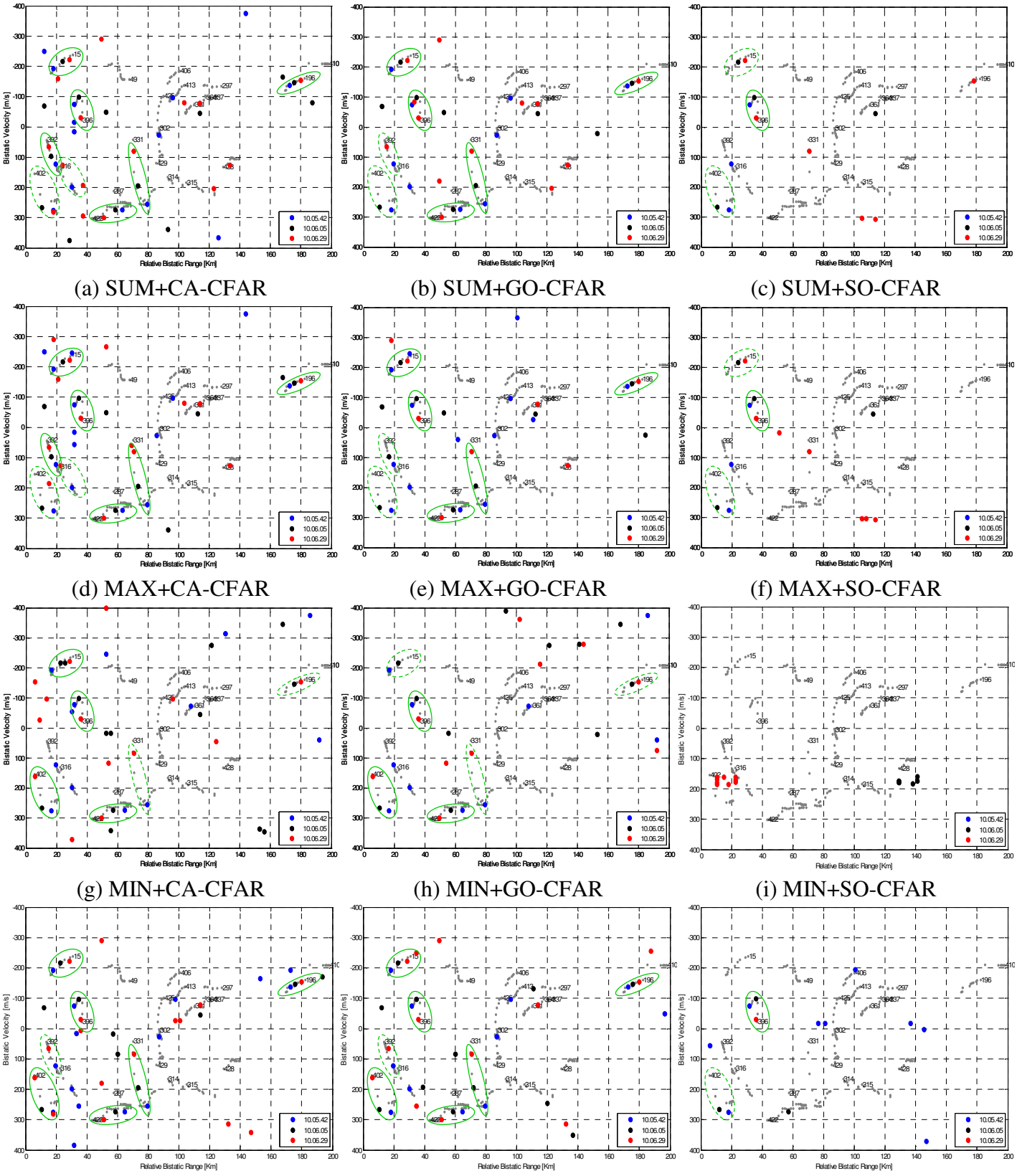

(a) SUM+CA-CFAR (b) SUM+GO-CFAR (c) SUM+SO-CFAR

(d) MAX+CA-CFAR (e) MAX+GO-CFAR (f) MAX+SO-CFAR

(g) MIN+CA-CFAR (h) MIN+GO-CFAR (i) MIN+SO-CFAR

(l) DEC+CA-CFAR (m) DEC+GO-CFAR (n) DEC+SO-CFAR

Figure 29 – Plot sequences in the Range-Velocity maps for the centralized integration strategies obtained using the channels at 89.8 MHz, 92.1 MHz and 93.8 MHz in the 3 subsequent acquisitions ($P_{fa}=10^{-4}$)

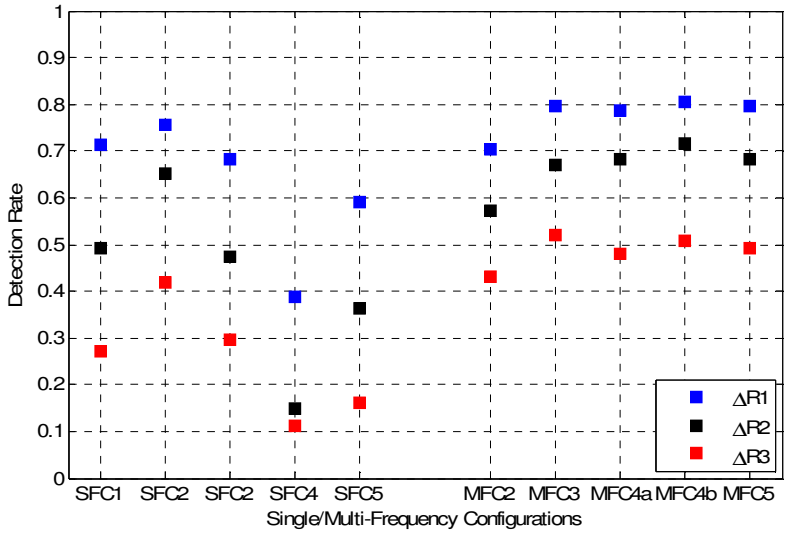

(a)

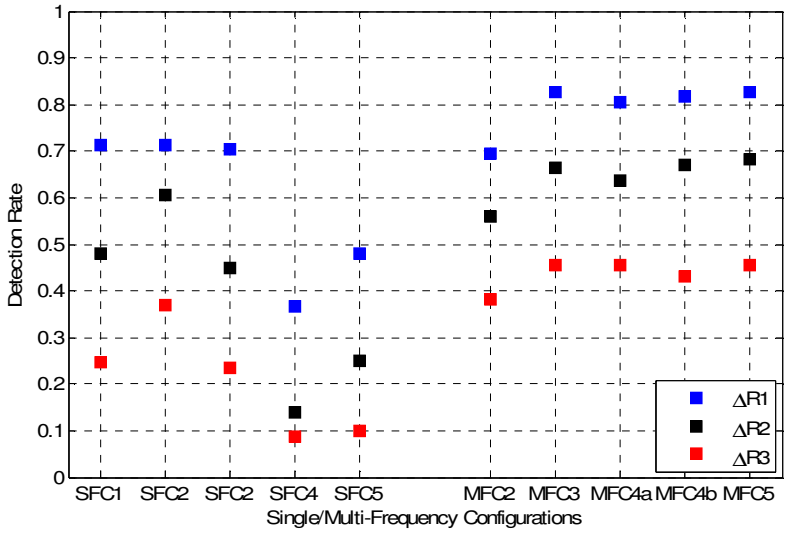

(b)

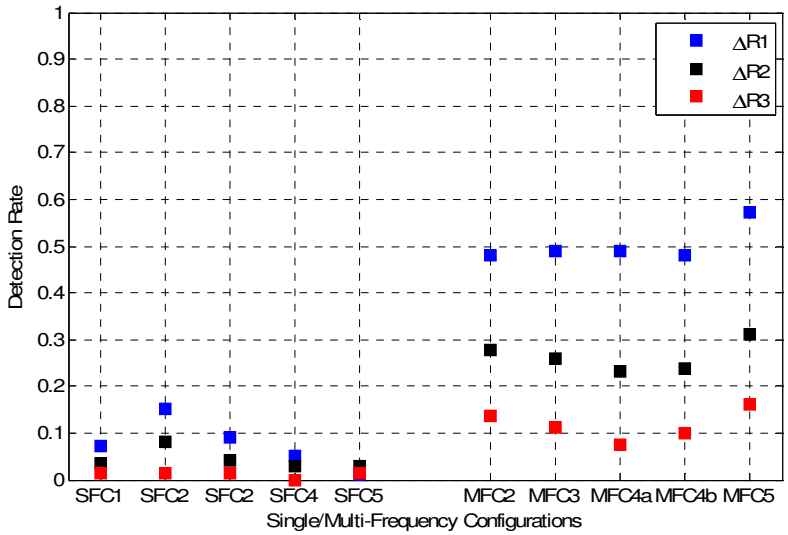

(c)

Figure 30 – Detection performance comparison among the different single frequency channels (SFC1-5) and the decentralized integration strategies (for MFC2-5) for $P_{fa}=10^{-3}$ using: (a) CA-CFAR; (b) GO-CFAR; (c) SO-CFAR.

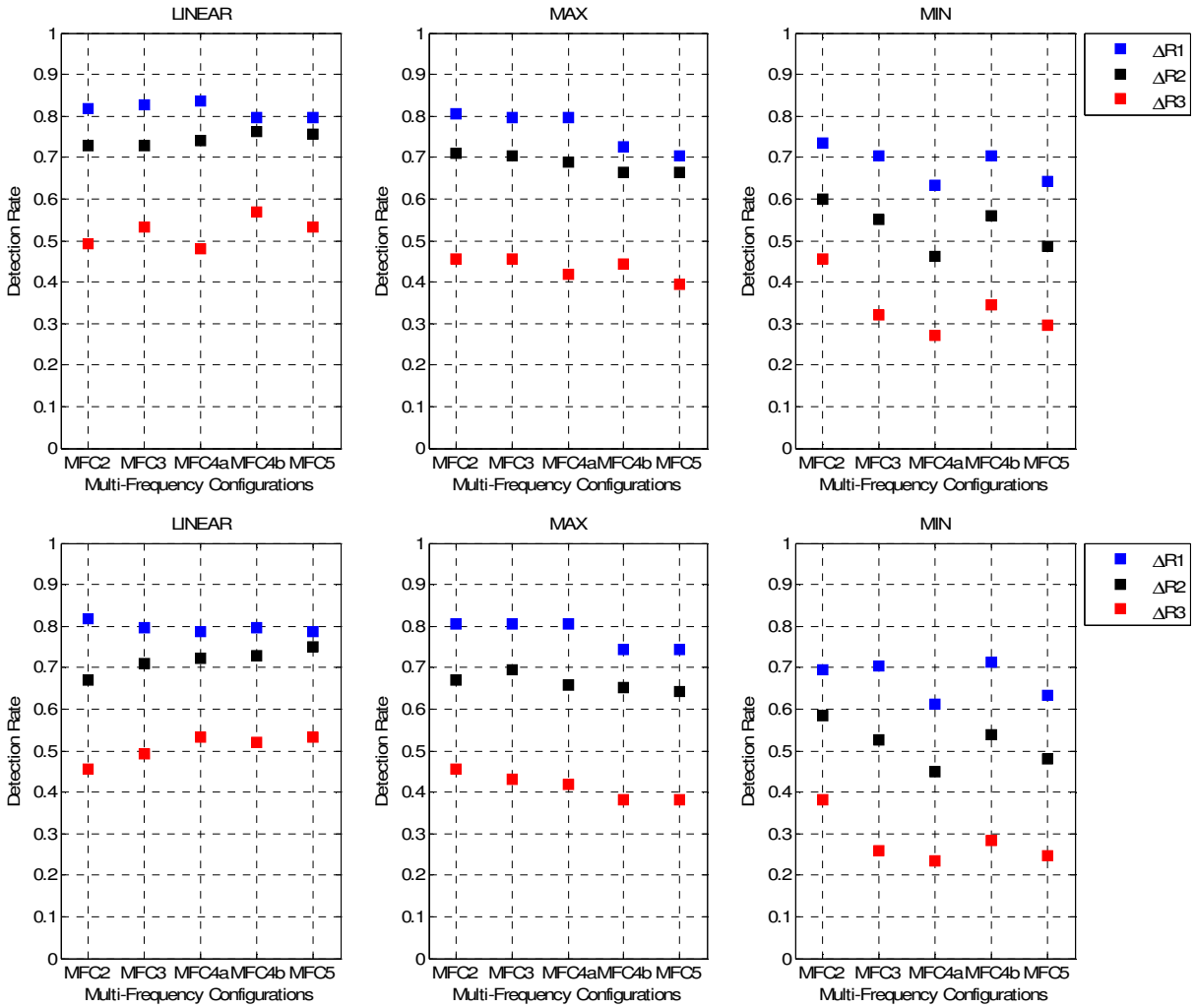

Figure 31 – Detection performance comparison among the different centralized integration strategies (for MFC2-5) for $P_{fa}=10^{-3}$ using: (a) CA-CFAR; (b) GO-CFAR.

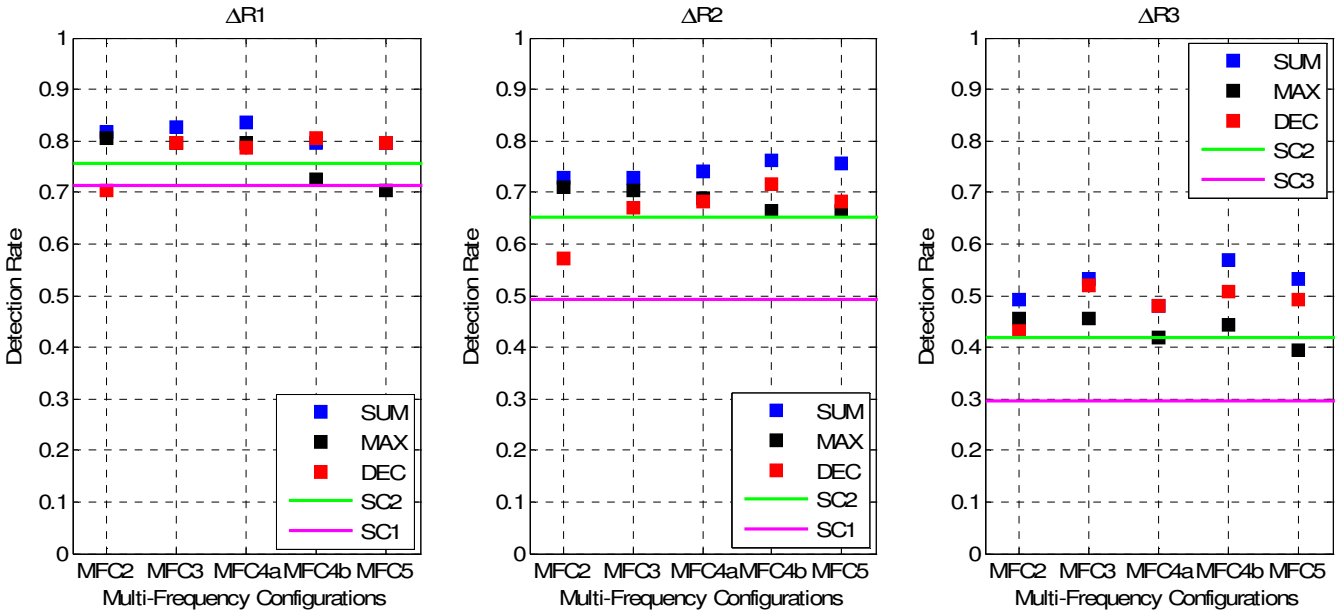

Figure 32 – Detection performance comparison among the best performing integration strategies (for MFC2-5) using a CA-CFAR detection scheme ($P_{fa}=10^{-3}$).

VIII ICS-554B

VIII.1 *Introduction*

The two dual channel prototypes described in the previous sections represent the basis for the development of a new version of a multichannel PBR. In particular, the acquisition of a new device, named ICS-554B, allows the extension of the developed prototypes to a new one with up to four receiving channels. This new device allows the acquisition of data with up to four different antennas, thus offering the possibility to exploit several new receiver configurations: for example, it is possible to set up a receiving configuration with two reference and two surveillance antennas, with different polarizations, thus having a simultaneous acquisition with a couple of antennas (reference and surveillance) in vertical polarization and another couple in horizontal polarization. Moreover, it is possible to have one reference antenna and two (or three) surveillance antennas, aiming at performing not only target detection but also localization (Direction of Arrival – DOA – estimation), and so on. The main features of this new acquisition device are described in the sub-section VIII.2 , while sub-section VIII.3 is dedicated to the description of software programs developed for ICS-554B management. The analysis and tests performed to validate its performance with data acquired with the antennas are reported in sub-section VIII.4 . Sub-section VIII.5 is dedicated to the description of a new acquisition campaign carried on 29th and 30th April 2009 with this new device. Finally, the first results obtained in terms of cancellation and detection capability are reported in sub-section VIII.6 and VIII.7 , respectively.

VIII.2 *ICS-554B main features*

ICS-554B (see Figure 33) is a four channel, 14-bit A/D module in a PCI Mezzanine Card (PMC) format. It has a nominal signal input impedance of 50 Ohms, and conforms to the PCI 2.2 (64-bit, 66 MHz) standard, with Master Burst Mode (DMA) capability. This version (five different versions are available, identified with letters from A to E) has a 105 MHZ maximum sample rate per channel, and a one million gate Field Programmable Gate Array (FPGA). The internal sample clock oscillator is a 100 MHz fixed frequency crystal.

Figure 34 shows a simplified block diagram of the ICS-554B board. The board uses four 14-bit Analog-to-Digital Converters (ADCs), Analog Devices AD6645. The ICS-554 includes a 66 MHz/64-bit PCI bus interface conforming to the PCI 2.2 specification. The PCI interface uses the QuickLogic QL5064 chip to support a master burst transfer (DMA) interface. The ICS-554 can generate PCI bus interrupts at any user-programmed interval (number of samples acquired).

The sampling clock and the trigger can be either internal or external. The internal ADC clock is a crystal oscillator with a fixed frequency of 100 MHz; the external clock signal may be either a TTL level or sinewave signal with a frequency in the range 30 – 100 MHz.

The ADCs can be operated in a number of different modes. In the continuous mode, data is continuously converted on all selected channels and supplied to the PCI Bus interface upon application of a trigger signal, until the acquisition is disabled. In capture mode, a fixed number of samples are acquired upon each application of the trigger. The number of samples acquired at each application of the trigger is programmable with a resolution of four samples per channel or less, up to the maximum capacity of the buffer. The programmable ADC output decimator can reduce the output data rate by a factor of up to thirty-two.

The outputs of the ADCs are applied to a bank of four quad digital down-converter (DDC) modules, which are Graychip GC4016 devices; specifically, each GC4016 module includes four independent DDC channels, thus allowing the simultaneous down conversion of up to 16 arbitrary signal bands (e.g. 16 FM channels) . Note that the ADC outputs are also connected to a Xilinx FPGA for direct processing of the ADC data. A crossbar switch is supplied as standard firmware in the FPGA to enable the user to select either the ADC output or the DDC output, under program control. This FPGA is almost entirely available for user applications, providing a powerful signal processing capability. The ICS-554 also offers 1 MByte of onboard memory storage organized as two independent 0.5 MByte FIFOs, thus

providing for simultaneous wideband and narrowband operation. The PCI interface is PCI 2.2 compatible, providing a fast 64-bit, 66 MHz DMA interface.

The ICS-554 supports coherent sampling on single channels (from trigger interval to trigger interval), across multiple channels on the same board or across multiple boards. The latter capability provides for beam forming and time-of-arrival applications.

ICS-554B technical specifications are summarized in the following:

- four analog input channels (ADCs)
- ADC resolution: 14 bits
- input impedance: 50Ω
- full scale input: 1.2 V_{pk-pk} (about 5.5 dBm)
- input signal bandwidth: 2 ÷ 200 MHz
- internal or external clock and trigger
- maximum sampling rate: 100 MHz for four channel, simultaneous
- minimum sampling rate: 30 MHz for four channel, simultaneous
- internal sample clock oscillator: 100 MHz fixed frequency crystal
- Spurious Free Dynamic Range (SFDR) > 85 dB
- SNR > 71 dB
- user programmable FPGA (one million gates)
- programmable decimation of the ADC data stream
- SMA coaxial connectors
- maximum DDC output bandwidth:
    - 10 MHz (sampling frequency = 100 MHz, four channel output)
    - 5 MHz (sampling frequency = 100 MHz, eight channel output)
    - 2.5 MHz (sampling frequency = 100 MHz, 16 channel output)
- minimum DDC output bandwidth:
    - 4.9 KHz (sampling frequency = 100 MHz, 16 channel output)

The ICS-554 provides the ability to select the number of channels to be used, under software control. From one to four channels may be selected. When one ADC channel is enabled, the ICS-554 stores the data from ADC channel 1 into FIFO 1. The other three channels are unused. When data is read over PCI Bus, only the data for channel 1 will be read. When two ADC channels are enabled, the ICS-554 stores the data from ADC channel 1 into FIFO 1, and the data from ADC channel 3 into FIFO 2. The other two channels are unused. When data is read over PCI Bus, only the data for channels 1 and 3 will be read. When three ADC channels are enabled, the ICS-554 stores the data from ADC channel 1 into FIFO 1, and the data from ADC channels 3 and 4 into FIFO 2. Channel 2 is unused. When data is read over PCI Bus, only the data for channels 1, 3 and 4 will be read. When four ADC channels are enabled, the ICS-554 stores the data from ADC channels 1 and 2 into FIFO 1, and the data from ADC channels 3 and 4 into FIFO 2. When data is read over PCI Bus, data for all four channels will be read.

VIII.2.1 Graychip

As previously mentioned, ICS-554B includes four Graychip GC4016 DDC chips, each containing four identical down-conversion circuits, giving a total of up to 16 individual output channels. A block diagram of a single GC4016 device is shown in Figure 35. The crossbar switch allows the user to route any input source to any downconverter channel. The data inputs to each of the GC4016 chips consist of four independent 14-bit data buses from the ADC outputs, so that any of the output channels may use any of the A/D input channels as its data source.

Each GC4016 output channel can be configured to select and downconvert a signal band from the input data stream centred on a specific input frequency (the IF or tuning frequency).

Each of the four identical down-converters on the DDC chip accepts a real sample rate up to 100 MHz, down-converts a selected IF frequency to zero, filters the signal, decimates the signal rate by a programmable factor ranging from 32 to 16384 and then resamples the channel to adjust the sample rate up or down by an arbitrary factor. The channels on a DDC may be combined to produce wider band and/or oversampled outputs or to process complex input data. The chip contains two user-programmable output filters per path which can be used to arbitrarily shape the received data spectrum. These filters can be used as Nyquist receive filters for digital data transmission. The chip also contains a resampling filter to provide additional filtering and to allow the user complete flexibility in the selection of input and output sample rates. Two downconverter paths can be merged to be used as a single complex input down-conversion circuit. Two paths may also be combined to support wider band output rates or oversampled outputs. Four paths may be combined to support both wider band output and oversampling.

The downconverters are designed to maintain over 115 dB of spur free dynamic range and over 100 dB of out of band rejection. A five stage CIC and 20 bit internal data paths support this high dynamic range digital signal processing requirement. Each downconvert circuit accepts 14-bit inputs and produces 24-bit outputs. The frequencies and phase offsets of the four sine/cosine sequence generators can be independently specified, as can the decimation and filter parameters of each circuit.

Groups of DDC output channels that feed into the same FIFO memory, i.e. the upper or lower 8 downconverter channels must use the same bandwidth (i.e. same decimation factor). Thus the upper 8 downconverter channels may use a different bandwidth than the lower 8 downconverter channels. Each channel can be programmed independently for filter coefficients and input selection, centre (IF) frequency, phase and gain. Each downconverter channel contains three filters in sequence to lowpass filter and isolate the downconverted signal(s), see Figure 36. Users have the option to download filter coefficient sets provided by ICS with the software device drivers for the ICS-554B, or to use their own custom filter coefficients.

The maximum signal bandwidth that can be processed by a single channel is dependant upon the clock frequency, the decimation ratio and the type of filter, or the filter coefficients. By combining channels, the signal bandwidth can be increased, as described below. The GC4016 provides a number of options for combining channels and converting the standard complex data output format to real data. The DDCs in the Graychips contain multichannel mode functionality. The maximum single channel output bandwidth is approximately 2.5 MHz. This output bandwidth can be doubled by combining two channels using the Split-I/Q mode. Four channels may be combined to provide three to four times the single channel output bandwidth. Two channels can be combined to process complex input data, doubling the input bandwidth. Four channels can be combined to both process complex input data and to double the output bandwidth of the chip. Two or four multichannel modes may also be used in the complex to real mode.

Figure 36 illustrates the structure of a single downconverter channel; there are four such downconverters in each of the four DDC chips. A Numerically Controlled Oscillator (NCO) and mixer are used to quadrature downconvert a signal from the tuning frequency to baseband. A positive tuning frequency is normally used to downconvert the signal; however, a negative tuning frequency can be used to invert the output spectrum.

The CIC (Cascade Integrate Comb) filter decimates the inputs from the NCO by a factor N, where N is from 8 to 4096. The inputs have to be scaled before this filter to prevent overflow. This scaling is done in the shift down block indicated in Figure 36: the user must select (via software) the desired values in order to avoid overflow.

Coarse gain is set for each channel in the CFIR register and it can be used to boost the channel's gain by up to 42 dB.

The output of the coarse gain circuit is filtered in the CFIR (Compensating FIR) filter stage. This stage is a 21-tap decimate by 2 filter with programmable 16-bit coefficients. Since this filter decimates by two, a stopband must be created in that portion of the spectrum that would alias into the signal of interest.

The second stage decimate by two filter (Programmable FIR filter – PFIR) is a 63-tap decimate-by-2 filter with programmable 16-bit coefficients. Fine gain is applied at the output of the PFIR and rounded to 24 bits. Overflows are detected and hard limited. Overflows can be directed to the channel overflow detection block. The PFIR filter passband must be flat in the region of the signal of interest, and have the desired out of band rejection in the region that will alias into the signal's bandwidth after decimation. The externally downloaded coefficients can be used to tailor the spectral response to the user's needs. For example, it can be programmed as a Nyquist (typically a root-raised-cosine) filter for matched filtering of digital data. The user downloaded filter coefficients are 16 bit 2's complement numbers.

The resampler will independently filter and change the data rate of each channel. The most common application of the resampler is to increase the sample rate of the data so that it will match a desired symbol or bit rate. It can also be used as an additional filter to optimize the passband or stopband response of the channel.

VIII.3 *Software for ICS-554B management*

Proper software programs (in Matlab and C) have been developed for ICS-554B management. These programs can be divided in two main groups:

- data acquisition;
- data reading and conversion.

Software for data acquisition allows the definition of the following main parameters (some directly related to device functioning, some to the desired acquisition):

- *acquisition duration*, refers to the duration of a single acquisition, resulting in a new data file stored (the approach is the same already described for dual channel prototypes, were consecutive acquisition of about 1.15 sec duration were performed)

- *total acquisition duration*, refers to the total amount of time covered by data acquisition. During this time, several acquisition can be performed, each one of duration specified by the *acquisition duration* parameter; time between two consecutive acquisitions can be specified directly by user, or can be directly related to the time necessary for data storage, so that an acquisition in performed, acquired data are written in a file (data saving), and a new acquisition is then immediately performed. Obviously, due to the onboard Digital Down-Conversion (and decimation) capability, the amount of data for single acquisition can be highly reduced with respect to the whole FM bandwidth acquisition, so that the time between two consecutive acquisitions can be widely reduced with respect to 23-25 seconds necessary with the NI PXI-5122 based prototypes.

- *ADC sampling frequency*

- *DDC decimation factor*, refers to the desired final sampling rate, that is the rate of the output data flow per DDC channel, (e.g. 200KS/s for FM channels); this parameter is obviously directly related to the specified *ADC sampling frequency*

- *clock*, can be internal or external, and represents the reference for sampling rate and system synchronization. If internal, the *ADC sampling frequency* value is fixed to 100MHz, if external, sampling rates depends on the specified value and on the characteristics of the used external clock. In this case, as for the dual channel wide-band prototypes, NI PXI-5404 (see sub-section V.1.2) has been used as clock generator

- *number of used input (ADC) channels*, from one to four

- *number of desired output (DDC) channels*, up to 16, as previously described. It is also possible to specify if the DDCs will be used in the acquisition or not. For example, to perform the acquisition of the whole FM bandwidth, a solution is to exclude the DDCs from the acquisition process, and to store the signals after ADC. This possibility has been also investigated during tests, as described in the following.

- *correspondence between input (ADC)channels and output (DDC) channels, list of desired output frequency channels*; these two parameters are directly related each other, and are used to completely define each specific data acquisition in terms of input signals (receiving antennas) and output channels. For example, let us assume to perform an acquisition with two input channels (reference and surveillance antennas) and 16 output FM radio channels (obviously divided in two groups, 8 FM channels for the reference antenna and the 8 FM channels – i.e. frequencies – for the surveillance antenna). By indicating the ICS-554B ADC input channels with capital letters *A*, *B*, *C* and *D*, assume, without loss of generality, to connect the reference and surveillance antennas to channels *A* and *B*, respectively. The desired 8 output FM radio frequencies are indicated with lowercase letters from *a* to *h*. In order to set the correspondence between input channels and output radio frequencies, we need to define the physical path of the sampled input signals (after ADCs) through the device, specifically through the four Graychip chips and through the four down-conversion paths inside each Graychip. This correspondence can be easily achieved by defining two strictly related maps, named *tuning frequency map* and *input selection map*. In the considered example, if we want to use the first two DDC modules to extract the 8 FM radio channels from the reference antenna input and the two remaining DDCs for the 8 FM channels from the surveillance antenna, the two masks will be defined as follows:

tuning frequency map	a	b	c	d	e	f	g	h	a	b	c	d	e	f	g	h
input selection map	A	A	A	A	A	A	A	A	B	B	B	B	B	B	B	B

It is easy to understand that the first four instances of the two maps refer to the four down-conversion circuits of the first Graychip, the following four to the second one, and so on. Due to the presence of a crossbar switch in each Graychip module (see Figure 35), different association maps can be defined with reference to the same acquisition, also by sending two or more input channels (A, B, …) to the same DDC. So, for example, the following masks are allowed:

tuning frequency map	a	b	a	b	c	d	c	d	e	f	e	f	g	h	g	h
input selection map	A	A	B	B	A	A	B	B	A	A	B	B	A	A	B	B

tuning frequency map	a	b	c	d	a	b	c	d	e	f	g	h	e	f	g	h
input selection map	A	A	A	A	B	B	B	B	A	A	A	A	B	B	B	B

If more than two inputs antennas are used, obviously the maximum number of FM radio channels that can be extracted for each input is reduced. For example, by using four antenna (one as reference and three for surveillance, or different combinations), it is easy to understand that the maximum allowed number of radio channels per input is four (*a*, *b*, *c* and *d*). In this case, a typical tuning frequency/input selection map can be one of the following:

tuning frequency map	a	b	c	d	a	b	c	d	a	b	c	d	a	b	c	d
input selection map	A	A	A	A	B	B	B	B	C	C	C	C	D	D	D	D

tuning frequency map	a	a	a	a	b	b	b	b	c	c	c	c	d	d	d	d
input selection map	A	B	C	D	A	B	C	D	A	B	C	D	A	B	C	D

or different combinations.

A key point in the acquisition software architecture is that each consecutive acquisition produces the storage of a single file, independently by the selected configuration (number of ADC input channels, use/not use of DDCs, number and frequency of extracted FM channels, and so on). Referring to previous examples, each stored binary file for acquisition will contain the data flow of all the 16 down-converted FM radio channels, acquired with two or more antennas. Files relative to consecutive acquisitions of the same system configuration are stored in a folder named with date and hour of acquisition starting (e.g. PBR_yyyymmdd_hhmmss), and are identified by a sequential number (e.g. PBR_DDC_001, PBR_DDC_002, and so on, where DDC identificates that in the considered configuration DDCs are used). In the same folder an *info-file* is also stored, that contains important information common to all the acquisitions performed in the same system configuration. In particular, the following information is stored in this *info-file*:

- *acquisition time*: date and time, the same of the folder
- *acquisition duration*
- *number of used input (ADC) channels*
- *ADC sampling frequency*
- *DDC sampling frequency*, that is the final sampling rate of output data (extracted FM radio channels)
- *correspondence between input (ADC)channels and output (DDC) channels, list of desired output frequency channels*

As it is apparent, this information is essential to correctly identify main acquisitions' characteristics and also for the following steps, consisting in data reading and conversion.

Software for data reading and conversion, implemented in Matlab, allows the extraction of data flows relative to all the down-converted FM radio channels from each file stored for single acquisition, according to information contained in the *info-file*. In particular, binary data are properly scaled according to the device vertical range (1.2 V_{pk-pk}) and storage characteristics (for example, during data acquisition and file creation, output samples with 24 bits length are stored with a 4 bytes – 32 bits – actual memory allocation, thus resulting in a padding of least significant 8 bits with all ones: this padding obviously modifies the actual value of the acquired sample, but this effect is known by ICS-554B operating manual and can be easily corrected by simply dividing each sample by 2^8). At the end of the file reading and conversion process, a matrix is created which has as many rows as the number of FM radio channels acquired (16 in the acquisition examples described above); the sequence of FM radio channels inside this matrix, i.e. the row where each extracted FM radio channel is placed, exactly matches the tuning frequency/input selection map.

This matrix represents the starting point for the following analysis and for the application of PBR processing (disturbance cancellation, 2D-CCF evaluation, etc.) to acquired data.

VIII.4 *Tests and controlled experiments*

As it is apparent from the previous description, the presence of four DDC modules in the ICS-554B allows the acquisition of single FM channels of interest (obviously the same considerations apply to different waveforms of opportunity, depending on the signal bandwidth), with a final sampling rate much lower than the value needed in order to sample the whole FM bandwidth (20 MHz, from 88 to 108 MHz). And this is one of the main differences with respect to the acquisition device, namely the A/D converter, used in the dual channel prototypes described in section V : it is now possible to acquire directly the FM channels of interest, thus reducing the final sampling rate up to 200 KS/s (and correspondingly the data flow to be managed), instead of acquiring the whole FM bandwidth at a higher sampling rate and then extracting via software (off-line) the single FM channels of interest. This capability is obviously very important for the realization of a real-time PBR system.

As already described for the two dual channel prototypes (see Appendix E in section V) several tests were performed in controlled situations also with ICS-554B, aiming at verifying the device compliance to its specifications (analysis without useful signals in input) and at the characterization of the channel decorrelation, in order to evaluate the theoretical disturbance cancellation capability achievable with this new receiver (single antenna acquisitions).

VIII.4.1 Noise power evaluation

As already described in Section V , a proper characterization of thermal noise power in the device channels is very important both for the verification of system compliance to its specification and for the following evaluation of system theoretical cancellation capability, which is strictly related to correlation coefficient ρ (see equation V.12), and therefore to SNR.

Main goal of this analysis was the identification of possible system anomalies introduced by:

- systematic disturbance (bias) due to A/D conversion;
- data scaling (decimation factors are programmed via software by user);
- data conversion (from a single file per acquisition to a matrix with as many rows as the number of FM radio channels acquired – see sub-section VIII.3);
- use of shielded cables;

- intermodulation products due to external clock;
- decorrelation effects due to the physical paths of acquired signals inside the device.

Different configurations have been considered in this analysis, and different acquisitions for the same configuration have been performed, also in different days, in order to exclude the possible effects of other factors (for example the device temperature): as expected, there is no impact of such factors in the device performance.

Two ADC input channels (*A*, *B*, *C* or *D*) are selected in each acquisition, the first one is associated with the first two ICS-554B Graychips (8 output channels, numerated from 1 to 8), the second one to the remaining two Graychips (8 output channels, numerated from 9 to 16), with a mask of this type:

tuning frequency map	a	b	c	d	e	f	g	h	a	b	c	d	e	f	g	h
input selection map	A	A	A	A	A	A	A	A	B	B	B	B	B	B	B	B

Output channels are selected so as to span the whole FM frequency bandwidth, 88 ÷ 108 MHz, with steps of 0.5 MHz.

All the test acquisitions described in the following were performed using the signal from NI PXI-5404 (see sub-section V.1.2 in Appendix D) as Clock Generator. Two different configurations have been considered for noise power evaluation: with nothing connected to device input SMA-connectors, except for a 50Ω impedance, and only with the short shielded cables (plus the same 50Ω impedance) used in real data acquisitions to connect the 25mt cables to ICS-554B (the presence of these short cables is due to the difference of connectors between antenna cables – BNC – and ICS-554B input channels – SMA). As previously indicated, the comparison between these two configurations aimed at evaluating the possible presence of system anomalies introduced by shielded cables. Measured noise powers with shielded cables are reported in Table 12, while Table 13 reports values obtained without cables. In both the tables also the date and time of each acquisition is indicated. The change of input channel pair in the acquisitions without shielded cables (from A-B, C-D to A-D, B-C) is simply due to the physical impossibility to close simultaneously two adjacent input channels with 50Ω impedances.

As it is apparent by the comparison between the two tables, the presence of shielded cables does not introduce anomalies in measured values. Obtained values oscillate from -61 and -81 dBm, but this high variation is mainly due to a specific frequency, 88MHz; this possible anomaly has been further investigated, as will be described in the following. Differences up to 5 dBm can be observed between two selected input channels, for the same output frequency, but these differences are not systematically present in the performed analysis, so that seem to be random.

		CHANNEL A 1-8	CHANNEL B 9-16		CHANNEL C 1-8	CHANNEL D 9-16
Frequency		**Pow_in (dBm)**			**Pow_in (dBm)**	
88 MHz [24 MHz]	29/09/2008 13.20	-68.60	-64.99	29/09/2008 13.29	-61.88	-68.40
88,5 MHz [23,5 MHz]		-78.60	-72.83		-74.26	-77.61
89 MHz [23 MHz]		-79.00	-72.94		-74.58	-77.90
89,5 MHz [22,5 MHz]		-79.29	-73.03		-74.94	-78.25
90 MHz [22 MHz]		-79.44	-73.07		-75.34	-78.58
90,5 MHz [21,5 MHz]		-79.49	-73.13		-75.80	-78.85
91 MHz [21 MHz]		-79.41	-73.20		-76.11	-78.87
91,5 MHz [20,5 MHz]		-79.33	-73.34		-76.28	-78.69
92 MHz [20 MHz]	29/09/2008 13.21	-77.65	-72.15	29/09/2008 13.29	-75.82	-77.99
92,5 MHz [19,5 MHz]		-78.84	-73.45		-76.27	-78.01
93 MHz [19 MHz]		-78.74	-73.70		-76.18	-77.71
93,5 MHz [18,5 MHz]		-78.62	-73.95		-76.03	-77.35
94 MHz [18 MHz]		-78.55	-74.10		-75.83	-76.94
94,5 MHz [17,5 MHz]		-78.13	-73.98		-75.61	-76.47
95 MHz [17 MHz]		-77.51	-73.69		-75.43	-76.09
95,5 MHz [16,5 MHz]		-76.55	-73.29		-75.38	-75.91
96 MHz [16 MHz]	29/09/2008 13.22	-75.26	-72.87	29/09/2008 13.29	-74.96	-76.07
96,5 MHz [15,5 MHz]		-75.20	-73.26		-75.70	-76.77
97 MHz [15 MHz]		-75.39	-73.67		-75.86	-77.27
97,5 MHz [14,5 MHz]		-75.94	-73.90		-75.74	-77.56
98 MHz [14 MHz]		-76.39	-73.77		-75.25	-77.43
98,5 MHz [13,5 MHz]		-76.61	-73.45		-74.50	-76.92
99 MHz [13 MHz]		-76.64	-73.05		-73.52	-76.14
99,5 MHz [12,5 MHz]		-76.81	-72.87		-72.66	-75.33
100 MHz [12 MHz]	29/09/2008 13.23	-76.91	-72.60	29/09/2008 13.30	-71.73	-74.51
100,5 MHz [11,5 Hz]		-78.03	-73.16		-71.82	-74.48
101MHz [11 MHz]		-78.65	-73.43		-71.99	-74.52
101,5 MHz [10,5 MHz]		-79.07	-73.62		-72.41	-74.75
102 MHz [10 MHz]		-79.47	-73.79		-73.09	-75.23
102,5 MHz [9,5 MHz]		-79.59	-73.77		-73.92	-75.78
103 MHz [9 MHz]		-79.57	-73.83		-74.77	-76.34
103,5 MHz [8,5 MHz]		-79.46	-73.97		-75.62	-76.80
104 MHz [8 MHz]	29/09/2008 13.25	-75.91	-70.39	29/09/2008 13.30	-73.29	-75.23
104,5 MHz [7,5 MHz]		-79.63	-74.99		-76.89	-77.15
105 MHz [7 MHz]		-79.58	-75.40		-77.15	-76.85
105,5 MHz [6,5 MHz]		-80.08	-76.15		-77.27	-76.63
106 MHz [6 MHz]		-80.14	-76.39		-77.00	-76.05
106,5 MHz [5,5 MHz]		-80.08	-76.38		-76.52	-75.42
107 MHz [5 MHz]		-79.75	-76.08		-75.87	-74.88
107,5 MHz [4,5 MHz]		-79.30	-75.59		-75.39	-74.47
108 MHz [4 MHz]	29/09/2008 13.26	-78.84	-74.41	29/09/2008 13.30	-74.63	-73.99

Table 12 – Measured noise power levels with shielded cables

		CHANNEL A 1-8	CHANNEL D 9-16		CHANNEL B 1-8	CHANNEL C 9-16
Frequency		**Pow_in (dBm)**			**Pow_in (dBm)**	
88 MHz [24 MHz]	**01\10\2008 10.31**	-74.98	-71.09	**01\10\2008 10.26**	-69.52	-72.08
88,5 MHz [23,5MHz]		-78.36	-75.71		-77.43	-78.53
89 MHz [23 MHz]		-78.44	-76.07		-77.65	-78.42
89,5 MHz [22,5MHz]		-77.92	-75.90		-77.87	-78.42
90 MHz [22 MHz]		-76.82	-75.02		-77.97	-78.36
90,5 MHz [21,5MHz]		-75.51	-73.75		-78.05	-78.40
91 MHz [21 MHz]		-75.35	-73.68		-78.14	-78.54
91,5 MHz [20,5MHz]		-76.36	-74.71		-78.31	-78.85
92 MHz [20 MHz]	**01\10\2008 10.31**	-77.06	-74.86	**29/09/2008 17.38**	-76.78	-77.19
92,5 MHz [19,5MHz]		-78.44	-76.24		-77.14	-78.12
93 MHz [19 MHz]		-78.94	-76.51		-77.01	-78.46
93,5 MHz [18,5 MHz]		-79.35	-76.82		-76.75	-78.59
94 MHz [18 MHz]		-79.66	-77.12		-76.35	-78.52
94,5 MHz [17,5MHz]		-79.72	-77.30		-75.85	-78.23
95 MHz [17 MHz]		-79.27	-77.11		-75.24	-77.76
95,5 MHz [16,5 MHz]		-78.30	-76.59		-74.57	-77.13
96 MHz [16 MHz]	**01\10\2008 10.31**	-76.96	-76.02	**01\10\2008 10.27**	-74.64	-76.81
96,5 MHz [15,5MHz]		-76.96	-76.28		-74.27	-76.53
97 MHz [15 MHz]		-77.64	-77.06		-73.69	-75.87
97,5 MHz [14,5MHz]		-78.80	-77.98		-73.40	-75.47
98 MHz [14 MHz]		-79.75	-78.33		-73.42	-75.35
98,5 MHz [13,5MHz]		-80.15	-78.02		-73.86	-75.60
99 MHz [13 MHz]		-80.58	-77.74		-74.41	-75.92
99,5 MHz [12,5MHz]		-81.06	-77.73		-75.28	-76.46
100 MHz [12 MHz]	**01\10\2008 10:30:23**	-81.00	-77.49	**01\10\2008 10.28**	-75.67	-76.52
100,5MHz[11,5MHz]		-80.79	-77.09		-76.52	-77.04
101MHz [11 MHz]		-79.81	-75.99		-77.00	-77.18
101,5 MHz[10,5MHz]		-79.17	-75.30		-77.38	-77.29
102 MHz [10 MHz]		-79.39	-75.62		-77.64	-77.35
102,5 MHz [9,5MHz]		-79.39	-75.77		-77.95	-77.48
103 MHz [9 MHz]		-78.89	-75.38		-78.21	-77.60
103,5 MHz [8,5MHz]		-78.03	-74.61		-78.57	-77.90
104 MHz [8 MHz]	**01\10\2008 10.30**	-73.33	-70.67	**01\10\2008 10.28**	-74.79	-74.95
104,5 MHz [7,5MHz]		-77.28	-74.35		-79.18	-78.45
105 MHz [7 MHz]		-77.24	-74.54		-79.26	-78.31
105,5 MHz [6,5 MHz]		-77.88	-75.02		-79.49	-78.61
106 MHz [6 MHz]		-78.51	-75.39		-79.50	-78.44
106,5 MHz [5,5MHz]		-79.10	-75.78		-79.47	-78.24
107 MHz [5 MHz]		-79.60	-76.17		-79.27	-77.92
107,5 MHz [4,5MHz]		-80.37	-76.88		-79.05	-77.78
108 MHz [4 MHz]	**01\10\2008 10.29.53**	-80.67	-77.03	**01\10\2008 10.28**	-77.24	-76.76

Table 13 – Measured noise power levels without shielded cables

As previously indicated, even if most of obtained values are well in line with theoretical expectations, the above analysis shows the presence of a possible anomaly in correspondence of the frequency 88

MHz, where measured noise power levels are quite high. A similar behaviour is observed also for 104 MHz, even if with a lower difference with respect to other frequencies. Aiming at further investigating the reasons of these high values, an extensive analysis has been performed by evaluating the frequency power spectrum of the 16 200 KHz output-channels extracted in each acquisition, again spanning the whole FM bandwidth. This analysis showed, for the same considered output channel frequency, a similar behaviour between the sub-channels (DDC paths) associated to different input channels. For example, referring to input configuration with ADC channels *A* and *D*, Figure 37 shows the power spectrum of the 200 KHz output channel centered on the frequency 88 MHz, extracted with the first sub-channel (the first path inside the first DDC). As it is apparent, a *spike* is present in the power spectrum, with a shape similar to a sinusoidal tone, located at about -6.5 KHz with respect to center frequency. Same behaviour has been observed for the 9th sub-channel (i.e. the first path inside the third DDC), which is used to extract a 200 KHz channel centered around the same frequency, but with the *D* ADC input channel.

The same happens for the frequency 104 MHz, again for sub-channels 1 and 9 (first path inside first and third DDC, respectively); in particular, Figure 38 shows the power spectrum of the 200 KHz output channel centered around the frequency 104 MHz, extracted with the 9th sub-channel, in the configuration with input ADC channels *B* and *C* (so input *C* is associated to DDC output channels from 9 to 16). As in the previous example, a sinusoidal tone appears in the power spectrum, located at about 13 KHz with respect to center frequency.

Thermal noise is expected to show an uniform spectral distribution for all the considered frequencies, while the spikes in Figure 37 and Figure 38 indicate a not uniform behaviour. Figure 39 shows the histogram of the 200 KHz output channel centered on the frequency 104 MHz, extracted with the 9th sub-channel (ADC input channel *C*): as it is apparent, the histogram has the shape of a Rice function, defined as:

$$p_s(r) = \frac{r}{\sigma^2} e^{-\frac{(A^2+r^2)}{2\sigma^2}} \cdot I_o\left(\frac{rA}{\sigma^2}\right) u_{-1}(r) \qquad \text{(VIII.1)}$$

where

- $r = \sqrt{x^2 + y^2}$ is the modulus of random variables x and y, which represent the independent non-zero-mean Gaussian low-frequency analog components of thermal noise (as if an additional signal component is added to thermal noise),
- σ^2 is the variance of these variables,

- I_0 is the modified Bessel function of the first kind with order zero,
- A is the signal amplitude.

From theoretical considerations we expected a Rayleigh distribution of acquired data (see Figure 41), due to the absence of useful signals in input to the system, which is defined as

$$p_r(r) = \frac{r}{\sigma^2} e^{\frac{-r^2}{2\sigma^2}} u_{-1}(r) \qquad \text{(VIII.2)}$$

where

- random variable r is given by: $r = \sqrt{x^2 + y^2}$, and is the modulus of random variables x and y, which represent the independent zero-mean Gaussian low-frequency analog components of thermal noise,
- σ^2 is the variance of these variables.

Figure 40 and Figure 42 show the power spectra of different frequency channels (91.5 and 97 MHz, respectively): as it is apparent, these spectra are in line with theoretical expectations or are characterized by a reduced presence of spikes.

Then the same frequency channel was extracted with all the 16 DDC sub-channels, obtaining the same power spectra, thus yielding to the conclusion that the presence of an additional signal is strictly dependant by the extracted frequency channel. Aiming at further investigating this hypothesis, a wide-bandwidth spectral analysis was carried on, as described in the following.

Aiming at acquiring and storing the whole FM frequency bandwidth (20 MHz), the four Graychip (and hence the DDCs) were excluded by the receiving chain. The main difference with respect to the previously described acquisition is that now, after a direct RF sampling, sampled data are directly sent to the two FIFO memories of ICS-554B, and then stored. The acquisitions performed in this receiver configuration are referred to as *wide-band* acquisitions. Different sampling frequency values have been selected during this analysis: 35, 45, 56, 72 and 100 MHz. Wide-band acquisition have a shorter duration (about 0.5 sec) due to greater amount of data to be stored for a single acquisition (for example, a 0.5 sec acquisition at a sampling frequency of 56 MHz produces 28 millions of samples – 56 MB of data due to 14 bit/sample resolution) to be stored. This analysis aimed at verifying if the presence of the previously described spurious was due to DDCs or to different components of the receiving chain, as for example the external clock or the ADCs.

Figure 43 and Figure 44 show the *wide-band* power spectra obtained with 56 MHz and 72 MHz sampling frequencies, respectively. As it is apparent, the presence of several spikes in both the figures indicates that the DDCs are not directly responsible for the introduction of such distortions.

A new hypothesis made to explain the presence of these spurious was that they were produced by distortions due to intermodulation products of the (external) Clock Generator used to select the desired sampling frequency. So, new *wide-band* acquisitions were performed, by using the same Clock Generator (NI PXI-5404), and the NI PXI-5122 as A/D converter; this device does not allow the selection of the same V.R. used in the ICS-554B ADCs, so the nearest value (1 V_{pk-pk}, see Section V.1) was selected. Same values for acquisition duration (0.5 sec) and sampling frequencies were used.

Figure 45 and Figure 46 show the *wide-band* power spectra obtained with 56 MHz and 72 MHz sampling frequencies, respectively. As it is apparent, in this case the obtained distributions are well in line with expectations (except for the presence of two small spikes with sampling frequency equal to 56 MHz, located at ±14 MHz, see Figure 45), thus excluding the Clock Generator as source of the distortions experienced with ICS-554B.

VIII.4.2 Single antenna acquisitions

As already described for the dual-channel prototype tests and controlled experiments (see sub-section V.2.2), single antenna acquisitions have been performed also with ICS-554B aiming at evaluating the theoretical maximum cancellation level that can be obtained. Specifically, single antenna acquisitions have been performed both with the reference and the surveillance antenna (pointing of the two antennas is sketched in Figure 19 and Figure 20, respectively).

Due to the fixed V.R. of ICS-554B (1.2 V_{pk-pk}, corresponding to maximum RF input power of about 5.5 dBm), a splitter was inserted in the receiving chain during the single surveillance antenna acquisitions, while 3 splitters have been used during the single reference antenna acquisitions, because reference antenna is directly pointed towards the opportunity transmitters located in Monte Mario and Vatican City, thus resulting in a quite high received power. The presence of the splitters in the receiving chain also allowed us to acquire simultaneously with ICS-554B and with the dual-channel A/D converter (NI PXI-5122), in order to perform a performance comparison with a device already tested. Also in this case, the NI PXI-5122 V.R. was set to 1 V_{pk-pk} (about 4 dBm maximum input RF power) in order to perform an effective comparison between the two devices.

A detailed analysis of the data in both temporal and spectral domain in the considered scenario, suggested the selection of 8 FM radio channels inside the available frequency bandwidth, transmitted by Monte Mario or Vatican City, see Table 14.

Frequency (MHz)	**FM radio broadcast**	**Transmitter**
89.7	RAI Radio Uno	Monte Mario
93.3	Radio Vaticana	Vatican City
96.3	Radio InBlu	Vatican City
98.7	Virgin Radio	Monte Mario
100.3	RAI Auditorium	Monte Mario
102.4	Radio Radicale	Monte Mario
103.8	Radio Vaticana	Vatican City
105.0	Radio Vaticana One O Five	Vatican City

Table 14 – Selected FM radio channels for ICS-554B single antenna acquisitions.

Input signal was sent to different pairs of ICS-554B ADC input channels (*A*, …, *D*) according to the following association mask, where letters *a, b, …, h* represent the 8 FM channels of Table 14.

tuning frequency map	a	b	c	d	e	f	g	h	a	b	c	d	e	f	g	h
input selection map	A	A	A	A	A	A	A	A	B	B	B	B	B	B	B	B

Table 15 reports the cancellation values obtained for single antenna acquisitions performed with the reference antenna (in the scenario sketched in Figure 19). Each acquisition has a temporal duration of 1 sec, and an input (ADC) sampling frequency of 56 MHz. For sake of brevity, and without loss of generality, only the results obtained with three pairs of input channels (*A-B, B-C, C-D*) are shown.

Each table rows reports the vertical range and the following values:

- SNR values on the two channels
- theoretical cancellation value, obtained according to equation V.12
- measured cancellation value, evaluated as the ratio between the power levels measured, over a 200 kHz bandwidth, at the input and at the output of the cancellation filter.

	FM CH. (MHz)	SNR ChX [dB]	SNR ChY [dB]	CANC THEO [dB]	CANC MEAS [dB]
18112008_14.37.04 A \ B	**93.3**	77.7	77.8	74.7	65.7
	96.3	74.2	74.2	71.2	61.6
	103.8	74.6	74.6	71.6	63.7
	105	78.4	78.4	75.4	67.4
	100.3	59.7	59.8	56.7	48.1
	102.4	64.2	64.3	61.2	53.4
	98.7	51.8	51.8	48.8	36.3
	89.7	56.8	56.8	53.8	40.8
18112008_14.43.13 B\C	**93.3**	77.7	77.7	74.7	66.7
	96.3	74.3	74.2	71.2	61.4
	103.8	74.6	74.6	71.6	64.8
	105	78.4	78.3	75.3	68.2
	100.3	60.0	60.0	57.0	49.8
	102.4	64.1	64.1	61.1	54.3
	98.7	51.8	51.8	48.8	40.1
	89.7	57.1	57.0	54.0	45.0
18112008_14.41.30 C\D	**93.3**	77.7	77.7	74.7	70.1
	96.3	74.2	74.3	71.2	66.3
	103.8	74.5	74.5	71.5	69.0
	105	78.3	78.4	75.3	72.9
	100.3	59.9	60.0	56.9	51.9
	102.4	64.1	64.2	61.1	58.4
	98.7	51.6	51.6	48.6	42.1
	89.7	56.9	57.0	53.9	47.2

Table 15 – single (reference) antenna cancellation values.

Table 16 reports the cancellation values obtained for single antenna acquisitions performed with the surveillance antenna (in the scenario sketched in Figure 20).

As it is apparent, cancellation values obtained with surveillance antenna are in general more similar to corresponding expected values than the values obtained with the reference antenna, for all the considered FM radio channels; this is probably due to the presence, in the receiving chain used for single reference antenna acquisitions, of a three-splitters-cascade, thus resulting in an higher source of decorrelation with respect to the single surveillance antenna acquisitions. Moreover, for both the considered antennas, similar cancellation values are obtained for the same extracted FM radio channel with different ICS-554B input channels; these low differences, being the SNR values always the same for consecutive acquisitions of the same FM radio channel, appear to be related to a random modification (reduction or increase) of the correlation coefficient, for example due to the change in the

transmitted program content. However, these oscillations are not directly related to a malfunctioning of a specific device input channel.

	FM CH. (MHz)	SNR ChX [dB]	SNR ChY [dB]	CANC THEO [dB]	CANC MEAS [dB]
18112008_12.25.40 *A \ B*	**93.3**	42.0	42.0	39.0	35.3
	96.3	42.1	42.0	39.0	34.1
	103.8	40.2	40.2	37.2	36.5
	105	43.1	43.0	40.0	39.9
	100.3	31.5	31.6	28.5	26.7
	102.4	32.0	32.1	29.1	27.9
	98.7	37.7	37.6	34.6	30.4
	89.7	33.4	33.8	30.6	26.1
18112008_12.36.58 *B \ C*	**93.3**	42.1	42.1	39.1	36.6
	96.3	42.0	42.1	39.0	37.7
	103.8	40.3	40.2	37.2	33.5
	105	43.2	43.0	40.1	37.8
	100.3	31.6	31.5	28.5	26.7
	102.4	32.2	32.0	29.1	25.1
	98.7	37.6	37.6	34.6	32.9
	89.7	33.9	33.9	30.9	26.5
18112008_12.34.55 *C \ D*	**93.3**	42.1	42.1	39.1	38.5
	96.3	42.0	42.2	39.1	38.0
	103.8	40.1	40.0	38.5	38.3
	105	43.2	43.0	42.1	41.5
	100.3	31.5	31.5	29.5	29.2
	102.4	32.1	32.0	31.1	30.3
	98.7	37.6	37.6	34.6	28.6
	89.7	33.8	33.7	30.7	29.7

Table 16 – single (surveillance) antenna cancellation values.

As previously mentioned, the presence of one or more splitters in the receiving chains of these single antenna tests allowed the parallel acquisition of signals with the NI PXI-5122. Cancellation values obtained with reference and surveillance antenna are shown in Table 17 and Table 18, respectively (V.R. = 1 V_{pk-pk}).

It is easy to see that cancellation values obtained with the two different A/D converters are largely comparable.

	FM CH. [MHz]	SNR Ch0 [dB]	SNR Ch1 [dB]	CANC THEO [dB]	CANC MEAS [dB]
18112008_15.35.55	**93.3**	77.6	77.5	74.5	69.1
	96.3	73.9	73.8	70.9	67.2
	103.8	73.6	73.4	70.5	66.2
	105	77.3	77.1	74.2	70.0
	100.3	59.3	59.2	56.2	45.5
	102.4	63.4	63.2	60.3	56.9
	98.7	51.0	50.9	47.9	40.8
	89.7	56.8	56.7	53.7	48.8

Table 17 – single (reference) antenna cancellation values obtained with NI PXI-5122.

	FM CH. [MHz]	SNR Ch0 [dB]	SNR Ch1 [dB]	CANC THEO [dB]	CANC MEAS [dB]
18112008_12.08.44	**93.3**	41.0	40.9	38.0	35.7
	96.3	42.1	42.0	39.1	36.8
	103.8	40.0	39.8	36.9	34.7
	105	41.0	40.8	37.9	35.7
	100.3	31.1	30.9	28.0	25.8
	102.4	31.7	31.5	28.6	26.4
	98.7	37.3	37.2	34.2	31.8
	89.7	33.0	32.9	29.9	27.7

Table 18 – single (surveillance) antenna cancellation values obtained with NI PXI-5122.

VIII.4.3 Double antenna acquisitions

Similar acquisitions were performed in the same considered scenario, in a double antenna configuration. Surveillance antenna was directly connected to the ICS-554B, while a three-splitters-cascade was again used for the reference antenna, as already described in the previous sub-section.

An extensive analysis was performed in two different days, by acquiring the same 8 FM channels with different pairs of ICS-554B input channels; 15 consecutive acquisitions of 1.15 sec duration (total acquisition duration of about 33 sec, taking into account also the time needed for each acquisition data storage) were performed for each considered pair of input channels. In the following (see Table 19), without loss of generality, only the results obtained considering input channels *A-C* (surveillance-reference antenna), and *D-B* (surveillance-reference antenna), and for two of the 15 consecutive acquisition are shown. Obtained results are indeed largely comparable both in consecutive acquisitions with the same input configuration and between different input channel pairs.

As expected, obtained cancellation values are largely reduced with respect to the corresponding values obtained with single antenna acquisitions: this is obviously due to a great difference in SNR values on the two antennas, which results in lower values (in particular with respect to single reference antenna acquisitions) of theoretical cancellation, and also to sensibly reduced level of correlation between the signals collected with two different and differently pointing antennas with respect to the quasi-ideal scenario represented by a single antenna acquisition.

Also in this case, similar acquisitions were performed with the dual-channel A/D converter (NI PXI-5122); without loss of generality, Table 20 reports the results obtained for a single acquisition. As already seen in the comparison of the single antenna acquisitions, differences of few dBs can be observed for the two considered devices.

	FM CH. (MHz)	SNR ChX Ref [dB]	SNR ChY Rx [dB]	CANC THEO [dB]	CANC MEAS [dB]	N° Acq.
1122008_14.28.47 B (Ref)_D (Surv)	93.3	78.1	46.8	46.8	29.6	I Acq.
	96.3	74.1	44.8	44.8	27.5	
	103.8	73.7	43.4	43.4	16.5	
	105	77.9	48.6	48.6	29.1	
	100.3	59.6	35.1	35.1	24.3	
	102.4	63.8	35.8	35.8	8.2	
	98.7	51.9	42.5	42.0	14.8	
	89.7	56.6	38.5	38.5	24.5	
1122008_14.28.47 B (Ref)_D (Surv)	93.3	78.1	46.8	46.8	28.3	VII Acq.
	96.3	74.2	44.7	44.7	28.3	
	103.8	73.7	43.4	43.4	16.9	
	105	77.9	48.5	48.5	28.9	
	100.3	59.7	35.1	35.1	24.9	
	102.4	63.8	35.9	35.9	7.3	
	98.7	51.8	42.5	42.0	14.7	
	89.7	56.5	38.5	38.4	25.0	
18112008_14.54.56 C (Ref)_A (Surv)	93.3	77.7	44.8	44.8	26.1	IV Acq.
	96.3	74.2	44.7	44.7	27.3	
	103.8	74.5	42.2	42.2	17.9	
	105	78.4	47.7	47.7	30.6	
	100.3	59.8	34.8	34.8	26.1	
	102.4	64.3	34.4	34.4	9.1	
	98.7	51.8	41.0	40.7	14.8	
	89.7	56.8	37.2	37.2	24.8	
18112008_14.54.56 C (Ref)_A (Surv)	93.3	77.7	44.6	44.6	25.5	XV Acq.
	96.3	74.3	44.8	44.8	28.5	
	103.8	74.5	42.2	42.2	19.0	
	105	78.3	47.7	47.7	31.3	
	100.3	60.0	34.5	34.5	26.3	
	102.4	64.2	34.9	34.9	9.3	
	98.7	51.8	41.0	40.6	14.5	
	89.7	56.9	37.2	37.2	24.9	

Table 19 – double antenna cancellation values obtained with ICS-554B.

	FM CH. (MHz)	SNR ChX Ref [dB]	SNR ChY Rx [dB]	CANC THEO [dB]	CANC MEAS [dB]
18112008_15.43.36 Ch3ref_Ch1rx	**93.3**	77.6	44.4	44.4	25.9
	96.3	74.1	45.2	45.2	27.3
	103.8	73.7	42.7	42.7	16.0
	105	77.6	45.5	45.5	29.6
	100.3	59.2	35.0	35.0	27.2
	102.4	63.6	34.0	34.0	6.8
	98.7	51.5	39.8	39.5	15.9
	89.7	56.8	36.6	36.5	27.8

Table 20 – double antenna cancellation values obtained with NI PXI-5122.

VIII.5 *A new acquisition campaign*

A new acquisition campaign was carried on April 29th and 30th 2009 by Riva di Traiano (Civitavecchia) with the ICS-554B in the same location of the previously described acquisition campaign performed with the two wide-band PBR prototypes (see Section V and Figure 18 for a sketch of the acquisition geometry). All the acquisitions of this campaign with ICS-554B were performed using all the four device input channels, and so four directive antennas. As a consequence, only four different FM radio channels were extracted for each antenna (16 is the maximum number of output channels that can be simultaneously down-converted); specifically, following the considerations reported in Section V , the four selected FM radio channels are summarized in Table 21.

ID	Frequency (MHz)	FM radio broadcast	Transmitted polarization	Transmitted power [KWatt]
SFC1	89.8	M20	not available (maybe Vertical)	not available
SFC2	93.8	Radio Dim. Suono Roma	not available (maybe Vertical)	not availabe
SFC3	92.1	RAI R.2	Horizontal	70
SFC4	94.3	RAI R.3	Horizontal	70

Table 21 – Selected FM radio channels for ICS-554B acquisition campaign.

Different system configurations were exploited during this two-days acquisition campaign, and for each configuration a large number of sequential data acquisitions was performed (with different total acquisition durations); each single acquisition is of 1.15 or 2.15 sec duration, with a temporal spacing between two consecutive acquisitions given only by the time needed for the data storage (see Section VIII.3). According to the software description in Section VIII.3 , all the files relative to consecutive acquisitions of the same system configuration are stored in a folder named with date and hour of acquisition starting (e.g. PBR_yyyymmdd_hhmmss), and are identified by a sequential number (e.g. PBR_DDC_001, PBR_DDC_002, and so on), together with the *info-file*.

Specifically, 8 different system configurations have been considered during this acquisition campaign, as will be described in the following, aiming at verifying the performance of this new PBR receiver with respect to different parameters, such as antenna polarization, sampling frequency, single acquisition duration, and so on.

In Figure 47 the receiver location is sketched, together with the indication of antennas positions with respect to the selected transmitter of opportunity (Monte Argentario) and the Leonardo da Vinci Airport

in Fiumicino (Rome). All the antennas were fixed to the poles of a metallic fence, the reference antennas were usually placed on the north side of the terrace (except in one case), while the surveillance antennas on the south side. The distance between two adjacent poles (about 3 mt) is largely comparable with the FM signals wavelength (2.78 ÷ 3.41 mt). The main characteristics of the different exploited system configurations are summarized in the following tables (from Table 22 to Table 29).

Configuration **1**: 29/04/2009 **12.11.54** (see Figure 47)	
number of Reference antennas	1
number of Surveillance antennas	3
Reference antennas polarization	V
Surveillance antennas polarization	V
sampling frequency [MHz]	56
single acquisition duration [sec]	1.15
total acquisition duration [hh.mm]	01.30

Table 22 – Main characteristics of system configuration #1 (12.11.54).

Configuration **2**: 29/04/2009 **14.06.32** (see Figure 48)	
number of Reference antennas	1
number of Surveillance antennas	3
Reference antennas polarization	V
Surveillance antennas polarization	2V + 1H
sampling frequency [MHz]	56
single acquisition duration [sec]	1.15
total acquisition duration [hh.mm]	01.30

Table 23 – Main characteristics of system configuration #2 (14.06.32).

Configuration **3**: 29/04/2009 **16.22.04** (see Figure 49)	
number of Reference antennas	3
number of Surveillance antennas	1
Reference antennas polarization	V
Surveillance antennas polarization	V
sampling frequency [MHz]	56
single acquisition duration [sec]	1.15
total acquisition duration [hh.mm]	00.30

Table 24 – Main characteristics of system configuration #3 (16.22.04).

Configuration **4**: 30/04/2009 **12.31.07** (see Figure 50)	
number of Reference antennas	2
number of Surveillance antennas	2
Reference antennas polarization	1V + 1H
Surveillance antennas polarization	1V + 1H
sampling frequency [MHz]	72
single acquisition duration [sec]	1.15
total acquisition duration [hh.mm]	00.50

Table 25 – Main characteristics of system configuration #4 (12.31.07).

Configuration **5**: 30/04/2009 **13.57.25** (see Figure 47)	
number of Reference antennas	1
number of Surveillance antennas	3
Reference antennas polarization	V
Surveillance antennas polarization	V
sampling frequency [MHz]	72
single acquisition duration [sec]	1.15
total acquisition duration [hh.mm]	01.00

Table 26 – Main characteristics of system configuration #5 (13.57.25).

Configuration **6**: 30/04/2009 **14.47.12** (see Figure 47)	
number of Reference antennas	1
number of Surveillance antennas	3
Reference antennas polarization	V
Surveillance antennas polarization	V
sampling frequency [MHz]	72
single acquisition duration [sec]	2.15
total acquisition duration [hh.mm]	00.20

Table 27 – Main characteristics of system configuration #6 (14.47.12).

Configuration **7**: 30/04/2009 **15.39.54** (see Figure 48)	
number of Reference antennas	1
number of Surveillance antennas	3
Reference antennas polarization	V
Surveillance antennas polarization	2V + 1H
sampling frequency [MHz]	72
single acquisition duration [sec]	1.15
total acquisition duration [hh.mm]	00.30

Table 28 – Main characteristics of system configuration #7 (15.39.54).

Configuration **8**: 30/04/2009 **16.11.21** (see Figure 48)	
number of Reference antennas	1
number of Surveillance antennas	3
Reference antennas polarization	V
Surveillance antennas polarization	2V + 1H
sampling frequency [MHz]	72
single acquisition duration [sec]	2.15
total acquisition duration [hh.mm]	00.20

Table 29 – Main characteristics of system configuration #8 (16.11.21).

Unfortunately, with respect to the one described in Section V , in this acquisition campaign live ATC registrations were not available, so that it was impossible to perform again a comparison between real air traffic data and the detection results obtained with this new developed prototype. However, several analysis have been performed on the great amount of collected data, aiming at verifying the cancellation capability of this new receiver (ICS-554B) in the same acquisition scenario were the two wide-band PBR prototypes have been fielded. Acquired data also allow the verification of the detection capabilities

of ICS-554B, by exploiting the single FM radio channels and the proposed multi-frequency approaches. Moreover, the availability of data acquired with different antenna polarizations (both for reference and surveillance) allowed a new analysis of the impact of the opportunity waveform polarization in the system performance. Finally, the availability of more than two receiving channels gives us the possibility to exploit the problem of DOA estimation. Some of the results of the analysis performed on data acquired during the mentioned acquisition campaign are described in the following.

VIII.6 *Cancellation results for different configurations*

The first part of this sub-section is dedicated to a comparison between the performance (mainly in terms of cancellation values and related parameters) achieved with the system configurations 1 and 5 (see Table 22 and Table 26, respectively) characterized by the same number of reference and surveillance antennas, by the same polarization (only vertical), but exploiting a different sampling frequency, 56 and 72 MHz, respectively. For each considered configuration, two different levels of analysis can be performed:

- a performance comparison between the different surveillance antennas, for a fixed FM channel
- a performance comparison between the four different extracted FM radio channels, for each surveillance antenna.

These two configurations are analyzed in sub-sections VIII.6.1 and VIII.6.2 , respectively.

The second part of this sub-section deals with two configurations exploiting different antenna polarizations simultaneously, thus allowing an important evaluation of the impact of interferences in the PBR performance. A complete knowledge of these interferences, that represent a strong decorrelation source in the developed PBR system, is very important in order to develop proper techniques aimed at their complete removal, but this full characterization is not allowed by the use of antennas always in the same polarization. Specifically, sub-section VIII.6.3 is dedicated to the analysis of a system configuration with only a surveillance antenna in horizontal polarization, while in sub-section VIII.6.4 a configuration with both reference and surveillance antennas with different simultaneous polarizations is considered.

VIII.6.1 Configuration 1

The first considered parameter is represented by the theoretical cancellation value obtained over the different acquisitions (2321 and 1240 for configurations 1 and 5, respectively); this parameter, as highlighted in Section V is directly related to the SNR values measured over the different antennas (see equation V.13 and/or V.14); so, as expected, the trend of the theoretical cancellation curves and of the SNR values are very similar. This is the reason why the theoretical cancellations curves and the SNR curves will be both shown only once, while in the following, for sake of brevity, only the cancellation curves will be reported. Then, the measured cancellation value, evaluated as the ratio between the power

levels measured at the input and at the output of the cancellation filter (see Section V), is considered, aiming at a performance comparison between different antennas/FM channels and with respect to the reference theoretical cancellation values. Specifically, the difference between the theoretical and the measured cancellation values is carefully considered, representing a direct indication of the interference level affecting a specific FM channel or a specific antenna: in fact, the measured cancellation level, if considered alone, does not always yield to a significant performance evaluation (for example, if the cancellation level measured for 89.8 MHz is higher than the measured level for 93.8 MHz, this is not an automatic indication of a higher detection capability of 89.8 channel with respect to 93.8), while its difference with respect to the corresponding theoretical reference gives a more effective indication of the performance of the considered antenna/FM channel.

Figure 51(a) shows the theoretical cancellation values obtained for the three surveillance antennas, for all the acquisitions performed in configuration 1, for FM channel 89.8 MHz, while the SNR measured with the reference and the three surveillance antennas are plotted in Figure 51(b).

The Surv 1 antenna (see Figure 47 for the relative positions of the three surveillance antennas, Surv 1, Surv 2 and Surv 3) shows a higher theoretical cancellation with respect to the two other surveillance antennas; the three trends are very similar, and all the antennas suffer a reduction in the cancellation values of about 2dB between the acquisitions 1500 and 2000. As previously said, according to our expectations, the four SNR curves show a trend very similar to theoretical cancellation ones, and obviously the reference antenna SNR is higher than the surveillance antennas SNRs, due to antennas pointing.

Figure 52 shows the cancellation values measured with the three antennas: Surv 1 has a cancellation value higher than Surv 2 and 3, according to the results obtained in terms of theoretical cancellation. The three curves present a trend not constant over the different acquisitions (as already observed for theoretical cancellations), but with several spikes: this behaviour is a direct confirmation of what already described in III , where the strong dependence of PBR detection capabilities from both the instantaneous characteristics of the transmitted waveform and the e.m. environment (e.g. multipath) has been highlighted. In fact, even if the transmitted power for a given FM radio channel, and so the SNR (and the theoretical cancellation) is almost time-independent, due to the instantaneous, rapidly changing, characteristics of transmission and environment, there might be various times where the instantaneous performance has largely degraded characteristics for PBR purposes.

As it is apparent by a comparing Figure 51 and Figure 52, measured cancellation values are quite lower than the corresponding theoretical values, for all the three antennas. This is clearly evident in

Figure 53(a, b, and c), where a direct comparison between theoretical and measured cancellation is reported, for each surveillance antenna. Also the difference between these two values is shown. This difference is of about 28, 32 and 33 dB for Surv 1, Surv 2 and Surv 3, respectively: so, we can conclude that, for FM channel 89.8 MHz, the first surveillance antenna shows better cancellation performance, both in terms of absolute and differential values, while Surv 3 is the worse one.

Same analysis can be repeated also for the other FM channels. Specifically, for 93.8 MHz, Figure 54(a) shows the theoretical cancellation values obtained for the three surveillance antennas, while the corresponding measured cancellation values are plotted in Figure 54(b). In this case, Surv 2 has the higher theoretical cancellation value (Surv 1 for 89.8 MHz, see Figure 51), with a difference of about 4-5 dB with respect to the same antenna for 89.8 MHz. The same behaviour is not observed for the two other surveillance antennas: for Surv 1 the theoretical cancellation values are almost the same, for Surv 3 there is a reduction of about 3dB. Obviously, being the transmitter location the same for all the considered FM radio channels, if 93.8 MHz is characterized by a transmitted power higher than 89.8 MHz we can expect a general increase in SNR values and as a consequence in the theoretical cancellation values (notice that we do not know the transmitted power values for these two FM channels – see Table 21). And the hypothesis of an higher transmitted power can be justified by considering the measured SNR of the reference antenna for 93.8 MHz (Figure 55), which is about 5 dB higher than the corresponding SNR for 89.8 MHz (Figure 51(b)). But the same behaviour is not confirmed for the three surveillance antennas. A possible explanation of these different trends for different antennas is that the antenna gain patterns can show slight differences between each other: we can assume that the four used antennas are perfectly equal and have the same gain over the whole FM bandwidth, but in reality some differences can be experienced. Moreover, the different relative positions of the three surveillance antennas (with a distance between each other comparable with the opportunity signal wavelength) can justify the presence of different multipath effects suffered by the antennas.

By considering measured cancellation values (Figure 54(b)), these show a trend similar to the corresponding theoretical curves, except for a negative spike in correspondence of acquisition number 362. A comparison of measured cancellations between 93.8 and 89.8 MHz (Figure 54(b) and Figure 52, respectively) shows that the values obtained with 93.8 MHz are few dBs higher than the 89.8 MHz counterparts, and in this case Surv 2 is just 1 dB below Surv 1 (it was about 8-9 dB lower for 89.8 MHz). These differences are also confirmed by the direct comparison between theoretical and measured cancellation, reported in Figure 56(a, b, and c) for each surveillance antenna: the differences between these two values are now of about 23.5, 26 and 26.5 dB (28, 32 and 33 dB for 89.8 MHz), so that also

for this frequency Surv 1 is the antenna with the best cancellation performance, but Surv 2 and 3 show a performance increase with respect to 89.8 MHz.

The third considered FM channel is 92.1 MHz: as expected, in this case we can easily observe a significant increase in the theoretical cancellation values (Figure 57(a)) with respect to values obtained for 89.8 and 93.8 MHz. And this increase is confirmed by SNRs values, here not reported for sake of brevity: this is mainly due to the higher transmitted power for this FM channel (RAI, 70KW – see Table 21): as already mentioned, we do not exactly know the transmitted power levels for 89.8 and 93.8 MHz, but it is well known that these values are lower than RAI broadcasts.

Measured cancellation values are also higher than the 89.9/93.8 MHz counterparts (Figure 57(b)). The direct comparison between theoretical and measured cancellations (Figure 58a, b and c for Surv 1, Surv 2 and Surv 3, respectively) shows that also in this case Surv 1 is the antenna with better cancellation performance, while Surv 2 has the higher difference between theoretical and measured cancellation.

The fourth FM channel is 94.3 MHz (it is also broadcasting Radio RAI, with a transmitted power level of 70KW). Theoretical cancellation values (Figure 59(a)) are largely comparable with the 92.1MHz counterparts, even if for this FM channel Surv 2 shows the higher values. On the contrary, measured cancellations (Figure 59(b)) are much lower than the values obtained for 92.1 MHz; moreover, for each surveillance antenna we can observe an highly varying trend along the different acquisitions, with several spikes. This behaviour can be partially justified by considering the program content acquired for 94.3 MHz, which was classic music for the considered acquisition: classic music has a narrow actual bandwidth with respect to different kinds of music (rock, pop, and so on), thus resulting in degraded PBR performance. This bad behaviour is obviously confirmed by the direct comparison between theoretical and measured cancellations, for the three antennas (Figure 60a, b and c): the differences are always equal or higher than 35 dB.

In conclusion, for this configuration Surv 1 is the antenna with the best cancellation performance, both in terms of actual measured values and of difference respect to theoretical expectations, while Surv 3 is in general the antenna with the worse actual cancellations, and Surv 2 experiences the higher losses with respect to its theoretical reference.

The next step in the analysis is a performance comparison between the four different FM radio channels, for each surveillance antenna. In Figure 61(a), (b) and (c) theoretical, measured and difference between theoretical and measured cancellation values, respectively, are shown for the four considered FM channels acquired with Surv 1. As expected, and as already observed in the previous analysis for the different FM channels separately, 92.1 and 94.3 MHz show the highest (and similar) theoretical

cancellation values, while 89.8 and 93.8 MHz show a difference of about 6-7dB with respect to these two FM channels. Measured cancellation trend are quite different for the considered channels (Figure 61(b)), mainly due to the different program contents and propagation conditions experienced (e.g. multipath effects); 92.1 MHz shows better performance, 94.3 is the worst one. This results are also confirmed by considering the difference between theoretical and measured cancellations (Figure 61c): it is easy to notice that 92.1 MHz has lower losses (together with 93.8 MHz), while 94.3 MHz has the higher losses with respect to its reference.

Similar trends can be observed for theoretical cancellation values obtained with Surv 2 (Figure 62(a)); in this case 94.3 MHz shows the highest values, and there is a difference of about 5dB between 89.8 and 93.8 MHz (they were almost equal in the Surv 1, see Figure 61a). Measured cancellation values (Figure 62(b)) confirm the different behaviours for different extracted FM channels (almost constant trend in some cases, highly varying in other cases): 92.1 MHz is the channel with higher cancellation, 89.8MHz with lower. By considering also the differences between theoretical and measured cancellations (Figure 62(c)), 93.8 MHz is the channel with the lower cancellation loss, 94.3 MHz the one with the higher. We can also notice a general increase in this cancellation loss with respect to Surv 1.

Finally, for Surv 3 we can observe that 94.3 MHz is the FM channel with higher theoretical cancellation values (Figure 63(a)), 93.8 MHz with the lower values. In terms of measured cancellation (Figure 63(b)), 92.1 and 89.8 MHz are the best and the worst channel, respectively. As for Surv 2, 89.8 and 94.3 MHz are the FM channels with the largest difference between theoretical and measured cancellation (Figure 63(c)).

In conclusion, for this Configuration, the best performance in terms of cancellation capability has been achieved with the first surveillance antenna, and with the FM channel 92.1 MHz.

VIII.6.2 Configuration 5

The analysis reported in the previous sub-section have been repeated for the configuration 5 (see Table 26 for more details), where a different sampling frequency (72 MHz instead of 56) is considered. Notice that, for this configuration, a reduced number of consecutive acquisitions has been performed with respect to configuration 1 (1240 and 2321, respectively); however, we have a significant amount of acquisitions in order to perform an effective performance comparison.

Figure 64a shows the theoretical cancellation values obtained for FM channel 89.8 MHz; a comparison with the 56MHz counterparts (Figure 51) shows that obtained values are largely

comparable, but slightly lower. Moreover, in the 72 MHz case the trend is much more constant along the different acquisitions with respect to 56 MHz. A possible explanation of this behaviour can be found in the different effect of the two used sampling frequencies on the FM bandwidth (notice that we are referring to the direct RF sampling approach): with 72 MHz sampling frequency the 20 MHz of the FM bandwidth (88 ÷ 108 MHz) are subject only to one spectral folding in the ADC working bandwidth, while with 56 MHz sampling frequency the FM bandwidth is sampled after a double spectral folding. This difference can be responsible for the presence of higher decorrelation effects when signals are sampled with a lower sampling frequency.

By considering the measured cancellation values (Figure 64(b)), Surv 1 shows better cancellation performance, Surv 3 has the lower values, and these values are comparable with the 56 MHz counterparts (Figure 52), except for Surv 3, where a 5 dB reduction is observed. The difference between theoretical and measured cancellation values (Figure 65a, b and c) shows a slight advantage for 72 MHz configuration with respect to 56 MHz, except for Surv 3 (1 dB difference).

Summarizing the results obtained for 89.8 MHz, the cancellation performance with the two different sampling frequencies are largely comparable, with a little advantage for the higher value (72 MHz), due to *(i)* a slight reduction in terms of cancellation loss (i.e. the difference between theoretical and measured cancellation) and *(ii)* a more flat trend over the different acquisitions.

When considering the channel 93.8 MHz, theoretical cancellation of Surv 1 and Surv 2 is almost similar (Figure 66(a)), as already seen for configuration 1 (Figure 54(a)), and also Surv 3 shows a level about 8 dB lower. As for configuration 1, the cancellation of Surv 2 shows an increase of about 4.5dB when considering 93.8 MHz instead of 89.8 MHz. Again, a more flat trend is observed for this frequency with respect to the 56 MHz counterpart. Moreover, it is easy to notice that the higher value of sampling frequency has a positive impact on the measured cancellation values (Figure 66(b) and Figure 54(b) for 72 and 56 MHz, respectively), and on the cancellation losses (Figure 67 and Figure 56, respectively): the three surveillance antennas not only show higher measured cancellation values, but they are also losing less with respect to the relative theoretical reference values.

The same general behaviour can be verified when considering the FM channel 92.1 MHz (Figure 68a, b and Figure 69a, b and c).

Finally, when considering the FM channel 94.3 MHz, the cancellation performance (Figure 70a, b and Figure 71a, b and c) are slightly worse with respect to the 56 MHz counterparts. Moreover, the measured cancellation trend is highly varying during the different acquisitions: if we listen to the acquired program content for this FM channel, we can hear speech for most of the time; it is well known

that speech has a reduced effective bandwidth, and it is also characterized by pauses, thus yielding to degraded and rapidly changing PBR performance. However, due to an overall and similar reduction of both theoretical and measured cancellation values, the differences between these two values are comparable with the counterparts obtained with the lower sampling frequency.

In conclusion, also for this configuration Surv 1 is the antenna with the best cancellation performance, both in terms of actual measured values and of difference respect to theoretical expectations, while Surv 3 is in general the antenna with the worse actual cancellations, and Surv 2 experiences the higher losses with respect to its theoretical reference.

The next step in the analysis is a performance comparison between the four different FM radio channels, for each surveillance antenna. In Figure 72(a), (b) and (c) theoretical, measured and difference between theoretical and measured cancellation values, respectively, are shown for the four considered FM channels acquired with Surv 1; the same types of curves are reported in Figure 73(a, b and c) and in Figure 74(a, b and c) for Surv 2 and 3, respectively. Similar considerations apply in this case with respect to what already said for configuration 1 (sampling frequency 56 MHz). Also, these curves confirm the general reduction in cancellation loss when using an higher sampling frequency.

VIII.6.3 Configuration 2

This configuration (see Table 23 and Figure 48 for more details) is characterized by the presence of two surveillance antennas mounted on the same pole, with different polarizations (a third surveillance antenna is on an adjacent pole, with vertical polarization; also the reference antenna is in vertical polarization). This configuration, and the same applies for all the configurations exploiting different antenna polarizations simultaneously, allows an important evaluation of the impact of interferences in the PBR performance. In fact, the previously described analysis, performed over different antennas characterized by the same polarization (always vertical) suggest the presence of strong interferences (probably due to other transmissions) which strongly affect and limit the overall system performance, but when using a single polarization it is not possible to fully characterize the nature of these interferences. A complete knowledge of these interferences, that represent a strong decorrelation source in the developed PBR system, is very important in order to develop proper techniques aimed at their complete removal.

The importance of the simultaneous exploitation of different polarizations can be made more explicit with the following considerations. Assume that the selected transmission of opportunity is vertically polarized (TX_V) while the interference contribution (indicated with the letter *I* in the following) is

horizontally polarized (I_H); we can schematically represent the levels of the different contributions (direct signal, interference signal, noise) as sketched in Figure 75(a) and (b), where both the scenarios with surveillance antenna horizontally (RX_H) and vertically (RX_V) polarized are respectively considered (in Figure 75 *D*, *I* and *N* indicate the direct signal level, the interference level and the noise level, respectively). Being the transmission vertically polarized, RX_V is expected to receive more power than RX_H; as a consequence, the SNR measured for RX_V is expected to be higher than the RX_H SNR, and also the theoretical cancellation of the pair TX_V-RX_V will be, in general, higher than the value expected with the pair TX_V-RX_H (this is what is schematically represented in Figure 75(a) and (b)). Moreover, being the interference horizontally polarized (I_H), its impact will be higher in RX_H than in RX_V, where the same interference level is partially rejected due to the opposite antenna polarization. As a consequence, the measured cancellation level (CA_{meas}) can be strongly or slightly different by the theoretical reference value (CA_{theo}). Viceversa, with the same transmission (TX_V) and an interference vertically polarized (I_V), the surveillance antenna with the same polarization (RX_V) is expected to suffer the stronger interference impact.

As already mentioned, SNR (SNR = D/N) gives a direct indication about the theoretical cancellation, while the measured cancellation is directly related to the Signal-to-Interference Ratio (SIR = D/I). If SNR and SIR are known, we can evaluate the Interference-to-Noise Ratio (INR = I/N), given by

$$INR = I/N = SNR * SIR^{-1} \approx CA_{theo|dB} - CA_{meas|dB} \quad \text{(VIII.3)}$$

So INR gives an indication of the loss amount in terms of measured with respect to theoretical cancellation. Obviously, same considerations apply if the transmission of opportunity is horizontally polarized (TX_H).

In the following, when considering the performance obtained with this system configuration, the attention will be mainly focused on the comparison between the two surveillance antennas with different polarizations mounted on the same pole, referred to as Surv H and Surv V, while Surv 3 is the third surveillance antenna, vertically polarized, mounted on the adjacent pole.

Considering the frequency channel 89.8MHz, in Figure 76(a), (b) and (c) theoretical, measured and the difference between theoretical and measured cancellation values obtained with the three antennas are reported, respectively. Surv H shows a lower value of theoretical cancellation (Figure 76(a)), probably due to the reduced level of direct signal received (in these considerations 89.8MHz frequency channel transmitted from Monte Argentario is supposed to be vertically or cross-polarized), while Surv V receives more power, thus yielding to higher SNR and theoretical cancellation values. The INR of Surv

V (and of Surv 3, see Figure 76(c)) is about 10-11 dB higher than the value measured for Surv H: taking into account the previous considerations, we can assume the presence of an interference contribution vertically polarized. Table 30 reports the radio frequency channels (with carrier frequency equal or very close to 89.8 MHz) whose coverage includes the receiver site: for each channel, the transmitter location, the distance from the receiver site, the polarization (when available) and the expected power level at the receiver site are indicated.

Frequency (MHz)	FM radio broadcast	Transmitter	Distance [Km]	Transmitted polarization	Power [dBµV]
89.7	RAI R.1	Monte Mario (RM)	54	Horizontal	60
89.8	M2O	Monte Argentario	68	not available (maybe Vertical)	41
89.9	Latte e Miele	M.te Porzio Catone	68	not available	39
89.9	Tele Radio Orte	Soriano (VT)	53	not available	39

Table 30 –FM radio channels (near 89.8MHz) received at receiver site.

In this case, the stronger source of interference is represented by an horizontally polarized channel, in contrast with the previous hypothesis. However, it is not possible to absolutely assume that the interference source is represented by the horizontally polarized transmission.

For 93.8 MHz, by considering the strong difference (about 16 dB) in terms of theoretical cancellation values (Figure 77(a)) between Surv V and Surv H, we can reasonably assume that this transmission is vertically polarized. Figure 77(c) shows the difference between theoretical and measured cancellation, for the three surveillance antennas; a stronger interference level is observed for Surv V with respect to Surv H, but in this case the difference is only 3dB. So we can assume the simultaneous presence of horizontally and vertically (or cross-) polarized interferences. As for the previous case, Table 31 summarizes the radio frequency channels (with carrier frequency equal or very close to 93.8 MHz) whose coverage includes the receiver site. The stronger interference source is represented by a horizontally polarized transmission, but also a radio channel with polarization information not available is present, so we can assume that both these transmissions act as interference.

Frequency (MHz)	FM radio broadcast	Transmitter	Distance [Km]	Transmitted polarization	Power [dBµV]
93.7	RAI R.3	Monte Mario (RM)	54	Horizontal	60
93.7	RAI R.3	Canepina (VT)	49	not available (maybe Vertical)	48
93.8	Radio Dim. Suono Roma	Monte Argentario	68	not available	41

Table 31 –FM radio channels (near 93.8 MHz) received at receiver site.

Notice that a *positional* factor has also to be considered: Surv H is mounted below the Surv V (on the same pole); this relative position can justify the lower power level (useful and interference) received by the horizontally polarized antenna.

The third FM channel is 92.1 MHz. In this case, as expected Surv H shows a theoretical cancellation higher than Surv V (Figure 78a), in accordance with the polarization of this transmission. However, this difference is only of about 1dB; moreover, Surv 3 (vertically polarized) shows an higher theoretical cancellation value, and this behaviour (as previously mentioned) is mainly due to the relative positions between the antennas. Figure 78(c) shows that the Surv V INR is about 4.5 dB higher than Surv H INR: we can assume the presence of a vertically polarized interference. Radio frequency channels (with carrier frequency equal or very close to 92.1 MHz) whose coverage includes the receiver site are indicated in Table 32. In this case it is easy to assume that the main interference source are represented by the vertically polarized channels broadcast at 92.0 and 92.2 MHz.

Frequency (MHz)	**FM radio broadcast**	**Transmitter**	**Distance [Km]**	**Transmitted polarization**	**Power [dBµV]**
92.0	R.101	Monte Gennaro	81	Vertical	39
92.1	RAI R.2	Monte Argentario	68	Horizontal	63
92.2	RTL 102.5	M.te Terminillo	108	not available	43
92.2	RTL 102.5	Monte Gennaro	81	Vertical	42

Table 32 –FM radio channels (near 92.1 MHz) received at receiver site.

94.3 MHz frequency channel shows a very similar behaviour with respect to 92.1 MHz in terms of relative difference between theoretical cancellations (Figure 79(a)). In this case, the difference between vertically and horizontally polarized antennas in terms of INR is about 12 dB (Figure 79(c)): we can assume the presence of a vertically polarized interference source. Radio frequency channels (with carrier frequency equal or very close to 94.3 MHz) whose coverage includes the receiver site are indicated in Table 33: as it is apparent, the stronger FM broadcasts are vertically polarized.

Frequency (MHz)	**FM radio broadcast**	**Transmitter**	**Distance [Km]**	**Transmitted polarization**	**Power [dBµV]**
94.2	Radio Subasio	Albano Laziale	79	Vertical	46
94.3	RAI R.3	Monte Argentario	68	Horizontal	63
94.4	RAI R.2	M.te Terminillo	108	Horizontal	42
94.5	Radio Subasio	Monte Cavo	81	Vertical	50

Table 33 –FM radio channels (near 94.3 MHz) received at receiver site.

As already seen for the two previously described configurations, the same conclusions are drawn when considering, for each surveillance antenna, the theoretical (a), the measured (b) and the difference between theoretical and measured (c) cancellation values obtained with the four FM radio channels.

These sets of curves are reported in Figure 80, Figure 81 and Figure 82 for Surv H, Surv V and Surv 3, respectively, and are not commented in detail for sake of brevity.

VIII.6.4 Configuration 4

Last configuration considered in this work (see Table 25 and Figure 50 for more details) is characterized by the presence of two reference and two surveillance antennas, both with different polarizations, so that four different *reference-surveillance antenna pairs* can be considered in the analysis:

1. Ref V – Surv H
2. Ref V – Surv V
3. Ref H – Surv H
4. Ref H – Surv V

All these different pairs will be analyzed in the following in terms of cancellation capabilities, also by considering the presence of interference sources.

For each extracted FM radio channel, the comparison between the different antenna pairs is performed by considering four different sets of curves: the SNR values, the theoretical and measured cancellation values, and the difference between theoretical and measured cancellations (representing the INR value). The same analysis has also been repeated considering, in the same figure, the four FM channels for each antenna pair, but is not included in this work for sake of brevity.

Starting, as usual, with 89.8 MHz, the four mentioned sets of curves are reported in Figure 83(a), (b), (c) and (d), respectively. Specifically, SNR values (Figure 83a) for Ref V and Surv V are higher than the corresponding values for Ref H and Surv H, according to the hypothesis that this transmission is vertically polarized. Obviously, higher theoretical cancellation values are obtained with antenna pairs in which Surv V is included (see Figure 83b). On the contrary, when considering measured cancellation values and the differences with respect to the relative theoretical reference (Figure 83c and d, respectively), antenna pairs which include Surv H (Ref V – Surv H and Ref H – Surv H) show better performance. As already described in the previous sub-section for configuration 2, this behaviour can give rise to the hypothesis of a vertically polarized source of interference, but the previous analysis is not perfectly in line with this assumption.

Same results in term of SNR and theoretical cancellation values can be observed for 93.8 MHz (Figure 84(a) and (b), respectively) with respect to 89.8 MHz. In this case, measured cancellations are higher when considering pairs with Surv V (Figure 84c), but the pairs with Surv H show the lower cancellation losses, and so the lower INR values (Figure 84d), even if the difference with respect to the pairs with Surv V is reduced to 3.5 dB (it was about 12-14 dB for 89.8 MHz). This behaviour gives rise to the hypothesis of a simultaneous presence of vertically and horizontally polarized interference sources, and is confirmed by the analysis of the previous sub-section: the antenna pairs characterized by higher power levels are those with Surv V (according to the hypothesis that both 89.8 and 93.8 MHz are transmitted with vertical polarization), but at the same time, the pairs with Surv H experience the lower INR values (i.e. the lower difference between theoretical and measured cancellations).

When considering 92.1 MHz, and in particular the SNR values (Figure 85a), Ref V SNR is unexpectedly higher than Ref H SNR (92.1 MHz is broadcast with horizontal polarization): this can be justified by assuming that the antennas used in these PBR receiver have different gains for different polarizations, and specifically higher gain with vertical polarization. However, in this case the SNR difference for these two antennas is only 7 dB, much lower than the differences measured for 89.8 and 93.8 MHz. Surv H has an higher SNR than Surv V (about 2.5 dB), and as expected the higher theoretical cancellations are obtained with Surv H (Figure 85b). Moreover, Ref V – Surv H and Ref H – Surv H are also the pairs with lower INR values, thus giving a further confirmation of the vertically polarized interference source presence, as highlighted in the previous sub-section.

Finally, as expected, results obtained for FM radio channel 94.3 MHz (Figure 86) are largely comparable with 92.1 MHz (both the channels are horizontally polarized transmissions).

VIII.7 *Detection results for different configurations*

After the verification of the cancellation capabilities of this new receiver (ICS-554B) with reference to four of the eight system configurations considered during the acquisition campaign, this section is focused on the verification of the detection capabilities of ICS-554B, considering the detections obtained by exploiting the single FM radio channels, the integration between different polarizations (when available) and the proposed multi-frequency approaches. As already said, the unavailability of real ATC registrations for the same days and the same area of the acquisition campaign does not allow an extensive performance evaluation of the achieved detection probability and the actual false alarm rate. However, the sequences of the results obtained for different sets of consecutive data files on the same Range-Velocity map (after the application of a CA-CFAR autogate) are considered, separately for each of the selected FM radio channels and for each antenna, but also by evaluating the plot coincidences between different antennas (for example, when three surveillance antennas are available, the intersection between the plots obtained with Surv 1 and Surv 2, Surv 2 and Surv 3, and so on). A plot sequence can be easily recognized to belong to a possible target by observing that an approaching target has a positive bistatic velocity and the range rate of change is directly related to the magnitude of the bistatic velocity. Obviously, due to the absence of a *ground-truth* for an effective overall performance comparison, the analysis reported in the following sub-sections does not pretend to be fully exhaustive. However, they represent a good starting point for a comparative evaluation of the performance obtained with single FM radio channels, after the integration of signals acquired with different antenna polarizations, and with the already described multi-frequency approach. This comparison is performed by considering, for each configuration previously described, two or three sets of consecutive acquisitions where one or more targets are clearly visible, and evaluating the number of detections obtained with the single channels/antennas or with different channels/antennas combinations.

VIII.7.1 Configuration 1

The starting point for this short analysis of detections with configuration 1 (see Table 22) is represented by Surv 1 and FM radio channel 89.8 MHz. When considering the detections results achieved with single antennas, the nominal P_{fa} for CFAR threshold application is 10^{-4}, while when considering the intersection results between different antennas P_{fa} is set to 10^{-3}. Two plot sequences obtained considering 85 and 98 consecutive acquisitions are shown in Figure 87 and Figure 88,

respectively, together with the corresponding legends, showing the acquisition file numbers. After the individuation of these two sequences, the same sets of consecutive acquisitions have been considered for the two other surveillance antennas (Surv 2 and 3) and for the three other FM radio channels. The corresponding plot sequences are not reported in this work for sake of brevity: for each considered sequence (whose length is determined by considering the lower and the higher data file where a detection is observed for any antenna, for example if a sequence for Surv 1 involves data files from 10 to 20, and the same target is observed with Surv 2 on data files from 8 to 17, the sequence length is assumed to be 13 files, from 8 to 20) a table is filled, reporting for each antenna (or intersection between antennas) and for each radio channel the number of detections and the corresponding percentage with respect to the sequence length. Again, notice that these percentages do not pretend to give an effective indication of the detection probability of each considered channel/antenna, but are used only for a first level of performance assessment and comparison.

Table 34 summarizes the detection results obtained by considering the single surveillance antennas for the first exploited sequence, while in Table 35 are indicated the results obtained for the same data file sequence, but considering the plot coincidences between different antennas (hereafter referred to as *intersection a/b*, or *intersection a/b/c*, where *a*, *b* and *c* represent the surveillance antennas).

Sequence #1: from 290 to 416 (total: 127 consecutive data files)						
Frequency / Antenna	Surv 1		Surv 2		Surv 3	
89.8 MHz	44	34.6%	15	11.8%	15	11.8%
93.8 MHz	40	31.5%	31	24.4%	23	18.1%
92.1 MHz	64	50.4%	28	22%	28	22%
94.3 MHz	15	11.8%	11	8.7%	11	8.7%

Table 34 – detection results for the first considered sequence (single antennas)

Sequence #1: from 290 to 416 (total: 127 consecutive data files)								
Frequency / Antenna	intersection 1/2		intersection 1/3		intersection 2/3		intersection 1/2/3	
89.8 MHz	20	15.7%	14	11%	6	4.7%	6	4.7%
93.8 MHz	26	20.5%	20	15.7%	16	12.6%	16	12.6%
92.1 MHz	22	17.3%	19	15%	13	10.2%	8	6.3%
94.3 MHz	6	4.7%	4	3.1%	8	6.3%	1	0.8%

Table 35 – detection results for the first considered sequence (intersection between antennas)

Similarly, for the second considered sequence, Table 36 and Table 37 summarize the detection results obtained with single antennas and the plot coincidences between different antennas.

Sequence #2: from 1738 to 1848 (total: 111 consecutive data files)						
Frequency / Antenna	Surv 1		Surv 2		Surv 3	
89.8 MHz	47	42.3%	24	21.6%	35	31.5%
93.8 MHz	77	69.4%	65	58.6%	63	56.8%
92.1 MHz	77	69.4%	55	49.5%	66	59.5%
94.3 MHz	49	44.1%	36	32.4%	50	45%

Table 36 – detection results for the first considered sequence (single antennas)

Sequence #2: from 1738 to 1848 (total: 111 consecutive data files)								
Frequency / Antenna	intersection 1/2		intersection 1/3		intersection 2/3		intersection 1/2/3	
89.8 MHz	14	12.6%	24	21.6%	12	10.8%	6	5.4%
93.8 MHz	54	48.6%	49	44.1%	49	44.1%	40	36%
92.1 MHz	48	43.2%	62	55.9%	49	44.1%	43	38.7%
94.3 MHz	27	24.3%	34	30.6%	20	18%	19	17.1%

Table 37 – detection results for the first considered sequence (intersection between antennas)

Each row of the tables gives an indication of the detection performance of each antenna (or intersection between antennas) for a given FM radio channel, while each column gives an indication about the performance of the different FM channels, for a given antenna (or intersection between antennas).

For the first considered sequence Surv 1 is the antenna with the highest number of detections, for all the FM channels. 92.1 MHz is the best performing channel for Surv 1 and Surv 3, 93.8 MHz for Surv 2. For the second sequence, Surv 1 is again the best performing antenna, except for 94.3 MHz (Surv 3 is slightly better, just for one detection). 93.8 and 92.1 MHz are the best performing channels for Surv 1, 93.8 MHz for Surv 2, 92.1 for Surv 3.

This behaviour (Surv 1 has the best detection performance with all the extracted FM channels, 92.1 MHz is the best performing channel for Surv 1 and Surv 3, 93.8 for Surv 2) is a confirmation of the results obtained in the previous analysis (see sub-section VIII.6.1): specifically, higher measured cancellation has been obtained for all the FM channels with Surv 1 and 92.1 MHz is the radio channel with higher cancellation values and lower interference level both for Surv 1 and 3, while 93.8 shows the lower interference for Surv 2.

VIII.7.2 Configuration 5

In this case (see Table 26 for configuration details), three plot sequences have been considered, as shown in Figure 89, Figure 90 and Figure 91. As for the previous configuration, after the sequences identification, two tables are reported for each sequence (from Table 38 to Table 43), where the number of detections and the corresponding percentage with respect to the sequence length are summarized for each antenna (or intersection between antennas) and for each radio channel.

Sequence #1: from 92 to 204 (total: 113 consecutive data files)						
Frequency / Antenna	Surv 1		Surv 2		Surv 3	
89.8 MHz	28	24.8%	22	19.5%	17	15%
93.8 MHz	52	46%	61	54%	73	64.6%
92.1 MHz	68	60.2%	62	54.9%	61	54%
94.3 MHz	16	14.2%	8	7.1%	11	9.7%

Table 38 – detection results for the first considered sequence (single antennas)

Sequence #1: from 92 to 204 (total: 113 consecutive data files)								
Frequency / Antenna	intersection 1/2		intersection 1/3		intersection 2/3		intersection 1/2/3	
89.8 MHz	15	13.3%	16	14.2%	17	15%	14	12.4%
93.8 MHz	41	36.3%	50	44.2%	51	45.1%	40	35.4%
92.1 MHz	51	45.1%	43	38%	38	33.6%	35	31%
94.3 MHz	4	3.5%	6	5.3%	4	3.5%	2	1.8%

Table 39 – detection results for the first considered sequence (intersection between antennas)

Sequence #2: from 361 to 502 (total: 142 consecutive data files)						
Frequency / Antenna	Surv 1		Surv 2		Surv 3	
89.8 MHz	50	35.2%	39	27.5%	27	19%
93.8 MHz	77	54.2%	81	57%	95	67%
92.1 MHz	98	69%	96	67.6%	82	57.7%
94.3 MHz	27	19%	21	14.8%	27	19%

Table 40 – detection results for the second considered sequence (single antennas)

Sequence #2: from 361 to 502 (total: 142 consecutive data files)								
Frequency / Antenna	intersection 1/2		intersection 1/3		intersection 2/3		intersection 1/2/3	
89.8 MHz	27	19%	16	11.3%	21	14.8%	12	8.4%
93.8 MHz	58	40.8%	66	46.5%	56	39.4%	49	34.5%
92.1 MHz	70	49.3%	58	40.8%	57	40.1%	46	32.4%
94.3 MHz	9	6.3%	10	7%	12	8.4%	6	4.2%

Table 41 – detection results for the second considered sequence (intersection between antennas)

Sequence #3: from 743 to 921 (total: 179 consecutive data files)						
Frequency / Antenna	Surv 1		Surv 2		Surv 3	
89.8 MHz	55	30.7%	33	18.4%	24	13.4%
93.8 MHz	65	36.3%	75	41.9%	84	46.9%
92.1 MHz	106	59.2%	103	57.5%	98	54.7%
94.3 MHz	17	9.5%	20	11.2%	30	16.8%

Table 42 – detection results for the third considered sequence (single antennas)

Sequence #3: from 743 to 921 (total: 179 consecutive data files)								
Frequency / Antenna	intersection 1/2		intersection 1/3		intersection 2/3		intersection 1/2/3	
89.8 MHz	30	16.8%	23	12.8%	22	12.3%	18	10%
93.8 MHz	53	29.6%	57	31.8%	61	34.1%	47	26.3%
92.1 MHz	81	45.2%	78	43.6%	81	45.2%	67	37.4%
94.3 MHz	12	6.7%	12	6.7%	18	10%	9	5%

Table 43 – detection results for the third considered sequence (intersection between antennas)

For the first sequence, Surv 1 has the best detection performance for all the FM channels except 93.8 (Surv 3), while the best performing channel is 92.1 MHz for Surv 1 and 2, 93.8 for Surv 3.

For the second sequence, Surv 1 is again the best performing antenna, except for 93.8 MHz (Surv 3 is better). Notice that for 94.3 MHz Surv 1 and 3 show the same number of detections. 92.1 MHz is the best performing channel for Surv 1 and 2, 93.8 MHz for Surv 3.

For the third sequence, Surv 1 performs better for 89.8 and 92.1 MHz, Surv 3 for 93.8 and 94.3 MHz, while 92.1 is the best performing channel, regardless of the surveillance antenna.

Also in this case, the primacy of Surv 1 in relation to 89.8 and 92.1 MHz is well in line with the results achieved in the previous analysis, showing that these channels are characterized both by higher measured cancellation levels and lower interference level. The same applies for 92.1 MHz when comparing the FM channels performance for Surv 1 and 3.

Unfortunately, due to the absence of the real air traffic control data, a complete performance comparison, in terms of detection capability, between this configuration and the previous one is not allowed, so it is not possible to state if 72 MHz sampling frequency is better than 56 MHz or viceversa.

VIII.7.3 Configuration 2

Concerning this configuration (see Table 23 and Figure 48 for more details), the previous analysis showed that Surv H is characterized by a reduced interference level with respect to vertically polarized antennas, also due to its relative position (mounted below Surv V on the same pole). Now we are

interested in evaluating if this lower interference level is associated with a better detection capability of this antenna.

In this case, the individuation of plot sequences started from 92.1 MHz (again from Surv H): this is a direct consequence of the results of the previous analysis, which showed that this channel is one of the best performing for all the surveillance antennas both in terms of theoretical and measured cancellation, and of reduced cancellation loss (i.e. reduced interference level). The three considered plot sequences are shown in Figure 92, Figure 93 and Figure 94. As for the previous configurations, the performance comparison between antennas and FM channels in relation to these three sequences is made by considering the detection results summarized in the following six tables, from Table 44 to Table 49.

Sequence #1: from 865 to 978 (total: 114 consecutive data files)						
Frequency / Antenna	Surv H		Surv V		Surv 3 (V)	
89.8 MHz	32	28.1%	23	20.2%	25	21.9%
93.8 MHz	43	37.7%	58	50.9%	44	38.6%
92.1 MHz	68	59.6%	69	60.5%	81	71%
94.3 MHz	53	46.5%	48	42.1%	45	39.5%

Table 44 – detection results for the first considered sequence (single antennas)

Sequence #1: from 865 to 978 (total: 114 consecutive data files)								
Frequency / Antenna	intersection 1/2		intersection 1/3		intersection 2/3		intersection 1/2/3	
89.8 MHz	16	14%	20	17.5%	20	17.5%	14	12.3%
93.8 MHz	32	28.1%	27	23.7%	37	32.5%	23	20.2%
92.1 MHz	35	30.7%	51	44.7%	45	39.5%	28	24.6%
94.3 MHz	31	27.2%	32	28.1%	32	28.1%	24	21.1%

Table 45 – detection results for the first considered sequence (intersection between antennas)

Sequence #2: from 1807 to 1956 (total: 150 consecutive data files)						
Frequency / Antenna	Surv H		Surv V		Surv 3 (V)	
89.8 MHz	15	10%	14	9.3%	22	14.7%
93.8 MHz	29	19.3%	31	20.7%	44	29.3%
92.1 MHz	61	40.7%	38	25.3%	56	37.3%
94.3 MHz	39	26%	16	10.7%	19	12.7%

Table 46 – detection results for the second considered sequence (single antennas)

Sequence #2: from 1807 to 1956 (total: 150 consecutive data files)								
Frequency / Antenna	intersection 1/2		intersection 1/3		intersection 2/3		intersection 1/2/3	
89.8 MHz	9	6%	12	8%	13	8.7%	9	6%
93.8 MHz	17	11.3%	19	12.7%	27	18%	14	9.3%
92.1 MHz	27	18%	29	19.3%	23	15.3%	19	12.7%
94.3 MHz	12	8%	4	2.7%	7	4.7%	2	1.3%

Table 47 – detection results for the second considered sequence (intersection between antennas)

Sequence #3: from 2145 to 2222 (total: 78 consecutive data files)						
Frequency / Antenna	Surv H		Surv V		Surv 3 (V)	
89.8 MHz	36	46.2%	36	46.2%	39	50%
93.8 MHz	40	51.3%	57	73.1%	52	66.7%
92.1 MHz	44	56.4%	50	64.1%	49	62.8%
94.3 MHz	38	48.7%	42	53.8%	49	62.8%

Table 48 – detection results for the third considered sequence (single antennas)

Sequence #3: from 2145 to 2222 (total: 78 consecutive data files)								
Frequency / Antenna	intersection 1/2		intersection 1/3		intersection 2/3		intersection 1/2/3	
89.8 MHz	22	28.2%	26	33.3%	33	42.3%	22	28.2%
93.8 MHz	35	44.9%	31	39.7%	48	61.5%	32	41%
92.1 MHz	33	42.3%	32	41%	37	47.4%	25	32%
94.3 MHz	26	33.3%	26	33.3%	30	38.5%	20	25.6%

Table 49 – detection results for the third considered sequence (intersection between antennas)

For the first sequence, Surv H has the best detection performance for 89.8 and 94.3 MHz, Surv V for 93.8 MHz, Surv 3 for 92.1 MHz, while the best performing channels is 92.1 MHz for all the surveillance antennas. For the second sequence, Surv H is the best performing antenna for both 92.1 and 94.3 MHz, while Surv 3 (V) for 89.8 and 93.8 MHz. Again, 92.1 MHz is the best performing channel, regardless of the surveillance antenna. Finally, for the third considered sequence, Surv 3 performs better than Surv H and Surv V for 89.8 and 94.3 MHz, while Surv V is better for 93.8 and 92.1 MHz (but for 92.1MHz there is just one detection difference with respect to Surv 3). In this case, 92.1 MHz results to be the best performing channel only for Surv H, 93.8 MHz for the two vertically polarized antennas. Therefore, with the partial exception of this last sequence, 92.1 MHz as expected performs better, according to the high theoretical/measured cancellation and lower interference levels observed in the previously described analysis. Also the good detection results obtained for 89.8 and 93.8 MHz with the

two vertically polarized antennas are well in line with the analysis of this configuration in sub-section VIII.6.3).

VIII.7.4 Configuration 4

The analysis of sub-section VIII.6.4 suggested that, for this configuration, the antenna pairs with the best cancellation performance are those with horizontally polarized surveillance (Rev V – Surv H and Ref H – Surv H), except for 93.8 MHz, where pairs with Surv V perform better; these two pairs are also characterized by the lowest INR level, for all the considered FM radio channels. So we can expect the best detection performance coming from pairs with Surv H for all FM channels, except for 93.8 MHz. Also in this case 92.1 MHz (and Ref V – Surv H as antenna pair due to the slightly higher measured cancellation level with respect to the other pairs) was selected as the starting FM channel for sequences identification. The three considered plot sequences are reported in Figure 95, Figure 96 and Figure 97, while the detection results obtained with the different FM radio channels and antenna pairs are summarized in the following three tables, from Table 50 to Table 52.

Sequence #1: from 5 to 112 (total: 108 consecutive data files)								
Frequency / Antenna	Ref V - Surv H		Ref V - Surv V		Ref H - Surv H		Ref H - Surv V	
89.8 MHz	42	38.9%	24	22.2%	29	26.9%	22	20.4%
93.8 MHz	64	59.3%	68	63%	61	56.5%	55	51%
92.1 MHz	67	62%	70	64.8%	69	63.9%	67	62%
94.3 MHz	79	73.1%	28	25.9%	77	71.3%	35	32.4%

Table 50 – detection results for the first considered sequence (single antenna pairs)

Sequence #2: from 102 to 184 (total: 83 consecutive data files)								
Frequency / Antenna	Ref V - Surv H		Ref V - Surv V		Ref H - Surv H		Ref H - Surv V	
89.8 MHz	20	24.1%	3	3.6%	16	19.3%	3	3.6%
93.8 MHz	22	26.5%	37	44.6%	23	27.7%	34	41%
92.1 MHz	47	56.6%	40	48.2%	41	49.4%	47	56.6%
94.3 MHz	47	56.6%	16	19.3%	44	53%	24	28.9%

Table 51 – detection results for the second considered sequence (single antenna pairs)

Sequence #3: from 405 to 500 (total: 96 consecutive data files)								
Frequency / Antenna	Ref V - Surv H		Ref V - Surv V		Ref H - Surv H		Ref H - Surv V	
89.8	22	22.9%	5	5.2%	16	16.7%	13	13.5%
93.8	36	37.5%	60	62.5%	30	31.2%	34	35.4%
92.1	43	44.8%	44	45.8%	41	42.7%	45	46.9%
94.3	26	27.1%	12	12.5%	33	34.4%	17	17.7%

Table 52 – detection results for the third considered sequence (single antenna pairs)

For the first sequence, Ref V – Surv H is the best performing pair for 89.8 and 94. 3MHz (for 94.3 MHz together with Ref H – Surv H), Ref V – Surv V performs better for 93.8 MHz, while 92.1 MHz does not show significant differences between the four pairs. 94.3 MHz is the best performing channel when Surv H is used, 92.1 MHz when Surv V is used (together with 93.8 MHz for Ref V – Surv V).

For the second sequence, the pairs with Surv H perform better for 89.8 and 94.3MHz, and results similar to the first sequence are obtained for 93.8 and 92.1 MHz; 92.1 and 94.3 MHz show better detection performance when Surv H is used, 92.1 MHz when Surv V is used (together with 93.8 when also Ref V is used, i.e. Ref V – Surv V).

Finally, for the third sequence, the same results already seen for the second sequence are obtained (the main difference concerns the best performing channel, that is 92.1 MHz for all the pairs except for Ref V – Surv V, where 93.8 MHz performs better again)

Summarizing, the best performing pairs for 89.8 and 94.3 MHz are those with Surv H, Ref V – Surv V for 93.8 MHz, while 92.1 MHz has not great differences over the different antenna pairs. These results are well in line with the expectations.

Specifically, when considering the FM radio channel 94.3 MHz, there is a great difference in terms of detection performance when Surv H or Surv V is used: Surv H works really better. And this is a confirmation of the results achieved in the previous analysis (see sub-section VIII.6.4): Surv H measured cancellations are higher than in Surv V, and also the interference level is lower. Moreover, the presence of a vertically polarized interference strongly affects the Surv V pairs in terms of detection capability while Surv H performs an higher interference rejection.

Regarding 92.1 MHz FM channel, almost similar detection performance is achieved, regardless of the surveillance antenna polarization. And this result is confirmed by the comparison of measured cancellation and INR levels obtained with Surv H and Surv V in this case, with respect to 94.3 MHz: for 92.1 MHz the difference between the two polarizations are considerably reduced.

This comparison between these different frequencies is very interesting because it is easy to notice that, being the same the geometry (both considered channels are broadcasted by the same transmitter),

interference sources play a relevant role: in fact, if for example the interference is vertically polarized, the use of horizontally polarized antennas can be helpful. The general independence of 92.1 MHz detection performance by antenna polarization gives rise to the hypothesis that more than a single source of interference is simultaneously present, with different polarizations. However, regardless of the number and polarization of interference sources, 92.1 MHz is not surprisingly the best performing channel in this system configuration, due to the reduced overall interference level and high measured cancellations when compared to the three other FM channels.

As already deeply described in Section IV and experimentally verified with two wide-band PBR prototypes (see Section V , VI and VII), the coincidences of the detections at different FM channels can be exploited both for increasing the detection capability (by reducing the undesired degradation effects of the single channel waveform/environment characteristics) and for reducing the false alarms.

Obviously, since the ICS-554B based PBR prototype was developed, a key-point for the validation of its performance was the application of the introduced multi-frequency approach also to data acquired with this device. Due to the absence of real air traffic data for the same days and the same area of the described acquisition campaign, the multi-frequency approach application has been temporally postponed, because without a ground-truth the assessment of the detection performance improvement due to the simultaneous exploitation (and integration) of different FM radio channels with respect to single-channel operation is much more slow and complicated. And this is even truer if the great amount of data acquired during the April 2009 acquisition campaign with ICS-554B is taken into account: therefore, concerning the application of multi-frequency approach to these new data, the work is in progress at the moment of completing the writing of this thesis.

However, it is of great interest the possibility to extend the concept of multi-frequency approach to a multi-polarization integration, which was obviously not allowed with the dual-channel PBR prototypes. This is the reason why the conclusion of this Section, and in particular of the sub-section dedicated to the detection results obtained with configuration 4, exploiting different polarizations with both reference and surveillance antennas, is dedicated to the discussion of the first promising results achieved with the integration of data acquired with differently polarized surveillance antennas, hereafter referred to as polarimetric integration.

Specifically, the *fusion* approach is based on the exploitation of the different integration techniques already described and fully analyzed in the previous sections: centralized linear integration (*SUM*), decentralized integration (*L/N*), centralized non-linear integrations (*MAX* and *MIN*), see Section IV .

It can be useful to recall that the considered configuration (see Table 25 and Figure 50 for more details) is characterized by the presence of two reference and two surveillance antennas, both with

different polarizations, so that four different *reference-surveillance antenna pairs* can be considered in the analysis:

1. Ref V – Surv H
2. Ref V – Surv V
3. Ref H – Surv H
4. Ref H – Surv V

A key point, when considering the integration of different Range-Velocity maps, is the P_{fa} control: for this purpose, it is obviously not possible to integrate the maps obtained with pairs exploiting the same surveillance antenna, because thresholds for CFAR application are evaluated under the hypothesis of statistical independence of integrated data. Following this consideration, only the integration of a maximum of two of four pairs is allowed, and specifically the pairs with the same reference antenna, so Ref V – Surv H and Ref V- Surv V or Ref H – Surv H and Ref H – Surv V.

Also in this case the absence of real ATC data does not allow an overall performance assessment of the detection improvement achieved with the polarimetric integration. This is the reason why in this description the attention is focused on the plot sequences already described in this sub-section, and in particular on the first sequence and on frequency channel 92.1 MHz.

Aiming at a performance comparison between single antenna pairs and after polarimetric integration as complete as possible, an evaluation of the P_{fa} is also required. Specifically, a coarse evaluation of the false alarm rate of the different considered configurations has been obtained by summing all the plots obtained after the CFAR application to the map for each acquisition, and then dividing this number for the product between the single map size and the number of consecutive acquisitions (108 in this case). Obviously, when performing this summation, also the target detections of each acquisition are included in this P_{fa} coarse evaluation (this is a direct consequence of the ground-truth absence, in fact it is not possible to discriminate and carefully evaluate how many of the N plots of each acquisition are false alarms and how many are target detections). However, we expect that only a reduced number of the total amount of plots for each acquisition represent target detection, so this P_{fa} coarse evaluation can be considered satisfactory.

With reference to the first considered set of 108 consecutive acquisitions (from number 5 to 112), the plot sequences obtained after different polarimetric integrations are reported in eight figures: specifically, Figure 98 and Figure 99 refer to the linear polarimetric integration (SUM) with Ref V (i.e. Ref V – Surv H and Ref V – Surv V) and Ref H (i.e. Ref H – Surv H and Ref H – Surv V), respectively, Figure 100 and Figure 101 refer to MAX polarimetric integration (with the two Ref V pairs and the two

Ref H pairs, respectively), Figure 102 and Figure 103 are relative to the MIN polarimetric integration, finally Figure 104 and Figure 105 refer to the decentralized (DEC) polarimetric integration (in this configuration a 2/2 logic was used).

As it is apparent, the number of detection is increased with respect to single pair case, in particular a comparison between Figure 95 (which refers to the same sequence, observed with Ref V – Surv H pair) and Figure 98 (SUM polarimetric integration with the same reference antenna) clearly shows that *(i)* the number of detections for the considered sequence is increased, and *(ii)* new target sequences are now clearly individuate, located at higher bistatic ranges: 25, 40, 65, 75, 80 and 100 bistatic km (for a clear identification of these sequences, they are mainly located in the region of bistatic velocities included between -100 and 100m/s). Similar results are obtained with the other polarimetric integration schemes, in particular good detection results are obtained with SUM (Ref H) and with MAX (both with Ref V and Ref H), while MIN and DEC integration techniques show quite poor results.

However, it is also easy to notice that the number of false alarms after polarimetric integrations is not equal to the single pair situation, and also it is not the same between different integration schemes. This is clearly visible in the two following tables, where detection results and coarse P_{fa} evaluation for the considered polarimetric integration schemes are summarized. Specifically, Table 53 reports the results obtained when considering the polarimetric integration of Ref V pairs (i.e. Ref V – Surv H and Ref V – Surv V), while Table 54 is referred to the results achieved after the integration of Ref H pairs, namely Ref H – Surv H and Ref H – Surv V pairs. In order to perform a direct and immediate performance comparison, the results of Table 50 are also reported, which refer to the number of detections measured with the single antenna pairs, properly splitted in the two new tables.

Sequence #1: from 5 to 112 (total: 108 consecutive data files)												
CONFIGURATION →	Ref **V** - Surv H		Ref **V** - Surv V		SUM		MAX		MIN		DEC	
number of detection	67	62%	70	64.8%	86	79.6%	86	79.6%	73	67.6%	73	67.6%
P_{fa} estimation	$1.61 \cdot 10^{-4}$		$1.63 \cdot 10^{-4}$		$2.60 \cdot 10^{-4}$		$2.01 \cdot 10^{-4}$		$2.09 \cdot 10^{-4}$		$2.58 \cdot 10^{-4}$	

Table 53 – performance comparison for the first considered sequence (single antenna pairs versus polarimetric integrations with Ref V pairs)

Sequence #1: from 5 to 112 (total: 108 consecutive data files)												
CONFIGURATION →	Ref **H** - Surv H		Ref **H** - Surv V		SUM		MAX		MIN		DEC	
number of detection	69	63.9%	67	62%	89	82.4%	86	79.6%	66	61.1%	72	66.7%
P_{fa} estimation	$1.58 \cdot 10^{-4}$		$1.69 \cdot 10^{-4}$		$2.47 \cdot 10^{-4}$		$1.96 \cdot 10^{-4}$		$2.16 \cdot 10^{-4}$		$2.44 \cdot 10^{-4}$	

Table 54 – performance comparison for the first considered sequence (single antenna pairs versus polarimetric integrations with Ref H pairs)

As it is apparent, a significant increase in the number of detection for the considered sequence is achieved, with both the reference antennas (Ref V pairs and Ref H pairs), in particular when SUM

and/or MAX polarimetric integrations are performed. MIN and DEC also result, except for one case, in increased detections, but with a reduced improvement with respect to SUM and MAX.

However, notice that this general increase of detection performance is paid in terms of number of false alarms appearing in the maps. Even if this growth is not so high, and the coarse evaluated P_{fa} is still in line with the imposed nominal value (10^{-4}), this reduced P_{fa} control can represent a potential limiting factor when dealing with the application of a tracking algorithm to the output maps.

Aiming at effectively exploiting the detection performance improvement due to polarimetric integration by achieving a proper P_{fa} control, the different integration schemes are applied together with a slight modification of the CFAR detection schemes thresholds. Specifically, when considering the polarimetric integration of Ref V pairs – obviously the same applies for Ref H pairs – the P_{fa} values obtained for the two single pair configuration (Ref V – Surv H and Ref V – Surv V) are assumed as benchmark values for the P_{fa} estimation desired after polarimetric integration; therefore, CA autogate gain is changed aiming at approximating as more as possible, after the application of each polarimetric integration scheme, these P_{fa} benchmark values. When a P_{fa} value lower or equal to these benchmarks has been obtained, the corresponding gain value is assumed as the autogate gain for the threshold setting. This approach is aimed at verifying if such a scheme for the P_{fa} control strongly affects the polarimetric integration detection performance, so if after this threshold enhancement a significant decrease of target detections is experienced. The results of this threshold modification are reported in Table 55 and Table 56 for Ref V pairs and Ref H pairs, respectively (also in this case the results of Table 50 are reported, which refer to the number of detections measured with the single antenna pairs). As it is apparent by comparing the estimated P_{fa} values obtained with the different polarimetric integration schemes of these two tables with the corresponding values of Table 53 and Table 54, a significant reduction has been achieved for all the considered schemes, and the obtained values are now lower than the corresponding single pairs values. Moreover, the number of detections for the considered sequence largely comparable with the previously obtained results, and only a very limited reduction in terms of detection performance is experienced.

Sequence #1: from 5 to 112 (total: 108 consecutive data files)												
CONFIGURATION →	Ref **V** - Surv H		Ref **V** - Surv V		SUM		MAX		MIN		DEC	
number of detection	67	62%	70	64.8%	84	77.8%	84	77.8%	68	63.0%	70	64.8%
P_{fa} estimation	$1.61\cdot10^{-4}$		$1.63\cdot10^{-4}$		$1.59\cdot10^{-4}$		$1.54\cdot10^{-4}$		$1.60\cdot10^{-4}$		$1.61\cdot10^{-4}$	

Table 55 – performance comparison for the first considered sequence (single antenna pairs versus polarimetric integrations with Ref V pairs) with *P_{fa} control*

Sequence #1: from 5 to 112 (total: 108 consecutive data files)												
CONFIGURATION →	Ref **H** - Surv H		Ref **H** - Surv V		SUM		MAX		MIN		DEC	
number of detection	69	63.9%	67	62%	85	78.7%	85	78.7%	65	60.2%	71	65.7%
P_{fa} estimation	$1.58 \cdot 10^{-4}$		$1.69 \cdot 10^{-4}$		$1.55 \cdot 10^{-4}$		$1.52 \cdot 10^{-4}$		$1.62 \cdot 10^{-4}$		$1.57 \cdot 10^{-4}$	

Table 56 – performance comparison for the first considered sequence (single antenna pairs versus polarimetric integrations with Ref H pairs) with P_{fa} *control*

As an example, Figure 106 shows the plot sequences obtained after linear polarimetric integration (SUM) with Ref V (i.e. Ref V – Surv H and Ref V – Surv V). A visual comparison with Figure 98 clearly shows the significant reduction of false alarms, while the considered sequence is still clearly visible, as well as the new sequences located at higher bistatic ranges, even if a slight reduction in the number of detections is experienced.

VIII.8 *Conclusions*

The development of a multi-channel PBR prototype allowed to expand the analysis performed with the two wide-band prototypes, aiming at further enhancing the surveillance capabilities of the PBR system. Specifically, the availability of data acquired with different antenna polarizations (both for reference and surveillance channels) allowed a new analysis of the impact of the opportunity waveform polarization in the system performance. The results of these analysis indicate that the exploitation of different polarization, also by integrating the polarimetric information simultaneously available when using more than one reference/surveillance receiving channel, make the detection scheme robust with respect to both the content of the broadcast radio program and the propagation channel conditions. In particular, the limiting factor represented by the presence of interference sources, such as other FM radio transmissions acting as co-/inter-channel interference, can be significantly contained by exploiting different polarizations. This is confirmed by the achieved improvement in the system detection performance due to the polarimetric integration. In addition, also in this case, the multi-frequency approach is expected to yield significant improved detection performance with respect to the single FM radio channels. Moreover, the use of a receiver with on-board DDC capability allowed us to sensibly reduce both the temporal distance between consecutive acquisitions (now long duration streaming acquisitions with up to four simultaneous receiving antennas are available) and the time needed for the (off-line) analysis of stored data (there is no more need for a software extraction of the FM radio channels of interest). This important feature, together with the exploitation of proper processing techniques (implemented in parallel research activities of the research group I was inserted in, see for example [26]) for the computational load reduction of cancellation and 2D-CCF evaluation, is essential for PBR real-time operations.

Finally, the availability of more than two receiving channels gives us the possibility to exploit the problem of DOA estimation. This is also an open problem, under investigation at the moment of completing this thesis. New acquisition campaigns are planned, to be performed in the near future, aiming at further investigating these open problems, also by exploiting new receiver sites and/or new transmitters of opportunity, and providing an extensive performance assessment of the detection capabilities of this new PBR prototype when considering multi-frequency and/or polarimetric integration approaches. In fact, the recent acquisition of a Mode-S/Automatic dependent surveillance-broadcast (ADS-B) receiver allows tracking ADS-B aircrafts and the identification of Mode-S equipped aircrafts. For each cooperative target, it allows a complete real-time identification, 3-D localization and

tracking, including information such as ModeS address (i.e. flight ID), Callsign, Country, Altitude, Latitude, Longitude, Vertical Rate, Ground Speed, Track (heading angle with respect to North), and so on. This receiver will made possible the registration of live air traffic data in the acquisition campaign locations, thus resulting in the complete availability of the ground-truth required for an extensive and complete PBR system performance evaluation.

VIII.9 *Figures*

Figure 33 – ICS-554B.

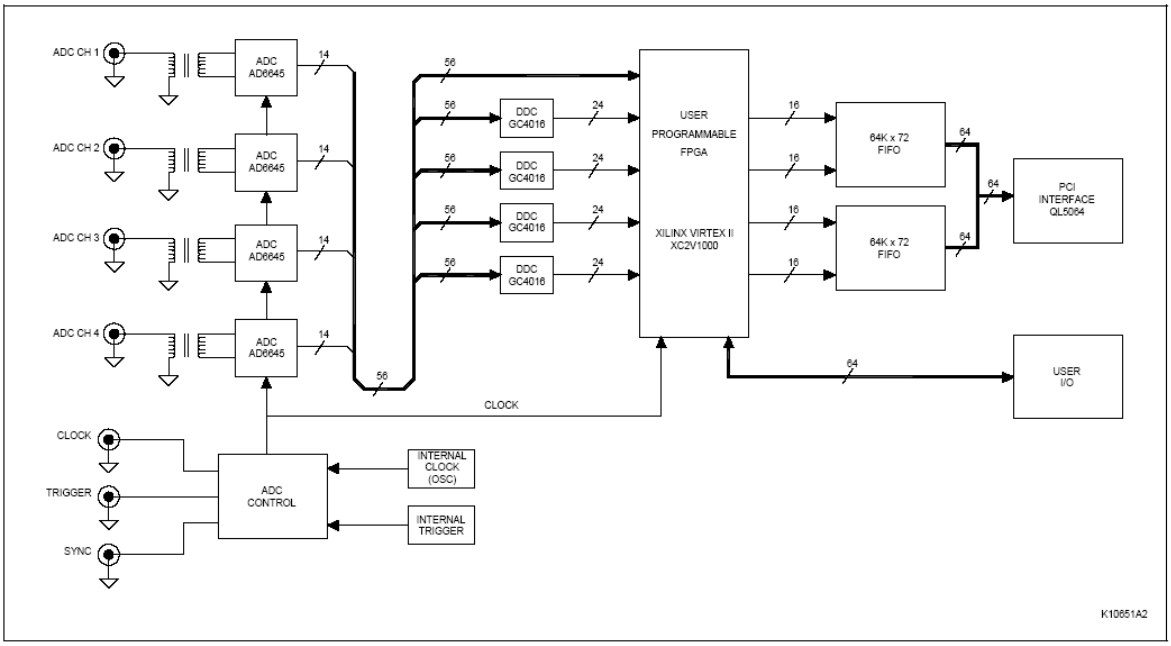

Figure 34 – ICS-554B block diagram.

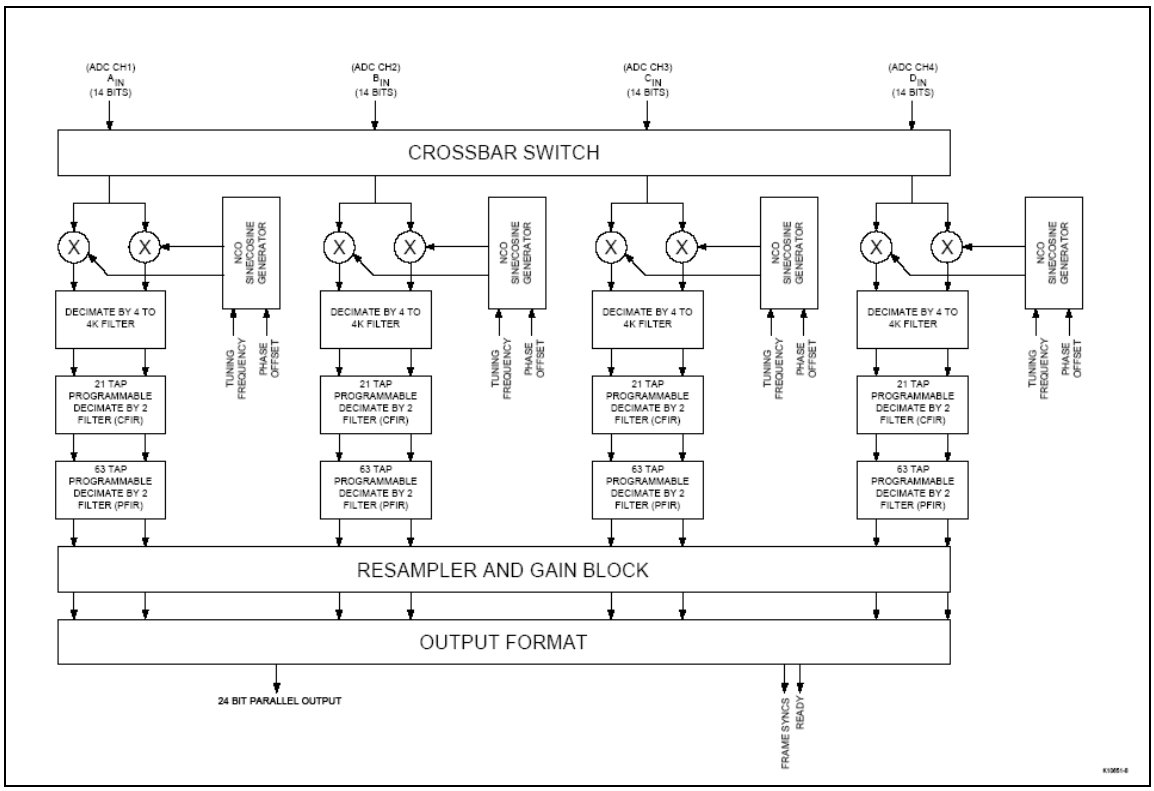

Figure 35 – GC4016 block diagram.

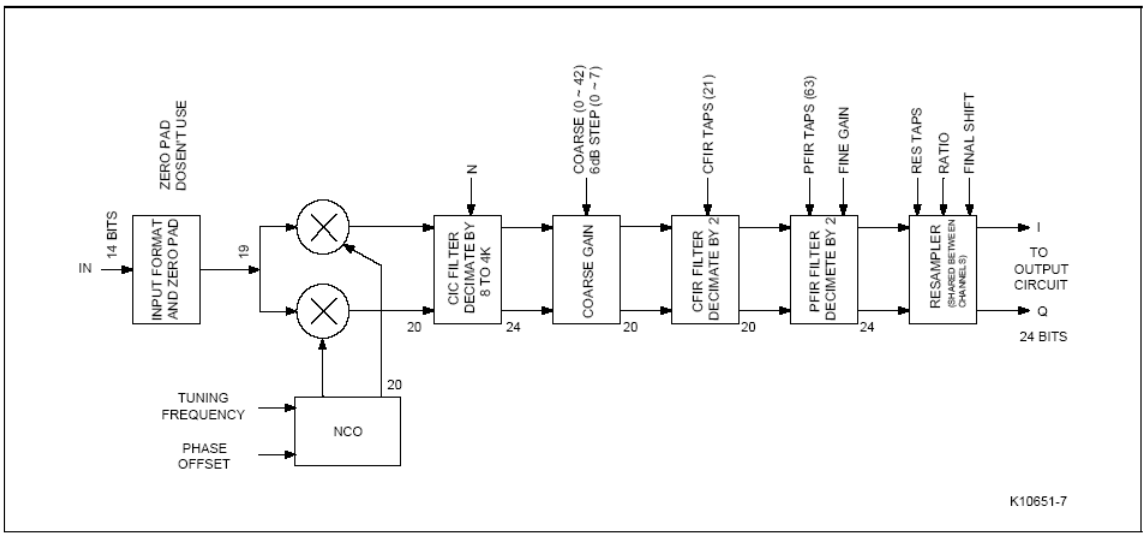

Figure 36 – GC4016 single channel block diagram.

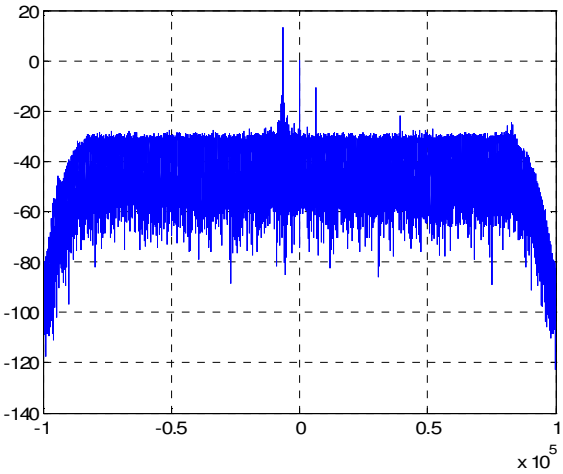

Figure 37 – Power spectrum of channel *A* input signal, first sub-channel output (88 MHz).

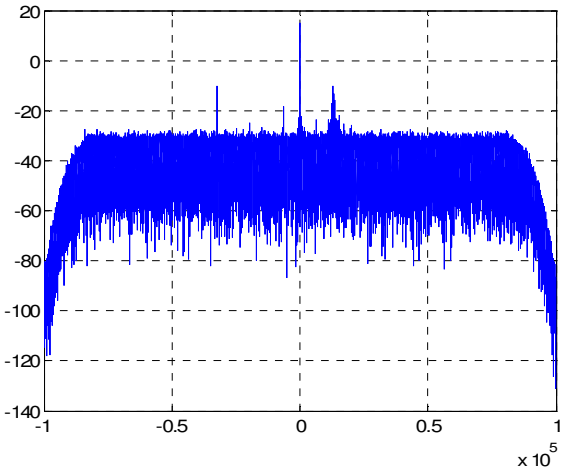

Figure 38 – Power spectrum of channel *C* input signal, 9th sub-channel output (104 MHz).

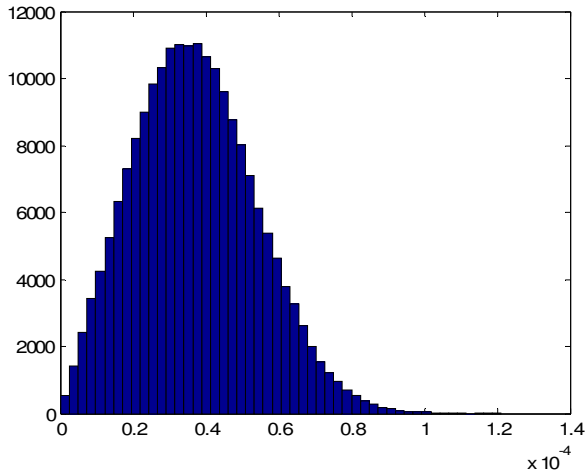

Figure 39 – Histogram of channel *C* input signal, 9th sub-channel output (104 MHz).

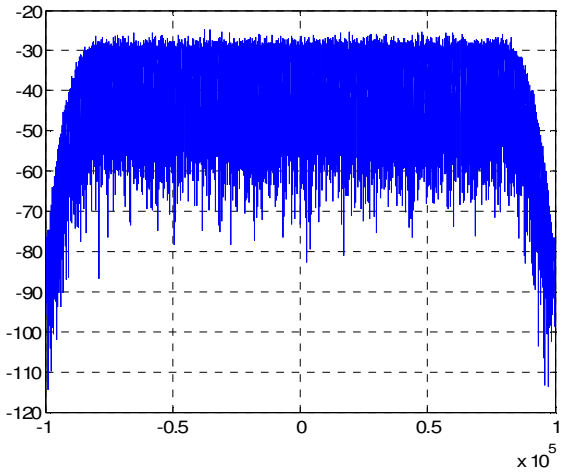

Figure 40 – Power spectrum of channel *A* input signal, 8th sub-channel output (91.5 MHz).

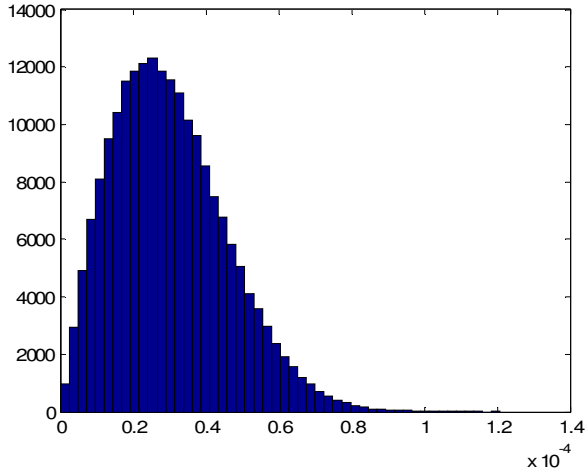

Figure 41 – Histogram of channel *A* input signal, 8th sub-channel output (91.5 MHz).

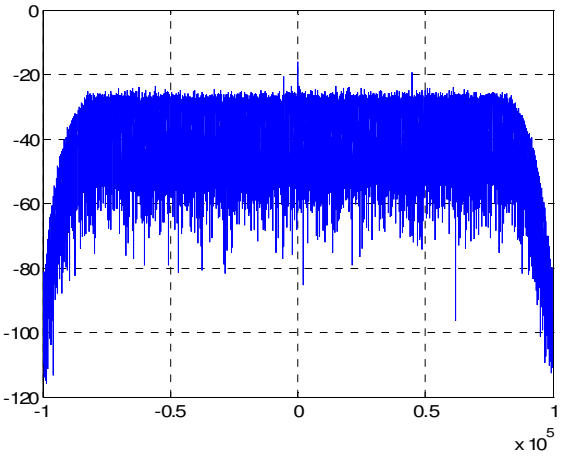

Figure 42 – Power spectrum of channel *B* input signal, 11th sub-channel output (97 MHz).

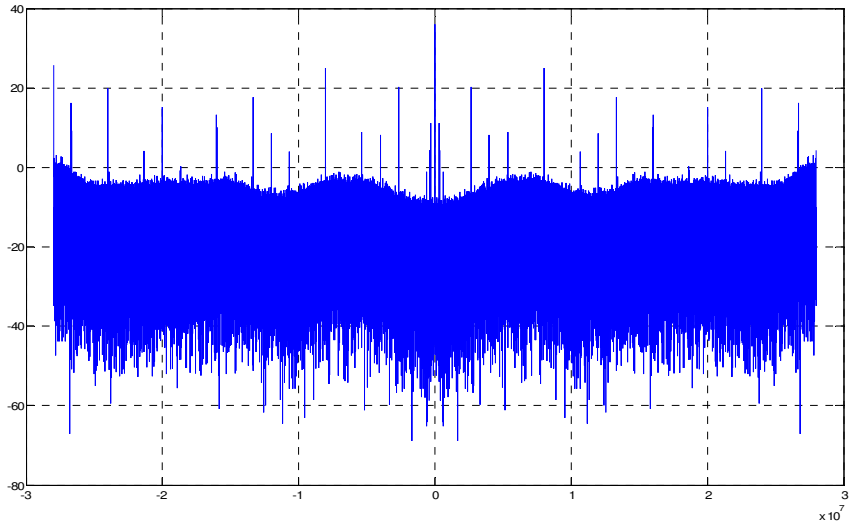

Figure 43 – *wide-band* power spectrum (acquis. duration = 0.5 sec, sampling freq. = 56 MHz).

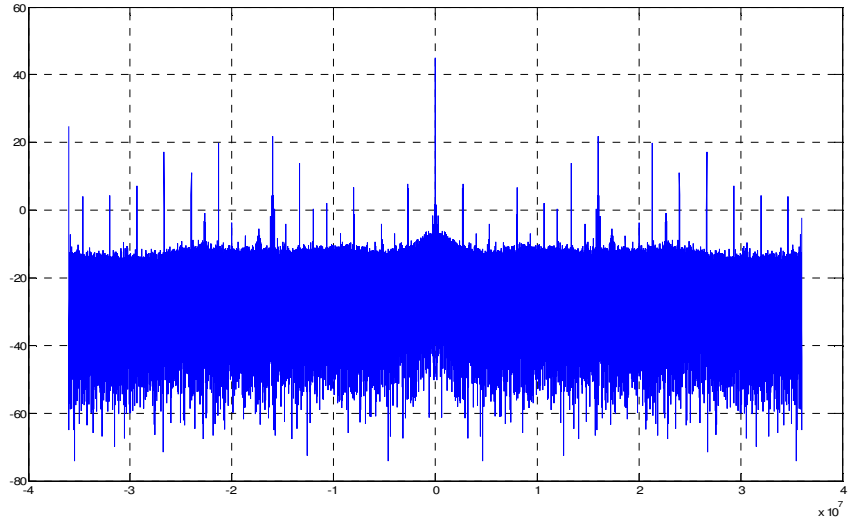

Figure 44 – *wide-band* power spectrum (acquis. duration = 0.5 sec, sampling freq. = 72 MHz).

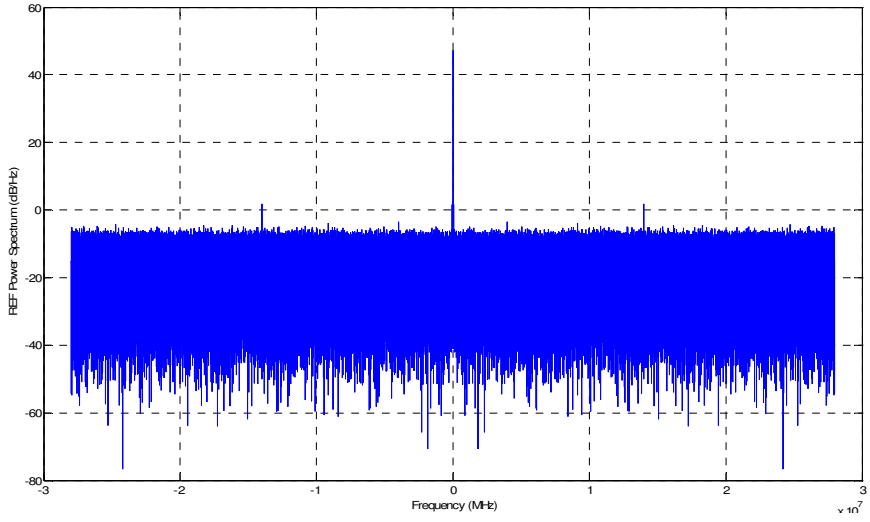

Figure 45 – *wide-band* power spectrum (NI PXI-5122, sampling freq. = 56 MHz).

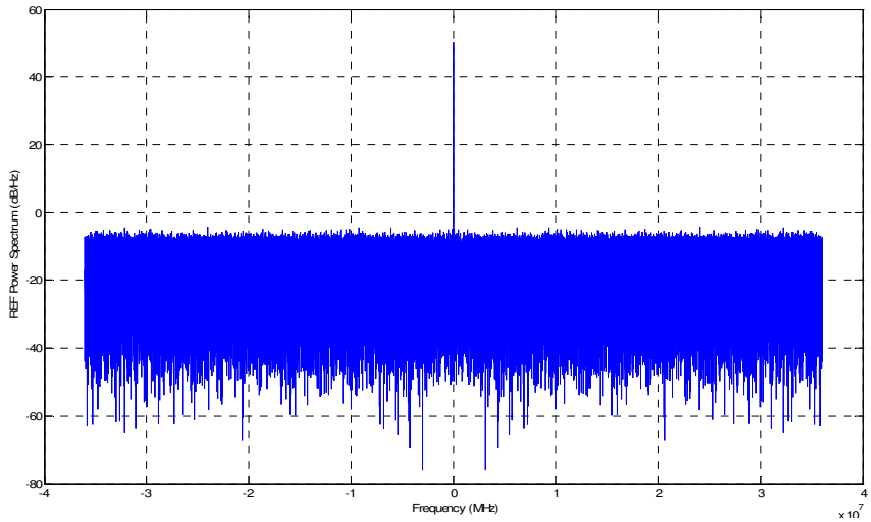

Figure 46 – *wide-band* power spectrum (NI PXI-5122, sampling freq. = 72 MHz).

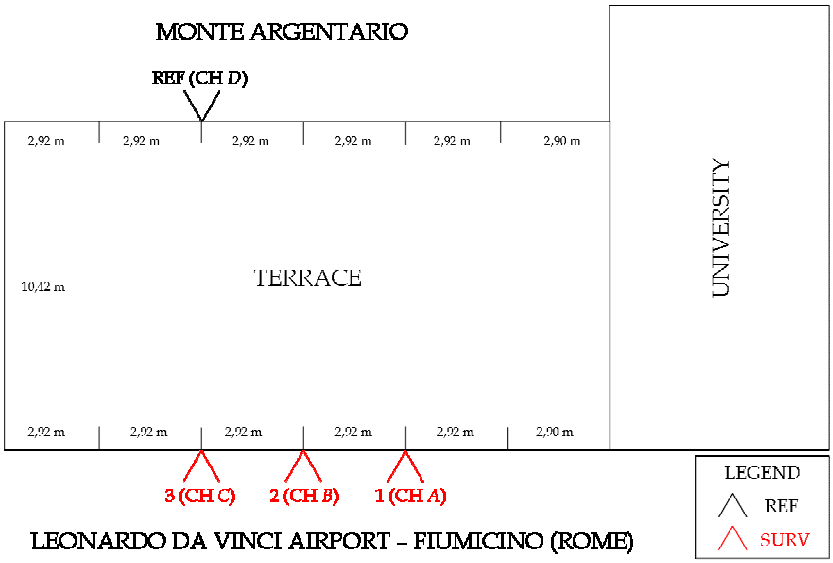

Figure 47 – Sketch of the receiver site (also configurations 1, 5 and 6).

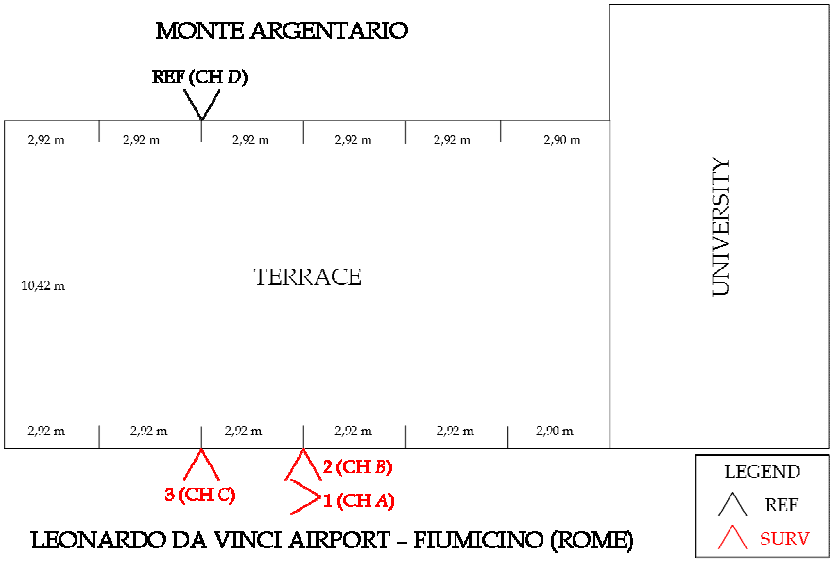

Figure 48 – Sketch of the receiver site – configurations 2, 7 and 8.

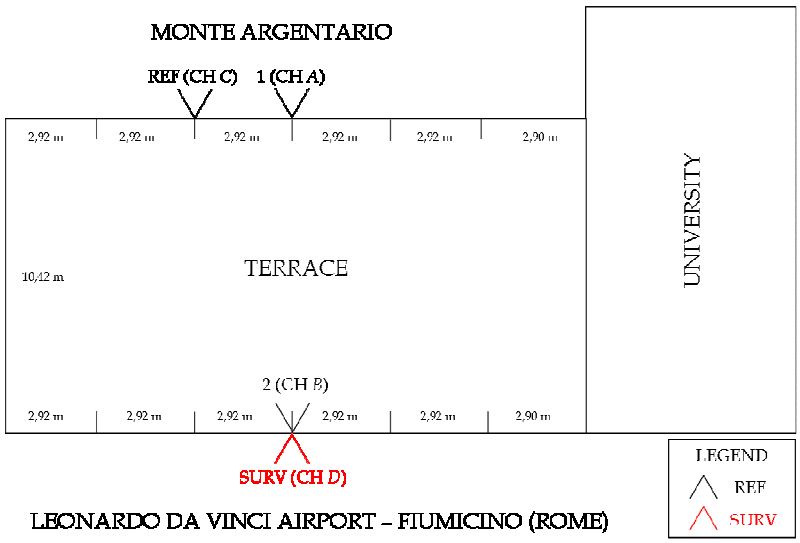

Figure 49 – Sketch of the receiver site – configuration 3.

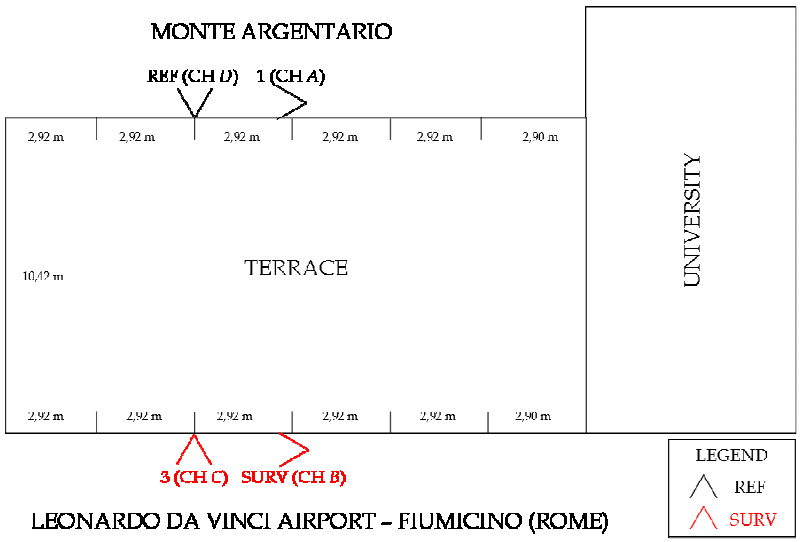

Figure 50 – Sketch of the receiver site – configuration 4.

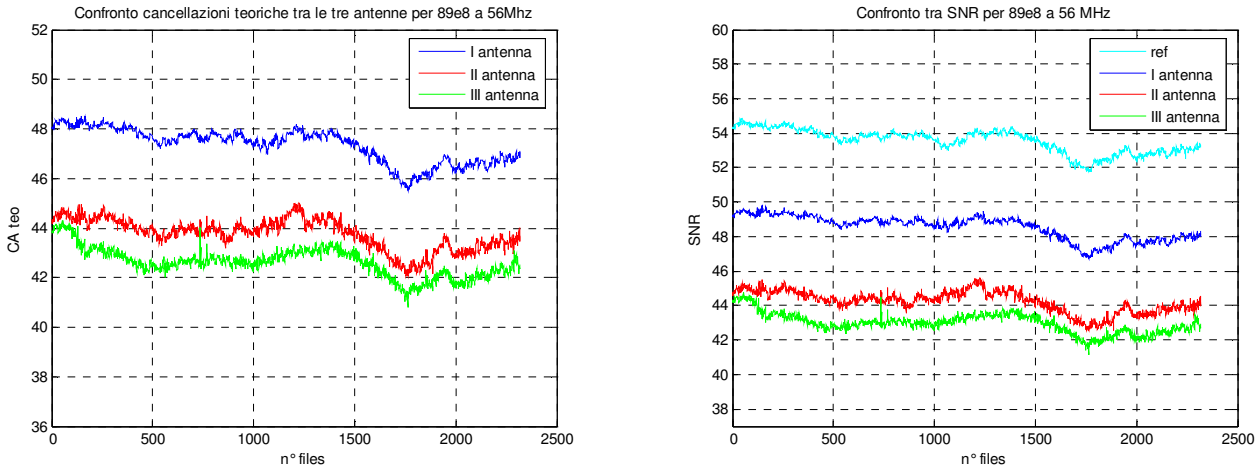

(a) (b)

Figure 51 – Theoretical cancellation values obtained with the three antennas of Configuration 1 (a) and SNR values obtained with the four system antennas (b) [FM channel: 89.8 MHz].

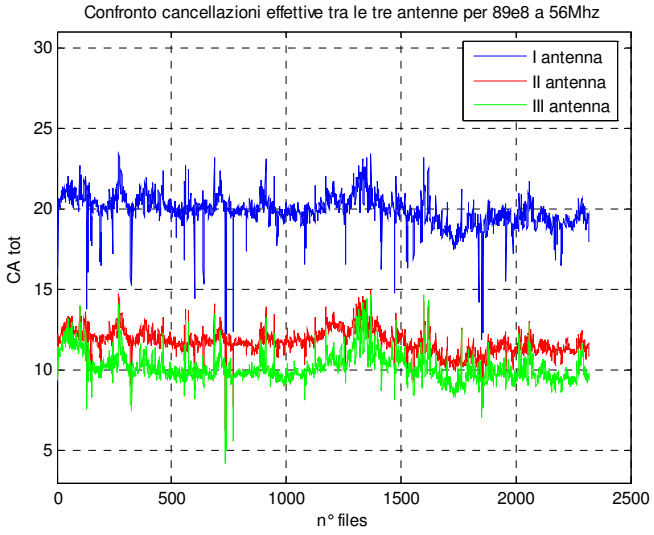

Figure 52 – Measured cancellation values obtained with the 3 antennas of Conf. 1 @ 89.8 MHz.

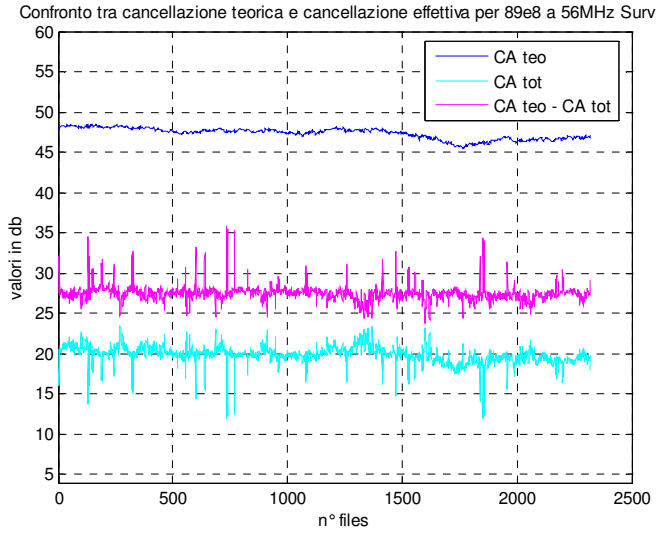

(a)

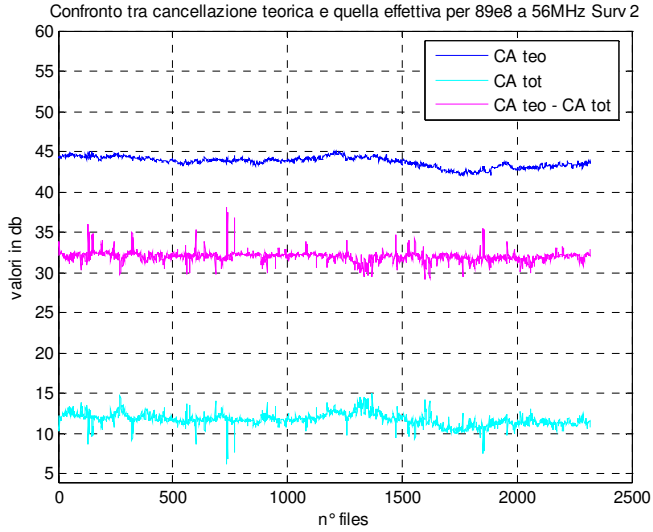

(b)

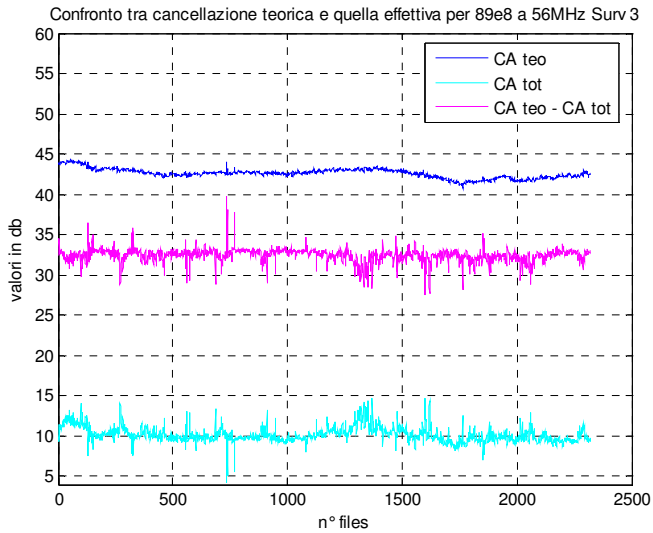

(c)

Figure 53 – Comparison between theoretical and measured cancellation values for the three antennas of Configuration 1: Surv 1 (a), Surv 2 (b) and Surv 3 (c) [FM channel: 89.8 MHz].

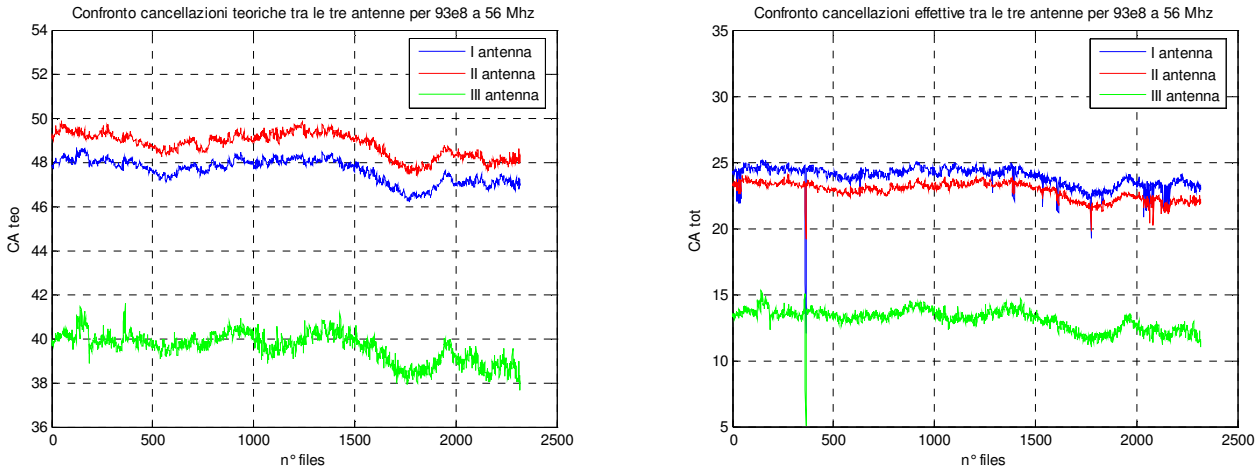

(a) (b)

Figure 54 – Theoretical (a) and measured (b) cancellation values obtained with the three antennas of Configuration 1 [FM channel: 93.8 MHz].

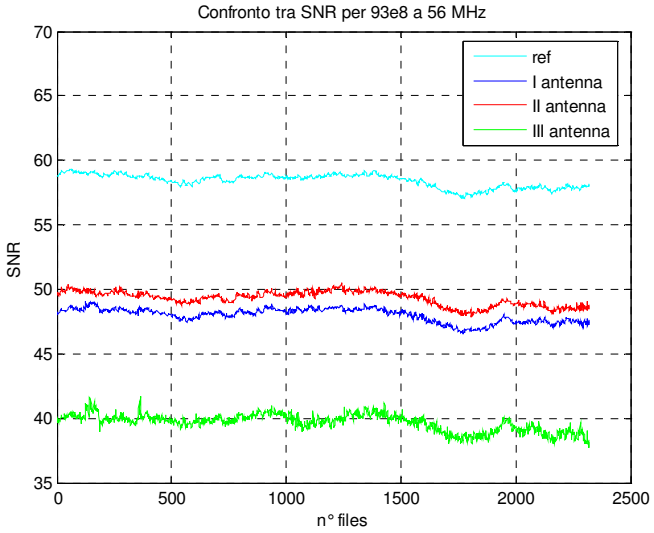

Figure 55 –SNR values obtained with the four system antennas [FM channel: 93.8 MHz].

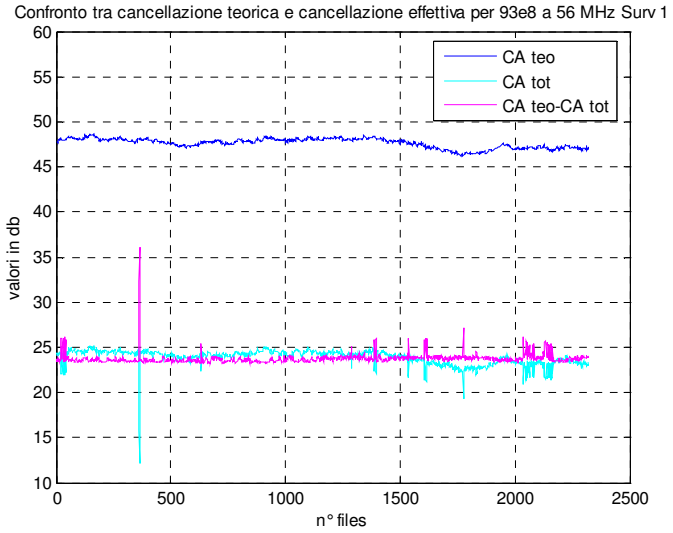

(a)

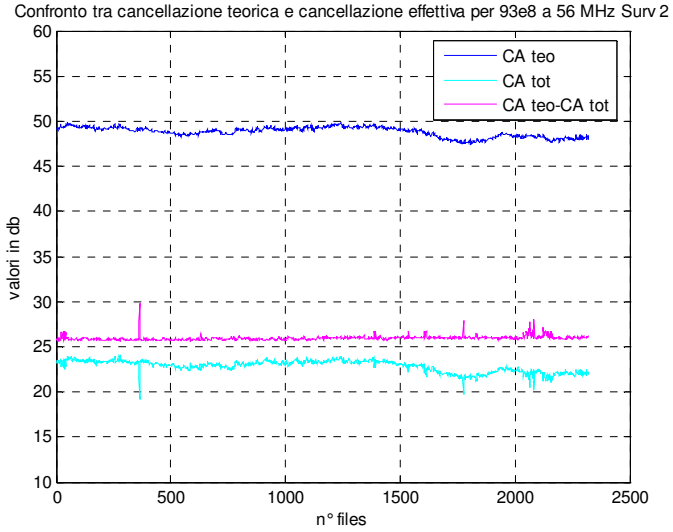

(b)

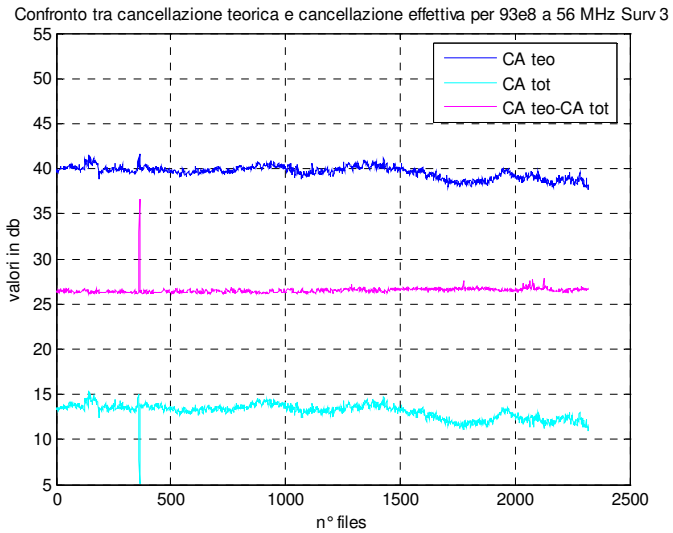

(c)

Figure 56 – Comparison between theoretical and measured cancellation values for the three antennas of Configuration 1: Surv 1 (a), Surv 2 (b) and Surv 3 (c) [FM channel: 89.8 MHz].

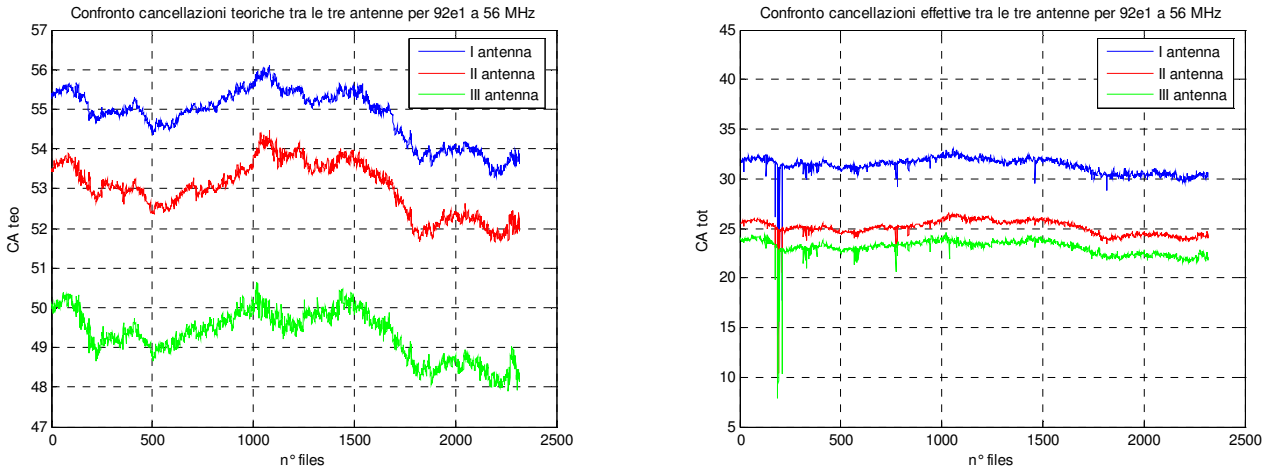

(a) (b)

Figure 57 – Theoretical (a) and measured (b) cancellation values obtained with the three antennas of Configuration 1 [FM channel: 92.1 MHz].

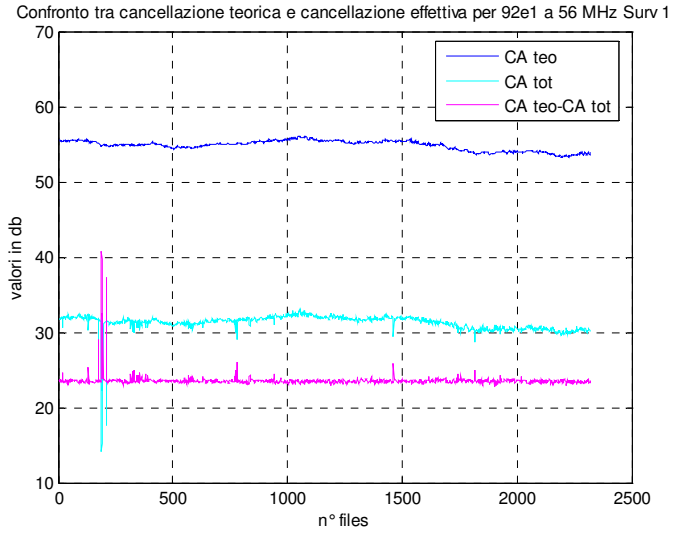

(a)

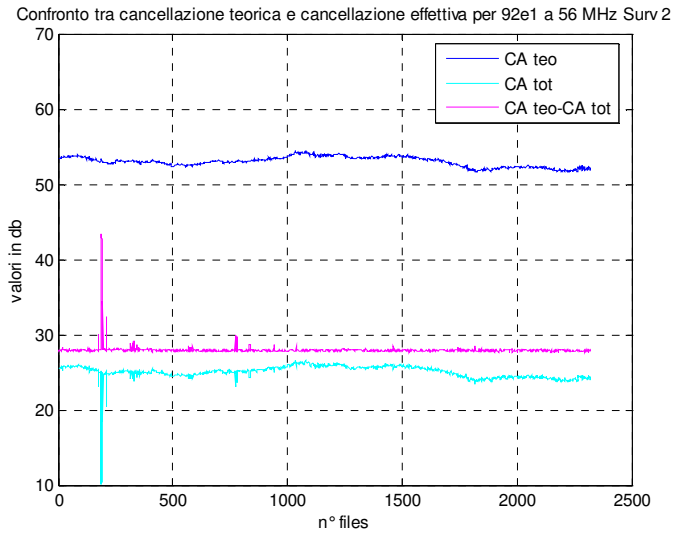

(b)

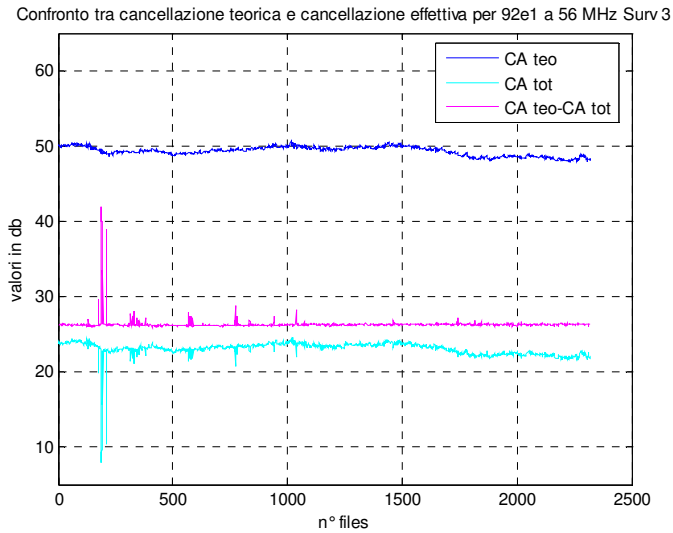

(c)

Figure 58 – Comparison between theoretical and measured cancellation values for the three antennas of Configuration 1: Surv 1 (a), Surv 2 (b) and Surv 3 (c) [FM channel: 92.1 MHz].

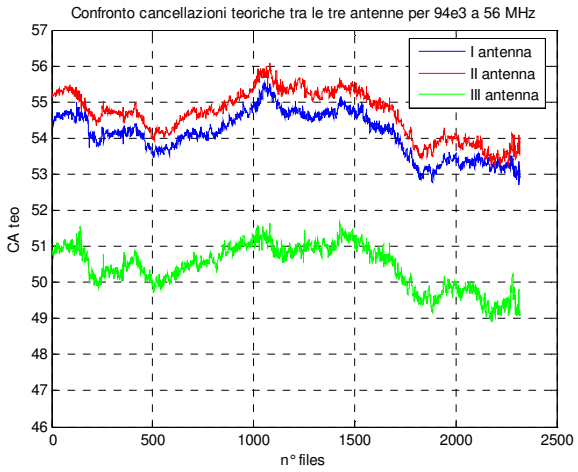

(a)

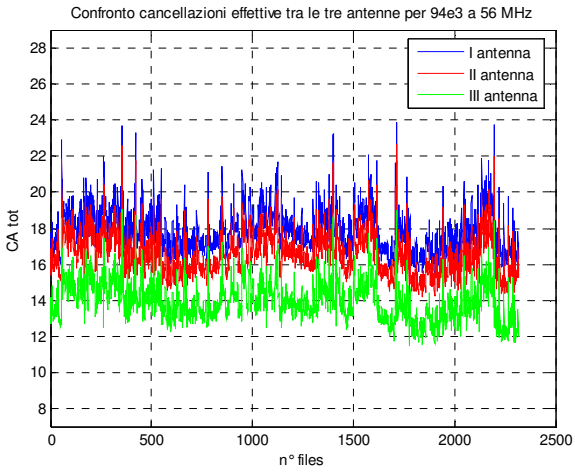

(b)

Figure 59 – Theoretical (a) and measured (b) cancellation values obtained with the three antennas of Configuration 1 [FM channel: 94.3 MHz].

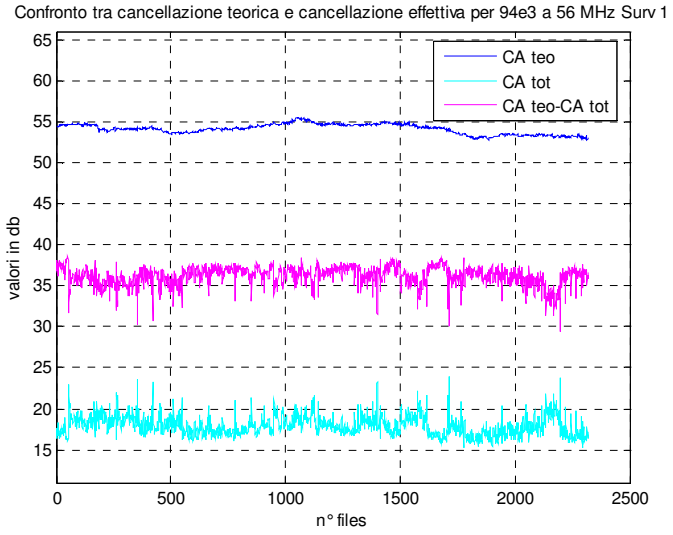

(a)

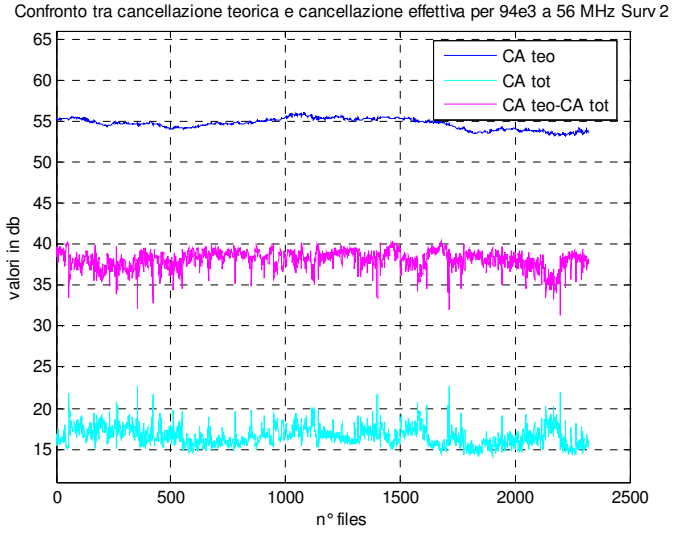

(b)

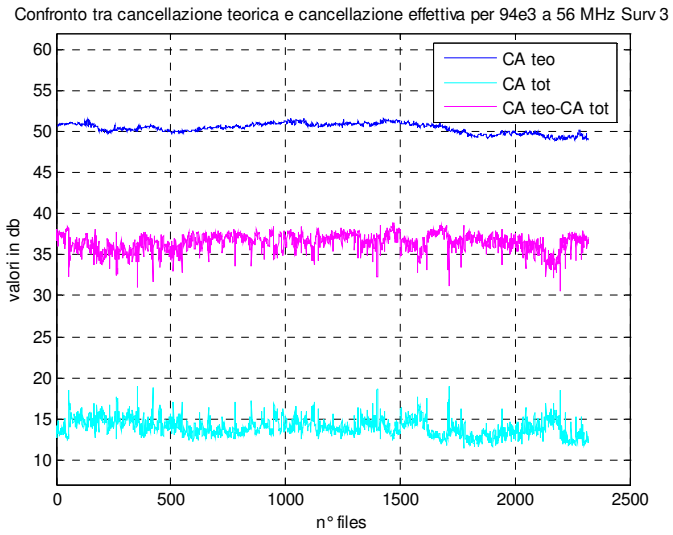

(c)

Figure 60 – Comparison between theoretical and measured cancellation values for the three antennas of Configuration 1: Surv 1 (a), Surv 2 (b) and Surv 3 (c) [FM channel: 94.3 MHz].

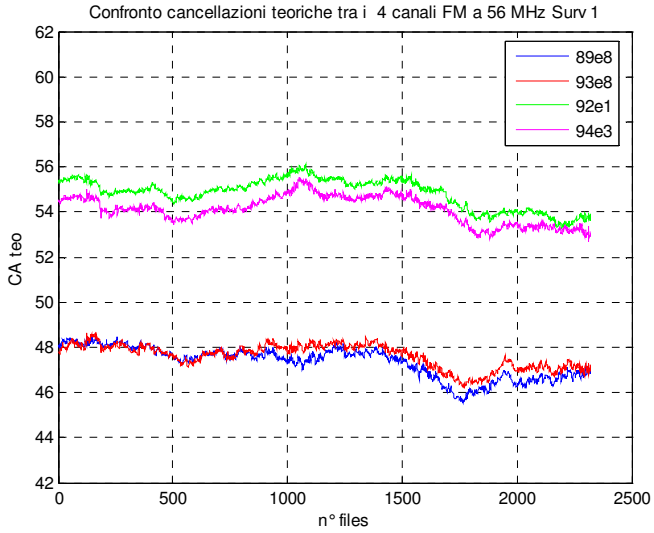

(a)

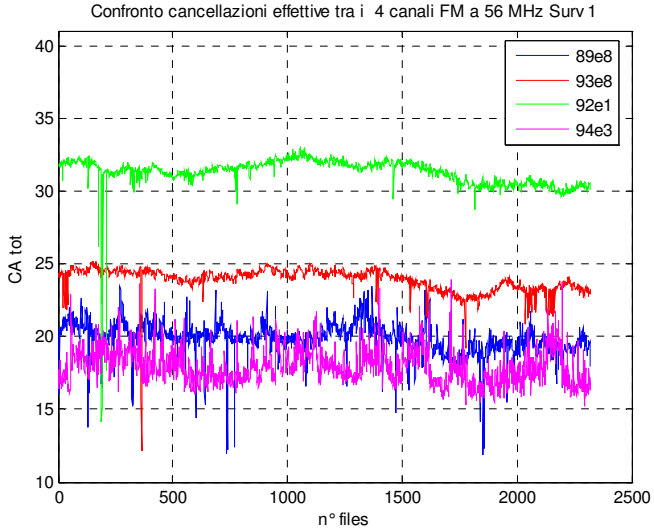

(b)

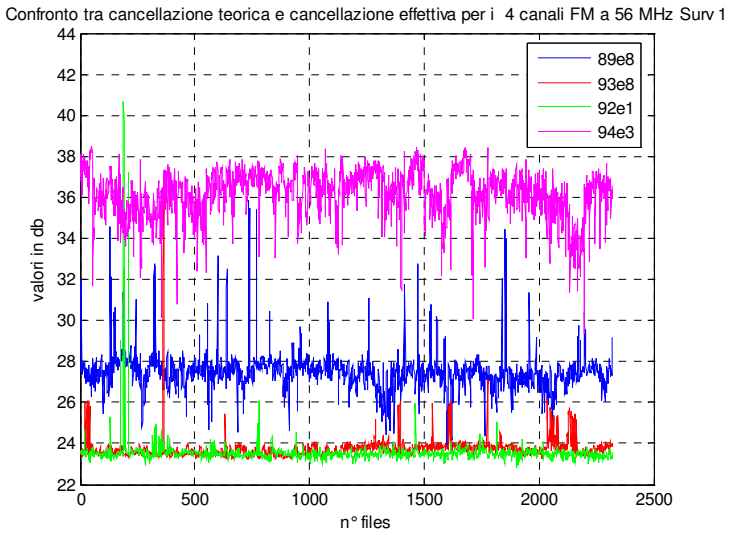

(c)

Figure 61 – Theoretical (a), measured (b) and difference between theoretical and measured (c) cancellation values obtained with the four FM channels [Conf. 1 – Surv 1].

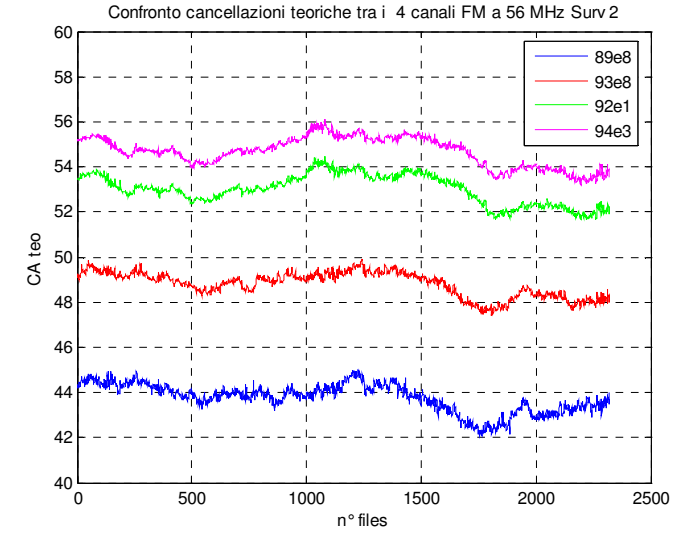

(a)

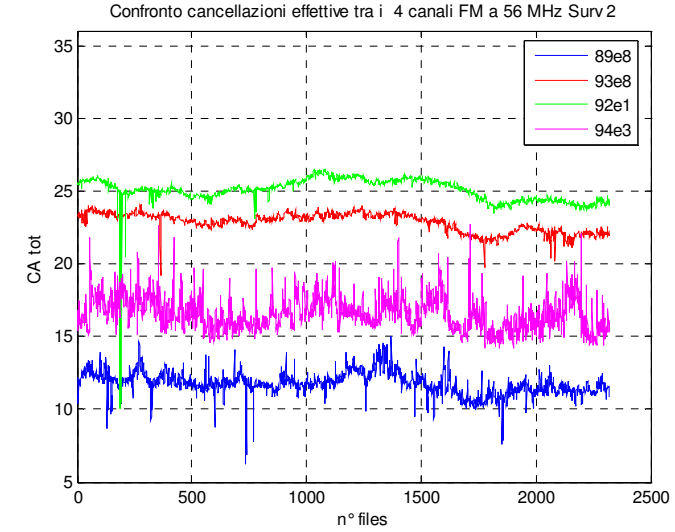

(b)

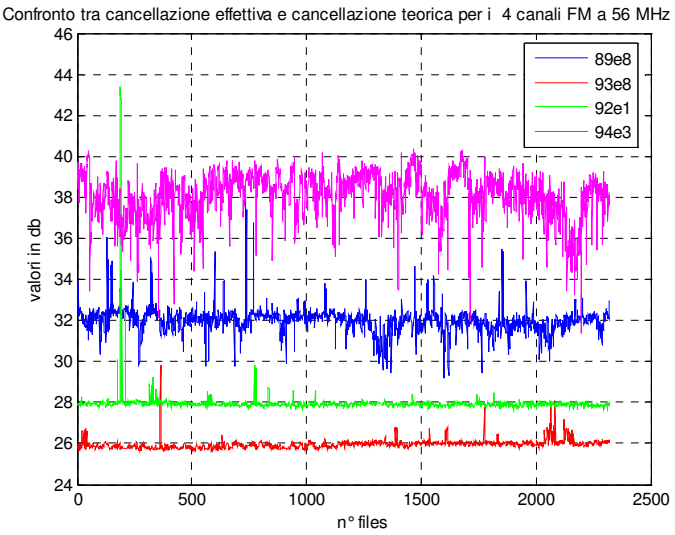

(c)

Figure 62 – Theoretical (a), measured (b) and difference between theoretical and measured (c) cancellation values obtained with the four FM channels [Conf. 1 – Surv 2].

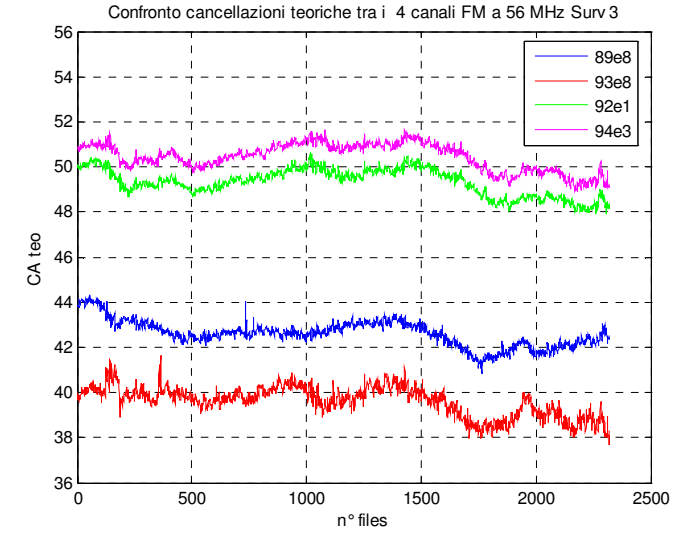

(a)

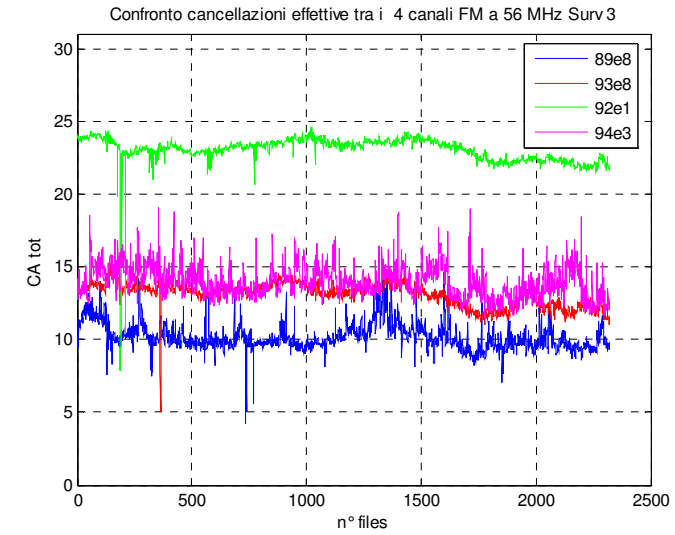

(b)

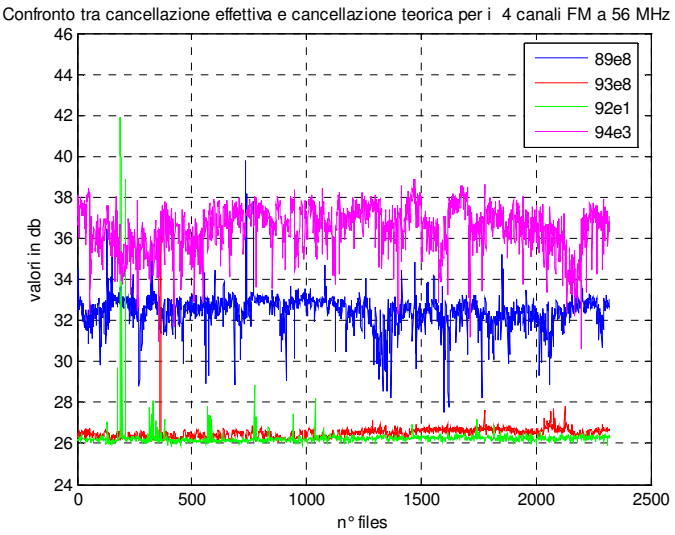

(c)

Figure 63 – Theoretical (a), measured (b) and difference between theoretical and measured (c) cancellation values obtained with the four FM channels [Conf. 1 – Surv 3].

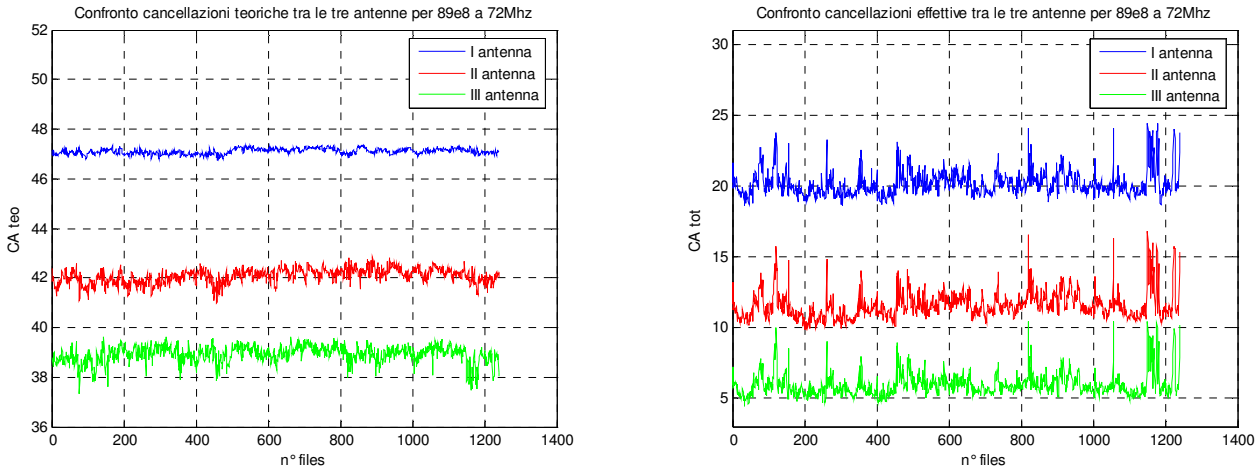

(a) (b)

Figure 64 – Theoretical (a) and measured (b) cancellation values obtained with the three antennas of Configuration 5 [FM channel: 89.8 MHz].

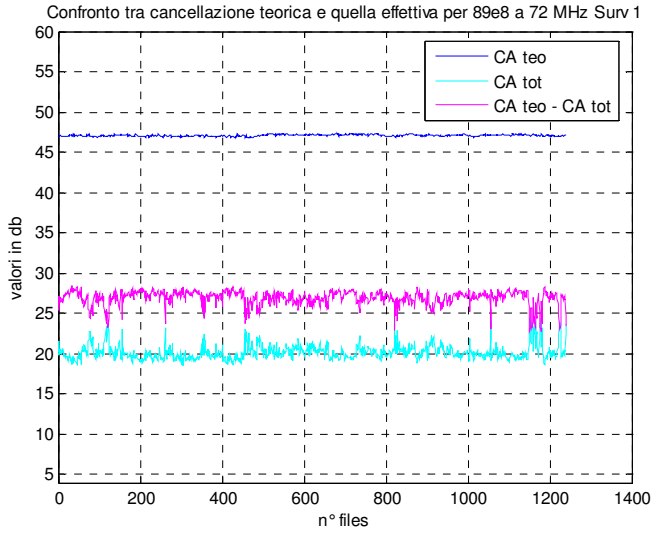

(a)

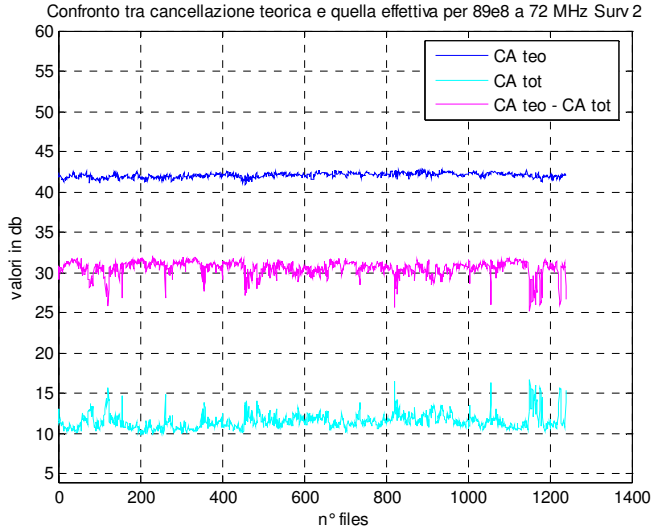

(b)

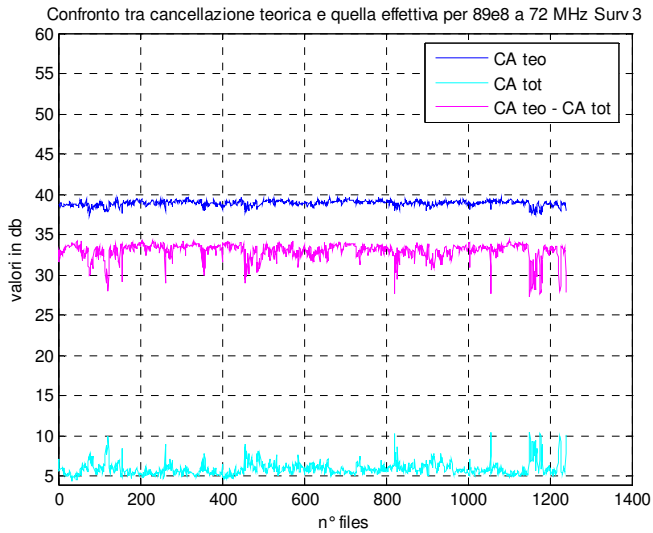

(c)

Figure 65 – Comparison between theoretical and measured cancellation values for the three antennas of Configuration 2: Surv 1 (a), Surv 2 (b) and Surv 3 (c) [FM channel: 89.8 MHz].

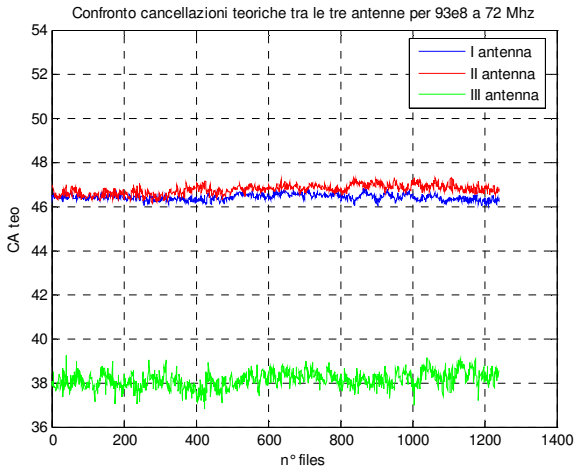

(a)

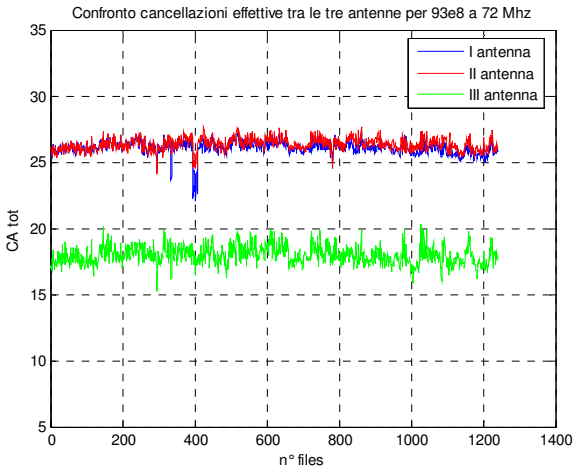

(b)

Figure 66 – Theoretical (a) and measured (b) cancellation values obtained with the three antennas of Configuration 5 [FM channel: 93.8 MHz].

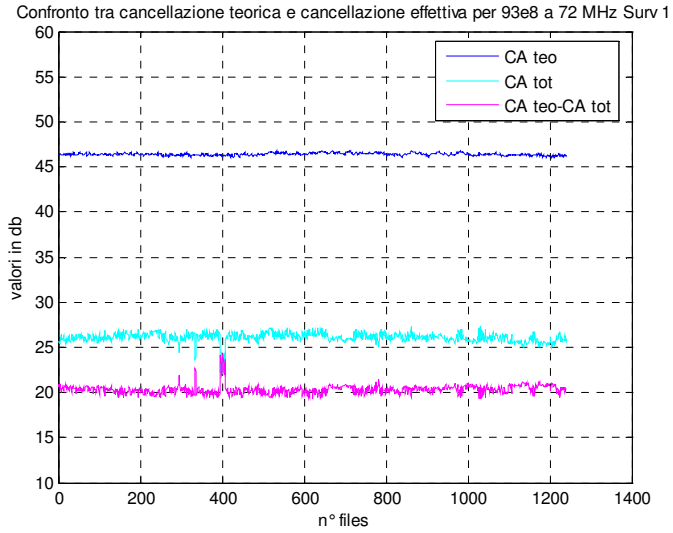

(a)

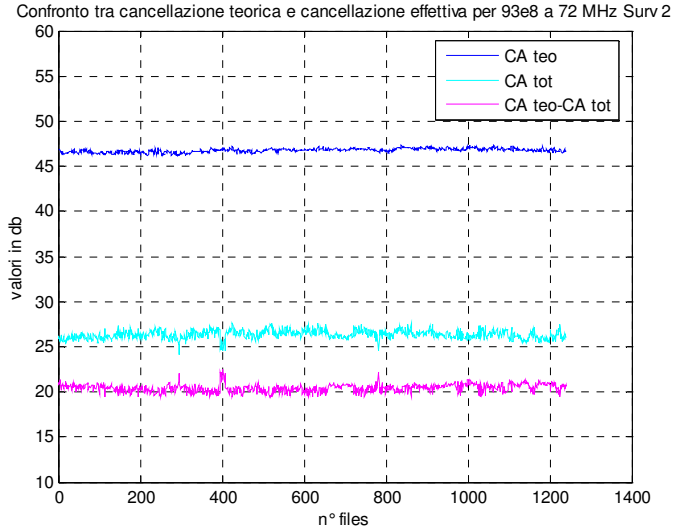

(b)

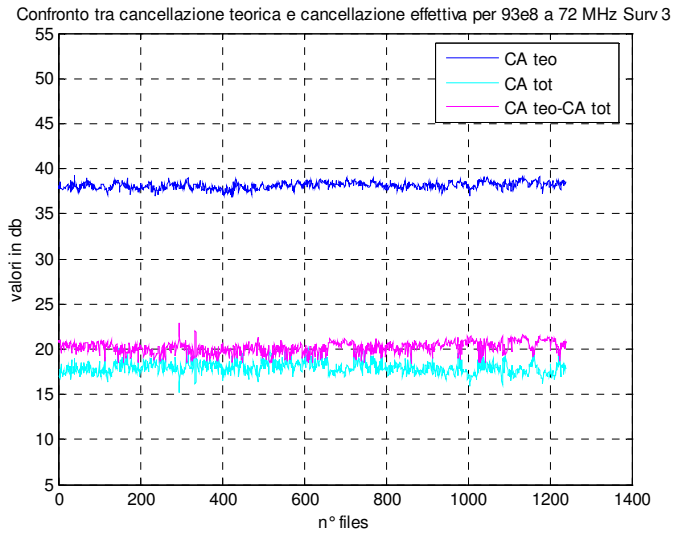

(c)

Figure 67 – Comparison between theoretical and measured cancellation values for the three antennas of Configuration 2: Surv 1 (a), Surv 2 (b) and Surv 3 (c) [FM channel: 93.8 MHz].

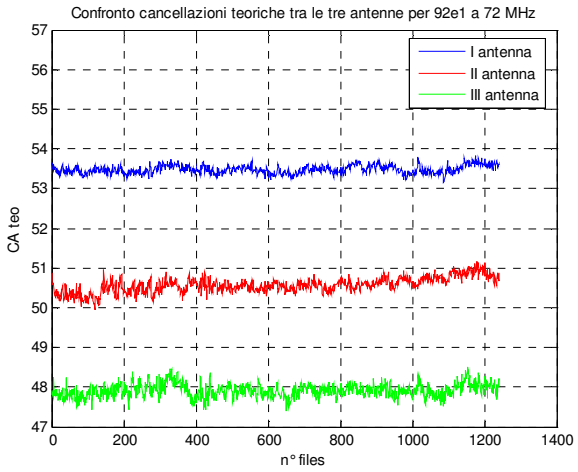

(a)

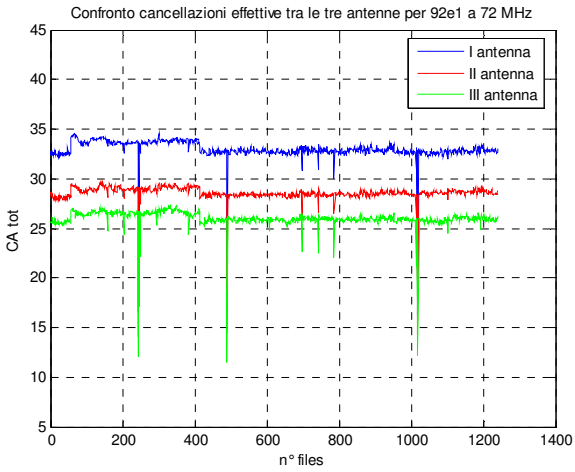

(b)

Figure 68 – Theoretical (a) and measured (b) cancellation values obtained with the three antennas of Configuration 5 [FM channel: 92.1 MHz].

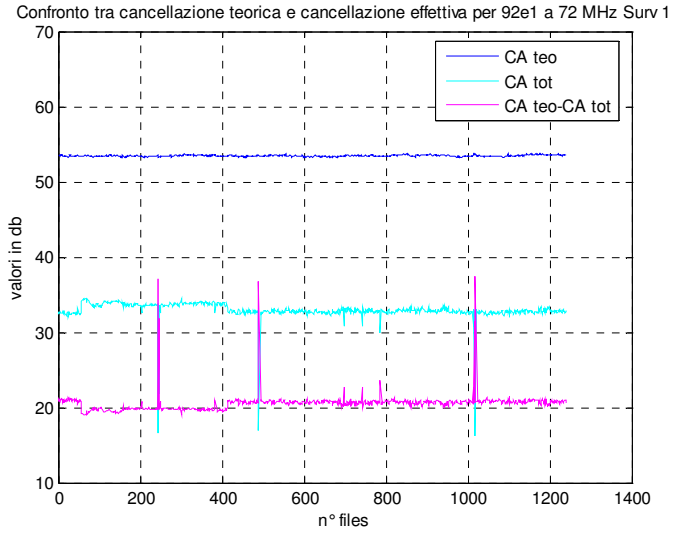

(a)

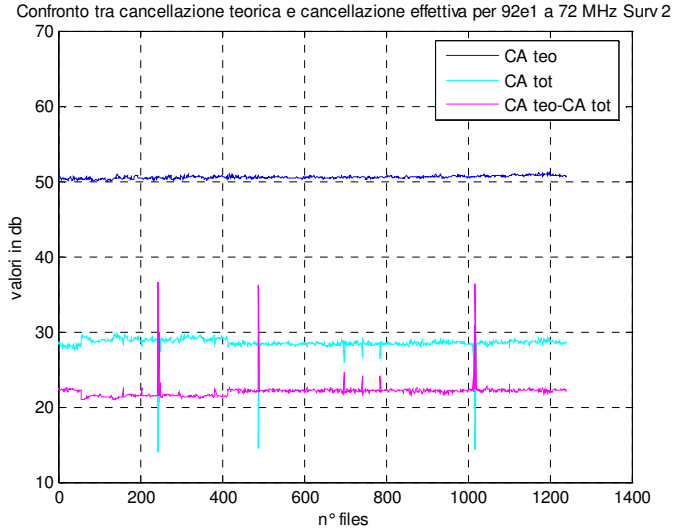

(b)

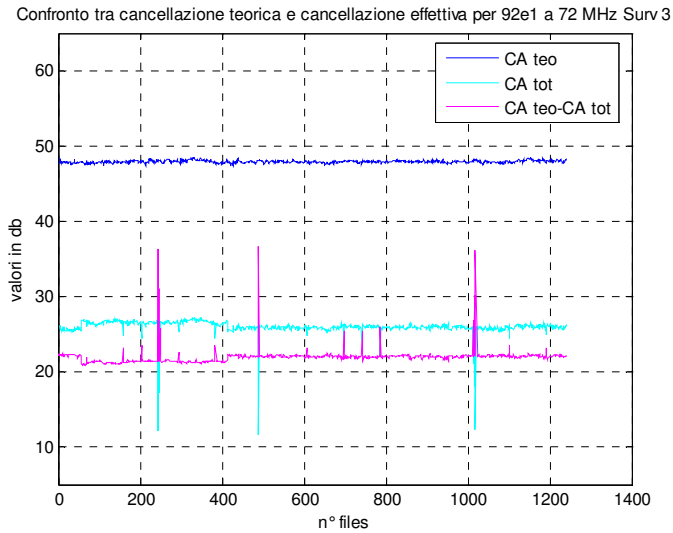

(c)

Figure 69 – Comparison between theoretical and measured cancellation values for the three antennas of Configuration 2: Surv 1 (a), Surv 2 (b) and Surv 3 (c) [FM channel: 92.1 MHz].

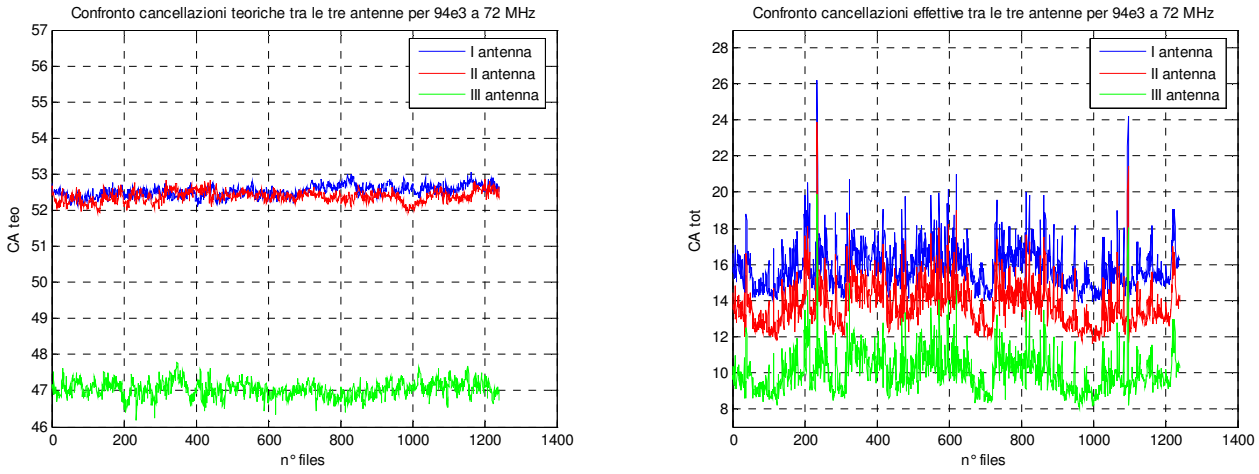

(a) (b)

Figure 70 – Theoretical (a) and measured (b) cancellation values obtained with the three antennas of Configuration 5 [FM channel: 94.3MHz].

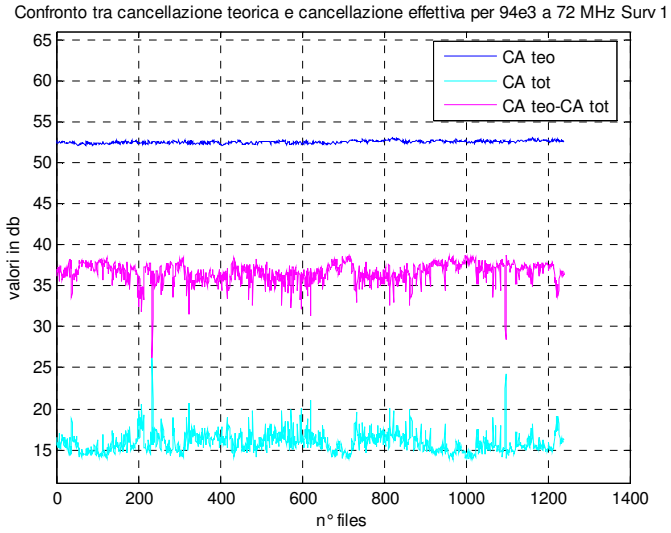

(a)

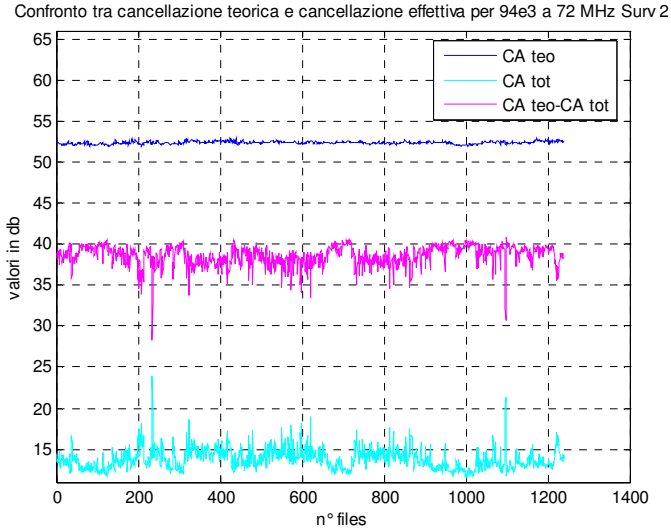

(b)

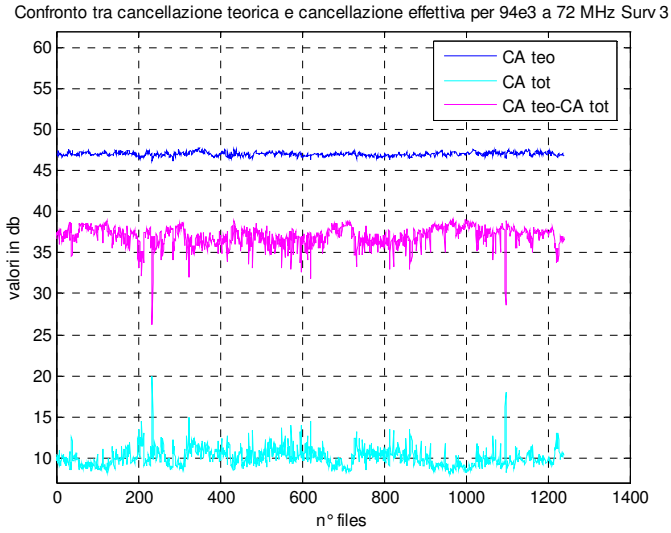

(c)

Figure 71 – Comparison between theoretical and measured cancellation values for the three antennas of Configuration 2: Surv 1 (a), Surv 2 (b) and Surv 3 (c) [FM channel: 94.3MHz].

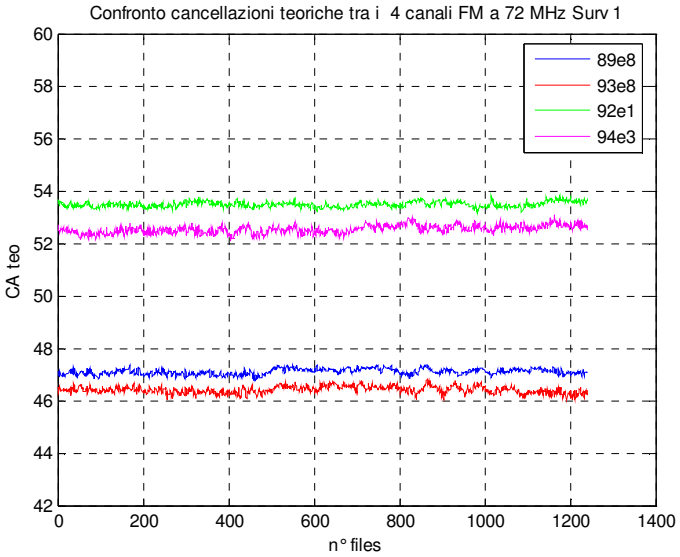

(a)

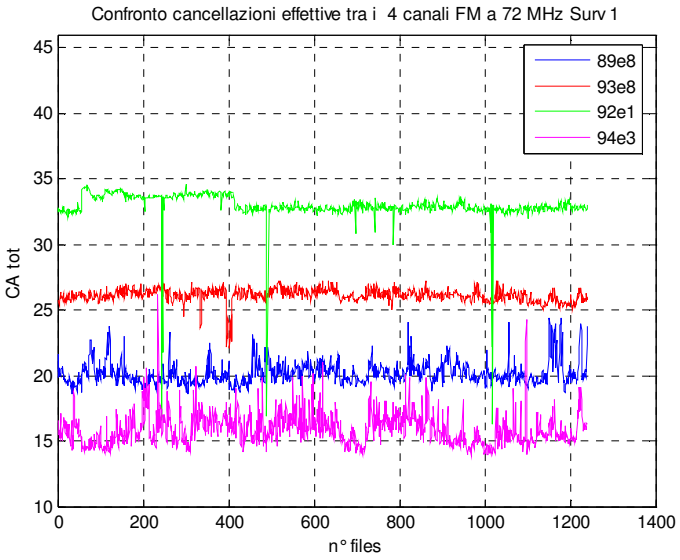

(b)

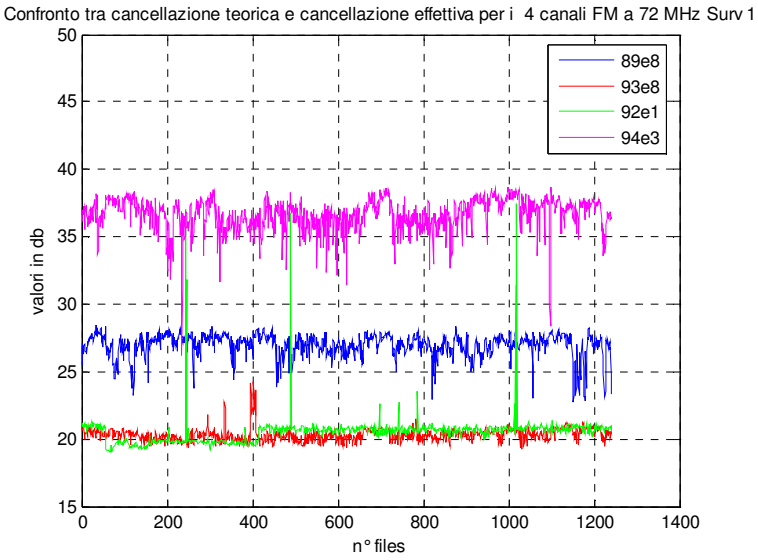

(c)

Figure 72 – Theoretical (a), measured (b) and difference between theoretical and measured (c) cancellation values obtained with the four FM channels [Conf. 5 – Surv 1].

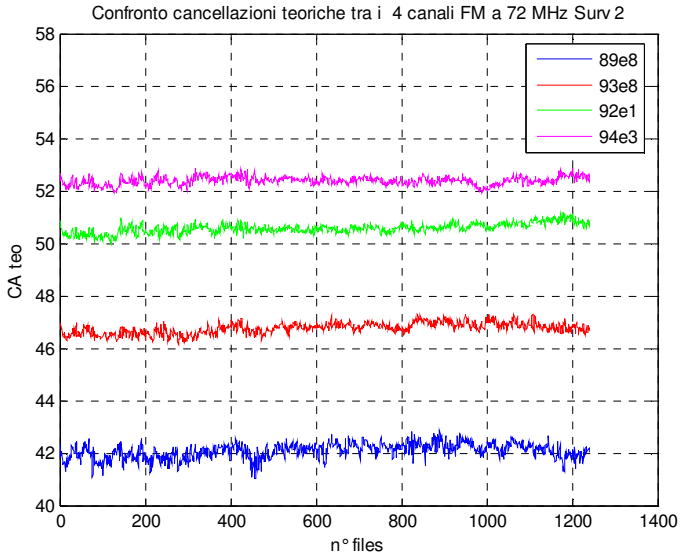

(a)

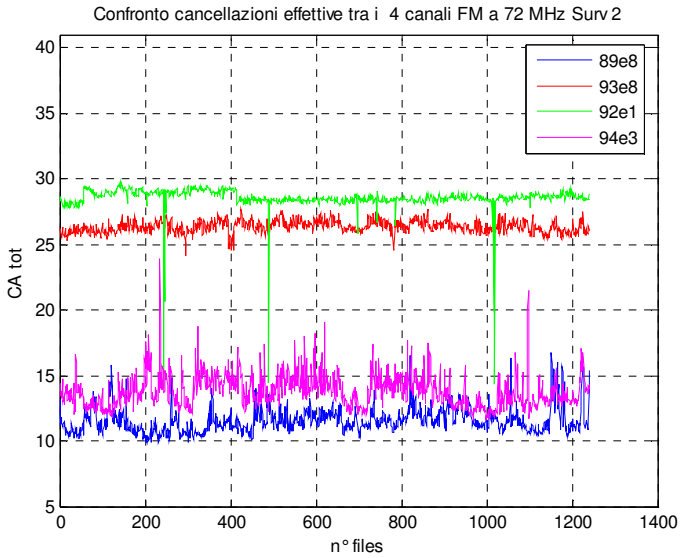

(b)

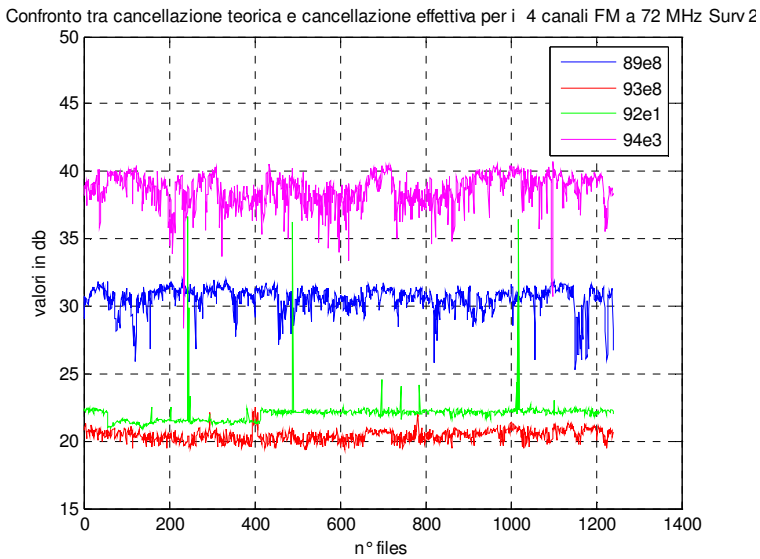

(c)

Figure 73 – Theoretical (a), measured (b) and difference between theoretical and measured (c) cancellation values obtained with the four FM channels [Conf. 5 – Surv 2].

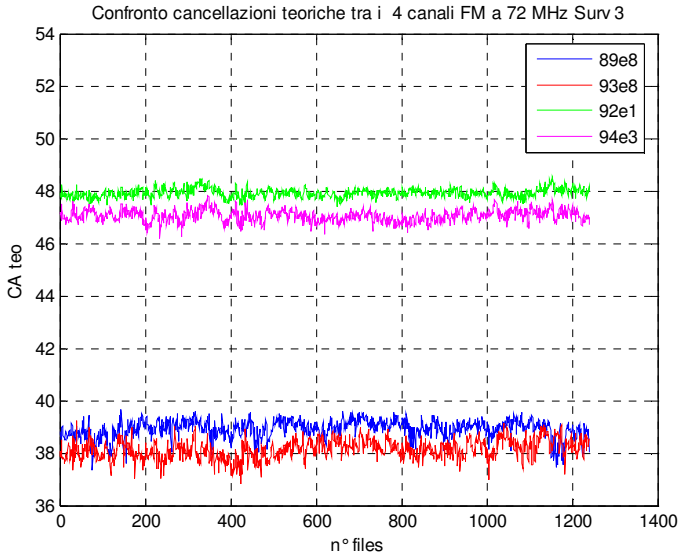

(a)

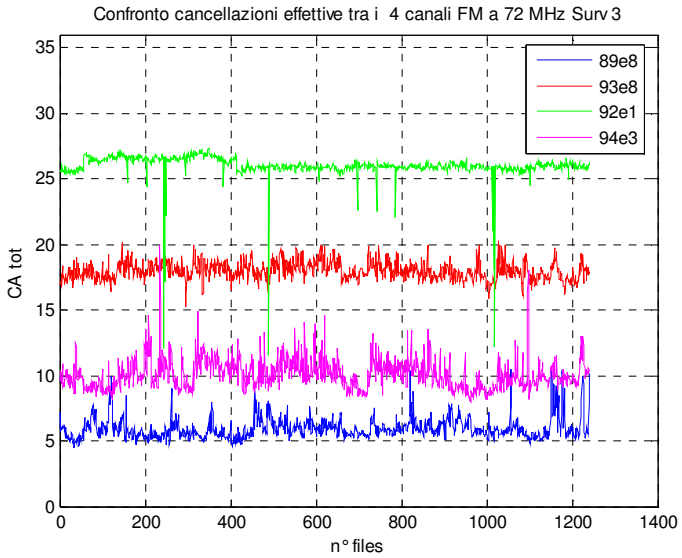

(b)

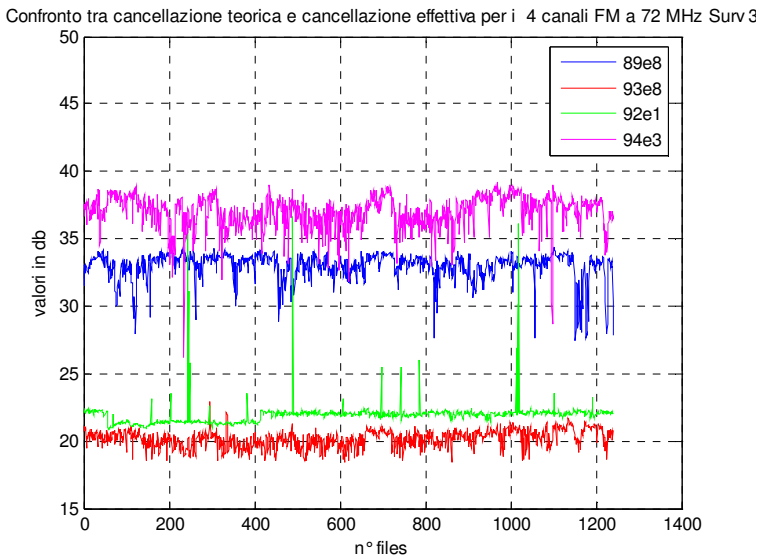

(c)

Figure 74 – Theoretical (a), measured (b) and difference between theoretical and measured (c) cancellation values obtained with the four FM channels [Conf. 5 – Surv 3].

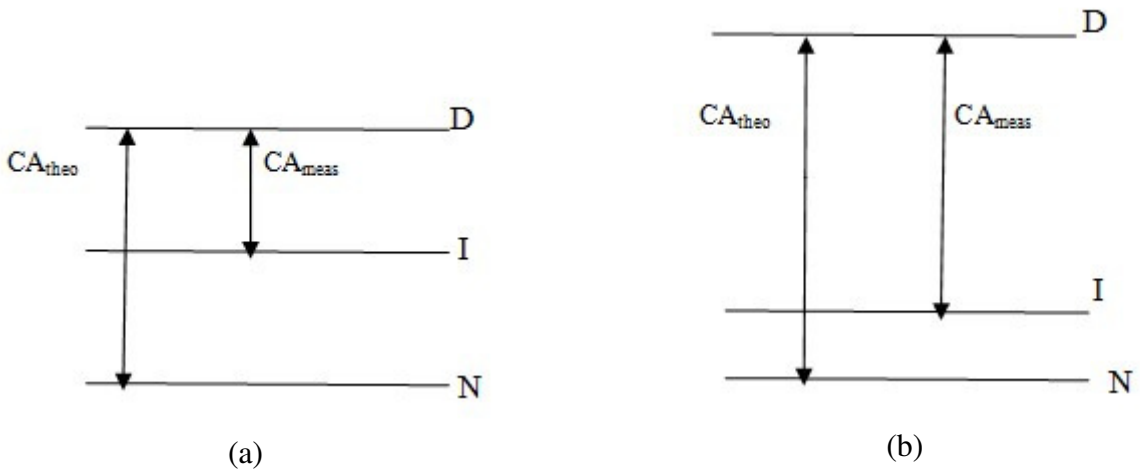

Figure 75 – Schematical representation of interference impact in the PBR system performance.

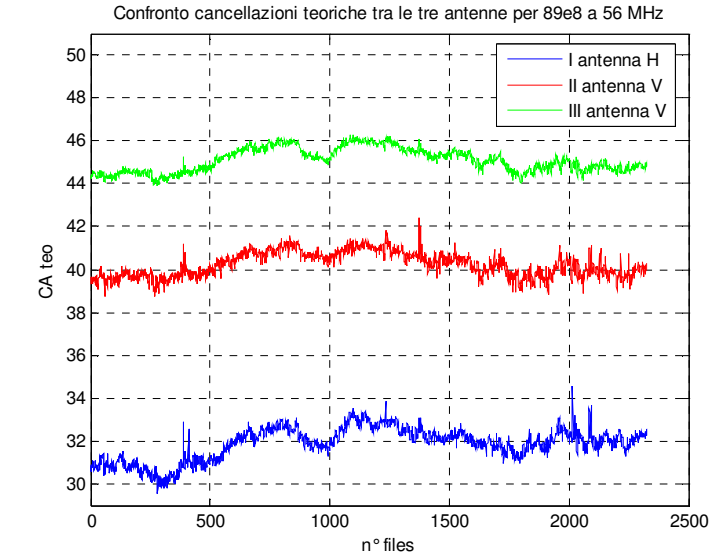

(a)

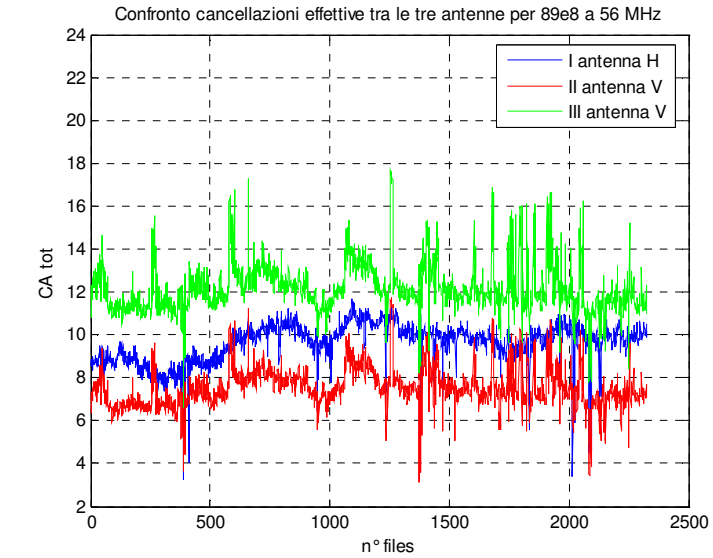

(b)

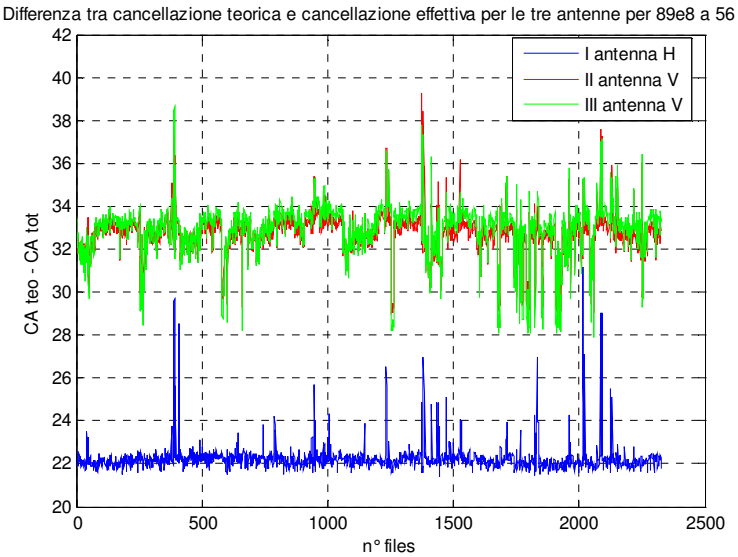

(c)

Figure 76 – Theoretical (a), measured (b) and difference between theoretical and measured (c) cancellation values obtained with the three antennas of Configuration 2 [FM channel: 89.8MHz].

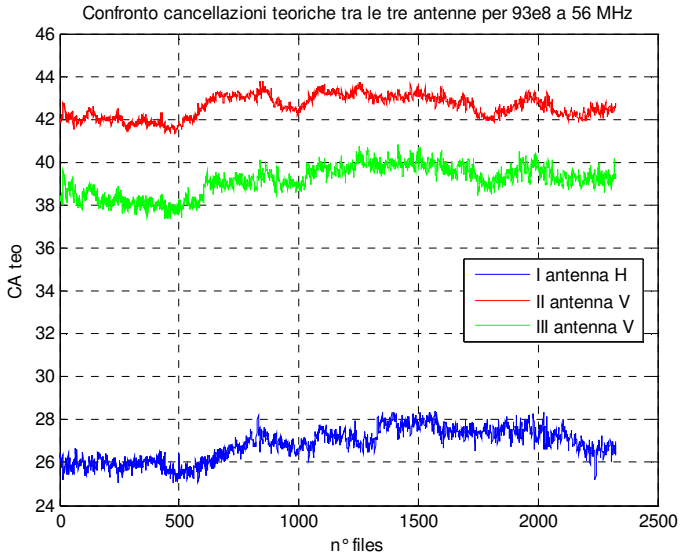

(a)

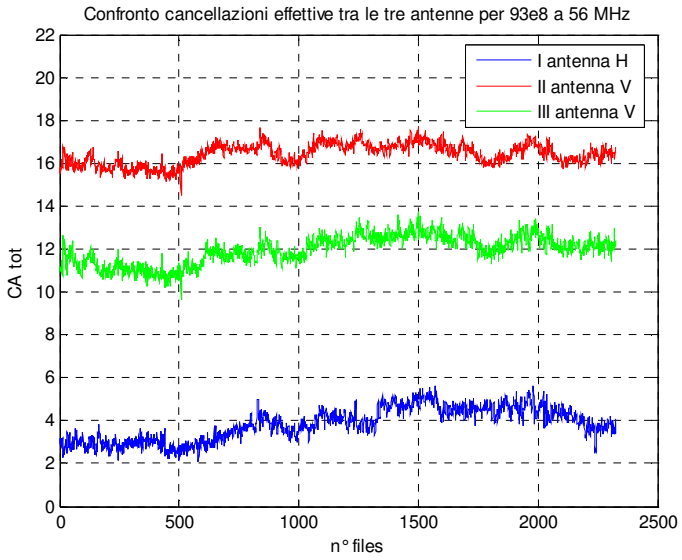

(b)

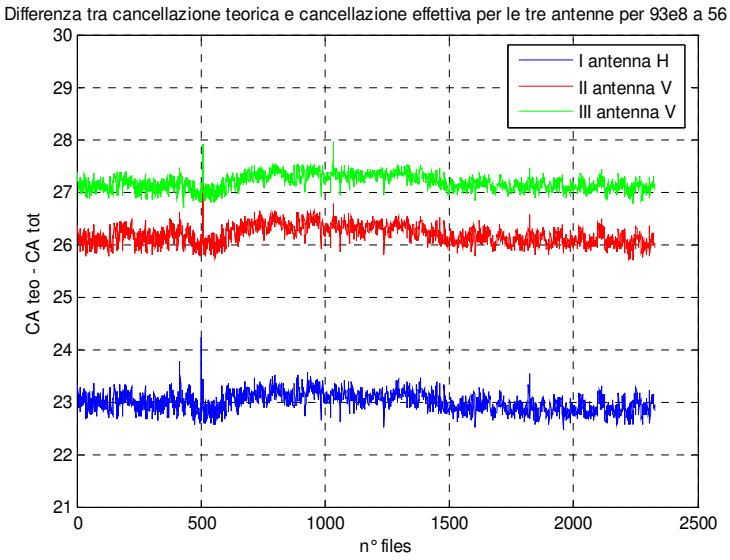

(c)

Figure 77 – Theoretical (a), measured (b) and difference between theoretical and measured (c) cancellation values obtained with the three antennas of Configuration 2 [FM channel: 93.8MHz].

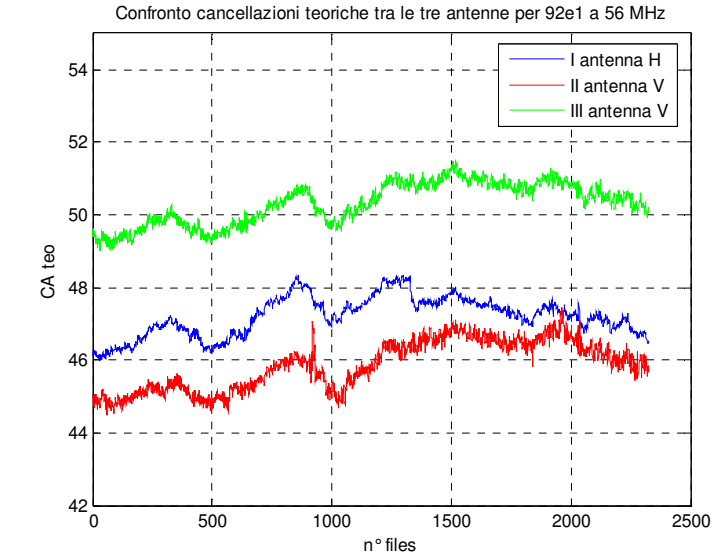

(a)

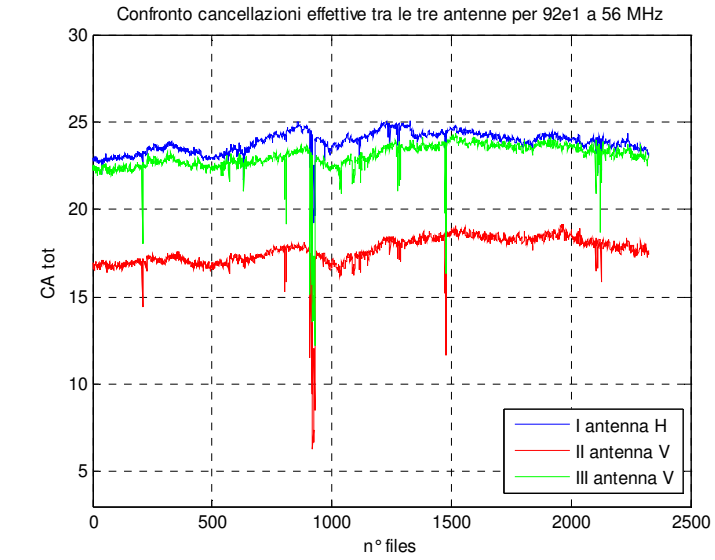

(b)

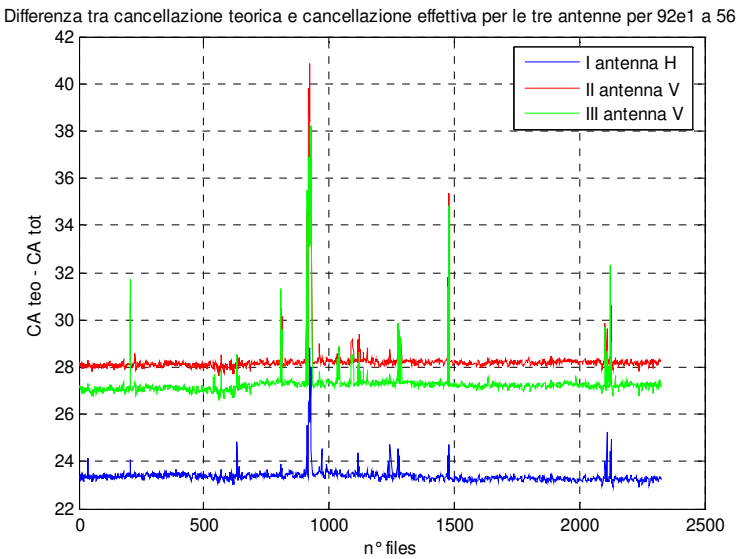

(c)

Figure 78 – Theoretical (a), measured (b) and difference between theoretical and measured (c) cancellation values obtained with the three antennas of Configuration 2 [FM channel: 92.1MHz].

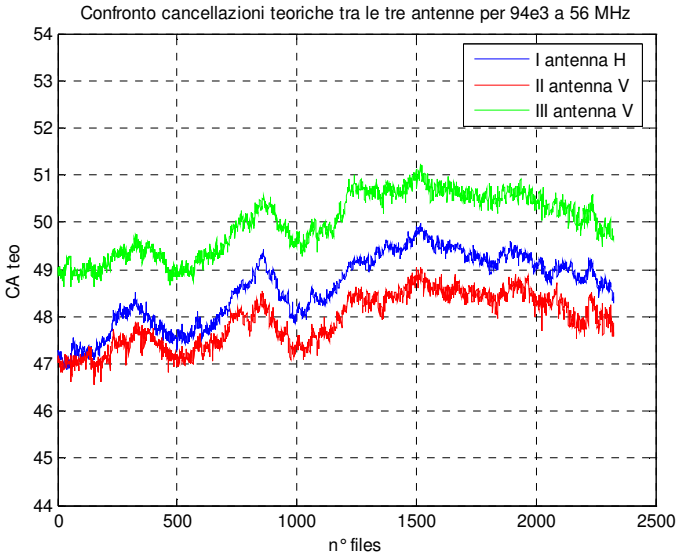

(a)

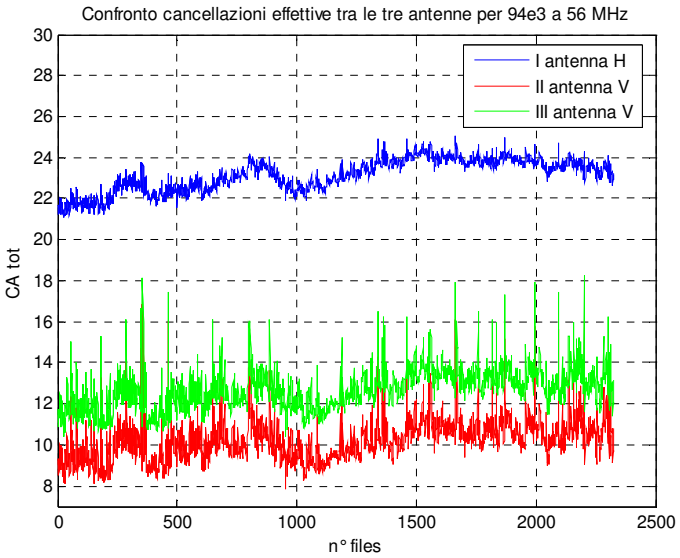

(b)

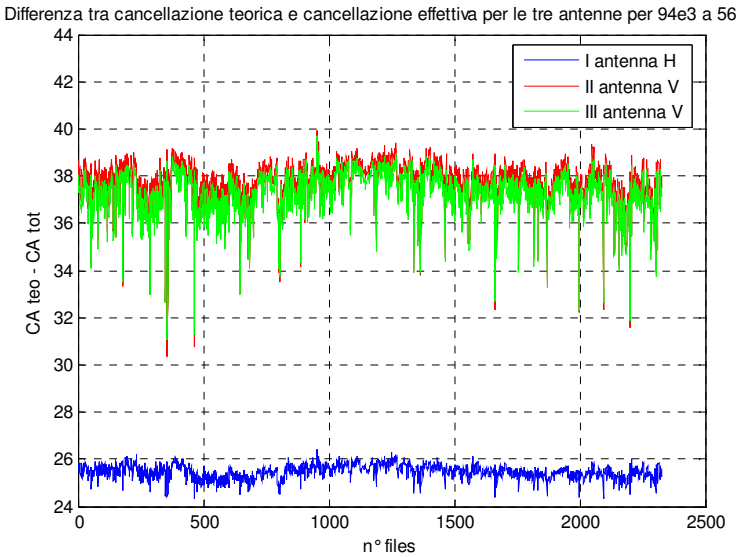

(c)

Figure 79 – Theoretical (a), measured (b) and difference between theoretical and measured (c) cancellation values obtained with the three antennas of Configuration 2 [FM channel: 94.3MHz].

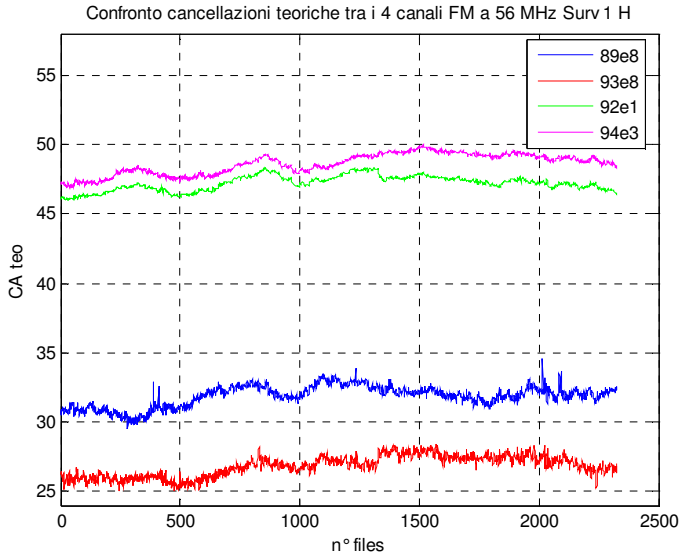

(a)

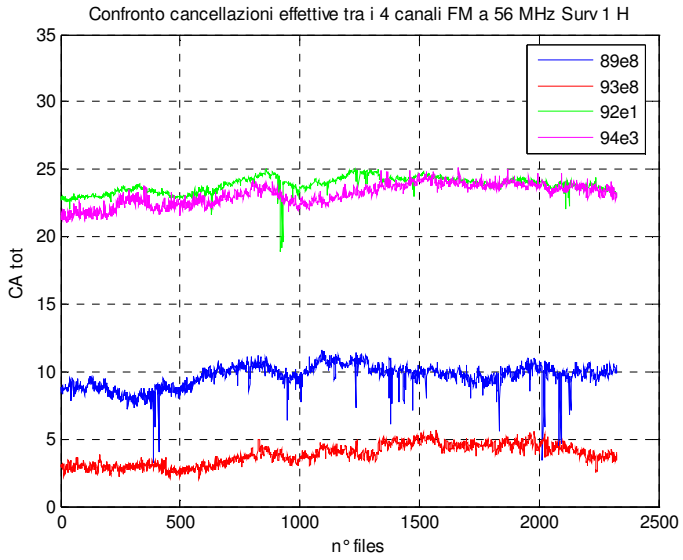

(b)

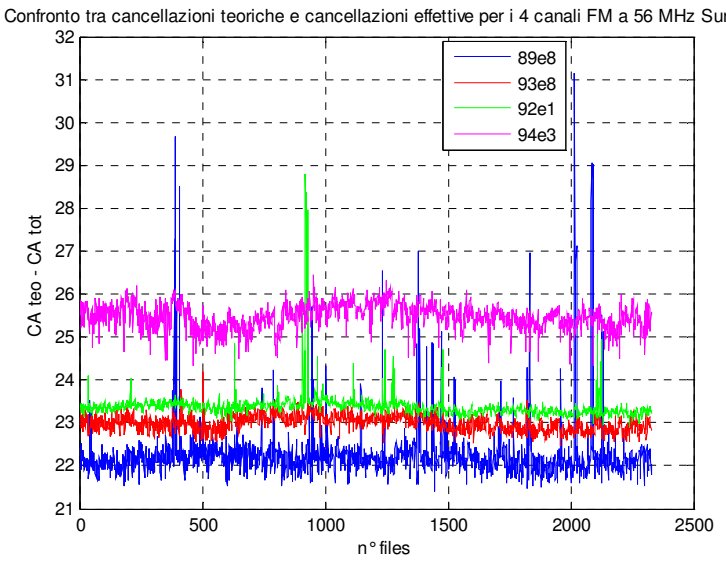

(c)

Figure 80 – Theoretical (a), measured (b) and difference between theoretical and measured (c) cancellation values obtained with the four FM channels [Conf. 2 – Surv 1 (H)].

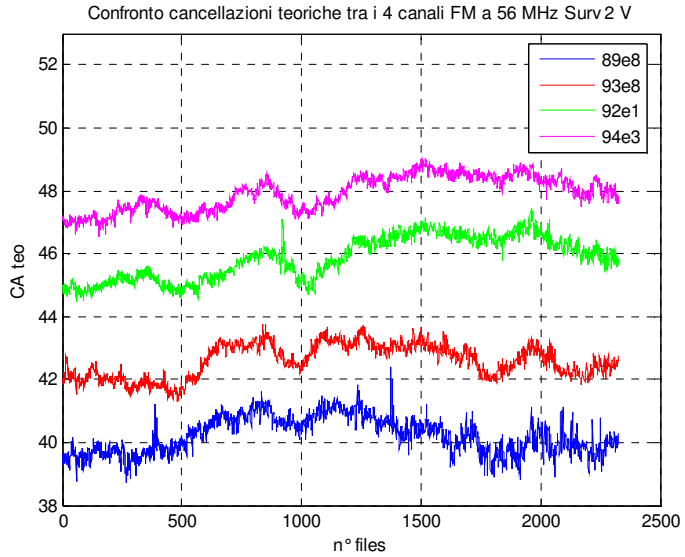

(a)

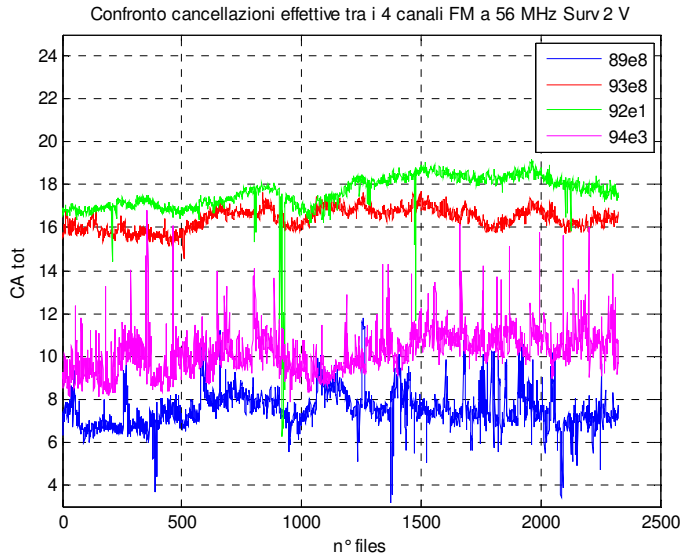

(b)

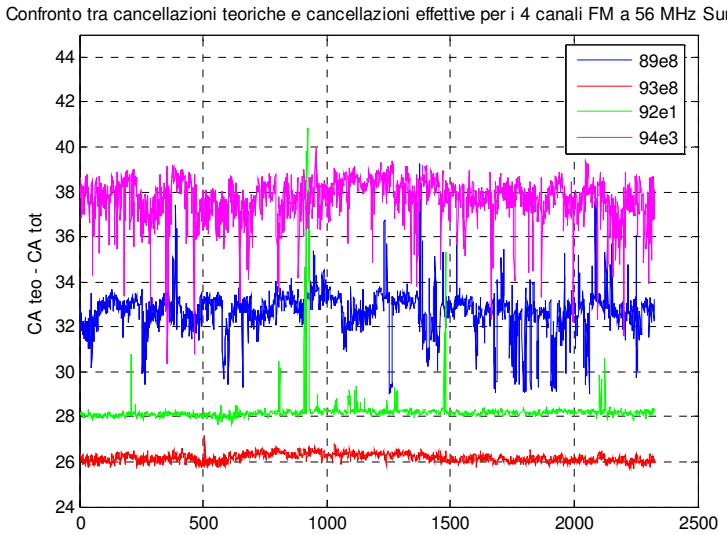

(c)

Figure 81 – Theoretical (a), measured (b) and difference between theoretical and measured (c) cancellation values obtained with the four FM channels [Conf. 2 – Surv 2 (V)].

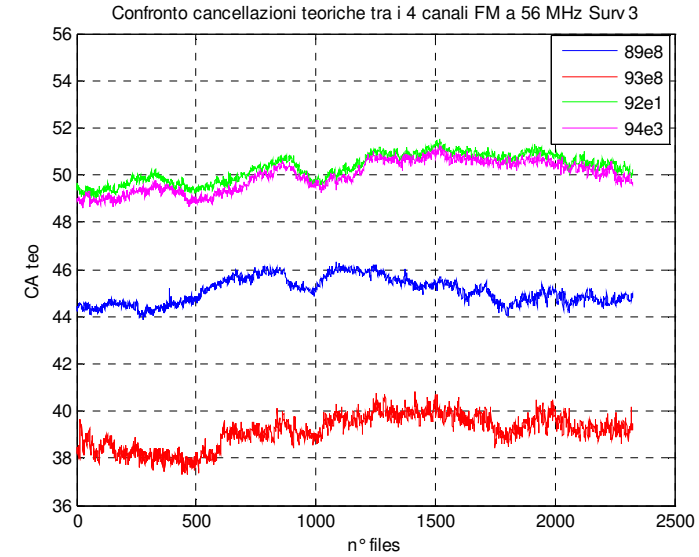

(a)

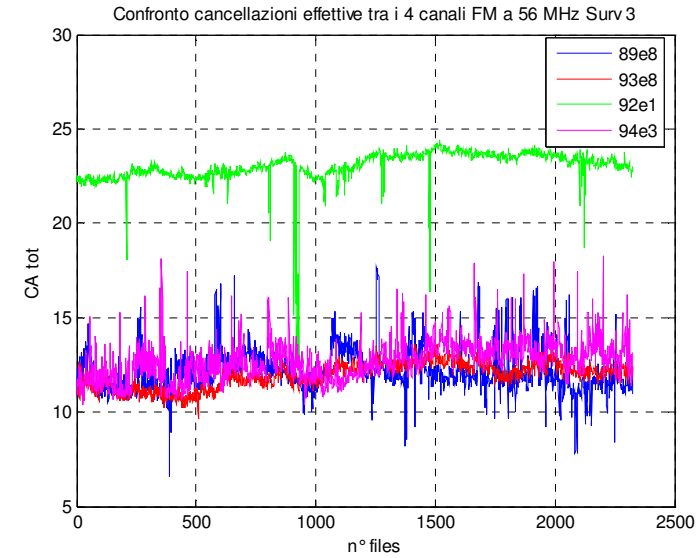

(b)

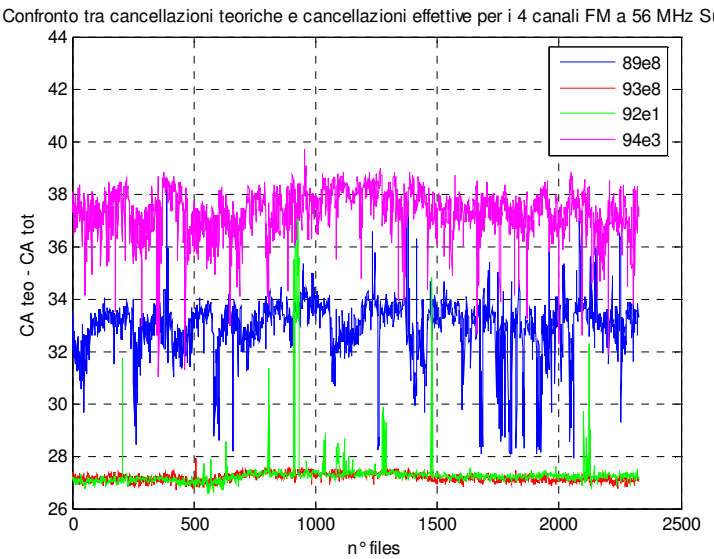

(c)

Figure 82 – Theoretical (a), measured (b) and difference between theoretical and measured (c) cancellation values obtained with the four FM channels [Conf. 2 – Surv 3 (V)].

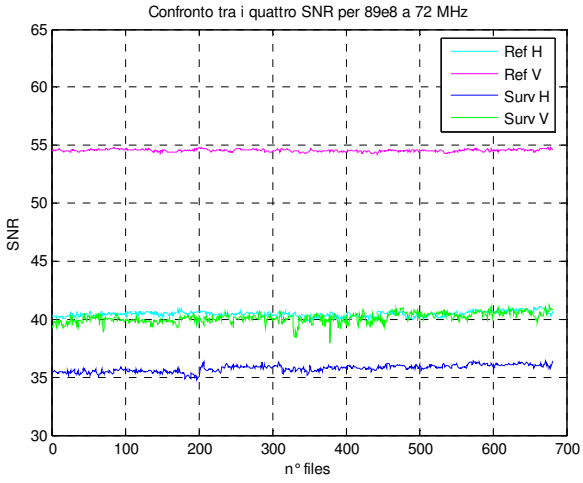

(a)

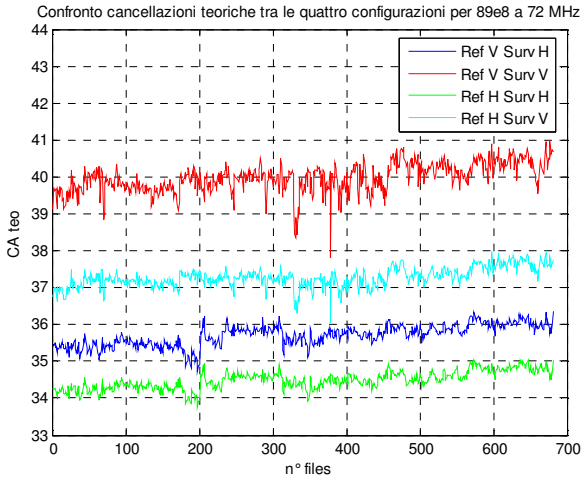

(b)

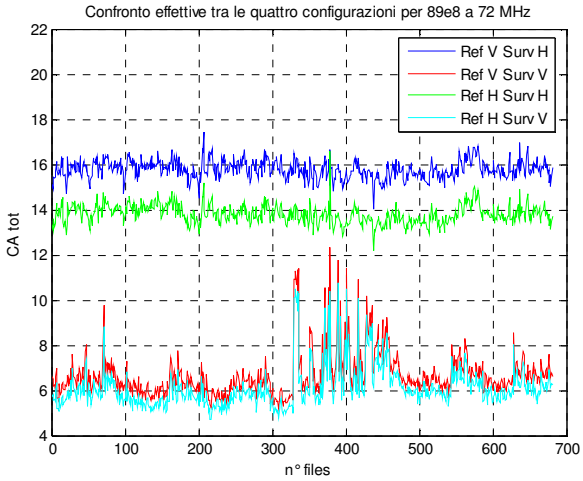

(c)

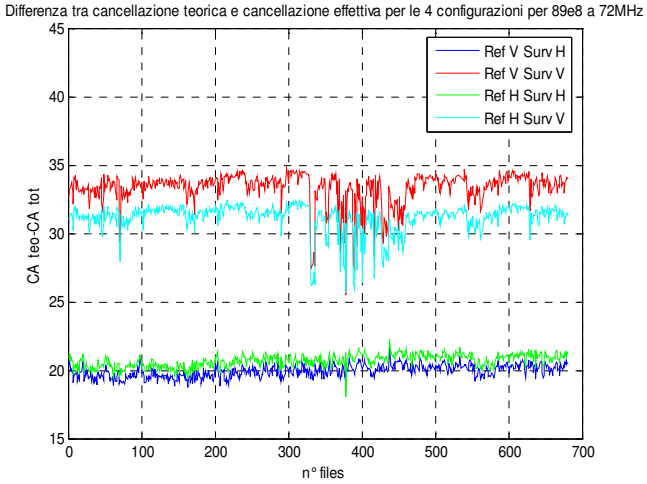

(d)

Figure 83 – SNR (a), theoretical (b), measured (c) and difference between theoretical and measured (d) cancellation values obtained with the four antenna pairs of Conf. 4 [FM channel: 89.8MHz].

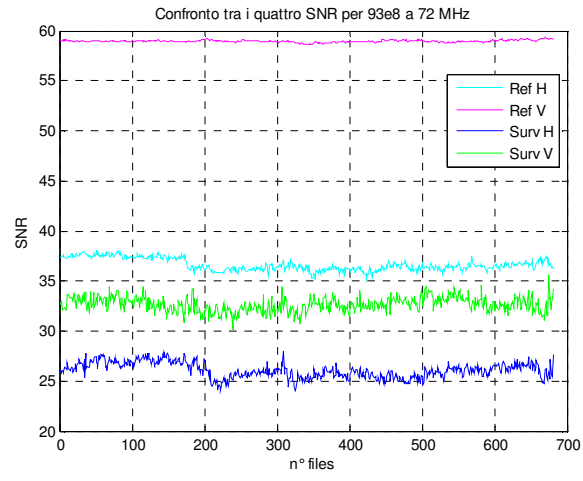

(a)

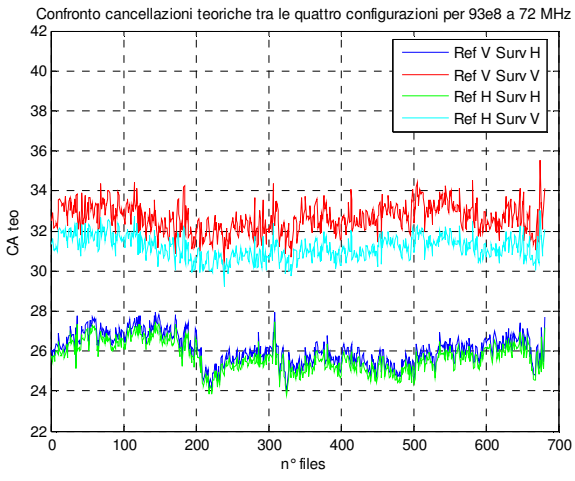

(b)

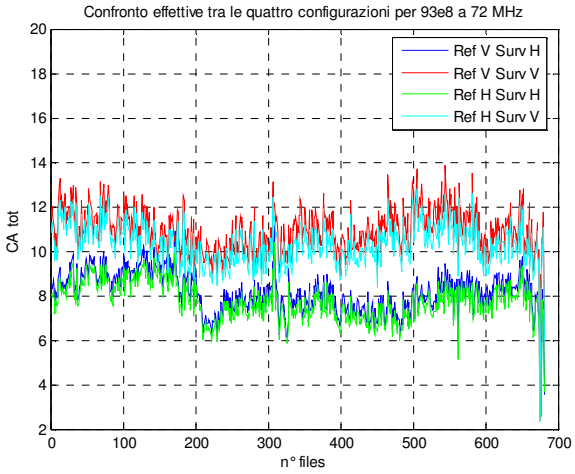

(c)

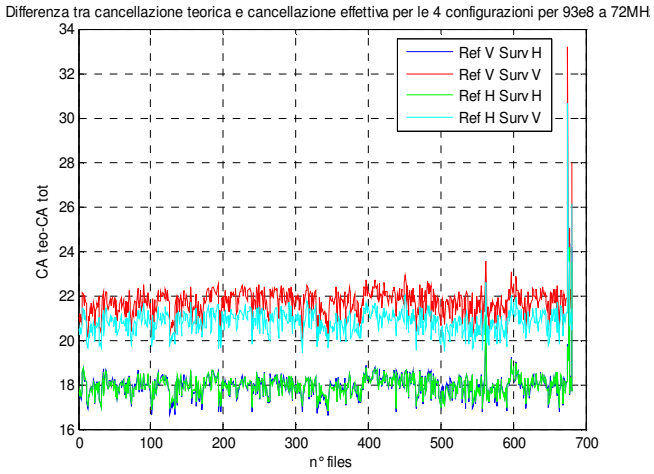

(d)

Figure 84 – SNR (a), theoretical (b), measured (c) and difference between theoretical and measured (d) cancellation values obtained with the four antenna pairs of Conf. 4 [FM channel: 93.8MHz].

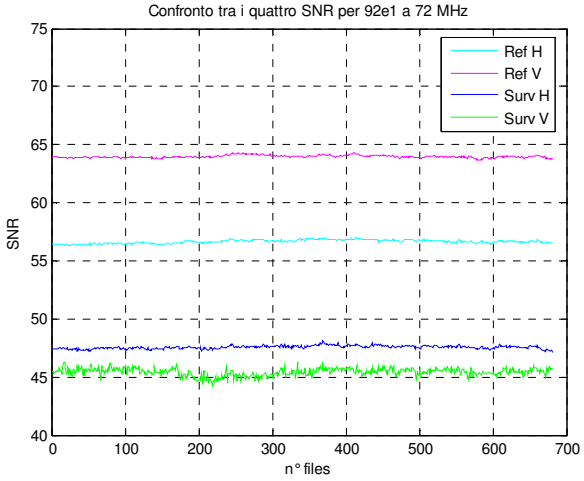

(a)

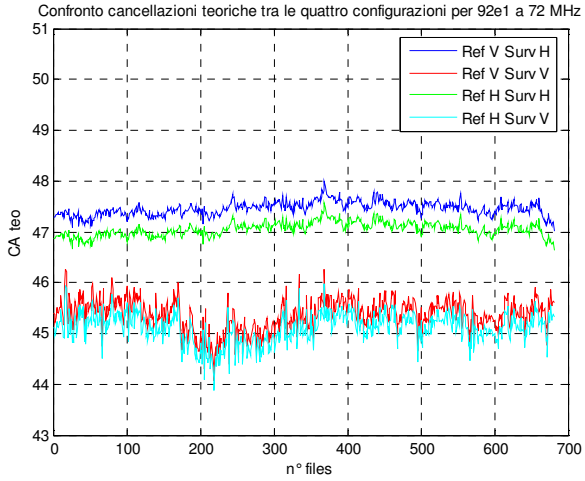

(b)

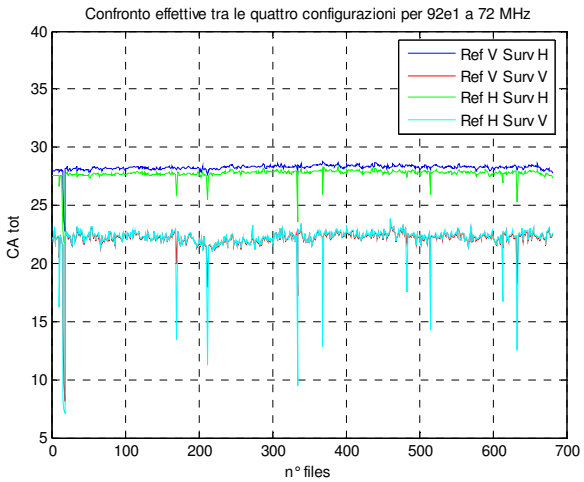

(c)

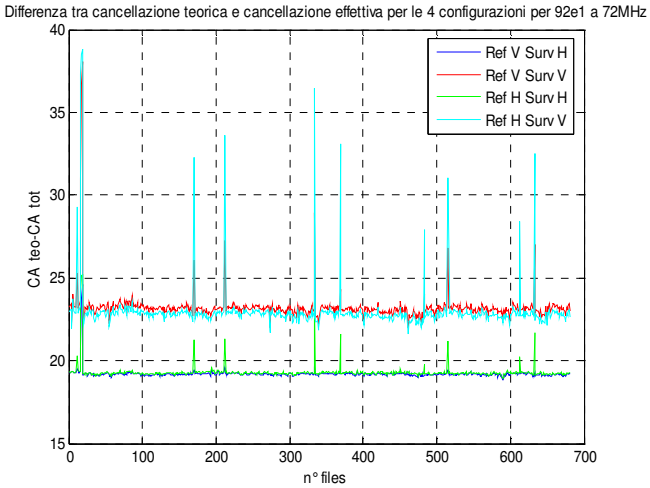

(d)

Figure 85 – SNR (a), theoretical (b), measured (c) and difference between theoretical and measured (d) cancellation values obtained with the four antenna pairs of Conf. 4 [FM channel: 92.1MHz].

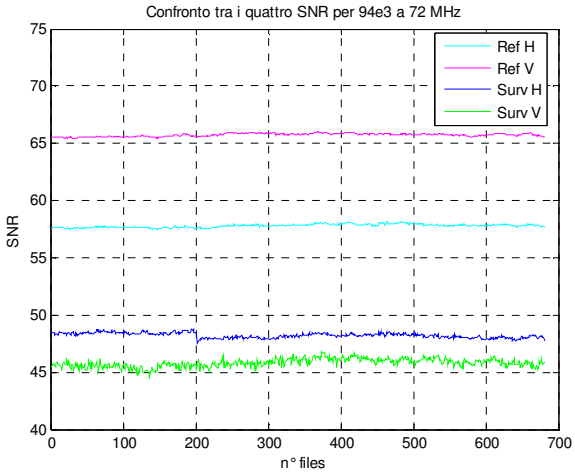

(a)

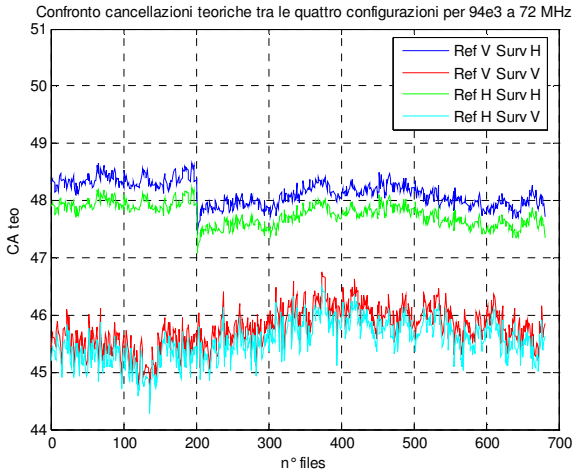

(b)

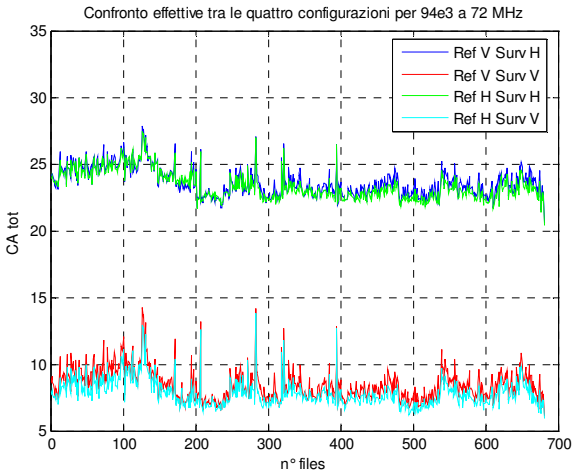

(c)

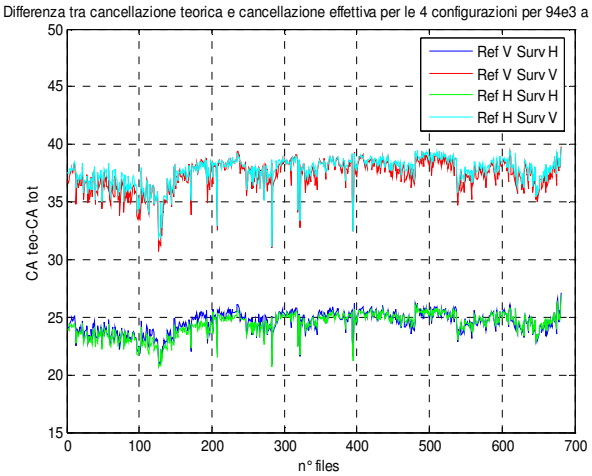

(d)

Figure 86 – SNR (a), theoretical (b), measured (c) and difference between theoretical and measured (d) cancellation values obtained with the four antenna pairs of Conf. 4 [FM channel: 94.3MHz].

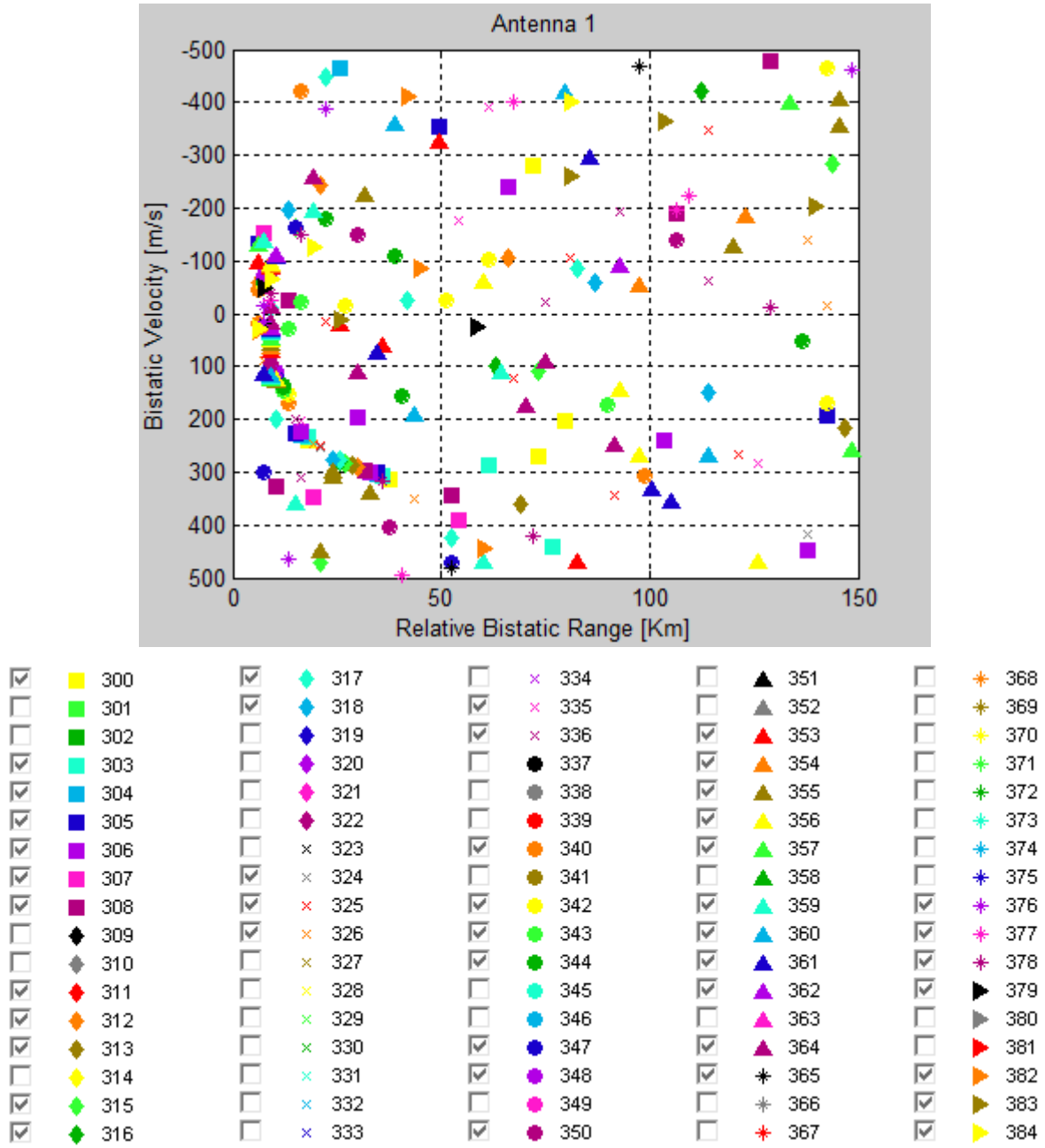

Figure 87 – Plot sequences in the Range-Velocity map for 85 consecutive acquisitions [Configuration 1, Surv 1, FM channel 89.8MHz].

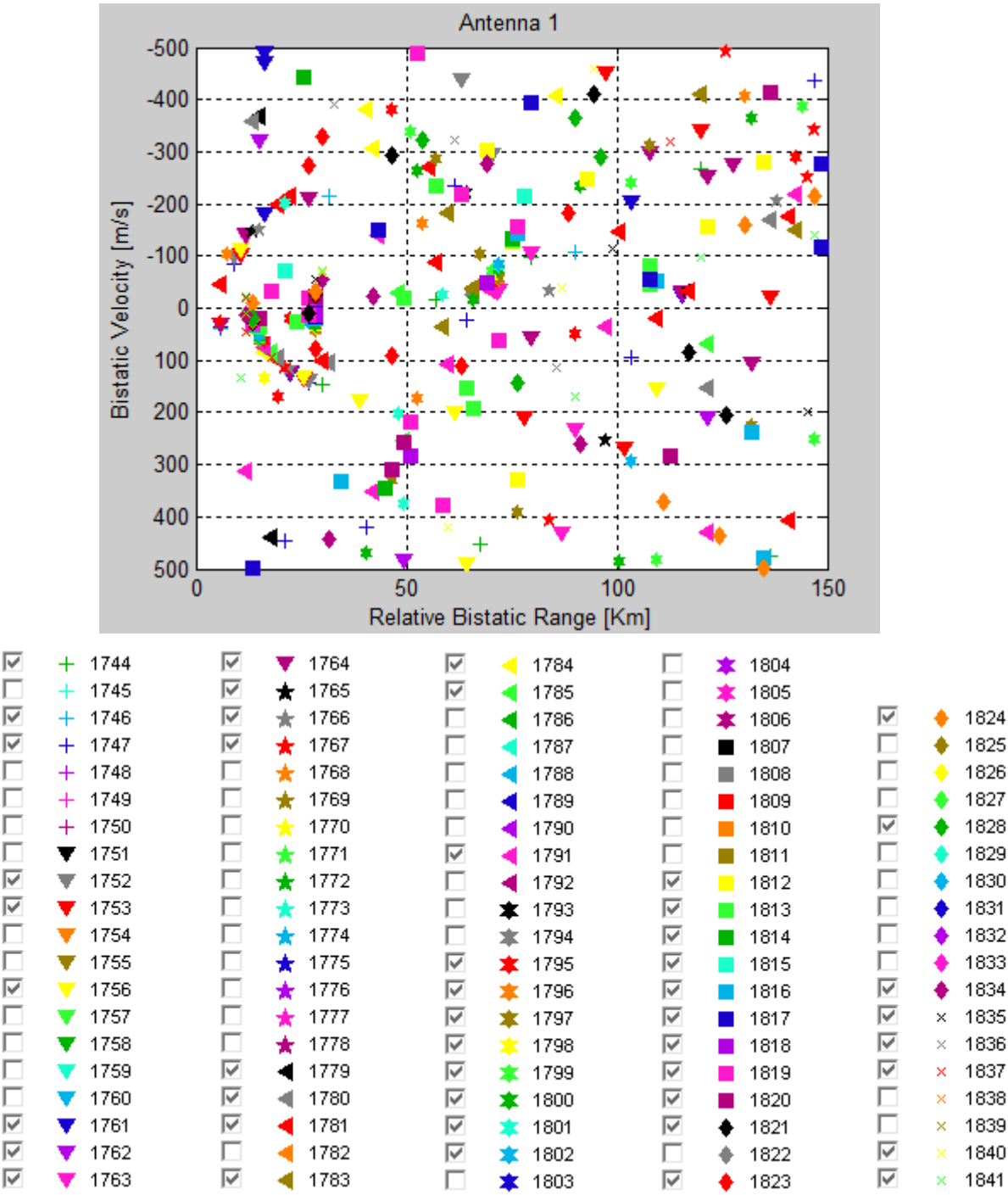

Figure 88 – Plot sequences in the Range-Velocity map for 98 consecutive acquisitions [Configuration 1, Surv 1, FM channel 89.8MHz].

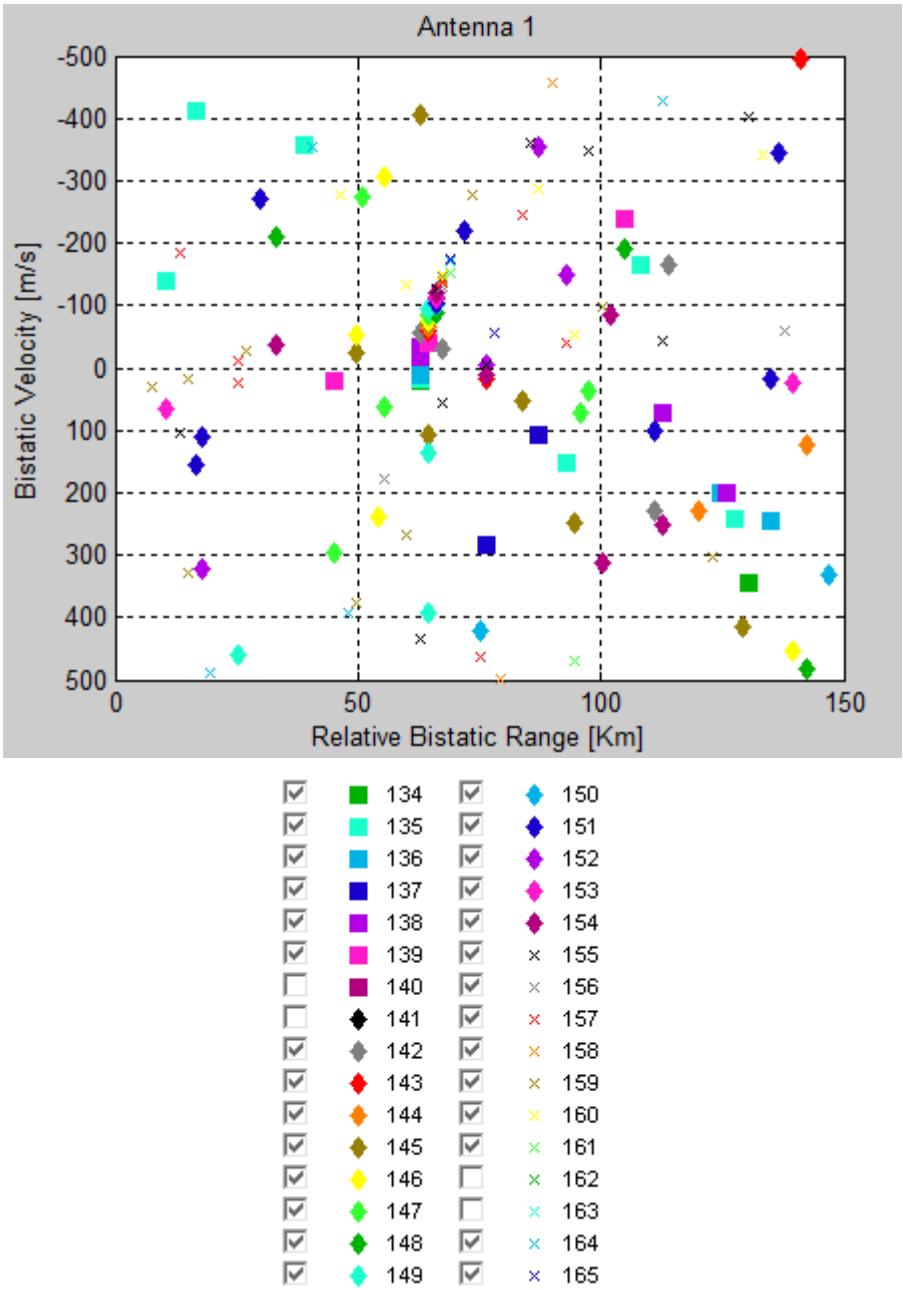

Figure 89 – Plot sequences in the Range-Velocity map for 32 consecutive acquisitions [Configuration 5, Surv 1, FM channel 89.8MHz].

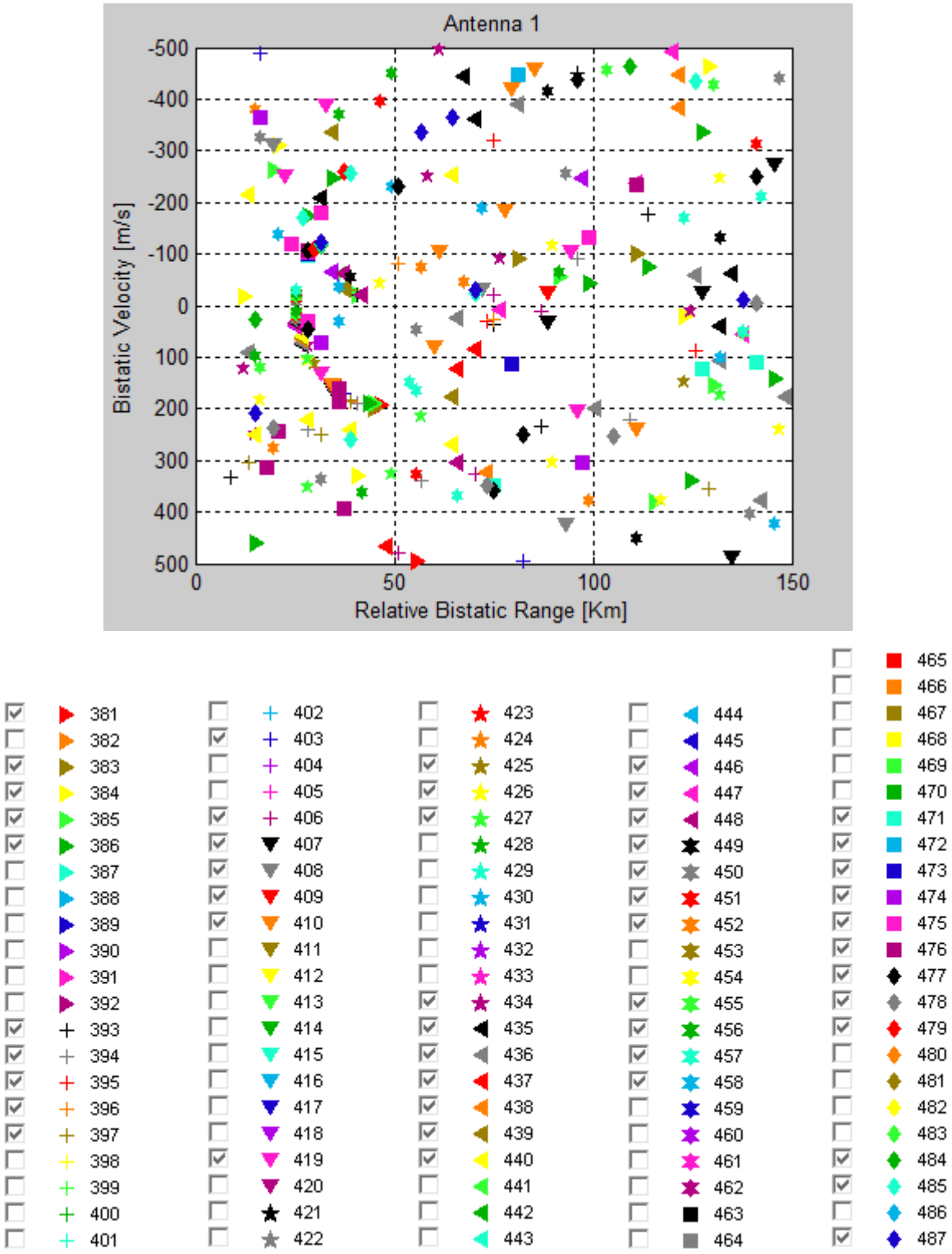

Figure 90 – Plot sequences in the Range-Velocity map for 107 consecutive acquisitions [Configuration 5, Surv 1, FM channel 89.8MHz].

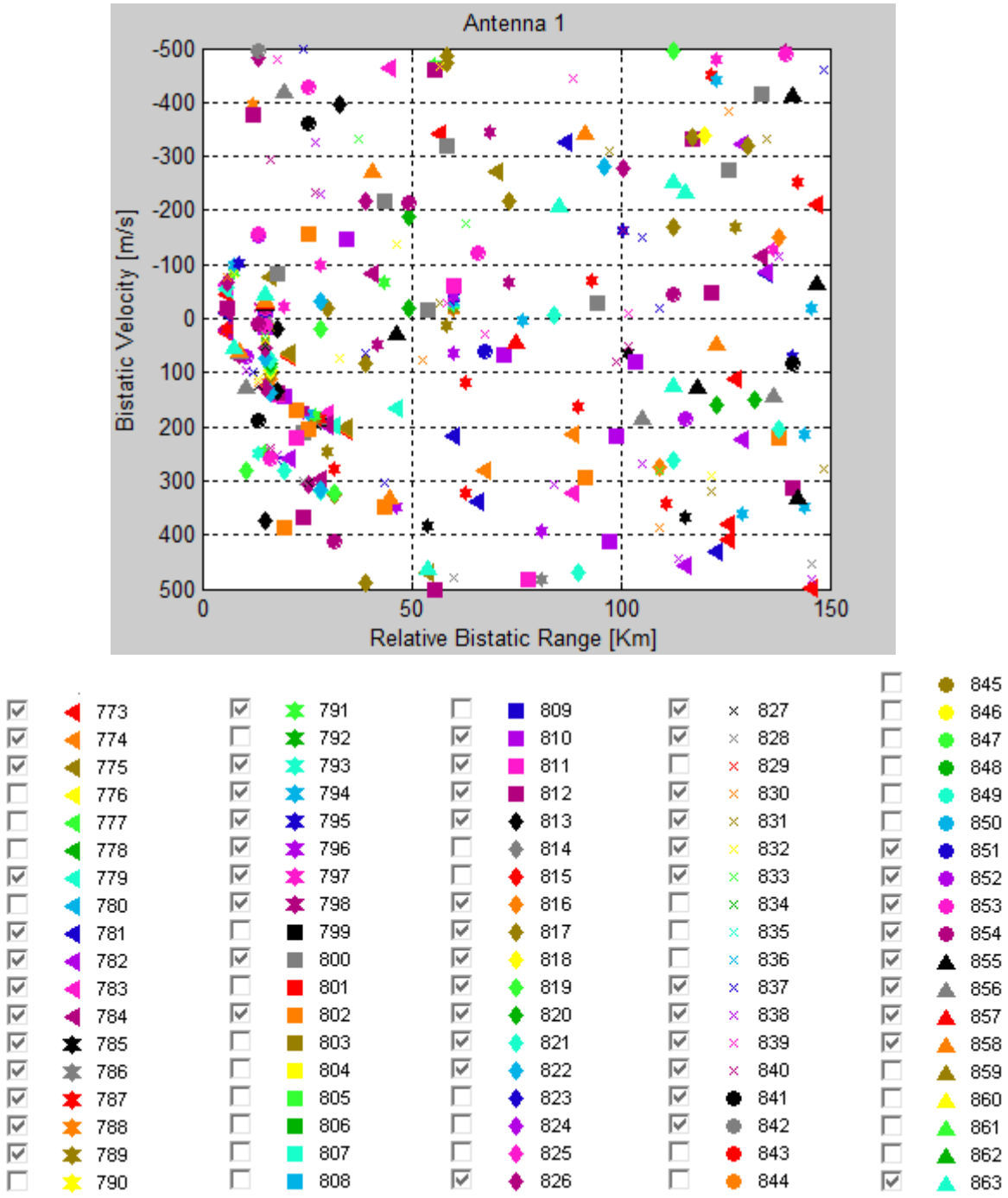

Figure 91 – Plot sequences in the Range-Velocity map for 91 consecutive acquisitions [Configuration 5, Surv 1, FM channel 89.8MHz].

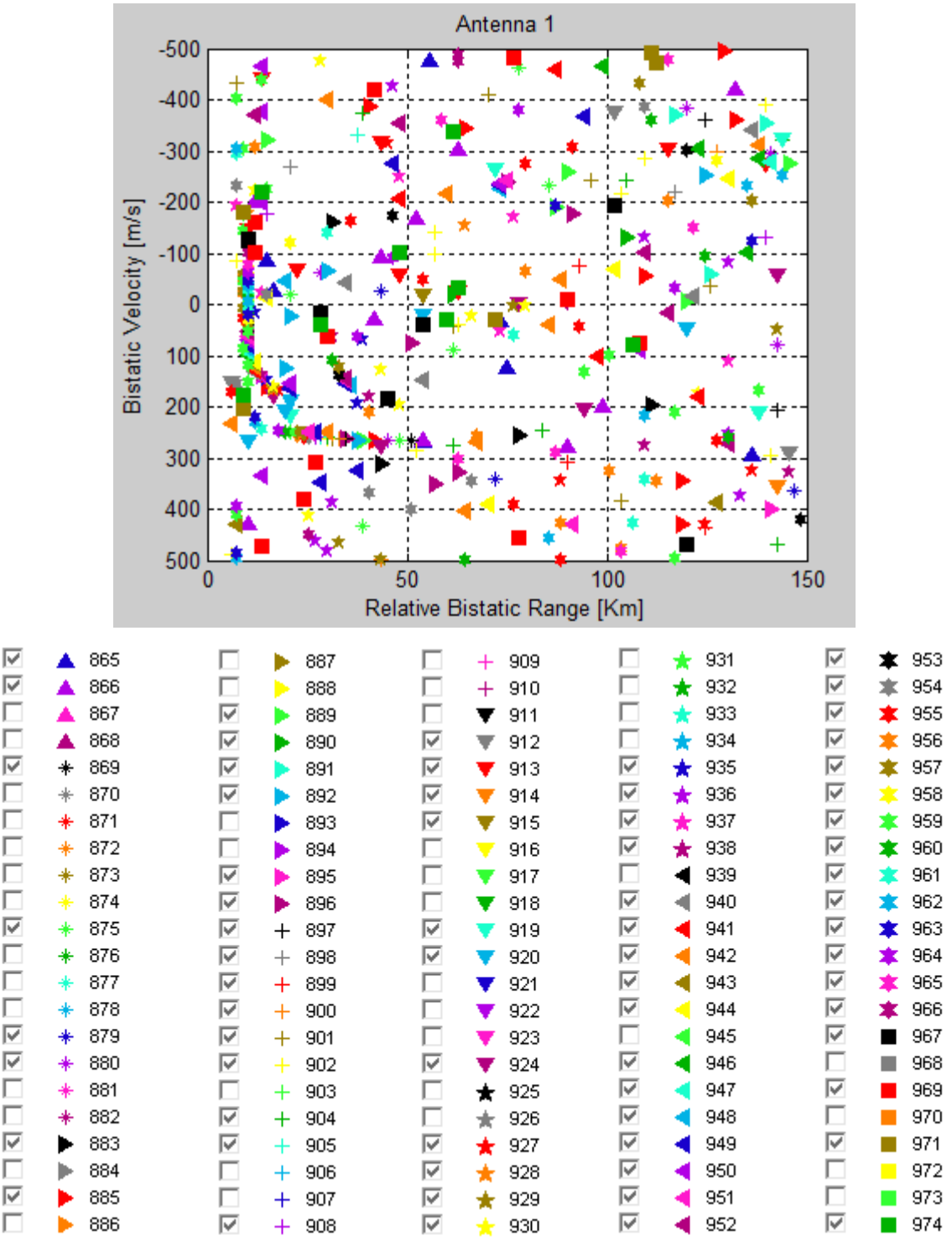

Figure 92 – Plot sequences in the Range-Velocity map for 110 consecutive acquisitions [Configuration 2, Surv 1, FM channel 92.1MHz].

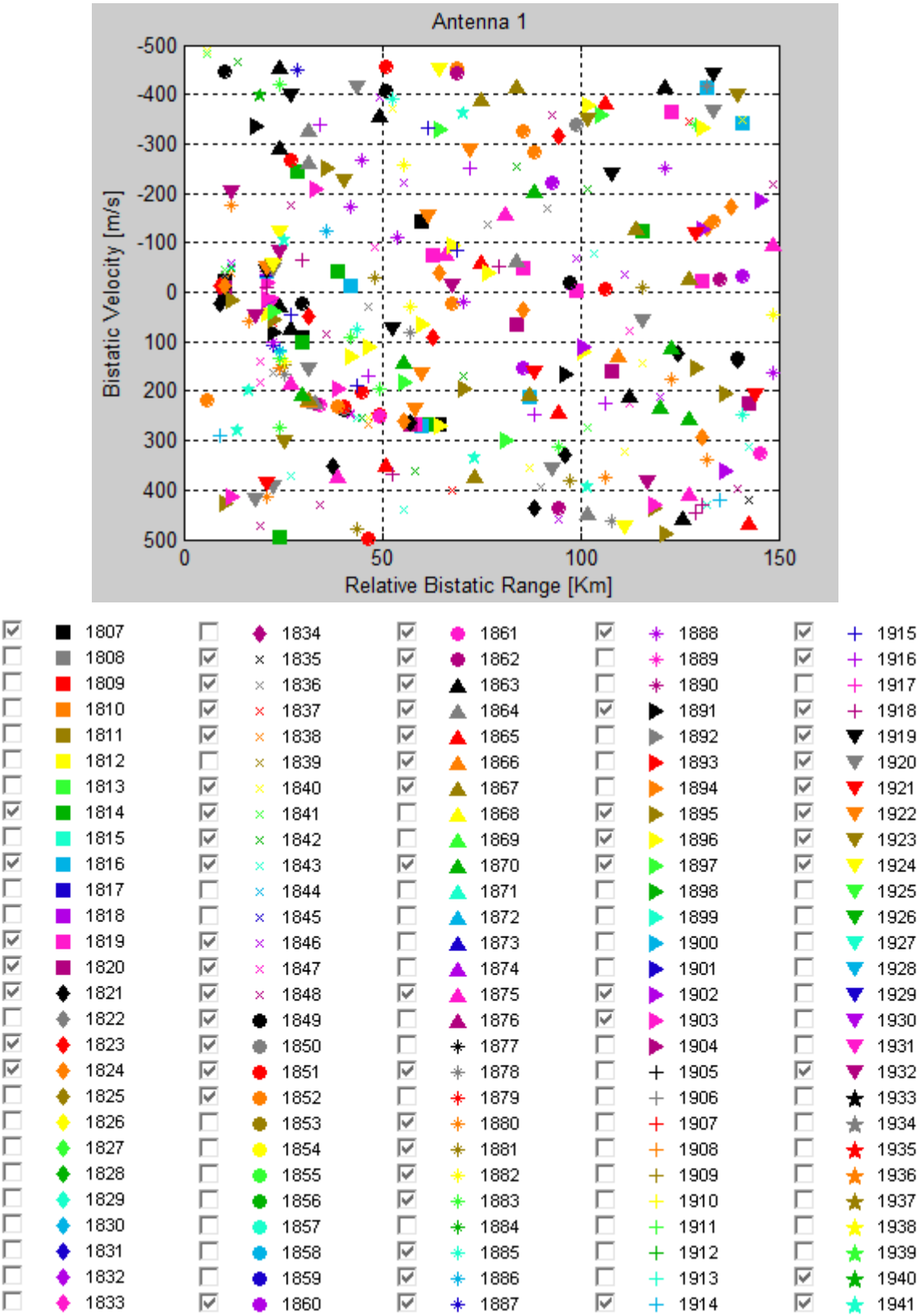

Figure 93 – Plot sequences in the Range-Velocity map for 135 consecutive acquisitions [Configuration 2, Surv 1, FM channel 92.1MHz].

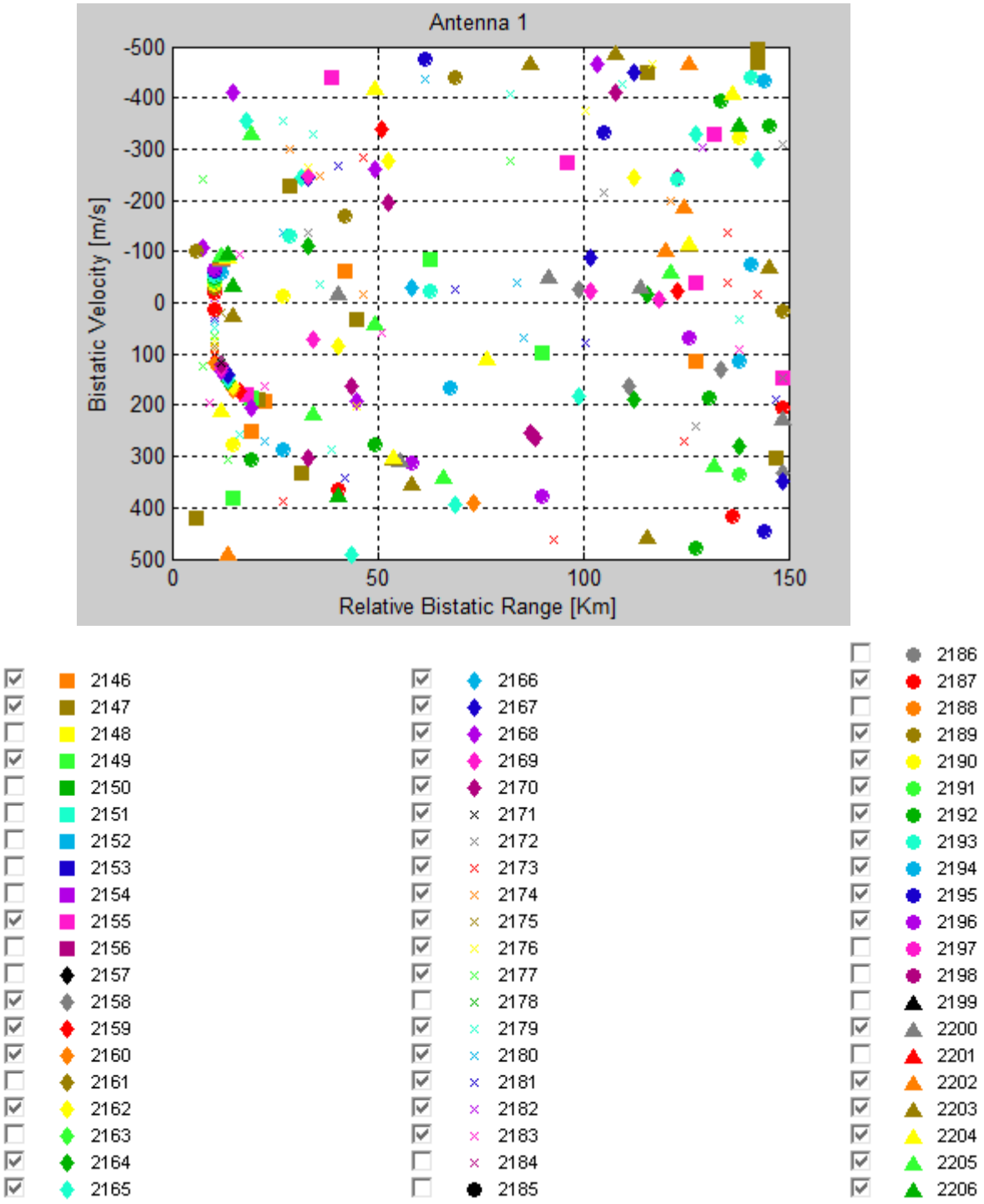

Figure 94 – Plot sequences in the Range-Velocity map for 61 consecutive acquisitions [Configuration 2, Surv 1, FM channel 92.1MHz].

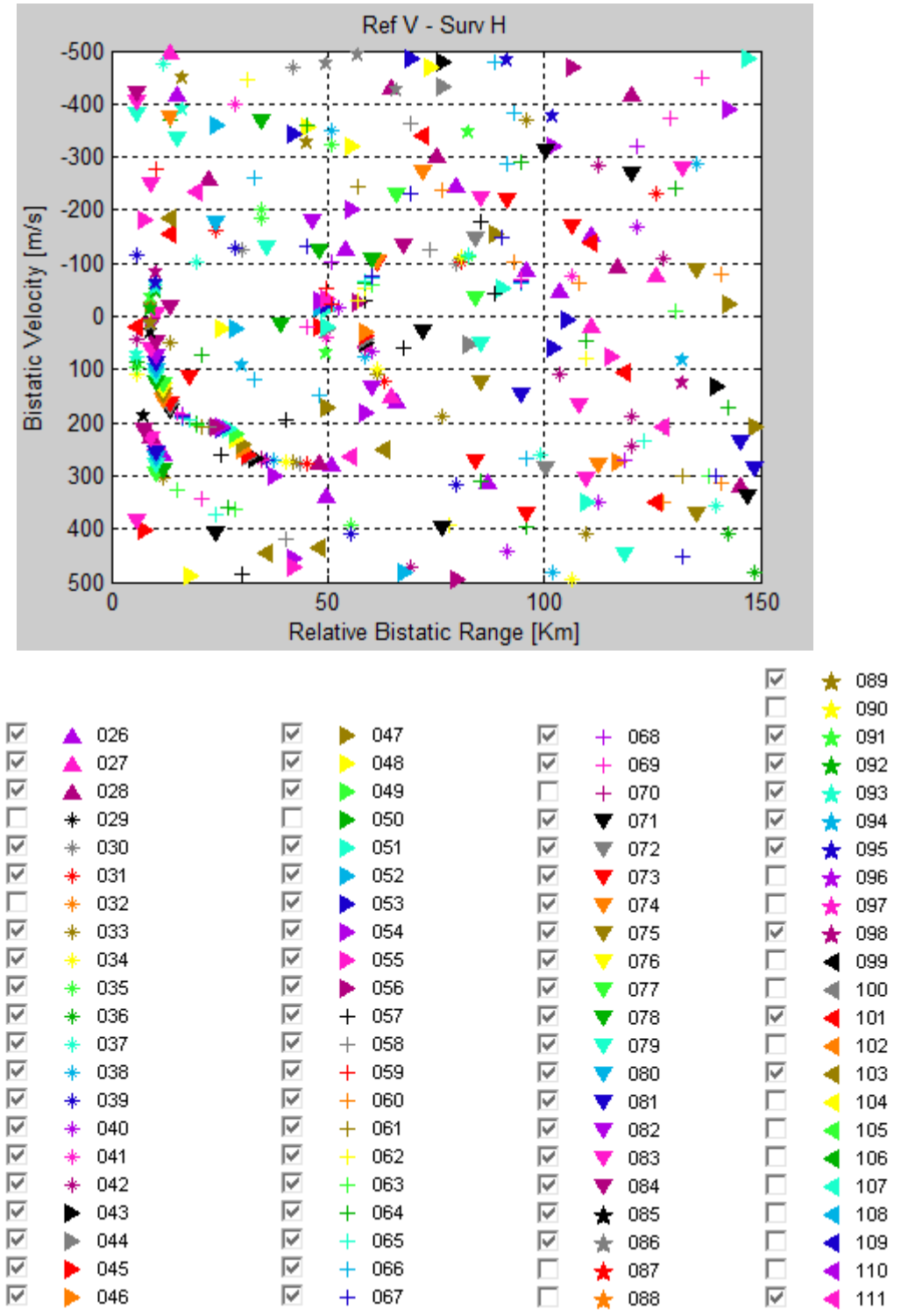

Figure 95 – Plot sequences in the Range-Velocity map for 86 consecutive acquisitions [Configuration 4, Ref V – Surv H, FM channel 92.1MHz].

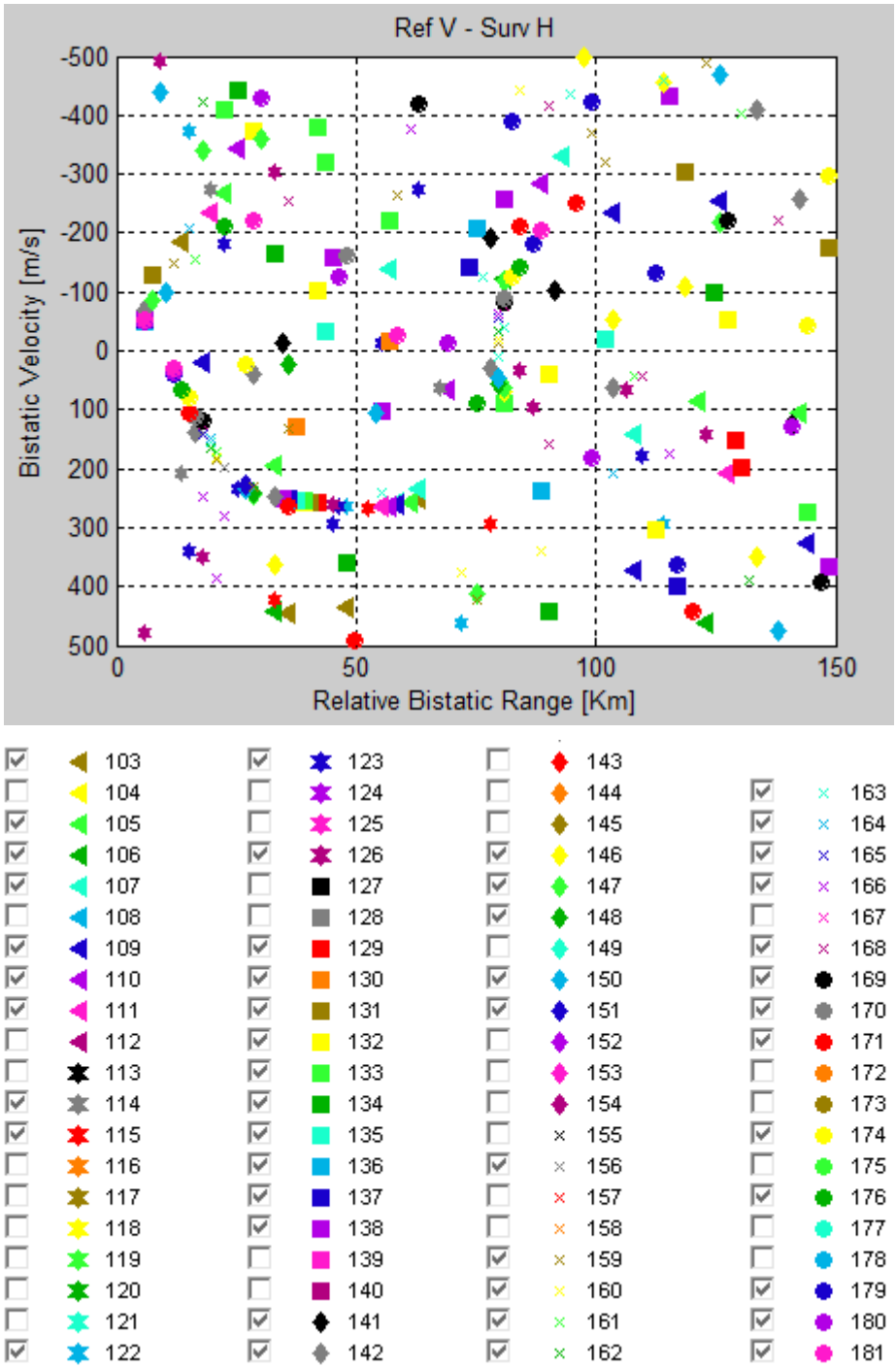

Figure 96 – Plot sequences in the Range-Velocity map for 79 consecutive acquisitions [Configuration 4, Ref V – Surv H, FM channel 92.1MHz].

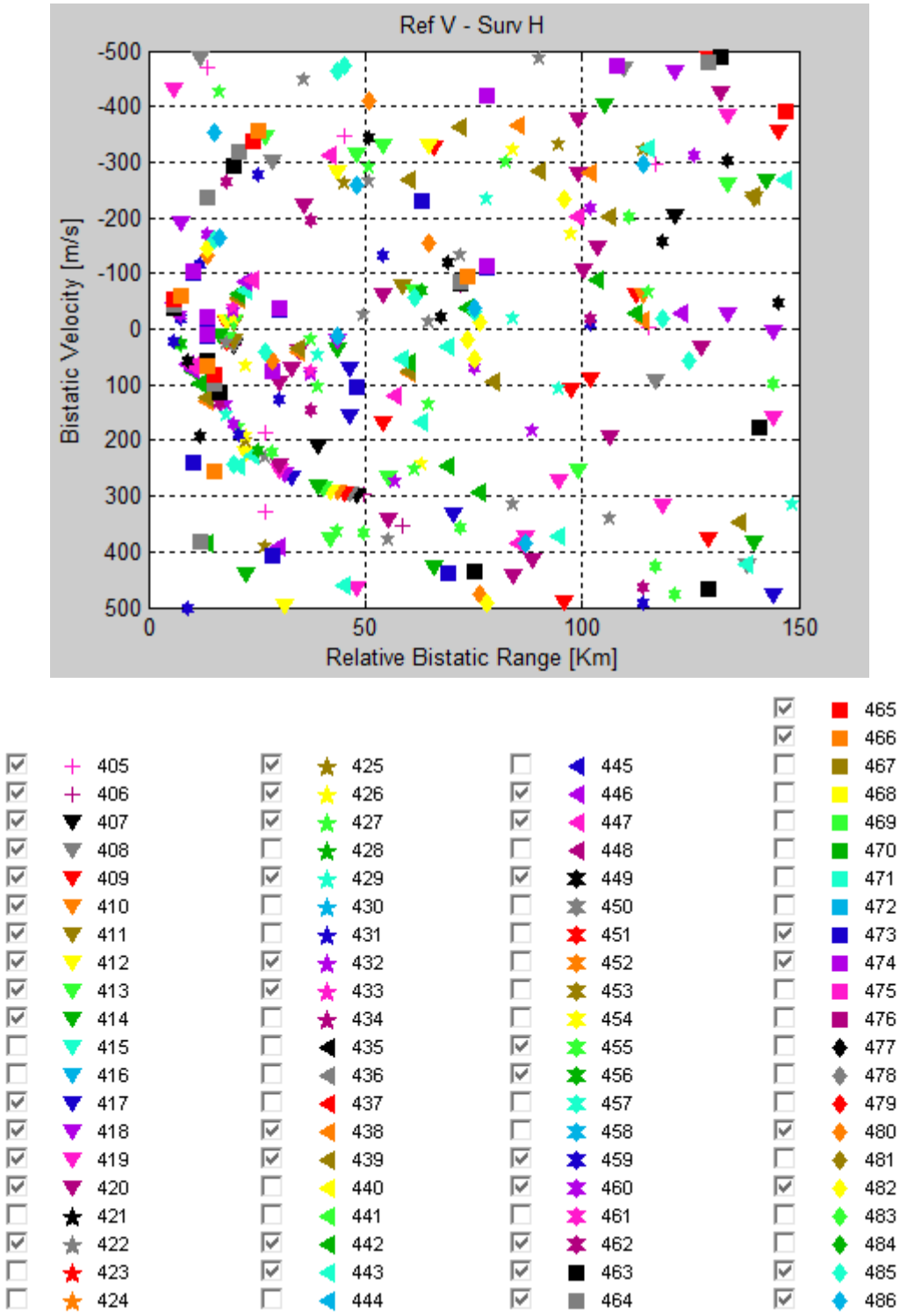

Figure 97 – Plot sequences in the Range-Velocity map for 82 consecutive acquisitions [Configuration 4, Ref V – Surv H, FM channel 92.1MHz].

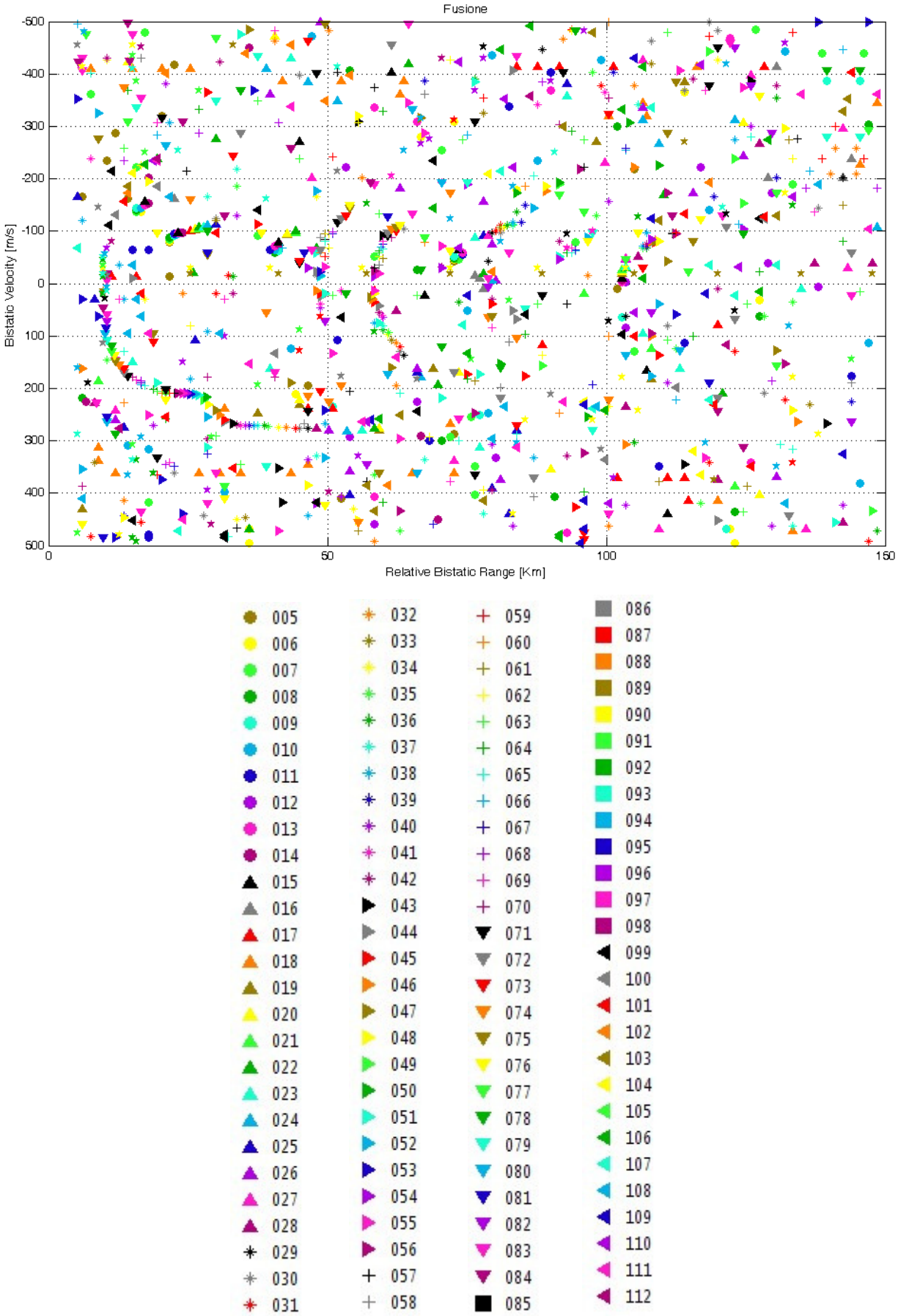

Figure 98 – Plot sequences in the Range-Velocity map for 108 consecutive acquisitions [Configuration 4, SUM of Ref V – Surv H and Ref V – Surv V, FM channel 92.1MHz].

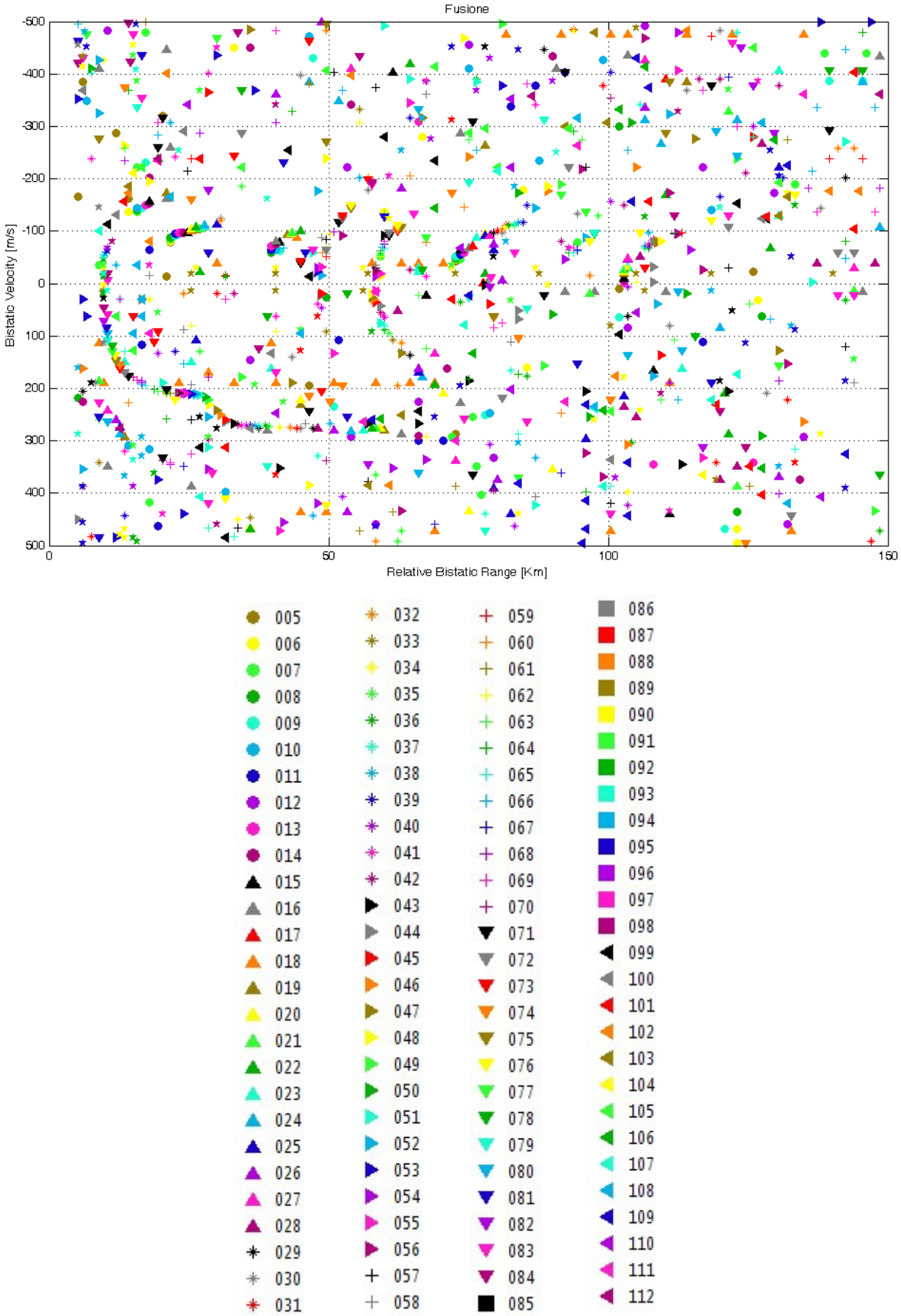

Figure 99 – Plot sequences in the Range-Velocity map for 108 consecutive acquisitions [Configuration 4, SUM of Ref H – Surv H and Ref H – Surv V, FM channel 92.1MHz].

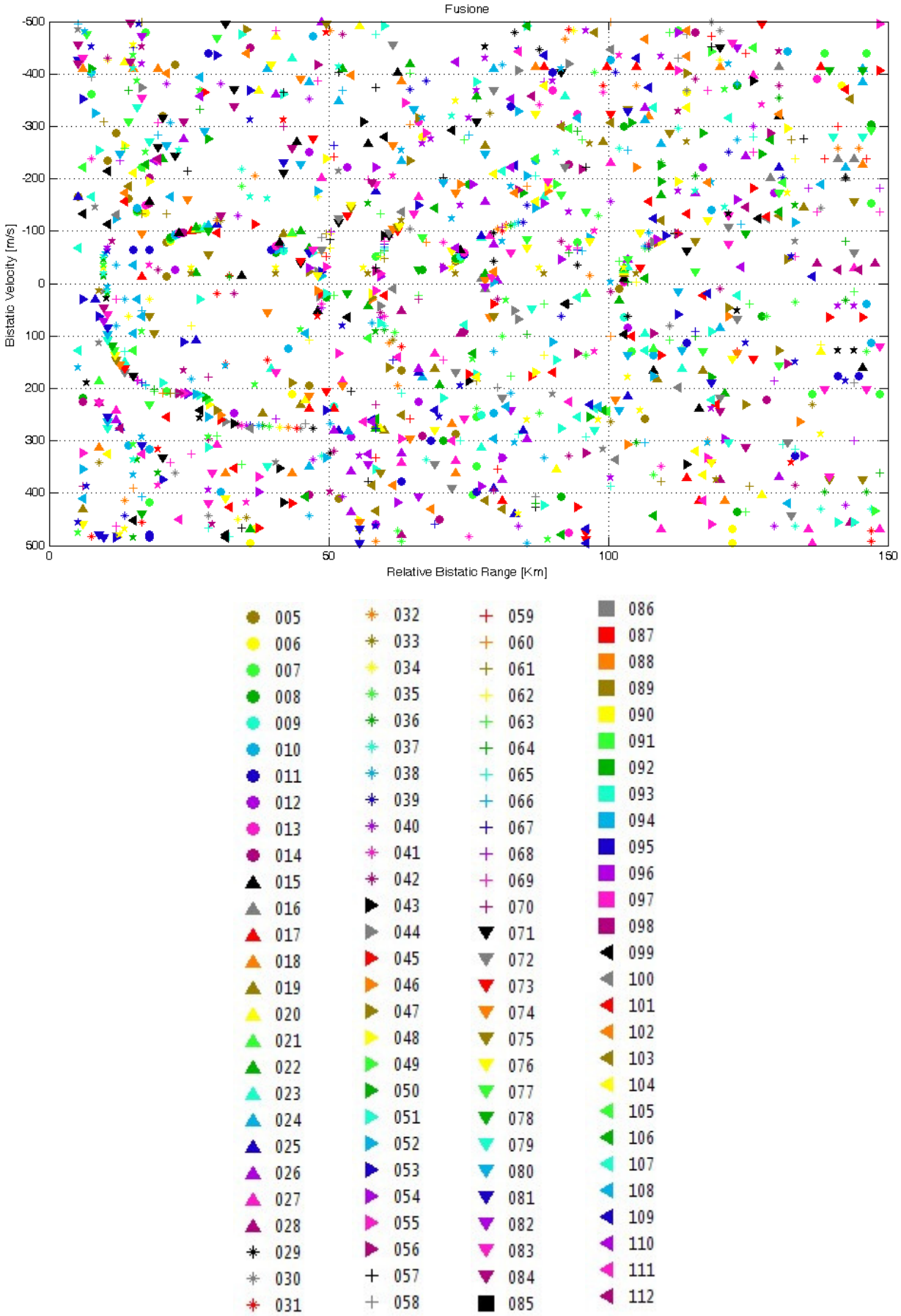

Figure 100 – Plot sequences in the Range-Velocity map for 108 consecutive acquisitions [Configuration 4, MAX between Ref V – Surv H and Ref V – Surv V, FM channel 92.1MHz].

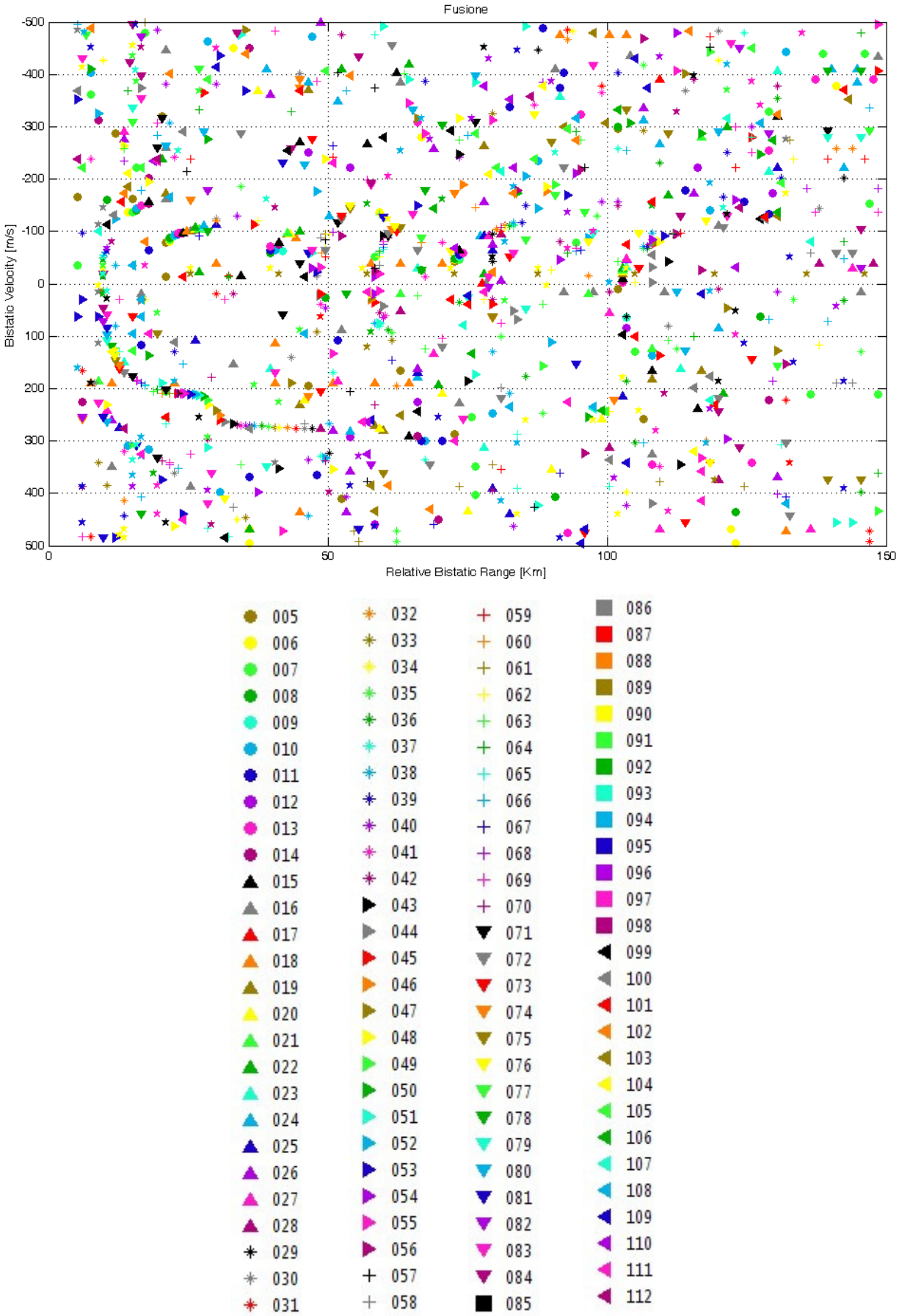

Figure 101 – Plot sequences in the Range-Velocity map for 108 consecutive acquisitions [Configuration 4, MAX between Ref H – Surv H and Ref H – Surv V, FM channel 92.1MHz].

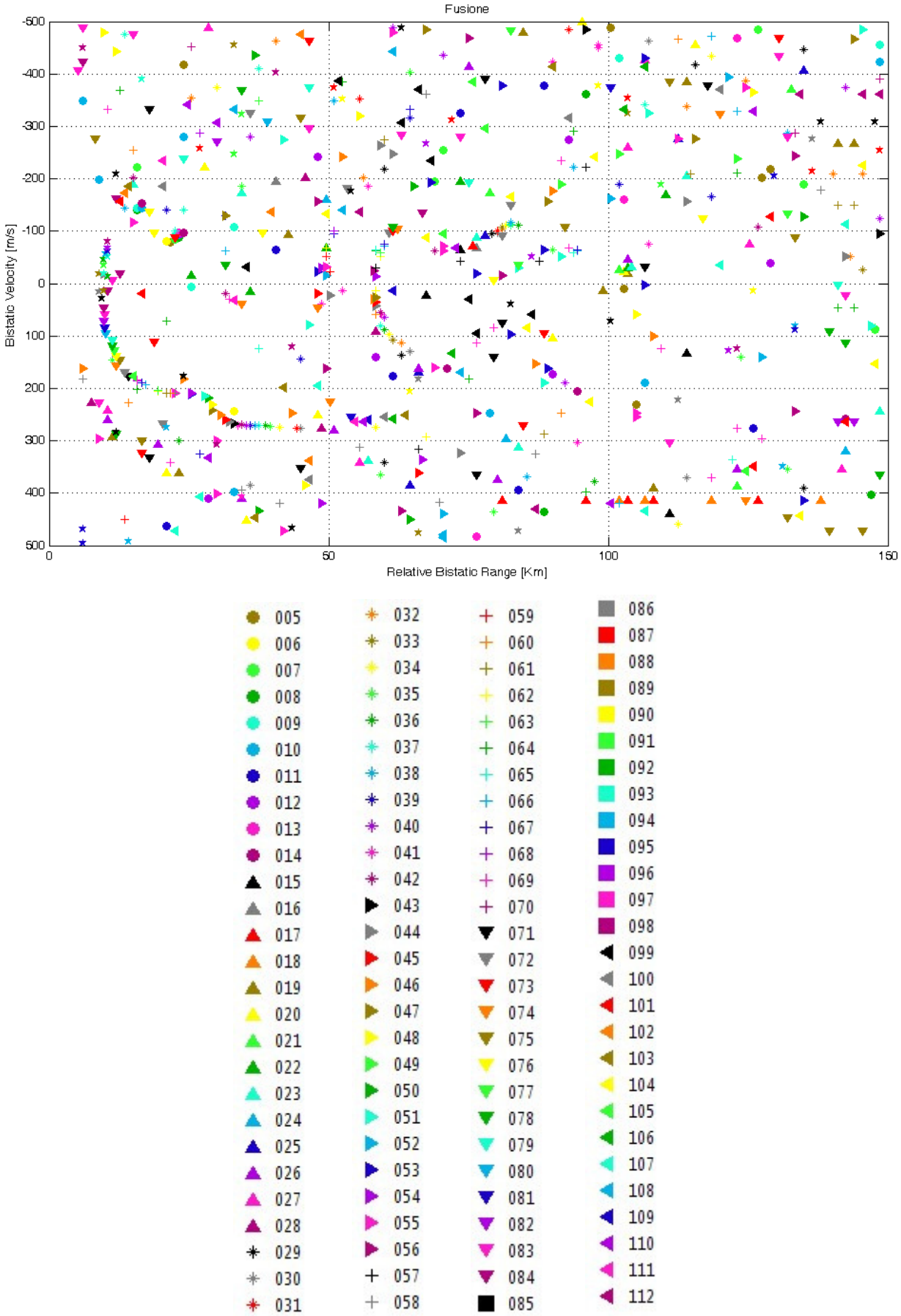

Figure 102 – Plot sequences in the Range-Velocity map for 108 consecutive acquisitions [Configuration 4, MIN between Ref V – Surv H and Ref V – Surv V, FM channel 92.1MHz].

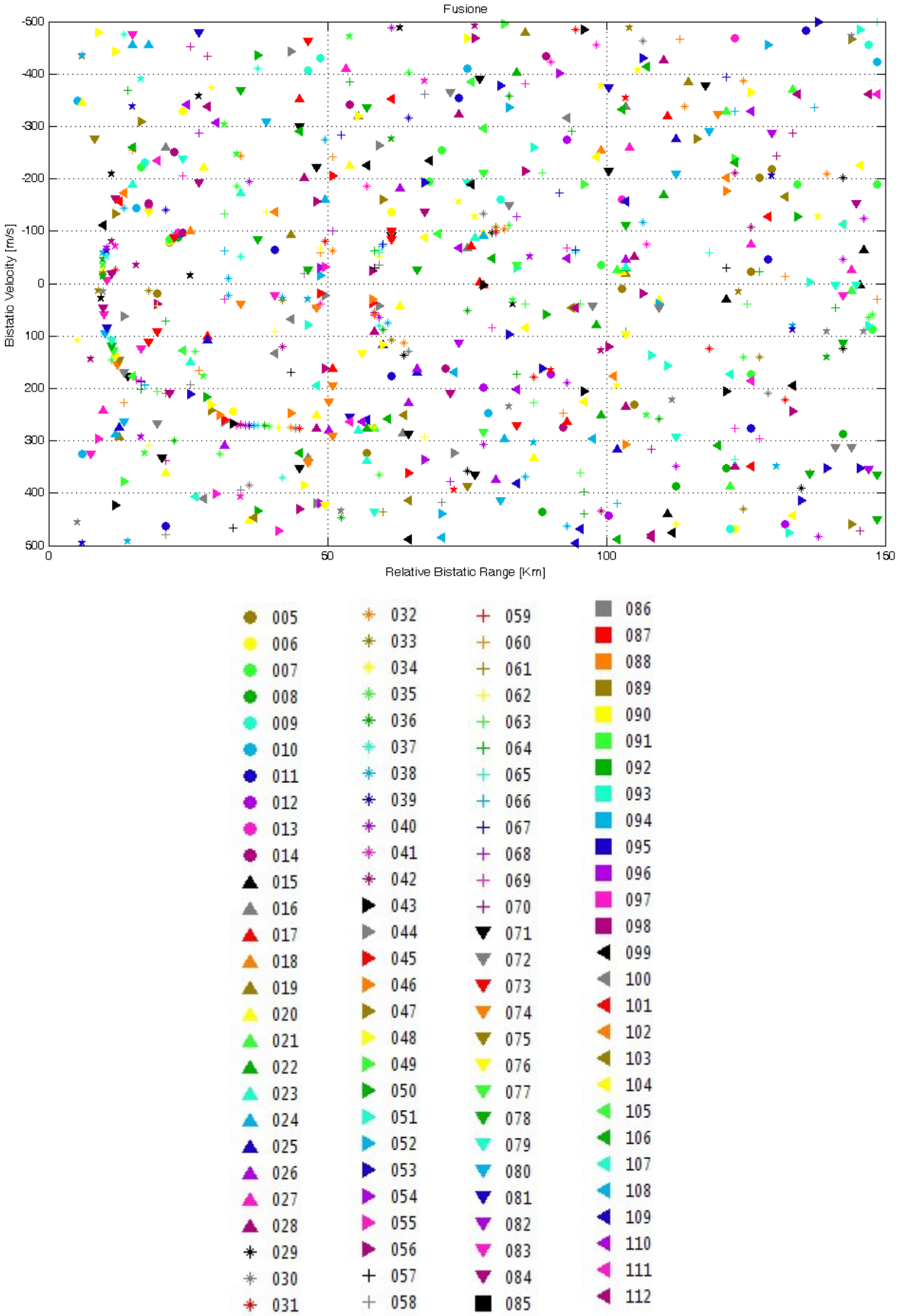

Figure 103 – Plot sequences in the Range-Velocity map for 108 consecutive acquisitions [Configuration 4, MIN between Ref H – Surv H and Ref H – Surv V, FM channel 92.1MHz].

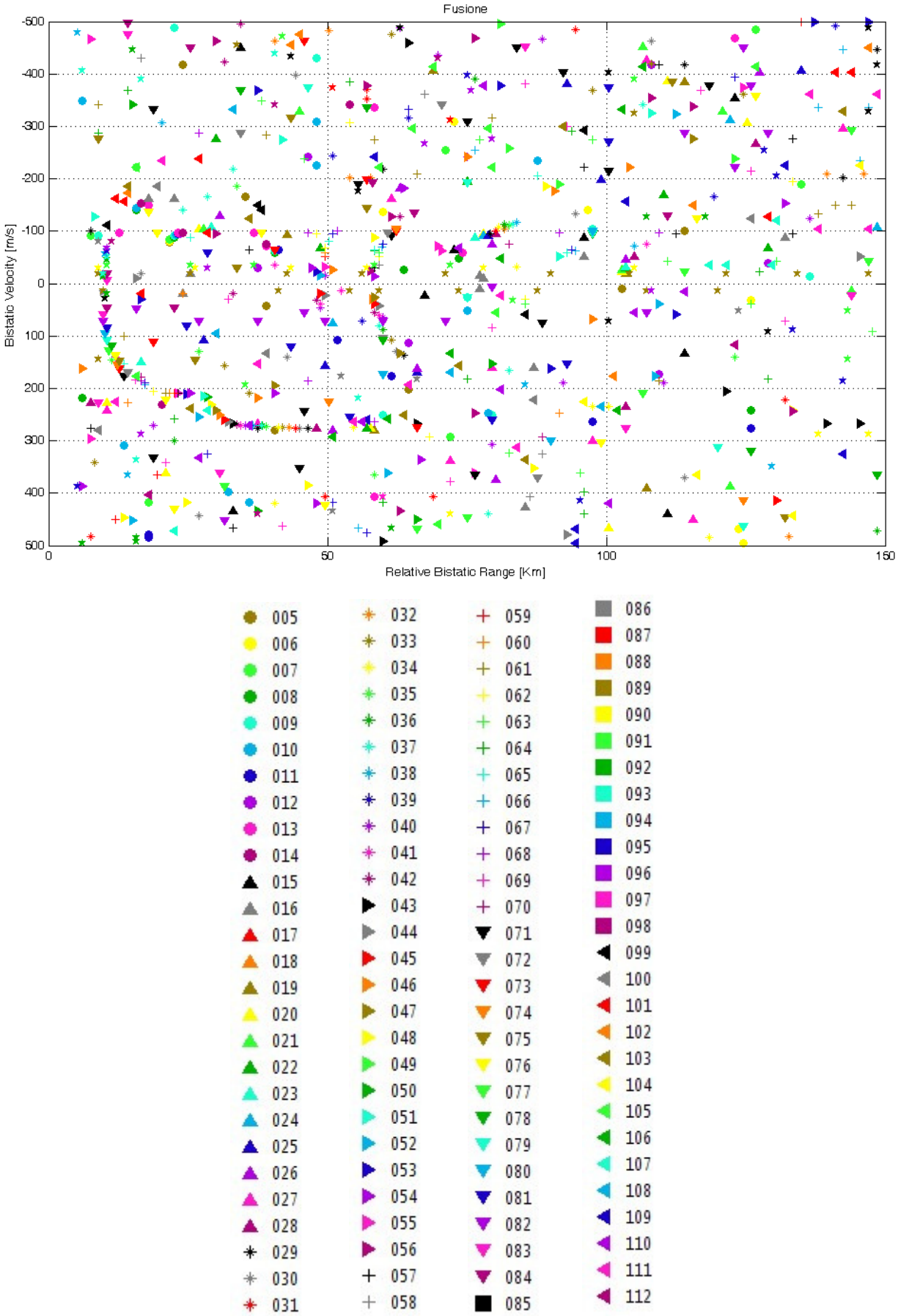

Figure 104 – Plot sequences in the Range-Velocity map for 108 consecutive acquisitions [Configuration 4, DEC with Ref V – Surv H and Ref V – Surv V, FM channel 92.1MHz].

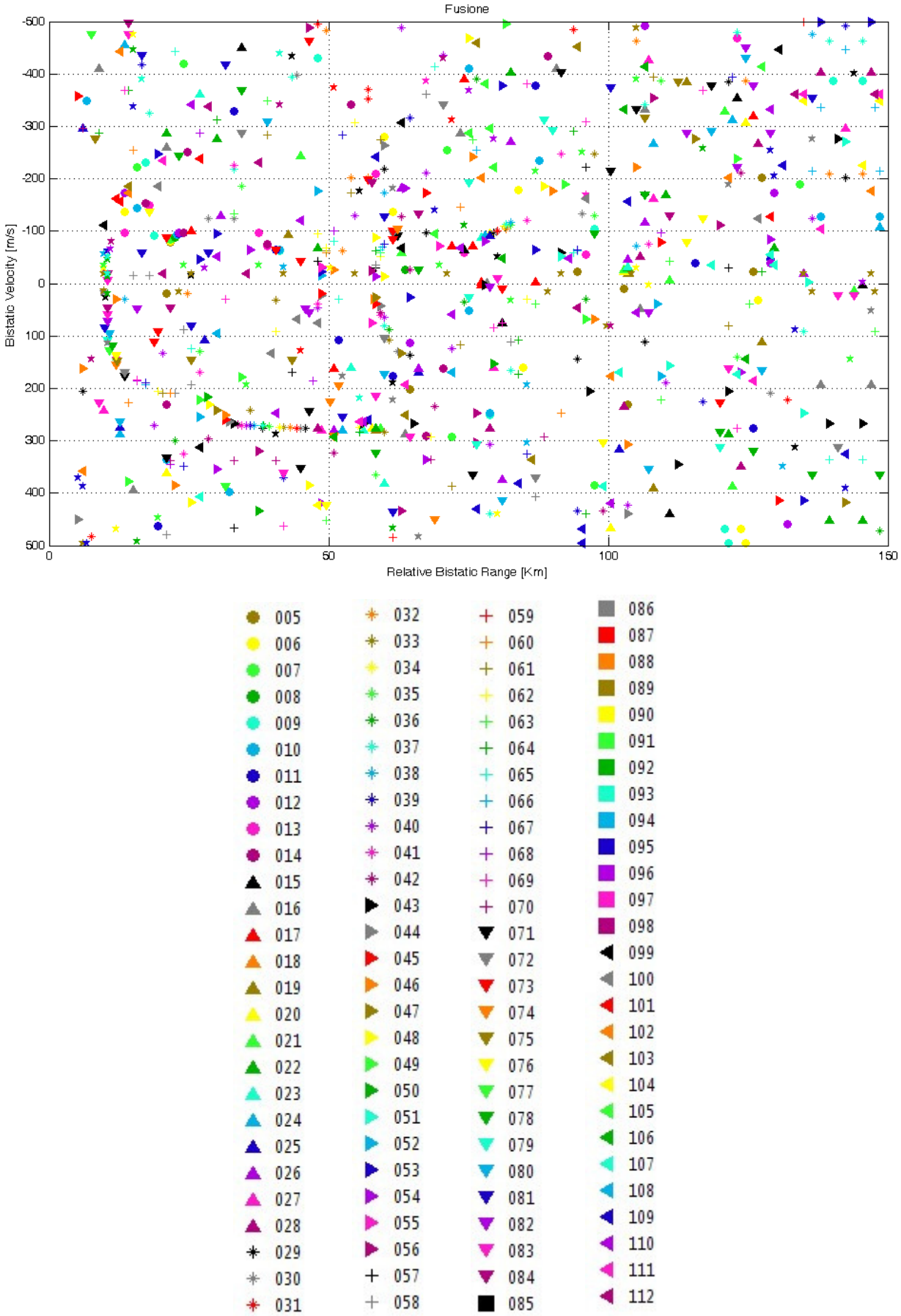

Figure 105 – Plot sequences in the Range-Velocity map for 108 consecutive acquisitions [Configuration 4, DEC with Ref H – Surv H and Ref H – Surv V, FM channel 92.1MHz].

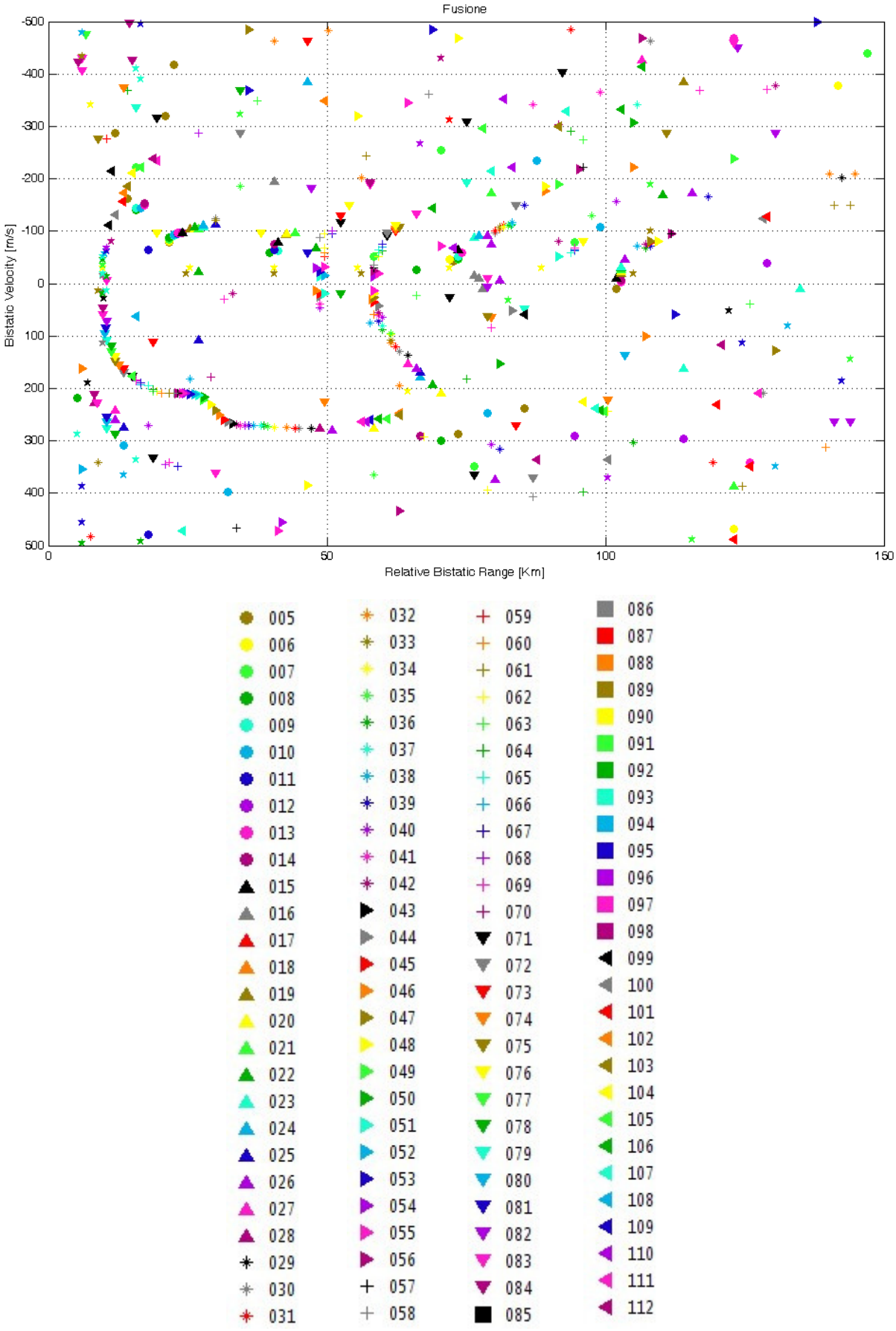

Figure 106 – Plot sequences in the Range-Velocity map for 108 consecutive acquisitions [Configuration 4, SUM of Ref V – Surv H and Ref V – Surv V, FM channel 92.1MHz, P_{fa} control].

IX EXPLOITATION OF DIFFERENT WAVEFORMS OF OPPORTUNITY: DIGITAL TV SIGNALS

IX.1 *Introduction*

As already said in the introduction of this thesis, among broadcast transmitters, digital transmissions such as Digital Audio Broadcasting (DAB) and Digital Video Broadcasting-Terrestrial (DVB-T) represent an interesting choice as waveform of opportunity for PBR system. Currently, digital broadcasting is proliferating and rapidly replacing the analogue counterparts. Specifically, with reference to television broadcast, a number of countries have already switched or planned to switch to the DVB-T standard. These signals show both excellent coverage and wider frequency bandwidth, which results in increased range resolution achievable. Following these considerations, the research activity of the group is also focused on digital broadcasting signals, aiming at realization of a multichannel passive radar prototype based on these signals. This is the reason why last section of this thesis is focused on DVB-T signals and on the problems arising from their use as opportunity waveform in PBR systems.

As previously mentioned, passive radar performs target detection and localization in the time delay/Doppler frequency plane by evaluating the 2D-CCF between the reference signal and the surveillance signal. In addition to the desired reflected target echo, several interferences might corrupt this system: due to the uncontrollable nature of the exploited waveform, the direct path interference (DPI) and the multipath reflections can mask the desired target signal, even in the presence of large delay/Doppler separation.

Basically, the presence of specific features of the DVB-T signal, as guard intervals and pilots [27], introduces a number of undesired deterministic peaks in the 2D-CCF, which might yield significant masking effect on the useful signal and produce false alarms. The level of these peaks cannot be reduced by increasing the integration time [14].

Different techniques have been proposed in order to remove these unwanted deterministic peaks in the DVB-T signal 2D-CCF. For example, in [14] a guard interval modification (blanking) in the reference

signal is proposed to cope with guard interval peaks, together with two complementary strategies to mitigate the peaks due to the pilots: the power equalization of pilot carriers in the reference signal, and the suppression of pilot carrier components in the reference signal prior to correlation.

In [15], firstly the guard interval blanking is applied to remove guard interval peaks; the pilots are modified directly on the pilot carriers, in order to remove the pilot peaks in the 2D-CCF. This approach has two advantages: *(i)* computational load reduction and *(ii)* convenient realization compared with the conventional filters and equalizers.

In both the mentioned approaches, pilots blanking and equalization are performed in two parallel stages, because the two algorithms cannot be applied simultaneously. Two different 2D-CCF are obtained which are then combined to obtain the final 2D-CCF where the undesired deterministic peaks have been removed following the consideration that the residual peaks in the two separate 2D-CCFs appear at different delay/Doppler locations.

Here a new approach for DVB-T 2D-CCF evaluation is proposed, aimed at removing the unwanted deterministic peaks without splitting the processing in two parallel stages: this is achieved by using a linear filter based on the knowledge of the expected value of the DVB-T signal Ambiguity Function (AF in the following).

This section is organized as follows: sub-section IX.2 briefly describes the DVB-T signal and the corresponding 2D-CCF. The new approach for 2D-CCF control is presented in sub-section IX.3 . The proposed approach is compared to existing ones in sub-section IX.4 with reference to a case study. Finally, some conclusions, together with some remarks for future works, are drawn in sub-section IX.5 .

IX.2 *DVB-T Signal*

The DVB-T signal is organized in frames [27]. Each frame, as sketched in Figure 107, consists of 68 orthogonal frequency division multiplexing (OFDM) symbols; four consecutive transmission frames constitute a super frame. Two main different transmission modes are foreseen in the DVB-T standard, *2k* and *8k*; each symbol has a specific useful part duration (T_U) and number of carriers, according to the transmission mode: specifically, each symbol is composed by a set of 1705 carriers in the *2k* mode and 6817 carriers in the *8k* mode. Carrier spacing is equal to $1/T_U$ (4.464 KHz in 2k mode and 1.116 KHz in 8k mode).

Four different nominal bandwidths are foreseen:

- 8 MHz, with elementary period T = 7/64μs (elementary period is the inverse of the nominal system clock rate, e.g. about 9.14 MHz for 8 MHz channels)
- 7 MHz, with T = 1/8μs
- 6 MHz, with T = 7/48μs
- 5 MHz, with T = 7/40μs

In addition to useful data, each symbol contains pilots (divided into continual and scattered) and TPS (Transmission Parameter Signalling), for receiver synchronization and transmission parameter estimation. TPS and continual pilots are transmitted at fixed carriers inside each symbol. Positions of scattered pilots are periodic over four OFDM symbols (super symbol), see Figure 108.

Modulation of data and TPS is normalized, while the pilots (continual and scattered) are transmitted at boosted power level (the average power $E_P = 16/9$).

Summarizing, OFDM symbol useful part (T_U) is composed of:

- data, with three different modulation schemes: QPSK, 16-QAM, 64-QAM;
- continual pilots, transmitted at fixed carriers;
- scattered pilots, transmitted at fixed carriers over four symbols;
- Transmission Parameter Signalling (TPS) pilots, transmitted at fixed carriers.

A cyclic prefix copying the last part of each OFDM symbol (named guard interval) is inserted in order to prevent possible inter-symbol interference (ISI) in OFDM. Four different durations of the guard

interval (T_G) are foreseen: 1/32, 1/16, 1/8 or 1/4 of the useful part duration T_U. Main parameters of *2k* and *8k* mode DVB-T signal for 8 MHz channels are shown in Table 57.

Parameter	**2k mode**	**8k mode**
Number of carriers	1705	6817
Duration T_U	224 µs	896 µs
Guard interval duration T_G (1/32)	7 µs	28 µs
Guard interval duration T_G (1/16)	14 µs	56 µs
Guard interval duration T_G (1/8)	28 µs	112 µs
Guard interval duration T_G (1/4)	56 µs	224 µs
Total bandwidth	7.61 MHz	7.61 MHz

Table 57 – Main parameters of 2k and 8k mode DVB-T signals

The AF is defined as [17]:

$$\left|\chi(\tau, f_d)\right|^2 = \left|\int_{-\infty}^{+\infty} u(t)u^*(t+\tau)\exp(j2\pi f_d t)dt\right|^2 \qquad \text{(IX.1)}$$

where *u(t)* is the DVB-T complex baseband signal, τ is the time delay and f_d is the Doppler frequency. As highlighted in [14] and [15], the AF of the DVB-T signal shows the presence of one main peak and many side peaks. These (unwanted) peaks are generated by the introduction, in the OFDM symbol, of the guard interval and pilot carriers. Specifically, in *2k* mode, the peak generated by guard interval occurs at τ = 224 µs (T_U), while the peaks due to pilot carriers can be divided into two categories (Figure 109): (i) intra-symbol peaks ($0 \leq \tau \leq T_s=T_U+T_G$), and (ii) inter-symbol peaks ($\tau > T_s$).

These peaks can mask the signal reflected from targets and/or introduce false alarms.

IX.3 *A new approach for 2D-CCF improvement*

As briefly described in the introduction of this section, different approaches have been proposed to improve the DVB-T signal CAF by removing these undesired peaks. The techniques proposed in [14] and [15] are summarized in the block diagram sketched in Figure 110.

However, these approaches intrinsically require frame synchronization and two different procedures performed in two parallel processing stages. In this section we present a new approach for the unwanted peaks removal that is performed by processing the reference signal with an appropriate linear filter with coefficients designed on the basis of the knowledge of the expected value of the DVB-T signal AF. A simplified block diagram of the proposed approach is sketched in Figure 111.

The approaches described in [14] and [15] only exploit the knowledge of pilot carrier positions inside the OFDM symbols for the removal of the unwanted deterministic peaks in the DVB-T signal. In particular, continual pilots have fixed positions from symbol to symbol, while scattered pilot carriers are inserted into the same positions every four OFDM symbols (named as *super-symbol*). Therefore, time synchronization is firstly required as a necessary operation.

After the frame synchronization of the reference signal, the guard interval blanking removes the guard interval peak. Then, the intra-symbols and the inter-symbols peaks are removed through the pilot equalization and the pilot blanking, respectively. These two procedures are performed in two parallel stages, because blanking and equalization cannot be applied simultaneously. Two different 2D-CCFs are evaluated (CAF_1 and CAF_2 in Figure 110, where CAF stands for Cross-Ambiguity Function), as a result of the correlation between the target signal (after DPI suppression) and the two pre-filtered versions of the reference signal. Finally, CAF_3 is obtained by combining CAF_1 and CAF_2.

Figure 112(a) and Figure 112(b) show the DVB-T signal AF after the pilot equalization and pilot blanking procedures, respectively. Figure 113 shows the DVB-T signal AF obtained by combining these two procedures. As it is apparent, both the described approaches are able to mitigate the undesired deterministic peaks due to the presence of guard interval and pilot carriers in the OFDM symbols, but this removal is performed with two parallel stages (blanking and equalization cannot be applied simultaneously), and synchronization is required as a necessary operation. Finally, the non linear combination of two different CAFs can yield the presence of artefacts, especially when multiple targets are present. These are the reasons why we propose a new approach for Ambiguity Function improvement.

In this new approach, after DPI suppression, the unwanted peaks removal is performed by processing the reference signal with a linear filter based on the knowledge of the expected value of the DVB-T signal AF.

Assuming the independence of data and pilots in an OFDM symbol, we can write the DVB-T signal as the sum of two contributions, DATA and PILOTS:

$$s(t) = s_{DATA}(t) + s_{PILOTS}(t) \tag{IX.2}$$

As a consequence, we can also evaluate the expected value of the DVB-T signal Ambiguity Function, and in particular its autocorrelation function, as the sum of two contributions, a statistical one due to the data, and a deterministic one due to pilots:

$$E\{R(\tau)\} = E\left\{\int s(t+\tau)s^*(t)dt\right\} = \overline{R}_{DATA}(\tau) + R_{PILOTS}(\tau) \tag{IX.3}$$

Due to independence of data at different OFDM symbols, the autocorrelation of data is equal to zero for delays higher than the symbol useful part duration T_U (see Figure 114), while the autocorrelation of pilots is periodic of period $4T_S$ (*super-symbol* duration), see Figure 115, so that using an integration time equal to an integer number of *super-symbols*, the expected value of the AF has a periodic behaviour. Moreover, the minimum distance between two contiguous peaks in the DVB-T signal AF is directly related to the guard interval duration. Finally, there is a periodicity of a factor three in the positions of the scattered pilots, when considering two consecutive symbols (Figure 108).

In Figure 116 the overall result for the expected value of the DVB-T signal AF, that is the combination of Figure 114 and Figure 115, is shown, while Figure 117 shows the same result obtained with simulated data, generated according to the DVB-T standard (*2k* in this case). It is easy to notice the almost perfect correspondence between the expected value and the average AF of simulated data. And this correspondence will be as higher as the number of averaged symbols increase, according to what typically happens in passive radar systems, where long integration times are used in order to achieve reasonable SNR values.

Based on these properties, and on the knowledge of the expected value of the DVB-T signal AF, an appropriate filter can be designed to remove all sidelobes of the AF. This is easily shown to provide a very limited loss in SNR. The filter coefficients are obtained by solving a proper optimization problem, and the filter can be easily applied in the frequency domain by Fourier transforming the input data and

then performing the inverse Fast Fourier Transform (FFT) on the filtered data, as sketched in Figure 118.

Figure 119 shows the DVB-T signal AF obtained after the application of the innovative approach proposed in this section (linear filter). It is easy to see that the performance of the described algorithm is largely comparable with the existing techniques (see Figure 113 for comparison): it is able to completely remove the undesired peaks in the AF due to the presence of the guard interval and of the pilot carriers in the OFDM symbols. Also the Peak-to-Sidelobe Level (PSL) achieved by the two approaches is largely comparable. However, the proposed approach does not require two complementary and parallel processing stages, thus reducing the overall computational load and the system complexity. Finally, a limited power loss is obtained, because the DVB-T signal CAF improvement is achieved without performing the guard interval and pilots blanking.

IX.4 *Performance comparison*

The performance of the different approaches for DVB-T signal 2D-CCF control has been analyzed in the previous section in the presence of a single target. In that case, the proposed approach has been shown to yield largely comparable performance with respect to existing ones. However, as a consequence of the parallel processing and the following non linear combination of two different 2D-CCF, the approach proposed in [14] and [15] is expected to yield undesired residual peaks in some particular scenarios, when more than one target is present, located at different time delays. For example, let us assume the presence of four different targets, at delays $\tau_1 = 109$ μs, $\tau_2 = 328$ μs, $\tau_3 = 503$ μs and $\tau_4 = 809$ μs, respectively. Target echo amplitudes are set so that they show the following levels at the output of the matched filter: -3 dB, -15 dB, -30 dB and -6 dB respectively. Figure 120 shows the 2D-CCF projection along τ when using the standard matched filter (original reference signal). The corresponding 2D-CCFs obtained by pre-filtering the reference signal using the approach in [14] and [15] and using the new proposed approach are reported in Figure 121(a) and Figure 121(b), respectively.

As it is apparent, in Figure 121 (a) some undesired residual peaks are present, which might yield false alarms and/or mask other weak targets. In fact, while the non linear minimum combination works extremely well for a single target, it shows a potential weakness when multiple or extended targets are present. Specifically, pilots equalization yields inter-symbol spurious sidelobes, and pilots blanking yields intra-symbol spurious sidelobes. When the spurious peaks are temporally displaced, the non linear combination (minimum operation) achieves the desired result. However, when the spurious peaks are co-located, the combination is not able anymore to remove them and false targets appear in the scene.

In contrast, the proposed approach is able to totally remove the undesired peaks with a single processing stage, so that the four injected targets appear as isolated peaks in the resulting 2D-CCF (Figure 121 (b)) and can be easily detected against the background. Moreover, it does not require the time synchronization of the received DVB-T stream, that is instead necessary to implement the previously proposed approaches.

Notice that the reference signal pre-filtering yields a mismatching with respect to the target signal which results in a SNR loss. This loss is evaluated as the ratio between the SNR at the output of the matched filter and the SNR at the output of the proposed linear filter. Therefore, the numerical value of this loss can be written as:

$$\text{SNR loss} = \frac{(\sum_k |s_k|^2)(\sum_k |a_k|^2)}{\left|\sum_k a_k s_k\right|^2} \qquad \text{(IX.4)}$$

where s_k are the target signal samples and a_k are the reference samples at the output of the filter (a_k=s_k^* in the matched filter).

The SNR loss obtained with the linear filter proposed in this paper is equal to about 0.77dB. Similarly, the SNR loss obtained by using the output of the equalization and blanking procedures are equal to 0.27dB and 0.94dB, respectively. Taking into account the non linear combination between these two procedures, we can conclude that SNR losses due to the new approach and the existing ones are largely comparable.

IX.5 *Conclusions*

A new approach for DVB-T signal CAF improvement has been proposed and compared to existing ones. The new technique exploits a linear filter based on the knowledge of the expected value of the DVB-T signal autocorrelation function to remove the undesired peaks in the CAF, which can mask the signals from targets and/or introduce false alarms. A reduced computational complexity and a limited power loss are achieved, by avoiding the parallel equalization/blanking procedures. The proposed approach is shown to yield comparable performance with respect to existing approaches. However, it appears not to require time synchronization and to be more robust in particular situations. For example, when the multiple or extended targets are present, the non linear combination of two 2D-CCFs is not always able to remove all the spurious sidelobes, thus resulting in the presence of false targets in the scene. Obviously, also the Doppler (Velocity) dimension has to be carefully taken into account when facing with the 2D-CCF evaluation issue; moreover, it is well known that these undesired peaks due to the presence of specific features of the DVB-T signal are also present in the Doppler domain. However, the positions of these peaks are predictable, and it is possible to find some periodical behaviour of these peaks also in the Doppler domain. So the linear filter introduced for CAF improvement can be extended to this domain aiming at completely removing the unwanted peaks in the map, while preserving the interesting advantages of a linear approach in terms of reduced computational complexity, not necessary synchronization and robustness to spurious sidelobes, with respect to existing techniques. The extension of this filter to Doppler domain is actually an open problem, but with work in progress in this direction.

IX.6 *Figures*

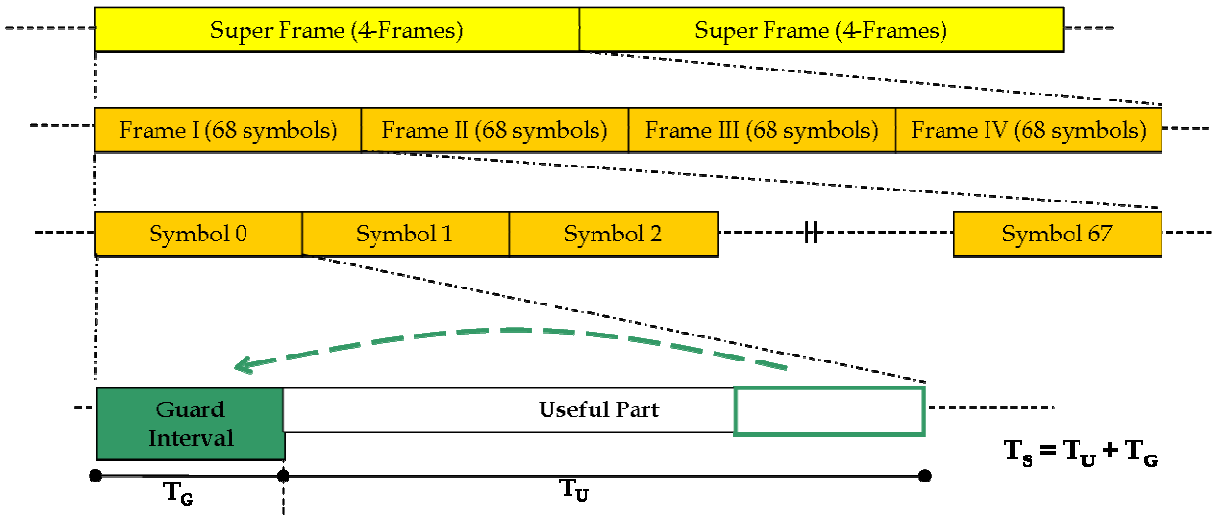

Figure 107 – DVB-T signal organization.

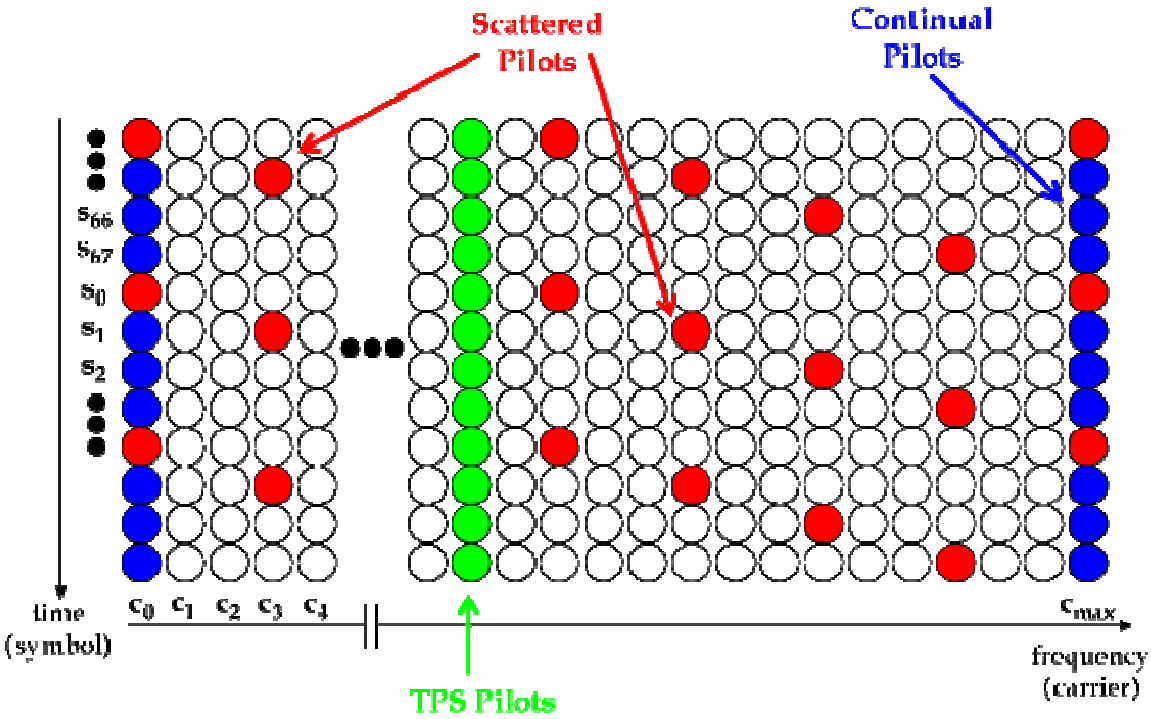

Figure 108 – DVB-T signal frame structure.

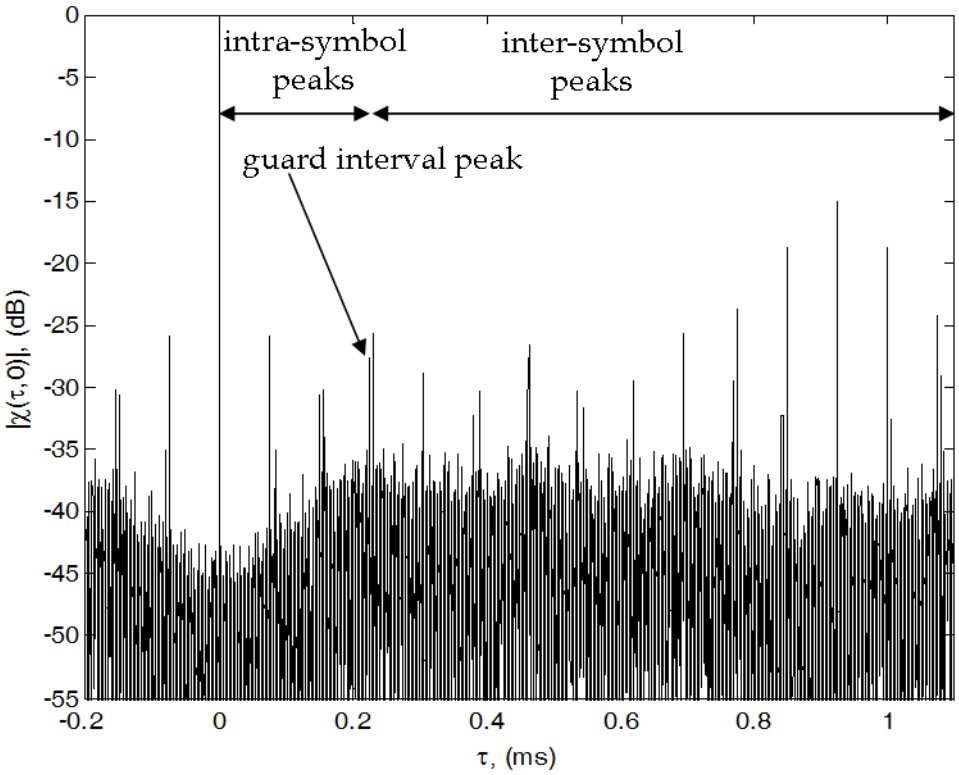

Figure 109 – DVB-T signal autocorrelation function.

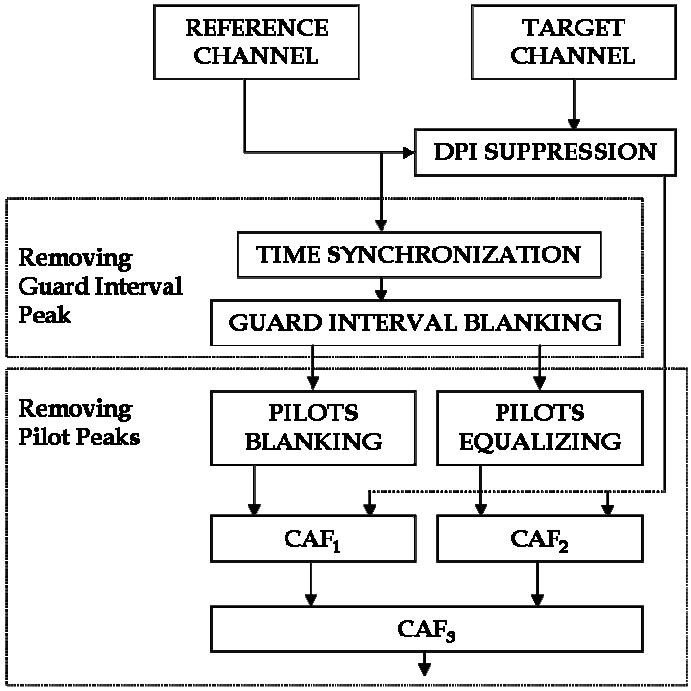

Figure 110 – Block diagram of the DVB-T signal 2D-CCF improvement techniques proposed in [14] and [15].

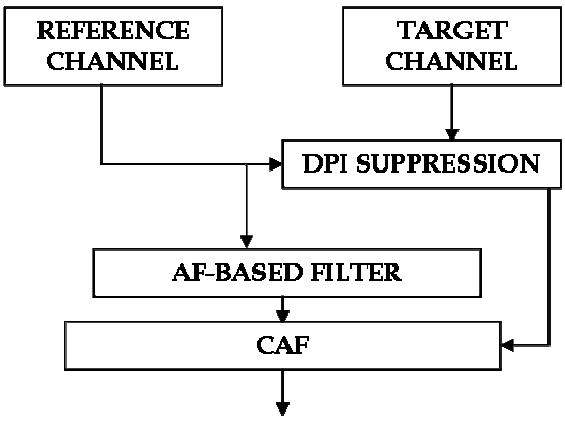

Figure 111 – Block diagram of the DVB-T signal 2D-CCF improvement technique based on a linear filter.

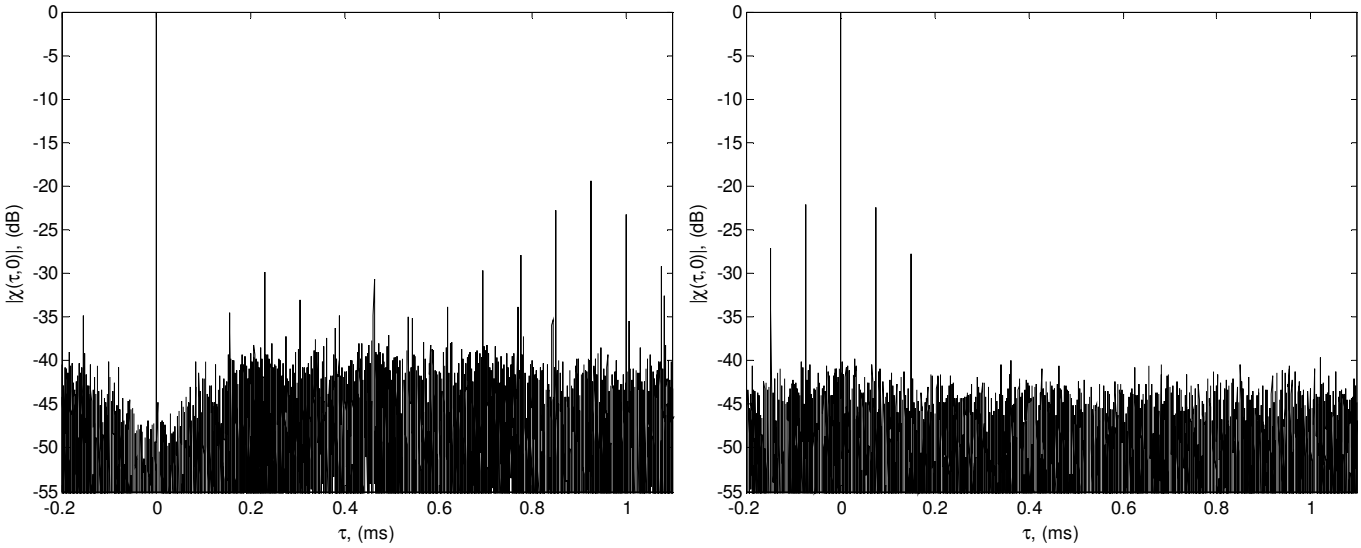

(a) (b)

Figure 112 – DVB-T signal AF after pilots equalizing (a), and after pilot blanking (b).

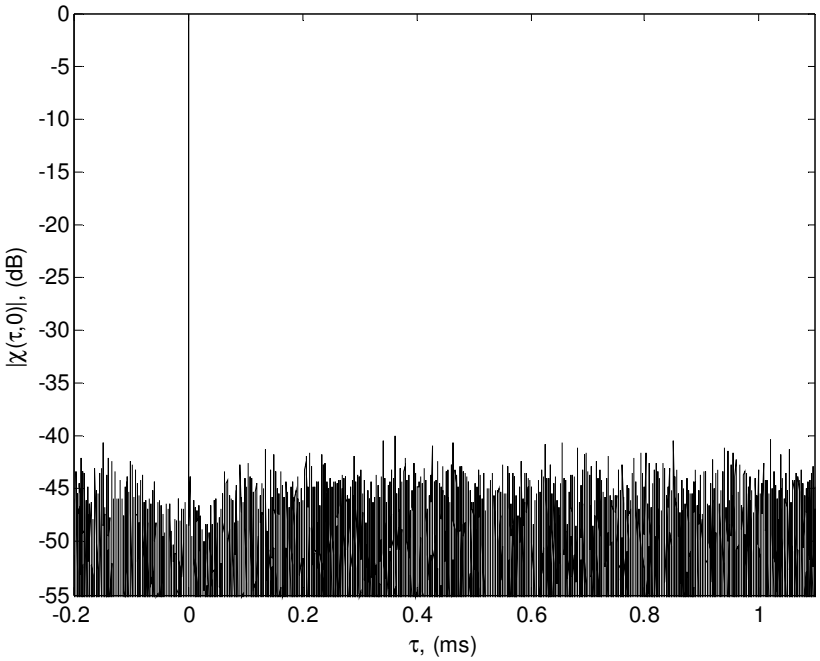

Figure 113 – DVB-T signal AF after combining equalization and blanking.

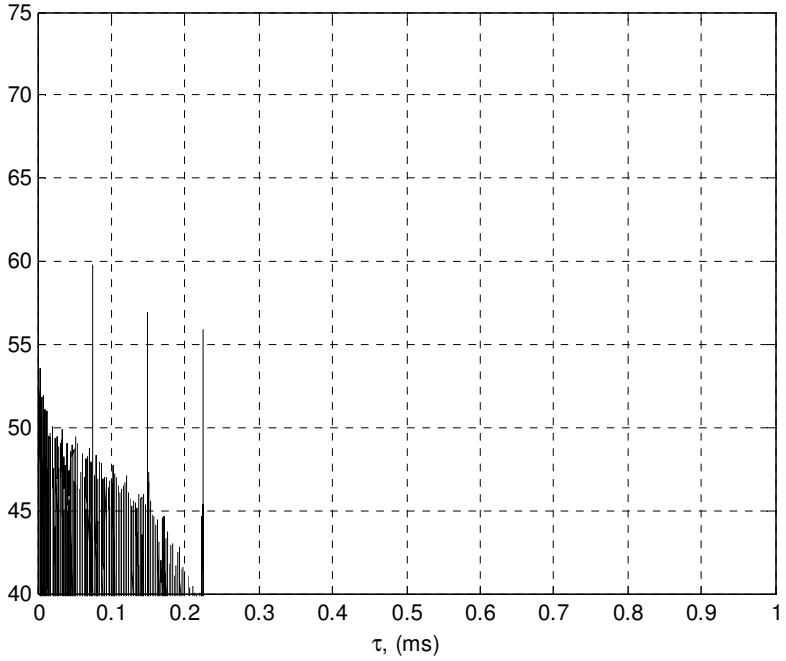

Figure 114 – DVB-T AF of data.

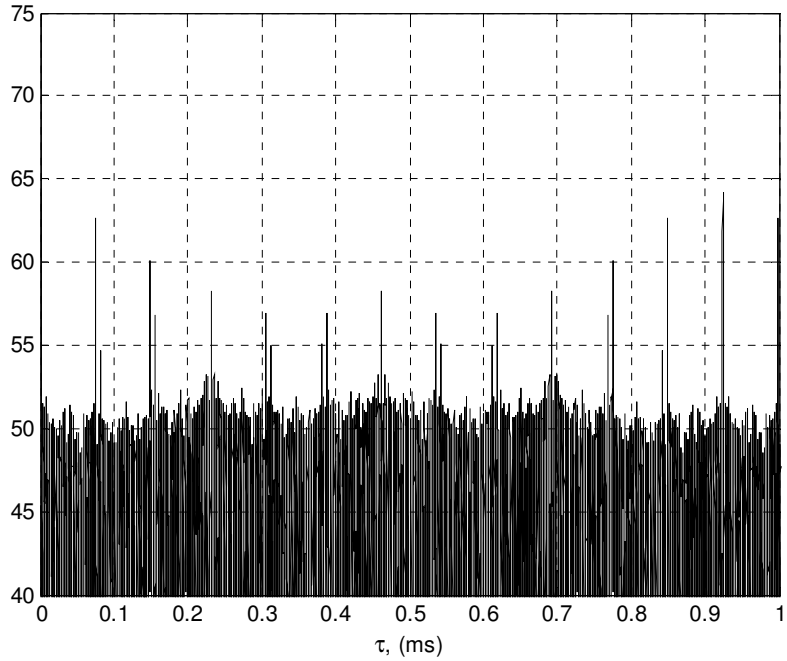

Figure 115 – DVB-T AF of pilots.

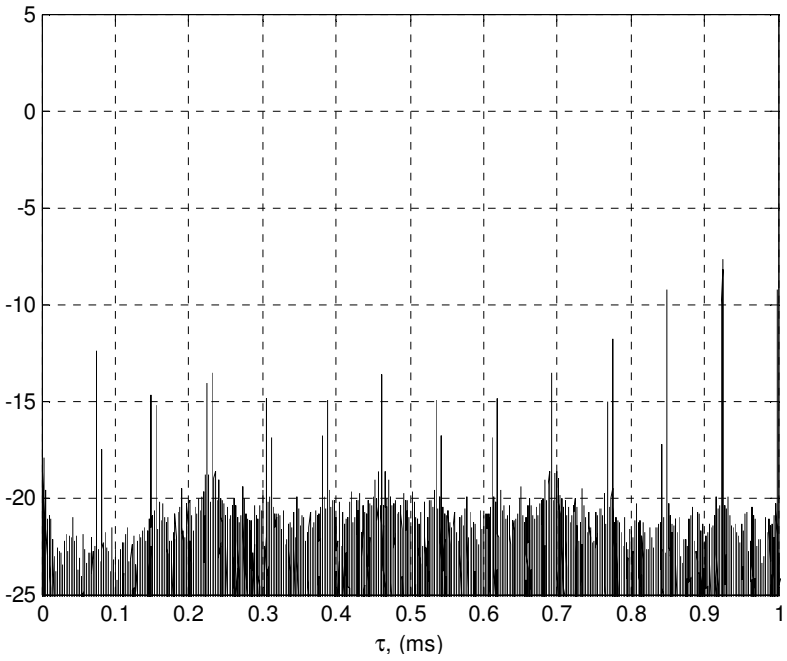

Figure 116 – Expected value of the DVB-T signal AF.

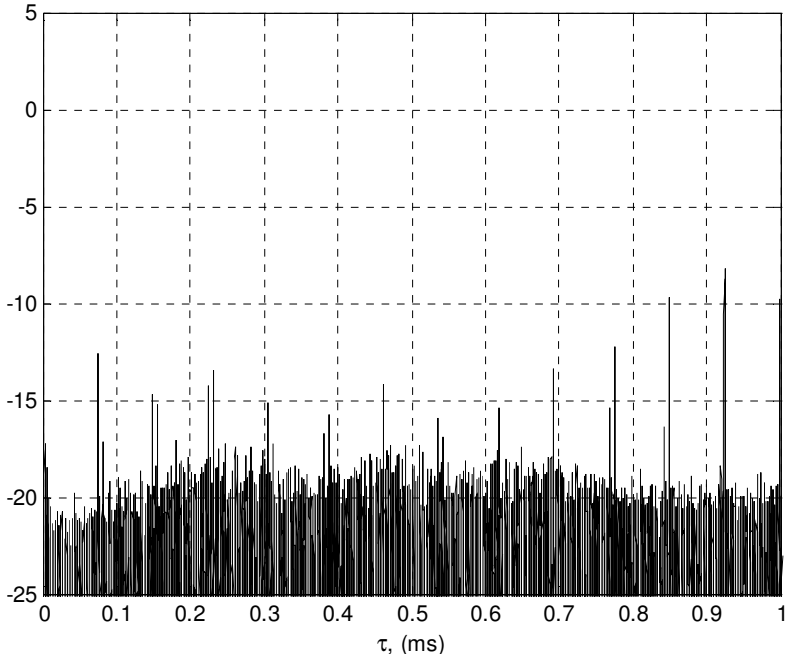

Figure 117 – Average AF of simulated data.

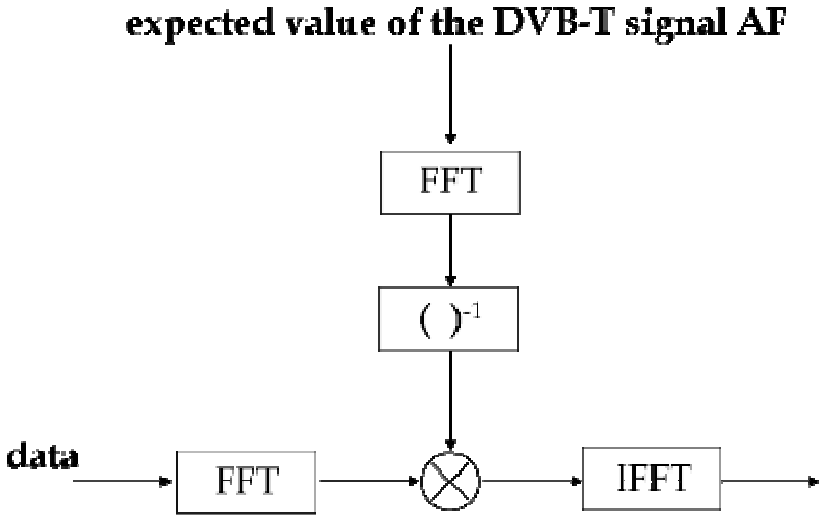

Figure 118 – Block diagram of the linear filter implementation.

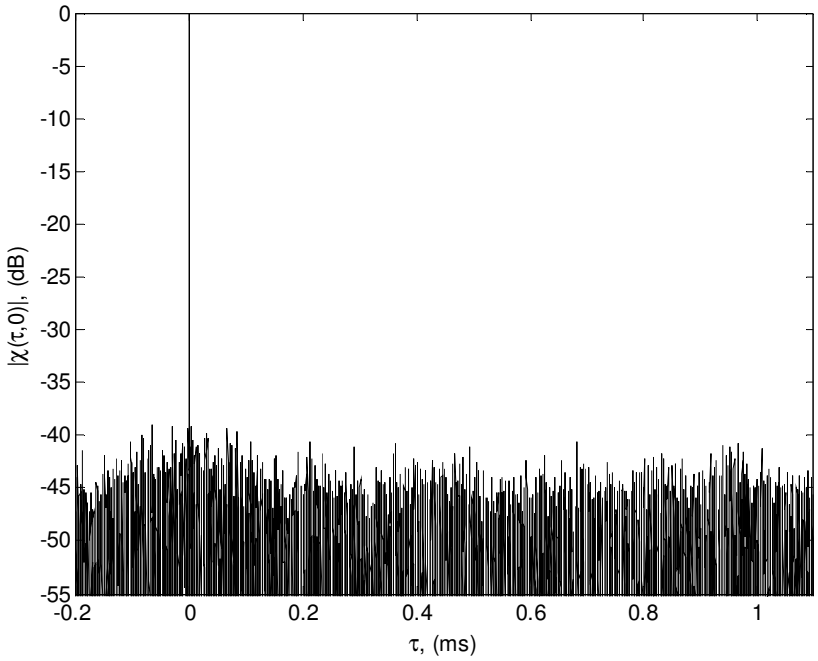

Figure 119 – DVB-T AF after application of the linear filter.

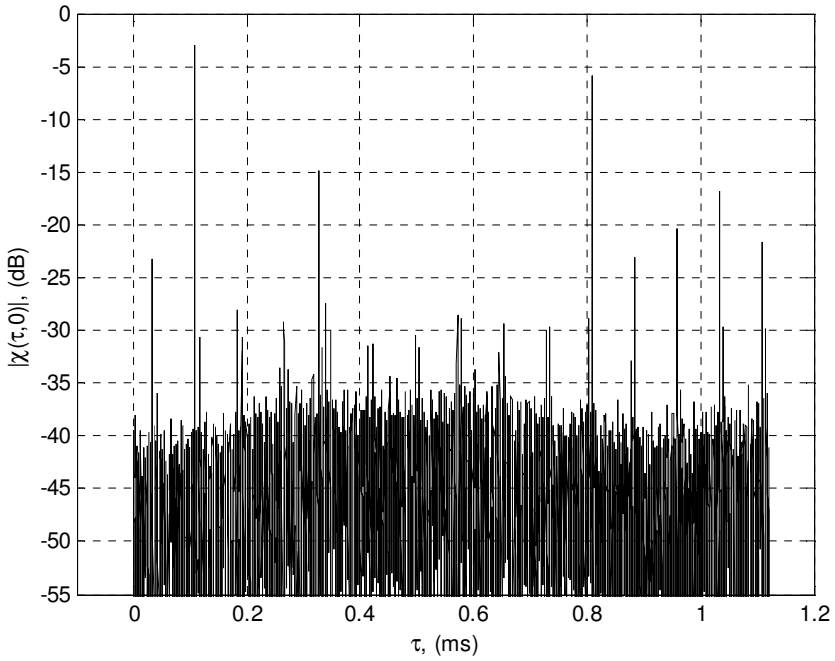

Figure 120 – 2D-CCF projection along τ.

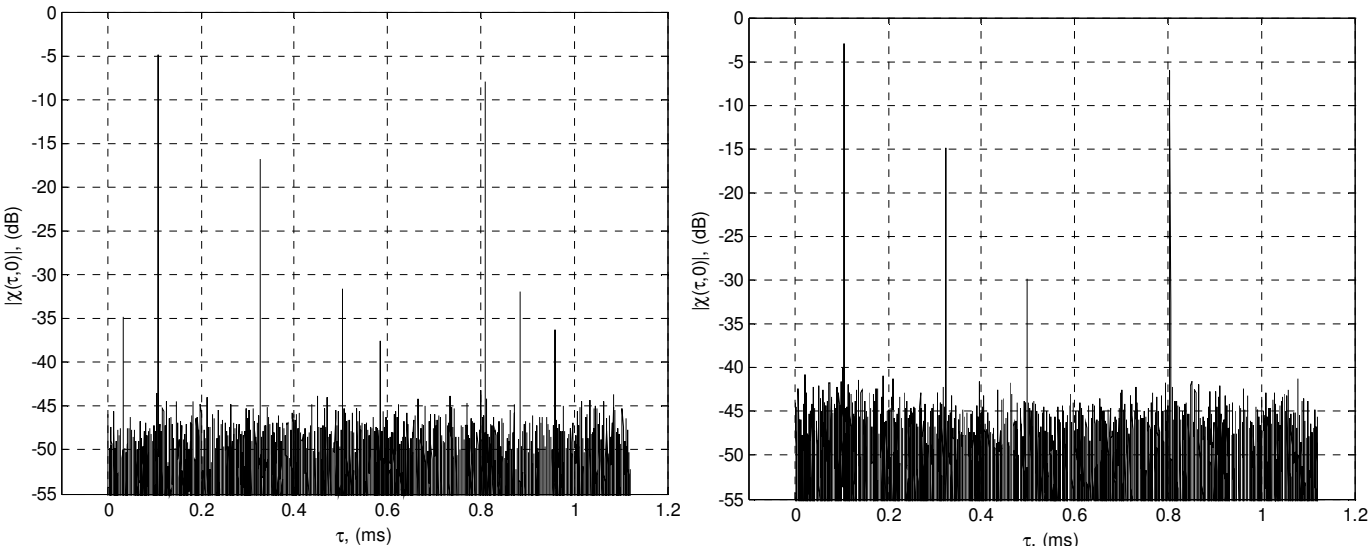

(a) (b)

Figure 121 – 2D-CCF projection along τ after combining equalization and blanking (a) and with the new approach based on a linear filter (b).

X REFERENCES

[1] Special Issue on Passive Radar Systems - IEE Proceedings on Radar, Sonar and Navigation, June 2005, Vol. 152, Issue 3, pp. 106-223.

[2] Griffiths, H.D., and Long, N.R.W.: 'Television based bistatic radar', IEE Proc. F, Commun. Radar Signal Process., 1986, 133, (7), pp. 649–657.

[3] Howland, P.E.: 'Target tracking using television-based bistatic radar', IEE Proc., Radar Sonar Navig., 1999, 146, (3), pp. 166–174.

[4] P.E. Howland, D. Maksimiuk, G. Reitsma, "FM radio based bistatic radar" IEE Proceedings on Radar, Sonar and Navigation, Volume 152, Issue 3, 3 June 2005 Page(s):107-115.

[5] Griffiths, H.D.; Baker, C.J., "Passive coherent location radar systems. Part 1: performance prediction" IEE Proc. Radar, Sonar and Navigation, Volume 152, No. 3, June 2005, pp.153-159.

[6] K.S. Kulpa and Z. Czekała, "Masking effect and its removal in PCL radar", IEE Proc. Radar Sonar Navig., Vol. 152, No. 3, June 2005, pp. 174-178.

[7] R. Cardinali, F. Colone, C. Ferretti, P. Lombardo, "Comparison of clutter and multipath cancellation techniques for passive radar", IEEE 2007 Radar Conference, Boston, (MA), USA, March 2007.

[8] F. Colone, R. Cardinali, P. Lombardo, "Cancellation of clutter and multipath in passive radar using a sequential approach", IEEE 2006 Radar Conference, Verona (NY), USA, April 24-27, 2006, pp. 393-399.

[9] F. Colone, D. W. O'Hagan, P. Lombardo, C. J. Baker "A multistage processing algorithm for disturbance removal and target detection in Passive Bistatic Radar", IEEE Transactions on Aerospace and Electronic Systems, Vol. 45, No. 2, April 2009, pp. 698-722.

[10] Baker, C.J.; Griffiths, H.D.; Papoutsis, I., "Passive coherent location radar systems. Part 2: waveform properties", IEE Proc. Radar, Sonar and Navigation, Volume 152, Issue 3, June 2005, pp.160-168.

[11] A. Lauri, F. Colone, R. Cardinali, C. Bongioanni, P. Lombardo, "Analysis and emulation of FM radio signals for passive radar", 2007 IEEE Aerospace Conference, Big Sky (MT), USA, 3-10 March 2007.

[12] D. Poullin, "Passive detection using digital broadcasters (DAB, DVB) with COFDM modulation", IEE Proc. on Radar Sonar Navig., Vol. 152, No. 3, June 2005, pp. 143-152.

[13] Coleman, C.; Yardley, H.; "Passive bistatic radar based on target illuminations by digital audio broadcasting", IET Radar, Sonar & Navigation, Volume 2, Issue 5, October 2008.

[14] R. Saini and M. Cherniakov, "DTV signal ambiguity function analysis for radar application", IEE Proc. on Radar, Sonar and Navigation, Vol. 152, No. 3, June 2005, pp. 133-142.

[15] Z. Gao, R. Tao, Y. Ma, and T. Shao, "DVB-T Signal Cross-Ambiguity Function Improvement for Passive Radar", Radar, 2006. CIE '06. International Conference on, pp. 1-4, 16-19 Oct. 2006.

[16] N. J. Willis, "Bistatic Radar", Scitech Publishing Inc., Raleigh, NC, 2nd ed, ISBN: 1-891121-45-6.

[17] M. Skolnik, "Introduction to radar systems", Mc Graw Hill , 2nd ed, 1984, ISBN: 0-07-Y66572-9.

[18] D. Barton, " Modern Radar Systems" Artech House Inc., Norwood, MA, 1988.

[19] J.V. Di Franco, W.L Rubin, "Radar detection", Artech House Inc., Dedham, MA, ISBN: 0-89006-092-4.

[20] C. Bongioanni, F. Colone, P. Lombardo, "Performance Analysis of a Multi-Frequency FM Based Passive Bistatic Radar", 2008 IEEE Radar Conference, Rome, Italy, May 26-30, 2008.

[21] P. P. Gandhi and S. A. Kassam, "Analysis of CFAR processors in nonhomogeneous background", IEEE Transactions on Aerospace and Electronic Systems vol. 24, pp. 427-445, July 1988.

[22] E.K. Al-Hussaini, "Performance of the `smaller of' and `greater of' detectors integrating M pulses", Proceedings of the IEEE, Volume 76, Issue 6, June 1988, pp:731 – 733.

[23] H. Rohling, "Radar WAR thresholding in clutter and multiple target situations", IEEE Transactions on Aerospace and Electronic Systems, vol. 19, pp. 608-621, July 1983.

[24] C. Bongioanni, F. Colone, S. Bernardini, L. Lelli, A. Stavolo, P. Lombardo, “Passive radar prototypes for multifrequency target detection”, Signal Processing Symposium 2007, Jachranka Village (Poland) 24-26 May 2007.

[25] P. Lombardo, F. Colone, C. Bongioanni, A. Lauri, T. Bucciarelli, “PBR activity at INFOCOM: adaptive processing techniques and experimental results”, 2008 IEEE Radar Conference, Rome, Italy, May 26-30, 2008.

[26] D. Langellotti, F. Colone, C. Bongioanni, P. Lombardo, “Comparative study of Ambiguity Function evaluation algorithms for Passive Radar”, International Radar Symposium IRS 2009, Hamburg, Germany, 9-11 September 2009, pp. 325-329.

[27] European Telecommunications Standard Institute, “Digital video broadcasting (DVB); framing structure, channel coding and modulation for digital terrestrial television”, EN 300 744, V1.1.2, 1997.